Structure and Properties of Interfaces Between Monolayer WS_2 and Dielectric Substrates

Katherine Milton

UNIVERSITY COLLEGE LONDON

Physics and Astronomy

Submitted to University College London (UCL) in partial fulfilment of the requirements for the award of the degree of Doctor of Philosophy.

Primary supervisor: **Alexander Shluger**
Secondary supervisor: **Anna Regoutz**
Examining committee: **Natalia Martsinovich, Dorothy Duffy**

Thesis submission date: **12th February 2025**

Declaration

I, **Katherine Milton**, confirm that the work presented in this thesis is my own. Where information has been derived from other sources, I confirm that this has been indicated in the thesis.

Katherine Milton
London, United Kingdom
12th February 2025

Abstract

This thesis utilises density functional theory and *ab initio* molecular dynamics methods to model a realistic interface between the transition metal dichalcogenide WS_2 and SiO_2, with confined water between the two materials.

The electronic structure of the bulk α-cristobalite phase of SiO_2 was first investigated, focusing on the characteristics of oxygen vacancies in various charge states. It was found that the oxygen vacancy configuration with a stabilising Si-Si bond (i.e. dimer configuration) for the positively charged oxygen vacancy is the most stable in α-cristobalite, in contrast to the α-quartz phase of SiO_2.

Subsequently, the impact of confined water at the WS_2/SiO_2 interface was examined. The structure and dynamics of the water at this interface demonstrated that it is strongly influenced by hydrogen bonding to silanol groups on the SiO_2 surface, resulting in a hydrogen bonding network in one layer with very few water-water hydrogen bonds.

Investigation of the electronic properties at this interface revealed that, on average, the band alignment is not significantly affected by the presence of confined water. However, at shorter timescales, in-gap states are formed between confined water and WS_2.

The oxidation of WS_2 was also studied, showing that water dissociates spontaneously only when both tungsten and sulphur atoms with dangling bonds are exposed at defect sites and edges.

Further efforts were made to employ machine learning to generate density functional tight binding repulsive potentials and confinement parameters for the

$SiO_2/H_2O/WS_2$ interface, allowing for exploration over longer timescales.

Impact Statement

Transition metal dichalcogenides hold significant potential for improving the efficiency of electronic devices, due to their high electron mobility and unique properties as two-dimensional materials. The presence of an intrinsic band gap makes transition metal dichalcogenides strong contenders to replace graphene, which has been extensively pursued as an effective 2D material for electronic applications.

Academically, this research establishes a foundational understanding of substrate interactions in transition metal dichalcogenides, specifically the influence of realistic SiO_2 interfaces with water adsorbates on the properties of monolayer WS_2. By addressing this knowledge gap, these findings enable more precise tailoring of transition metal dichalcogenide behaviour, driving advancements in device design, semiconductor physics, and the exploration of emerging 2D materials. These contributions are set to improve understanding of the impact of experimental practices.

Beyond academia, the outcomes of this work may have implications for the development of sustainable technology. As the global shift away from fossil fuels intensifies, hydrogen is expected to serve as a cornerstone of renewable energy systems. The demonstrated applicability of transition metal dichalcogenides for hydrogen evolution reaction catalysis paves the way for more efficient and scalable production methods. By exploring interfacial influences on material performance and the interaction between water and defect sites, this thesis establishes a foundation for optimising transition metal dichalcogenides in catalysis and electronic device technologies.

UCL Research Paper Declaration Form
referencing the doctoral candidate's own published work(s)

Please use this form to declare if parts of your thesis are already available in another format, e.g. if data, text, or figures:

- *have been uploaded to a preprint server*
- *are in submission to a peer-reviewed publication*
- *have been published in a peer-reviewed publication, e.g. journal, textbook.*

This form should be completed as many times as necessary. For instance, if you have seven thesis chapters, two of which containing material that has already been published, you would complete this form twice.

1. **For a research manuscript that has already been published** (if not yet published, please skip to section 2)

a) **What is the title of the manuscript?**

Difference in Structure and Electronic Properties of Oxygen Vacancies in *α*-Quartz and *α*-Cristobalite Phases of SiO_2

b) **Please include a link to or doi for the work**

https://doi.org/10.3390/ma16041382

c) **Where was the work published?**

Materials

d) **Who published the work?** (e.g. OUP)

MDPI

e) **When was the work published?**

07/02/2023

f) **List the manuscript's authors in the order they appear on the publication**

Katherine L. Milton, Thomas R. Durrant, Teofilo Cobos Freire, Alexander L. Shluger

g) **Was the work peer reviewed?**

30/01/2023

h) **Have you retained the copyright?**

yes

i) **Was an earlier form of the manuscript uploaded to a preprint server?** (e.g. medRxiv). If 'Yes', please give a link or doi)

no

If 'No', please seek permission from the relevant publisher and check the box next to the below statement:

☒

I acknowledge permission of the publisher named under ***1d*** *to include in this thesis portions of the publication named as included in* ***1c****. (CCBY)*

2. **For a research manuscript prepared for publication but that has not yet been published** (if already published, please skip to section 3)

a) **What is the current title of the manuscript?**

b) **Has the manuscript been uploaded to a preprint server?** (e.g. medRxiv; if 'Yes', please give a link or doi)

c) **Where is the work intended to be published?** (e.g. journal names)

d) **List the manuscript's authors in the intended authorship order**

e) **Stage of publication** (e.g. in submission)

3. **For multi-authored work, please give a statement of contribution covering all authors** (if single-author, please skip to section 4)

   Conceptualization, A.L.S. and K.L.M.; methodology, K.L.M. and T.R.D.; validation, K.L.M. and T.R.D.; formal analysis, K.L.M. and A.L.S.; investigation, K.L.M., T.R.D. and T.C.F.; data curation, K.L.M.; writing—original draft preparation, K.L.M. and A.L.S.; writing—review and editing, T.R.D. and A.L.S.; visualization, K.L.M.; supervision, A.L.S.; project administration, A.L.S.; funding acquisition, A.L.S.

   T.R.D was calculated the EPR of alpha-cristobalite. T.C.F. provided the pristine structure of alpha-quartz.

4. **In which chapter(s) of your thesis can this material be found?**

   Chapters 2 and 4

5. **e-Signatures confirming that the information above is accurate** (this form should be co-signed by the supervisor/ senior author unless this is not appropriate, e.g. if the paper was a single-author work)

Candidate

Katherine Milton

Date:

10/12/2024

Supervisor/ Senior Author (where appropriate)

Alexander Shluger

Date 10/02/25

UCL Research Paper Declaration Form

referencing the doctoral candidate's own published work(s)

Please use this form to declare if parts of your thesis are already available in another format, e.g. if data, text, or figures:

- *have been uploaded to a preprint server*
- *are in submission to a peer-reviewed publication*
- *have been published in a peer-reviewed publication, e.g. journal, textbook.*

This form should be completed as many times as necessary. For instance, if you have seven thesis chapters, two of which containing material that has already been published, you would complete this form twice.

1. **For a research manuscript that has already been published** (if not yet published, please skip to section 2)

a) **What is the title of the manuscript?**

Structure and Dynamics of Water Confined at the SiO2/WS2 Interface

b) **Please include a link to or doi for the work**

https://doi.org/10.1021/acs.jpcc.4c08392

c) **Where was the work published?**

The Journal of Physical Chemistry C

d) **Who published the work?** (e.g. OUP)

ACS

e) **When was the work published?**

17/02/2025

f) **List the manuscript's authors in the order they appear on the publication**

K. L. Milton, L. Hargreaves, A. L. Shluger

g) **Was the work peer reviewed?**

Yes

h) **Have you retained the copyright?**

Yes

i) **Was an earlier form of the manuscript uploaded to a preprint server?** (e.g. medRxiv). If 'Yes', please give a link or doi)

No

If 'No', please seek permission from the relevant publisher and check the box next to the below statement:

☒

*I acknowledge permission of the publisher named under **1d** to include in this thesis portions of the publication named as included in **1c** (under CCBY).*

2. **For a research manuscript prepared for publication but that has not yet been published** (if already published, please skip to section 3)

   a) **What is the current title of the manuscript?**

   b) **Has the manuscript been uploaded to a preprint server?** (e.g. medRxiv; if 'Yes', please give a link or doi)

   c) **Where is the work intended to be published?** (e.g. journal names)

   d) **List the manuscript's authors in the intended authorship order**

   e) **Stage of publication** (e.g. in submission)

3. **For multi-authored work, please give a statement of contribution covering all authors** (if single-author, please skip to section 4)

   Conceptualization, A.L.S. and K.L.M.; methodology, K.L.M and L.H..; validation, K.L.M; formal analysis, K.L.M. and A.L.S.; investigation, K.L.M.; data curation, K.L.M. and L.H. ; writing—original draft preparation, K.L.M. and A.L.S.; writing—review and editing, A.L.S.; visualization, K.L.M.; supervision, A.L.S.; project administration, A.L.S.; funding acquisition, A.L.S.

4. **In which chapter(s) of your thesis can this material be found?**

   Chapter 5

5. **e-Signatures confirming that the information above is accurate** (this form should be co-signed by the supervisor/ senior author unless this is not appropriate, e.g. if the paper was a single-author work)

Candidate

Katherine Milton

Date:

06/05/2025

Supervisor/ Senior Author (where appropriate)

Alexander Shluger

Date 06/05/25

UCL Research Paper Declaration Form

referencing the doctoral candidate's own published work(s)

Please use this form to declare if parts of your thesis are already available in another format, e.g. if data, text, or figures:

- *have been uploaded to a preprint server*
- *are in submission to a peer-reviewed publication*
- *have been published in a peer-reviewed publication, e.g. journal, textbook.*

This form should be completed as many times as necessary. For instance, if you have seven thesis chapters, two of which containing material that has already been published, you would complete this form twice.

1. **For a research manuscript that has already been published** (if not yet published, please skip to section 2)

   a) **What is the title of the manuscript?**

   Impact of confined water on the electronic structure of the SiO_2 and WS_2 interface

   b) **Please include a link to or doi for the work**

   https://doi.org/10.1021/acsami.4c19948

   c) **Where was the work published?**

   Journal of Applied Materials and Interfaces

   d) **Who published the work?** (e.g. OUP)

   ACS

   e) **When was the work published?**

   06/02/2025

   f) **List the manuscript's authors in the order they appear on the publication**

   Katherine L Milton, Alexander Shluger

   g) **Was the work peer reviewed?**

   Yes

   h) **Have you retained the copyright?**

   Yes

   i) **Was an earlier form of the manuscript uploaded to a preprint server?** (e.g. medRxiv). If 'Yes', please give a link or doi)

   No

   If 'No', please seek permission from the relevant publisher and check the box next to the below statement:

   ☒

   *I acknowledge permission of the publisher named under **1d** to include in this thesis portions of the publication named as included in **1c** (CCBY).*

2. **For a research manuscript prepared for publication but that has not yet been published** (if already published, please skip to section 3)

a) **What is the current title of the manuscript?**

b) **Has the manuscript been uploaded to a preprint server?** (e.g. medRxiv; if 'Yes', please give a link or doi)

c) **Where is the work intended to be published?** (e.g. journal names)

d) **List the manuscript's authors in the intended authorship order**

e) **Stage of publication** (e.g. in submission)

3. **For multi-authored work, please give a statement of contribution covering all authors** (if single-author, please skip to section 4)

   Conceptualization, A.L.S. and K.L.M.; methodology, K.L.M.; validation, K.L.M; formal analysis, K.L.M. and A.L.S.; investigation, K.L.M.; data curation, K.L.M.; writing—original draft preparation, K.L.M. and A.L.S.; writing—review and editing, A.L.S.; visualization, K.L.M.; supervision, A.L.S.; project administration, A.L.S.; funding acquisition, A.L.S.

4. **In which chapter(s) of your thesis can this material be found?**

   Chapters 1, 2, 5 and 6

5. **e-Signatures confirming that the information above is accurate** (this form should be co-signed by the supervisor/ senior author unless this is not appropriate, e.g. if the paper was a single-author work)

Candidate

Katherine Milton

Date:

10/02/2025

Supervisor/ Senior Author (where appropriate)

Alexander Shluger

Date 10/02/25

Acknowledgements

I would like to begin by expressing my gratitude to my supervisor, Alex Shluger, without whom this thesis would not have been possible. The in-depth discussions regarding my research have been instrumental to both my development and understanding as a scientist.

I would like to thank all the group members who have supported me throughout this journey. In particular, I wish to acknowledge Laura Hargreaves, Daria Kieczka, Thomas Durrant, and Teofilo Cobos Freire for their contributions to my work, as well as for the stimulating discussions and the time they dedicated to reflecting on my research. Furthermore, I appreciate the support and camaraderie of the entire group, which has made this experience enjoyable and kept me sane during more trying times.

I would like to thank Peter Grütter, Christoph Scheurer, and Chiara Panosetti for hosting me in their groups. My time with their groups was immensely informative, and I felt warmly welcomed. Additionally, I wish to thank Artem Samtsevych and Chiara Panosetti for their valuable contributions to the machine learning component of my research and for patiently addressing my numerous, often fundamental, questions.

Finally, I would like to thank my friends and family for their unwavering encouragement throughout my PhD journey; without them, I would have been quite lost. I am particularly grateful to Zoe Chu and Vicki Ling for their support during the Mayton Street years. My heartfelt thanks go to my partner, Ashley, whose constant support and care have been invaluable. I still can’t quite believe how many times you have read through my thesis chapters. Lastly, I would like to

thank my parents for their continued support and guidance throughout both my PhD and my life.

Contents

List of Figures

List of Tables

List of Abbreviations

FET	Field Effect Transistor
MOSFET	Metal Oxide Semiconductor Field Effect Transistor
HER	Hydrogen Evolution Reaction
TMD	Transition Metal Dichalcogenide
VBM	Valence Band Maximum
CBM	Conduction Band Minimum
DFT	Density Functional Theory
CT	Charge Transition
ODC	Oxygen Deficient centre
EPR	Electron Paramagnetic Resonance
Opal-CT	Opal Cristobalite Tridymite
LDA	Local Density Approximation
GTH	Goedecker-Teter-Hutter
BFGS	Broyden–Fletcher–Goldfarb–Shanno
PBE	Perdew-Burke-Ernzerhof
AIMD	*ab initio* Molecular Dynamics
TD-DFT	Time-dependent Density Functional Theory
GGA	Generalized Gradient Approximation
HSE	Heyd-Scuseria-Ernzerhof
VB	Valence Band
CB	Conduction Band
CTL	Charge Transition Level
TS	Transition State
OA	Optical Absorption

AE	All-Electron
vdW	van der Waals's
BZ	Brillouin Zone
CVD	Chemical Vapour Deposition
PVD	Physical Vapour Deposition
PMMA	poly(methyl methacrylate)
KS	Kohn-Sham
HF	Hartree-Fock
TC-LRC	Truncated Coulomb Long-Range Correction
α-Q	α Quartz
α-C	α Cristobalite
a-SiO_2	Amorphous SiO_2
ADMM	Auxiliary Density Matrix Method
CI-NEB	Climbing Image Nudged Elastic Band
GPW	Gaussian Plane Wave
GTO	Gaussian Type Orbital
BSSE	Basis Set Superposition Error
PBC	Periodic Boundary Condition
PW	Plane Wave
FFT	Fast Fourier Transform
CMD	Classical Molecular Dynamics
BOMD	Born-Oppenheimer Molecular Dynamics
SCF	Self-Consistent Field
TDKS	Time Dependent Kohn Sham
PES	Potential Energy Surface
MEP	Minimum Energy Pathway
IR	Infrared
ATR	Attenuated Total Reflection (ATR)
RH	Relative Humidity
HD-VSFG	Heterodyne-Detected Vibrational Sum Frequency Generation
HBond	Hydrogen Bond
BIL	Binding Interfacial Layer

DL	Diffuse Layer
WCA	Water Contact Angle
AFM	Atomic Force Microscopy
MLP	Machine Learning Potentials
JPD	Joint Probability Density
MSD	Mean Squared Displacement
$\boldsymbol{D}$	Diffusion Coefficient
HBN	Hydrogen Bonding Network
IPE	Internal Photoemission
XPS	X-ray Photoelectron Spectroscopy
PL	Photoluminescence
IPR	Inverse Participation Ratio
LDoS	Local Density of States
RBA	Rigid Band Alignment
VBO	Valence Band Offset
CBO	Conduction Band Offset
PEEM	Photoemission Electron Microscopy
NQE	Nuclear Quantum Effects
W-ZZ	Tungsten Zigzag Edge
MTB	Mirror Twin Boundaries
TPD	Temperature Desorption Spectroscopy
STEM	Scanning Transmission Electron Microscopy
UHV	Ultra High Vacuum
DFTB	Density Functional Tight Binding
ML	Machine Learning
NN	Neural Network
SCC	Self Consistent Charge
skf	Slater Koster File
PSO	Particle Swarm Optimisation
GPR	Gaussian Process Regression
QE	Quantum Espresso
RMSE	Root Mean Squared Error

Chapter 1

Introduction

1.1 Motivation

In recent years, transition metal dichalcogenides (TMDs) have shown great potential in many applications due to their stability, high electron mobility, and semiconductor-type band gap[3–8]. The applications explored so far have ranged across many areas, such as sensors[9,10], electrocatalysts in the hydrogen evolution reaction (HER)[11], flexible electronic devices[12], and components in field effect transistors (FETs)[1,13,14].

In all these applications, TMD films are deposited or grown on substrates, typically a dielectric.[3,15,16] In the case of FETs, a gate dielectric is required to prevent charge leakage when a voltage is applied. The gate dielectric must possess a sufficiently large band gap and a low defect density to inhibit electron leakage from the TMD into the gate electrode during FET operation. The most commonly used gate dielectrics at present are silica (SiO_2) and hafnia (HfO_2). Dielectric substrates are also commonly utilised in various applications, with typical options including Al_2O_3, mica, SiO_2, and, more recently, h-BN.

SiO_2 is widely employed in both academic and industrial settings, largely due to its insulating properties and cost-effectiveness. However, SiO_2 is known to form hydrophilic silanol (Si-OH) groups on its surface. This hydrophilicity can result in confined water at the SiO_2 and TMD interface, which is influenced by the preparation method.[17] Furthermore, relative humidity has been shown to affect the performance of TMD metal-oxide-semiconductor field-effect transistors (MOSFETs).[18] Despite this, the realistic interface of $SiO_2/H_2O/WS_2$ has not been thoroughly investigated, and the impact of this confined water remains poorly understood.

One barrier to modelling SiO_2 as a dielectric substrate is its amorphous nature in both academic and industrial settings. The surface of crystalline α-cristobalite SiO_2 has been proposed as a surrogate for amorphous silica, primarily because it mimics the density of silanol groups on amorphous surfaces.[19] However, the α-cristobalite phase of SiO_2 has not been thoroughly studied experimentally and theoretically due to the lack of high quality samples. In particular, the properties of common oxygen vacancy defects have not been established. The presence of such defects in devices can facilitate trap-assisted tunnelling of charge carriers from WS_2 into SiO_2, depending on the alignment of the defect energy levels with WS_2. Therefore, it is important to establish how well such defects in the model α-cristobalite can represent those in real amorphous SiO_2 substrates.

Focusing on the application of TMDs as electrocatalysts for HER, it is established that hydrogen is generated through the process of water splitting. This reaction primarily occurs at defects or at the edges of TMD flakes.[20] These sites are also recognised as oxidation sites, where the introduction of O_2 and/or H_2O can facilitate oxidation of TMDs, which may also enhance hydrogen evolution.[21] However, the precise mechanisms governing both water splitting and the oxidation processes involving water remain unclear, despite their significance for HER functionality and the degradation of TMDs.

Consequently, this thesis examines the $SiO_2/H_2O/WS_2$ interface to elucidate its properties. Furthermore, the defects of both α-cristobalite and WS_2 will be studied to analyse the properties of oxygen vacancies and the role of defects in WS_2 in the mechanism of oxidation.

1.2 Main Questions

I aim to examine both aspects of the $WS_2/H_2O/SiO_2$ interface: how the confinement affects the properties of water and how the presence of water impacts the properties of the WS_2 film. My objectives are to:

1. Characterise the oxygen vacancy defects in the α-cristobalite phase of SiO_2. This SiO_2 phase effectively replicates the density and character of silanol groups found on amorphous silica surfaces, making it suitable for theoretical calculations. However, the presence of defects can influence the tunnelling of charge carriers from semiconductors into the SiO_2 due to the alignment of defect energy levels. This consideration is particularly significant for evaluating the performance of SiO_2 as a gate dielectric in an FET.

2. Investigate how the confinement of water between SiO_2 and WS_2 affects the properties of water. This is significant as the SiO_2 substrate can hydrogen bond to water, potentially altering the behaviour of water confined at the interface. To my knowledge, no previous study has explored the influence of such hydrogen bonding interactions on the properties of confined water. By addressing this gap, I aim to enhance the fundamental understanding of water behaviour at these interfaces.

3. Explore how the electronic properties of WS_2 are affected by the confined water layer introduced by the SiO_2 substrate. A critical aspect of this study is understanding the band alignment at the $WS_2/H_2O/SiO_2$ interface. This is important for applications in MOSFETs, where maintaining charge carriers within the semiconductor (WS_2) and preventing migration into the gate dielectric is essential for proper device operation.

4. Understand how the amount of water influences both the confined water structure and the electronic properties of WS_2.

5. Investigate the role of interaction of H_2O with defects and edges at the WS_2 surface in the oxidation pathways of WS_2. This research aims to elucidate

the initiation of oxidation and assess the impact of defects and edges on this process.

1.3 Methods

To address these objectives, I employ computational approaches, namely static Density Functional Theory (DFT) and DFT-based molecular dynamics (*Ab Initio* Molecular Dynamics (AIMD)) simulations.

The decision to utilise DFT arises from its capacity to effectively describe electronic properties by calculating the ground state of a system, without imposing a significant computational cost.

AIMD simulations can effectively describe the dynamic properties of water by integrating the Newtonian dynamics of atomic nuclei with electronic structure calculations at each time step, thereby enabling the exploration of dynamic systems. In contrast, classical molecular dynamics, which are computationally cheaper, permit the representation of a system's movement and dynamics solely through the application of potentials, so do not account for the electronic structure.

This *ab initio* approach allowed us to investigate the structure and hydrogen bonding of confined water at the $SiO_2/H_2O/WS_2$ interface. The structures generated from AIMD can subsequently be utilised to understand the electronic properties of the system.

Together, the use of DFT and AIMD provides a comprehensive framework for understanding the interplay between SiO_2, confined water, and WS_2 at the interface, offering both electronic and dynamic insights critical to this study.

1.4 Main Results

By addressing the outlined questions, we have obtained the following main results.

- Oxygen vacancy defects have been calculated in α-cristobalite phase of SiO_2

in comparison with those in better studied α-quartz. The so called "dimer" configuration of the positively charged oxygen vacancy E'_{di}, characterised by the formation of a Si-Si bond, has been found to be the most stable in α-cristobalite. This configuration has not been experimentally observed in the amorphous or α-quartz phases of SiO_2, thus presenting new avenues for investigation of this defect. However, the oxygen vacancy stabilised by the formation of a Si-O bond (E'_{puck}) was not found in α-cristobalite despite it being the most stable configuration of the positively charged oxygen vacancy in α-quartz.

- I have calculated the structure and behaviour of confined water at the $SiO_2/H_2O/WS_2$ interface. This interface has not been previously investigated, and, to our knowledge, similar interfaces have not been studied using *ab-initio* methods.

- At the $SiO_2/H_2O/WS_2$ interface, the presence of silanol groups (Si-OH) on the SiO_2 surface significantly influences the average structure of water. The structure of water closely resembles that at the SiO_2/H_2O interface due to the hydrogen bonding between water molecules and the silanol groups. This similarity is particularly evident when the number of water molecules is reduced. The WS_2 exerts a limited influence on the structuring of water. Water molecules exhibit slight reorientation near the WS_2 surface, a phenomenon that becomes more pronounced with an increase in the number of water layers, resulting in greater distance from the silanol groups.

- The average band alignment between SiO_2 and WS_2 remains consistent with the introduction of confined water, exhibiting a typical straddling alignment. Furthermore, the band gap of confined water aligns closely with that of SiO_2. However, when examining fluctuations in water configurations, local in-gap states between WS_2 and H_2O are formed, which can alter the alignment for specific water configurations.

- Water can spontaneously dissociate at WS_2 edges or WS_2 vacancy defects, where both tungsten and sulphur with dangling bonds are present. When two or more water molecules are present at an armchair edge, water molecules can spontaneously dissociate on the edge. This dissociation is facilitated by a proton hopping between the water molecules. A similar proton hopping dissociation mechanism is also observed when both water and oxygen molecules are introduced in both zigzag and armchair edges, leading to the formation of species such as H_2O_2 from O_2.

1.5 Structure of Thesis

Chapter 2 offers an overview of the properties of FET devices, with particular emphasis on the impact of band alignment on interface characteristics, including band offset and defect energy levels. Subsequently, a summary of common oxygen vacancy defects in SiO_2 is presented. The basic properties of WS_2 and related TMDs are then discussed to explain the importance of the selected materials for electronic devices. The synthesis and preparation methods of TMDs is also highlighted to provide context on how H_2O can be confined at the WS_2/SiO_2 interface and an introduction to WS_2 defects is provided.

Chapter 3 will outline the theory and methodology underlying the theoretical techniques employed in this thesis. I will discuss the code used in this thesis, CP2K, with a focus on the specifics of the Gaussian plane wave basis sets and other relevant aspects of the code.

From Chapter 4 onwards, the main body of research is then presented.

In Chapter 4, the properties of α-cristobalite are introduced, and details of its structure are analysed and compared to α-quartz. The results of investigating E' centres are then presented.

Water at the $SiO_2/H_2O/WS_2$ interface is examined in Chapter 5. Background information on the interactions between SiO_2 and H_2O is provided, along with a brief overview of the interaction between TMDs and water. The dynamics and structure of water at the confined interface are subsequently discussed, with comparisons made to the water structures at the WS_2/H_2O and

SiO_2/H_2O interfaces.

Chapter 6 discusses the electronic properties of the $SiO_2/H_2O/WS_2$ interface, starting with an overview of previous research conducted in this area. The interaction between WS_2, H_2O, and SiO_2 will be examined, with calculated values being compared to experimental results.

Results concerning the oxidation of WS_2 are discussed in Chapter 7. This chapter begins with a comprehensive literature overview of TMD oxidation. The findings for water oxidation at WS_2 defects and edges are then presented.

In Chapter 8 the use of machine learning for modelling materials is introduced. The methodologies and theories underpinning machine learning, especially in relation to the semi-empirical density functional tight binding method, are explained. Subsequently, initial findings on employing machine learning to model the $WS_2/H_2O/SiO_2$ interface are presented.

Finally, in Chapter 9, I summarise the findings of my research, emphasising both the novelty and limitations of my work.

Chapter 2

Literature Overview

I commence this overview by examining the operation of MOSFETs. This provides essential background information that underpins the motivation for investigating SiO_2 defects and band alignment in this thesis.

2.1 MOSFET Functioning

The most commonly used FETs are silicon-based MOSFETs. The silicon material is doped in two ways: n-type and p-type. N-type doping, traditionally via the introduction of phosphorus, creates an excess of electrons in the material. These electrons can be transported along the silicon to the drain by application of a potential that allows electrons to move into the conduction band. The p-type doping, traditionally by the introduction of boron, works similarly, but holes are the predominant charge carriers instead of electrons.

To explain the functioning of MOSFETs, consider the schematic of an n-type MOSFET shown in Figure 2.1a. When a voltage is applied to the gate, it creates a positive potential across the gate dielectric. If this potential exceeds the threshold voltage, an inversion layer forms in the n-channel. This layer is characterised by an accumulation of electrons, enabling current conduction between the source and drain. Conversely, reducing the gate voltage below the threshold eliminates the inversion layer, turning the MOSFET off and preventing conduction.

An example of a TMD MOSFET can be seen in Figure 2.1b, where the TMD is the n-channel and interfaces with SiO_2 to ensure that there is no current leakage from the TMD to the back gate. Due to the 2D nature and easy manipulation of TMDs, they are optimal for reducing the channel length and thus increasing current.[22] Additionally, they have high carrier mobility, thus improving the device's efficiency.

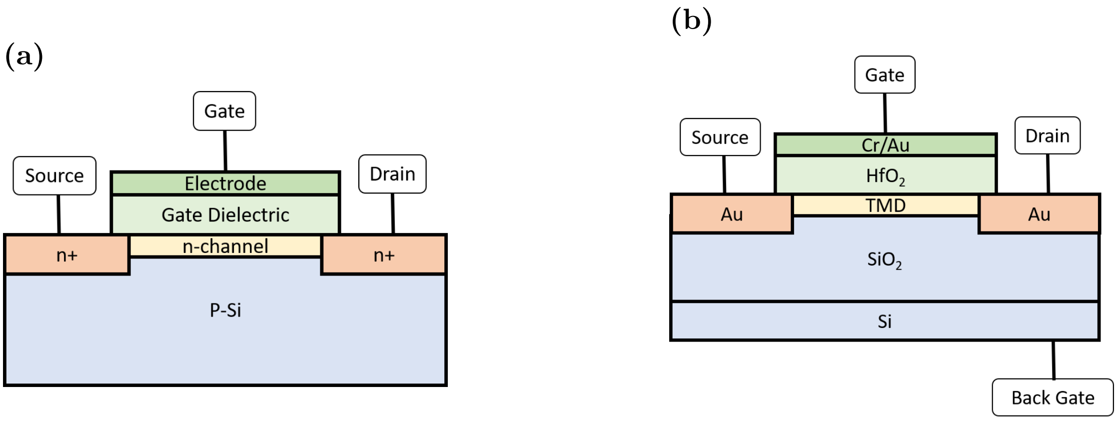

Figure 2.1 Schematic of MOSFET devices. **a)** traditional MOSFET set up of doped silicon based devices. **b)** MOSFET based on TMD semiconductors based on the work of Radisavljevic *et al.*[1]

2.1.1 Gate Dielectric

At the gate-to-channel and back gate-to-channel interface, when the thickness of the dielectric SiO_2 is reduced or defects are present in SiO_2, current leakage can occur. In the SiO_2/WS_2 system, current leakage involves the movement of charge carriers from the semiconductor channel (WS_2) into the insulating substrate (SiO_2). Current leakage leads to failure in FETs, as the device cannot be turned off due to consistent charge transfer across the interface. The tunnelling current through the oxide can be approximated[23] as

$$J_g = \frac{A}{t^2} e^{-2t\sqrt{\frac{2m*q}{\hbar^2}(\Phi_B - \frac{V_{ox}}{2})}}. \tag{2.1}$$

The current can be seen to depend exponentially on three terms: t, the thickness of the dielectric; the potential barrier height Φ_B; and the voltage drop across the dielectric, V_{ox}.

Here, I focus on the potential barrier height. The large band gap in dielectrics allows for the formation of high barriers. However, the exact barrier height also depends on the positioning of the semiconductor's valence band maximum (VBM) and conduction band minimum (CBM). If the band offset is sufficiently large and no defects are present, direct tunnelling is the exclusive mechanism for electron leakage (Figure 2.2a). Therefore, type I straddling gaps are desirable for interfaces with semiconductors and insulators. Conversely, when the band offset is reduced (Figure 2.2b), the Fowler-Nordheim tunnelling mechanism can occur under bias; tunnelling takes place from the semiconductor into the insulator CBM, subsequently leaking to the gate.[24] This highlights the significant importance of studying band alignment when examining the interface of a system.

However, tunnelling directly through or via the CBM of a dielectric to gate is not the sole mechanism responsible for electron leakage; another mechanism is trap-assisted tunnelling. In the trap-assisted tunnelling model, defect states within the material's band gap can function as acceptors for charge carriers. When the defect states' energy levels are aligned to the energy of the semiconductor CBM for n-type doping or VBM for p-type doping, charge carriers can hop between these states in a dielectric. In MOSFETs, this ultimately results in current flowing into the gate, causing device breakdown as the device is always on. The defect levels are determined by the band alignment of the materials and in-gap states; an example schematic is shown in Figure 2.2c.

Overall, it is crucial for the SiO_2/WS_2 interface under investigation to calculate the band offsets between the two materials. This accurate calculation of band alignment is essential for evaluating whether the use of WS_2/SiO_2 offers adequate band offset for device applications. Furthermore, as highlighted by the trap-assisted tunnelling mechanism, it is important that the positions of SiO_2 defect states in the band gap are understood.

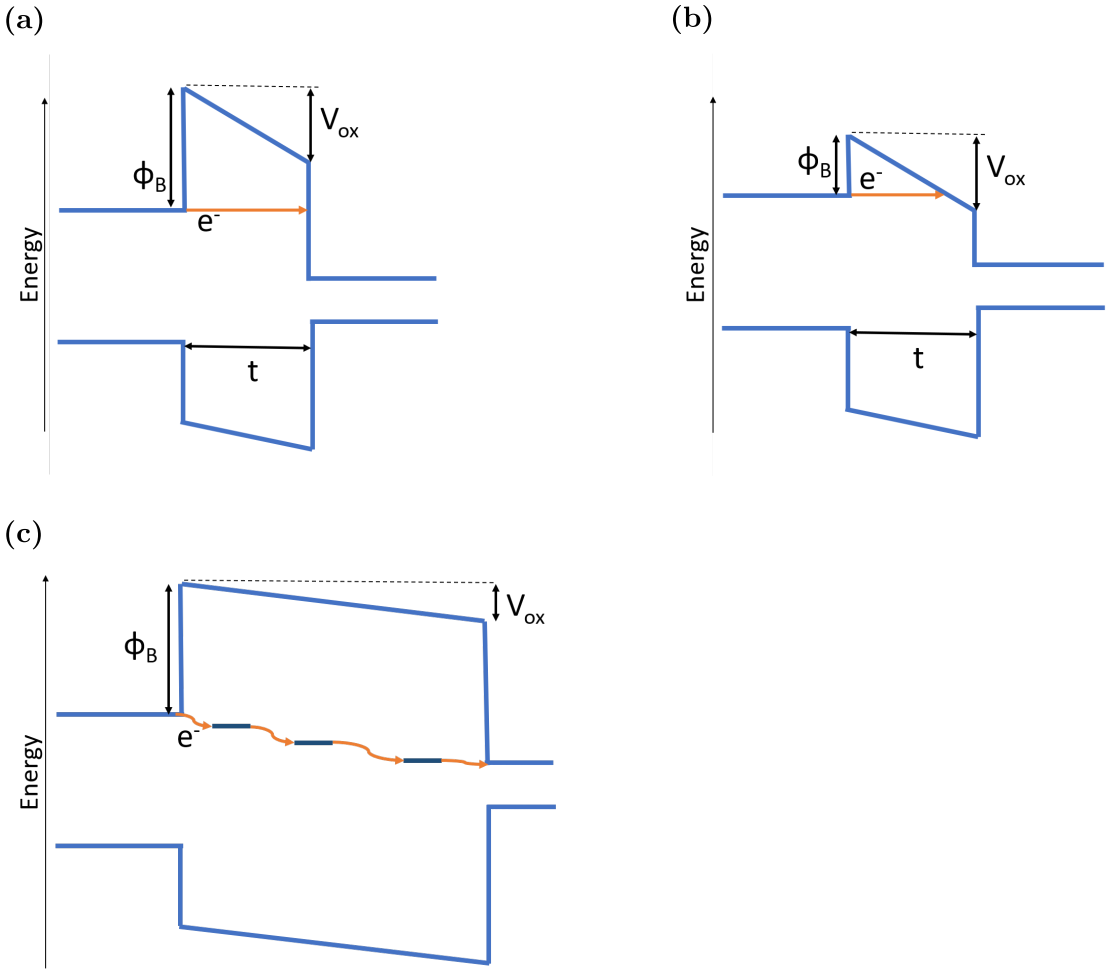

Figure 2.2 Description of band alignment at an interface between a semiconductor/dielectric/gate. The labels used in this figure are based on equation 2.1. **a)** Shows a diagram of direct tunnelling through an insulator. **b**) Shows the band alignment with a small band offset and potential drop across the insulator, facilitating Fowler-Nordheim tunnelling. **c)** Is a diagram of the trap-assisted tunnelling mechanism where the electron, shown in orange, hops between dark blue in gap defect states.

2.1.2 Oxygen vacancy configurations in SiO_2

To further investigate the defects in SiO_2, an overview of common oxygen vacancy defects in SiO_2 is presented. My focus is on the α-quartz (α-Q) phase of SiO_2, as it is the most extensively studied phase of SiO_2. Additionally, I will discuss amorphous SiO_2 (a-SiO_2) which is commonly utilised as the dielectric substrate in both academic and industrial settings.

Previous calculations demonstrate that a neutral O vacancy in α-Q and a-SiO_2 (in a-SiO_2 this defect is also called the Oxygen Deficiency Centre (ODC)

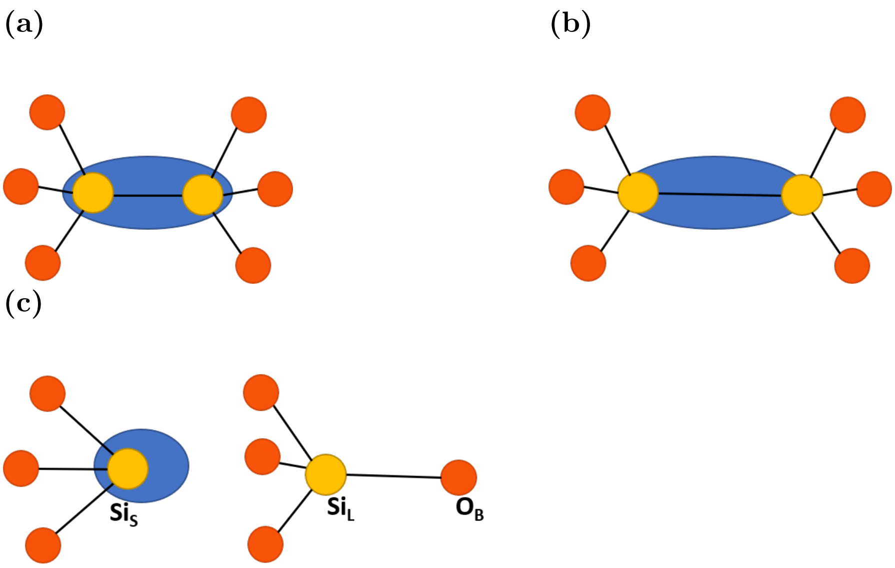

Figure 2.3 Schematic representation of oxygen vacancy defects in SiO$_2$.[2] Yellow atoms are silicon and red atoms are oxygen, the blue oval represents electron localization. (**a**) Neutral dimer configuration, such as ODC(I). (**b**) Positive dimer configuration, such as E'_{di} with elongated Si-Si bonds. (**c**) Puckered E'_1 centre, showing the back bond between Si$_L$ and the back oxygen in the surrounding ring, O$_B$. The labelling is consistent with α-quartz and is described in the text.

I[25,26]) is stabilised by forming a bond between two Si atoms that share two dangling electrons $O_3 \equiv Si - Si \equiv O_3$ or by partially or fully passivating these bonds with hydrogen atoms $O_3 \equiv$Si - H H - Si $\equiv O_3$.[27] The formation of a bare vacancy in α-Q is accompanied by a very strong displacement of the two Si atoms toward each other, see Figure 2.3a for the structure of this defect.[27,28] Some authors also suggested the existence of so-called unrelaxed neutral O vacancy in amorphous silica.[29] Hole trapping by neutral O vacancy or hydrogen de-passivation reactions can produce positively charged and paramagnetically active defects designated E' centres based on their EPR signal.[30,31] In α-Q, the most stable E' centre is the E'_1, which is a close relative to the family of E'_γ centres in a-SiO$_2$, the general structure of which can be seen in Figure 2.3c. The E' centre naming convention uses Greek letters for a-SiO$_2$ and Arabic numerals for α-Q. Recent electron paramagnetic resonance (EPR) studies distinguish at least 15 different EPR signals attributed to E' centres in different types of α-Q perturbed by different defects and impurities.[31–33]

Theoretical calculations predict the existence of two low energy relaxed structures of E' centres in pure α-Q: the so-called dimer, E'_{di}, and puckered,

E'_{puck}, configurations[34,35], see Figure 2.3. More E' centre configurations in a-SiO_2 have been proposed in refs.[2,36]. The dimer and puckered configurations differ strongly by the values of isotropic hyperfine constants. The dimer type configurations are characterized by similar hyperfine constants on the two Si ions neighbouring the vacancy of around 10 mT. Due to the similarity with observed hyperfine constants, in some papers this configuration has been attributed to the E'_δ centre[27,28]. However, the thorough analysis of the experimental EPR spectra of the E'_δ centre suggested a much more complex configuration for this defect involving four or five Si atoms[37,38]. In the dangling bond puckered configuration, the spin density is almost completely localized on one Si ion, which warrants a very strong hyperfine interaction with that Si of 42 mT, close to the measured experimental value[27,32].

In α-Q, the puckered configuration of the E' centre has been shown to be more stable than the dimer configuration in several quite different calculations[27,39,40] supporting the results of EPR measurements[30]. This is related to the structure of α-Q, which has two non-equivalent positions of Si in the crystal structure and, correspondingly, two slightly different Si-O bonds. The so-called Si_S-O and Si_L-O bonds, where Si_S is the Si atom associated with the shorter bond and Si_L – with the slightly longer one. The calculations show that the Si_L atom can back-bond to O to form the puckered configuration of the E'_1 centre, as discussed in more detail in Chapter 4. The most stable configuration of this E' centre has a forward projection of electrons on the Si_S towards the vacant O site. The less stable E'_{di} configuration has not yet been observed experimentally in either α-Q or a-SiO_2.[38]

However, there has been limited research into the oxygen vacancy of α-cristobalite, despite its use as a model for a-SiO_2 in theoretical calculations. Understanding its properties is crucial for assessing the potential for trap-assisted tunnelling at TMD/SiO_2 interfaces. The absence of both theoretical and experimental investigations makes it difficult to identify which defects will be stabilised in α-cristobalite SiO_2. Additionally, this research could yield valuable insights into E′ centres, which may be observable experimentally, including the

E'_{di} that has yet to be verified.

2.2 Transition Metal Dichalcogeindes

To understand the functioning of TMD based devices, I provide a general overview of the transition metal dichalcogenides family. The most studied transition metal dichalcogenide is MoS_2. However, many properties of WS_2 and MoS_2 are similar, allowing insights to be gained from the study of MoS_2. The potential of 2D materials for application in electronic devices relies on both the electronic and structural properties.

2.2.1 Structural Properties of TMDs

TMDs consist of one metal atom (M) (in groups 4,5 or 6) and two chalcogen atoms (X), following the general formula MX_2. There are three phases of TMDs: the hexagonal (H) phase, the tetragonal (T) phase, and the rhombohedral (R) phase, see Figure 2.4. The more prevalent H and T phases have three-atom thick layers, and the metal atom is sandwiched between the chalcogen atoms to form a layer. These layers are held together by weak van der Waals (vdW) forces. This allows the layers to be easily peeled from each other, analogous to graphene.

TMDs have a layered structure with three main phases: 2H, 3R, and 1T. These phases are differentiated by the coordination of M with the surrounding S and the stacking of layers. In the H phase, M is bonded in a trigonal prismatic manner with a D_{3h} symmetry. In the T phases, it is bonded octahedrally with a D_{3d} symmetry. The R phase also has trigonal prismatic coordination with $C^5{}_{3v}$ symmetry.[41] This difference in bonding leads to different properties, as generally 1T phases have metallic properties, and semiconductor properties are seen in 3R and 2H phases.[42] The 1 and 2 before each phase name show the number of layers; 1 being a single layer and 2 a bilayer etc. The most stable and commonly used phase is 2H. In this work only the monolayer is investigated, so the 1H phase of WS_2 is used.

The layered structure of TMDs ensures there are no dangling bonds

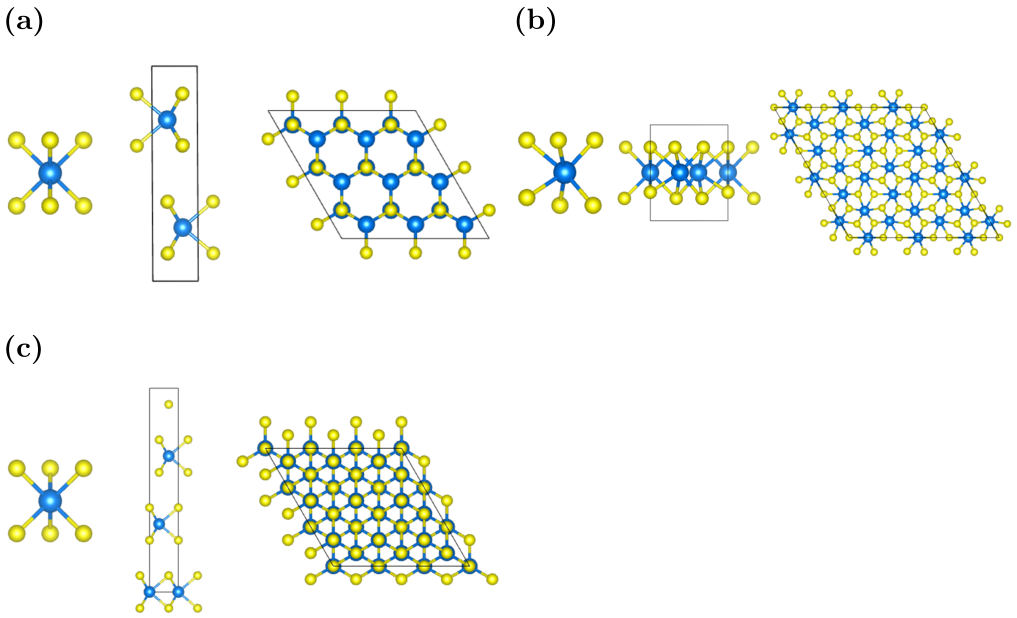

Figure 2.4 Bonding, stacking arrangement and top view of the three distinct phases of WS_2: **a**) 2H, **b**) 1T, and **c**) 3R. Tungsten atoms are shown in blue, and sulphur atoms in yellow.

perpendicular to the interface. This minimises interactions between TMDs and other materials at the interface and reduces interface roughness. The reduced interaction and roughness can reduce the number of possible scattering points and reduce the number of trap sites that are caused by surface defects. However, some interaction between the underlying substrate can induce rippling which can consequently increase scattering.[43]

2.2.2 Electronic Properties

The two-dimensional structure and absence of dangling bonds position TMDs favourably for use in electronic devices. However, the practical application of TMDs hinges on their electronic properties, such as their band gap.

The number of layers affects the band gap of the H phase, see Figure 2.5. When the TMD is in a monolayer, the band gap is direct, with the transition occurring at the K point in the Brillouin zone (BZ). However, when an additional layer is added to the TMD, the band gap becomes indirect between the Γ point in the valence band (VB) and to a Q point in the conduction band (CB). For WS_2 monolayers, the band gap is measured at 2.4 eV, as reported by both experimental studies[44] and GW theory.[45] Among the commonly studied semi-conducting TMD compounds, where M represents W or Mo and X represents S, Se, or Te, WS_2 exhibits the largest band gap.[46] In comparison, the related TMD, MoS_2, has a band gap of 2.27 eV, resulting in a minor difference of 0.13 eV from WS_2.[44,47] The band gap remains indirect but decreases as additional layers are added, ultimately reaching a bulk value. This is illustrated in Figure 2.5.

In addition to the semi-conducting band gap, there is intrinsic n-type doping in TMDs, which can be beneficial for FET functioning. The source of this has been debated in the literature. The current hypothesis suggests that doping comes from TMD defects, such as sulfur vacancies, or from charge transfer from the underlying substrate.[48,49]

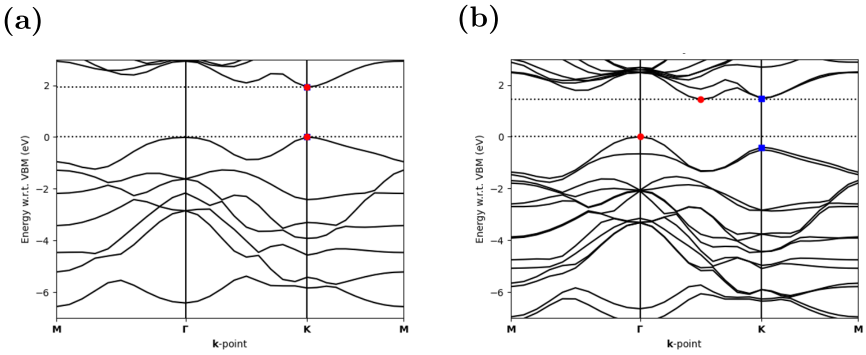

Figure 2.5 The calculated band structure of WS_2 using DFT, PBE functional and 6x6x1 Monkhorst-Pack grid. It illustrates the direct to indirect band gap transition change in WS_2. **a)** Band structure of a monolayer; **b)** band structure of a bilayer. The red circles indicate the lowest energy difference between the valence and conduction bands. If the lowest energy is an indirect band gap, the direct band gap is shown by a blue square.

2.2.3 Production

In pursuit of using WS_2 as a monolayer or few-layer system in various applications, two main production methods are used: direct growth on a substrate or exfoliation followed by deposition on a substrate[50].

The method of producing TMD flakes on substrates will induce different defects and defect densities depending on the conditions under which the TMD is synthesised or transferred onto the underlying substrate. Therefore, it is imperative to consider the impact of the production method on the performance of TMD semiconductors.

2.2.3.1 Direct Growth

A variety of methods exist for synthesising TMDs. For the interested reader, some of the more prevalent methods include: Chemical vapour deposition (CVD), physical vapour deposition (PVD), metal-organic CVD, metal transformation, chemical vapour transport (CVT), pulsed laser deposition, molecular beam epitaxy, spray pyrolysis, and atomic layer deposition.[51–53]

CVD is the most widely used technique due to its effective scalability and ability to produce large flake sizes with good thickness control.[54] However, vapour deposition methods utilise seeds to promote the growth of TMD flakes, which can result in overlapping flakes within the layers of the grown TMD. This leads to higher concentrations of defects, both from the starting material and from grain boundaries and dislocations.[55]

The issue of defects in the growth of thin layer TMDs persists, regardless of the production method employed. While new production techniques are being explored to minimise the defect density in TMD films, many of the existing TMDs still depend on these defect-prone production mechanisms. Consequently, it is essential to account for defects when examining the properties of TMDs produced using current growth methods.

However, most SiO_2 substrates used in MOSFETs are amorphous, resulting in a rough surface. Consequently, they are not ideal candidates for the growth of WS_2 using common direct growth methods such as CVD or MOCVD.[56–58] Therefore, it is more common to exfoliate TMDs onto SiO_2 rather than growing them directly on SiO_2.

2.2.3.2 Exfoliation

Exfoliation involves the separation of WS_2 layers from either the bulk material or from another substrate where TMD was initially grown. Exfoliation can be achieved by mechanical or chemical means. Both processes yield TMD layers with fewer defects; however, exfoliation presents scalability challenges and issues related to randomness, as both the number of layers and the orientation of the TMD are difficult to control.[46] Chemical exfoliation offers versatile methods that use different supports and solutions, with water or water-based solutions commonly employed. Sapphire substrates are commonly used for initial growth due to the smooth surface morphology and the high crystallinity of WS_2 produced[59,60]. However, The deposition of thin TMD films on substrates and/or further storage of heterostructures in ambient conditions can lead to the creation of thin water layers confined between a substrate and TMD films[61].

Mechanical exfoliation traditionally involves using scotch tape to transfer thin layers of 2D materials between substrates. Using this method means that any adsorbate on the surface of the substrate can be trapped underneath the TMD. Certain pre-exfoliation procedures, such as the use of oxygen plasma and high temperatures to remove ambient adsorbates, have improved both the yield and size of the produced flakes.[62] Other transfer methods exist, one of the most popular methods is the poly(methyl methacrylate) (PMMA)-assisted wet transfer, where solvents such as water or acetone are used to lift the TMDs from the underlying substrate with the support of PMMA and transfer the TMD to another substrate.[63] It is worth noting that this process also introduces water at the interface and/or additional solvent molecules.

Exfoliation can also occur via liquid phase exfoliation where, typically, the powder is dispersed in a liquid medium and then exfoliated into nanosheets, mostly by sonication. The solution used for this can vary significantly, but a large proportion of solutions used contain water, which, when in contact with SiO_2, can hydrogen bond to silanol groups.[46,64–67]

Therefore, mechanical exfoliation is expected to introduce water between WS_2 and SiO_2 due to the hydrophilicity of SiO_2, which adsorbs water under ambient conditions. Similarly, chemical exfoliation often involves water as a solvent. Therefore, in both methods, water is likely confined at the TMD/SiO_2 interface. Consequently, understanding the impact of confined water on WS_2 is crucial. This will allow identification of behaviours originating from confined water at this interface and contribute to clarifying the differences observed in the experimental results reported in the literature.[61] This effect can be viewed both as detrimental to the performance of some devices and as a source of fascination for fundamental studies of nanoconfinement of liquids[68,69]. In particular, understanding the behaviour of water in close proximity to materials under different conditions is important for a broad range of applications and scientific research.

2.2.4 Impact of Defects

As highlighted in the production section, defects are anticipated to be present in TMDs. These defects can serve as reaction sites for both oxidation and HER.

There are many defects in TMDs; for example, MoS_2 believed to have a density of 1×10^{11} to 1×10^{12} cm^{-2} defects when prepared by mechanical exfoliation[70], although for scalable methods such as CVD, the defect density is expected to be greater. These defects, thought to be impurities or sulphur vacancies, can mean that the Fermi level of the TMD is pinned, which can decrease the efficiency and application of TMDs as semiconductors.[71] Additionally, due to the ease of damage to the TMD and the difficulty in controlling the exact amounts of substitutional dopants, doping TMDs for use in MOSFET devices remains an ongoing field of research.[72]

Furthermore, growing TMDs requires the growth of flakes. These flakes introduce edges and grain boundaries where the flakes are grown closely together. Edges and grain boundaries are of particular concern for the oxidation of TMDs, as both can increase the oxidation rates of TMDs when exposed to oxygen and water.[73,74] Defects and their interaction with molecules will be discussed in more detail in Chapter 7.

Overall, an important part of understanding TMDs is understanding the defects and what properties they can induce in a system, especially when other molecules that may interact with defects are present.

2.3 Summary

This introduction shows that TMDs are set to play a significant role in future electronic devices. The 2D nature of TMDs does allow for an increase in scaling, and their high electron mobility sets TMDs up to be well suited for use as semiconductors in MOSFETs. The interaction between TMD WS_2 and the ubiquitous dielectric SiO_2 has not been thoroughly investigated, particularly in relation to the hydrophilicity of SiO_2 and the subsequent effect of confined water. Consequently, atomistic scale models that incorporate water and the interactions between these materials at the interface are necessary to understand the influence of water on the band alignment at the WS_2/SiO_2 interface.

Furthermore, I have explained how defects in SiO_2, if aligned correctly, may lead to electron leakage through trap-assisted tunnelling. Consequently, understanding the typical defects in the SiO_2 system is vital. I have highlighted that α-cristobalite SiO_2 lacks well-characterised oxygen vacancy defects. This is particularly significant as α-cristobalite serves as an effective theoretical model for amorphous silica due to its ability to reproduce the silanol group density of a-SiO_2. Therefore, further exploration of these defects in α-cristobalite is essential.

Finally, I have highlighted the role that defects in TMDs play, both for functioning of TMDs as semiconductors and as areas for oxidation. It is crucial to examine the impact of these defects, which are likely to arise from production techniques.

Chapter 3

Methodology

3.1 DFT Basics

This thesis employs *ab initio* methods, primarily Density Functional Theory (DFT). DFT determines the ground-state energy of a system based on electron density, as formulated through the Kohn-Sham (KS) equations. The KS approach builds upon the Hartree-Fock (HF) method, which introduced one-electron wavefunctions, and the Hohenberg-Kohn (HK) theorems, which established electron density as a fundamental descriptor of the ground state. Rather than revisiting these foundational principles, I focus on the KS equations, as the broader development of DFT has been extensively documented in the literature.[75–78]

3.1.1 Kohn-Sham Equations

The HK theorems allows for the total energy of a many-electron system to be described by the electron density. The KS equations then reformulate the electron density into a more manageable form expressing the electron density ($n(\mathbf{r})$) as fictitious non-interacting particles, which can be used to describe a real system of interacting particles, simplifying the complex many-body problem.

In order to describe this fictitious system, Kohn-Sham orbitals are introduced. These orbitals correspond to non-interacting single-particle wavefunctions $\psi_i(\mathbf{r})$, which are used to describe the electron density of the system as:

$$n(\mathbf{r}) = \sum_{i=1}^{N} |\psi_i(\mathbf{r})|^2, \tag{3.1}$$

where the sum runs over all occupied orbitals i.

This allows for the total energy of the system to be described as:

$$E[n(\mathbf{r})] = T_s(n(\mathbf{r})) + V_{ext}(n(\mathbf{r})) + U_H(n(\mathbf{r})) + E_{XC}(n(\mathbf{r})), \tag{3.2}$$

where each term represents a specific component of the total energy: $T_s(n(\mathbf{r}))$ is the kinetic energy of a system of non-interacting electrons with the same electron density as the electron density of real interacting electrons, $V_{ext}(n(\mathbf{r}))$ is the electron-nuclear Coulomb interaction, $U_H(n(\mathbf{r}))$ the Hartree term, representing the classical Coulomb interaction between electrons, and $E_{XC}(n(\mathbf{r}))$ is the exchange-correlation energy, which captures the many-body effects. Both exchange and correlation are energy terms which arise from quantum mechanics and cannot be described classically. Exchange energy is due to Pauli repulsion, where fermions cannot have the same quantum state, leading to repulsion between electrons of the same spin. Correlation energy arises from how one electron interacts with the rest of the electrons in the system.

It is noted that the nuclei-nuclei repulsion energy is not present here due to the Born-Oppenheimer approximation which allows for the separation of nuclear and electronic terms.

The Kohn-Sham orbitals are used to solve a single-particle Schrödinger-like equation:

$$[-\frac{1}{2}\nabla^2 + V_{eff}(n(\mathbf{r}))]\psi_i(\mathbf{r}) = \epsilon_i\psi_i(\mathbf{r}). \tag{3.3}$$

Here ϵ_i is the eigenvalue associated with orbital ψ_i, and V_{eff} is the effective potential that the electrons experience.

The effective potential $V_{eff}(n(\mathbf{r}))$ is given by

$$V_{eff}(n(\mathbf{r})) = V_{ext}(n(\mathbf{r})) + U_H(n(\mathbf{r})) + V_{XC}(n(\mathbf{r})). \tag{3.4}$$

The KS equations are solved iteratively using a self-consistent field (SCF) method. Starting from an initial guess for the electron density, the Kohn-Sham orbitals and eigenvalues are calculated. These orbitals are used to update the electron density, and the process is repeated until the total energy reaches a minimum, yielding the ground-state energy and electron density.

One of the key challenges in DFT is the accurate description of the Exchange Correlation (XC) energy E_{XC}. The exact form of the exchange-correlation energy functional is unknown. Therefore, DFT relies on approximations for this term.

3.1.2 The Exchange Correlation Functional

The XC functional is a key component of DFT, capturing the complex quantum mechanical interactions between electrons. Various approximations to the XC functional exist to make DFT computationally feasible. One of the most basic of these approximations is the Local Density Approximation (LDA).

In LDA, it is assumed that the electron density is uniform or changes very slowly across space. This allows for the XC energy to be calculated as if each small region of space behaves like a uniform electron gas. The LDA exchange-correlation energy is given by:

$$E_{XC}^{LDA}[n(\mathbf{r})] = \int d^3\mathbf{r} n(\mathbf{r}) V_{XC}^{LDA}(n), \tag{3.5}$$

where $V_{XC}^{LDA}(n)$ is the exchange-correlation potential, which depends only on the local electron density n.

While LDA is useful for systems like metals, where electron density variations are small, it is limited in accuracy for systems with significant density variations, such as molecules and semiconductors, where electron-electron interactions are more complex.

To improve upon LDA, the Generalised Gradient Approximation (GGA) includes terms that account for the gradient of the electron density $\nabla n(\mathbf{r})$. This allows GGA functionals to capture more complex interactions, making them more accurate for a wider range of systems. The GGA exchange-correlation energy is expressed as:

$$E_{XC}^{GGA}[n(\mathbf{r})] = \int d^3\mathbf{r} n(\mathbf{r}) V_{XC}^{GGA}(n, \nabla n), \tag{3.6}$$

where the exchange-correlation potential $V_{XC}^{GGA}(n, \nabla n)$ now depends on both the local electron density and its gradient.

Different GGA functionals incorporate this density dependence in different ways, leading to a variety of popular functionals. In this work, the PBE GGA functional is used, which is a widely adopted functional due to its balance between accuracy and computational cost.

While GGA improves on LDA, further accuracy can be achieved by including a portion of Hartree-Fock (HF) exact exchange in the functional. This leads to hybrid functionals, which combine DFT exchange and HF exchange. The exchange correlation energy in a hybrid functional is given by:

$$E_{XC}^{hybrid} = (1-\alpha) E_X^{DFT} + \alpha E_X^{HF} + E_C^{DFT}, \tag{3.7}$$

where α is the fraction of exact exchange used, E_X^{DFT} is the DFT exchange energy, E_X^{HF} is the HF exact exchange energy, and E_C^{DFT} represents the DFT correlation energy. Two common hybrid functionals are B3LYP and PBE0. In the case of PBE0, 25% of the exchange energy comes from HF exact exchange (α=0.25).

3.1.2.1 PBE0-TC-LRC Functional

The PBE0-TC-LRC hybrid functional, as implemented in CP2K, is described in the literature, where TC refers to truncated Coulomb and LRC denotes long-range correction.[79] This XC functional applies a cutoff radius (R_c), within which exact exchange is included, while beyond this limit, the exchange contribution is set to zero. Additionally, a LRC is introduced using a semi-local density functional based on the PBE exchange. The LRC accounts for the PBE exchange hole, where an electron at position **r** creates a local deficiency in electron density of the same spin due to the Pauli exclusion principle. This is due to the TC approach effectively capturing short-range interactions within R_c, but it does not account for long-range, non-local electron effects. The energy is calculated as:

$$E_{XC}^{PBE0-TC-LRC} = aE_x^{HF,TC} + aE_x^{PBE,LRC} + (1-a)E_x^{PBE} + E_C^{PBE} \tag{3.8}$$

Overall, this functional allows for less computationally demanding hybrid calculations, therefore, allowing a large system size with more electrons to be calculated using an exact exchange functional.

3.2 CP2K

This work uses CP2K software to perform DFT calculations, a comprehensive review of this software can be found in reference[80]. CP2K uses Gaussian plane wave (GPW) basis sets; here, atom-centred Gaussian functions are the primary basis set, which represent the Kohn-Sham density matrix, and the plane waves are used as an auxiliary basis set.

I will begin by providing a brief description of both the Gaussian basis set and the plane wave basis sets utilised in CP2K. Subsequently, the dual application of these basis sets used in CP2K's execution of DFT is detailed.

3.2.1 Gaussian Basis Sets

The Gaussian basis sets comprise atomic-centred functions that represent electron density using Gaussian functions, which describe the localisation of electron density around the atomic nucleus. A primitive Gaussian functional is defined by:

$$g_i(\mathbf{r}) = Y^{l_i}_{m_i}(\theta, \psi)\mathbf{r}^{l_i} \sum_j c_{ij} \exp(-\alpha_j \mathbf{r}^2), \tag{3.9}$$

where $Y^{l_i}_{m_i}(\theta, \psi)$ represents the spherical harmonic that characterises the angular component of an atomic orbital, while the radial part ($\mathbf{r}^{l_i} \sum_j c_{ij} \exp(-\alpha_j \mathbf{r}^2)$) is expressed as a linear combination of Gaussian functions. Multiple Gaussian functions can be combined to get atomic orbitals. This is expressed by:

$$\phi_\mu(\mathbf{r}) = \sum_i d_{i\mu} g_i(\mathbf{r}) \tag{3.10}$$

where $d_{i\mu}$ is the corresponding contraction coefficients. The molecular orbitals are then represented as the linear combination of these atomic orbitals.

The linear combination of Gaussian functions allows for a better description of the electron density around a nucleus; the number of Gaussians that are used depends on the specific basis set applied.

The electron density using the Gaussian type orbital (GTO) basis set is therefore described as:

$$n(\mathbf{r}) = \sum_{\mu\nu} P_{\mu\nu} \phi_\mu(\mathbf{r}) \phi_\nu(\mathbf{r}), \tag{3.11}$$

here $P_{\mu\nu}$ is the density matrix element. The Gaussian type orbital basis set offers a significant advantage when addressing larger systems. Gaussian basis sets offer the computational advantage of performing calculations in real space. As a result, the total energy, Kohn-Sham matrix, and forces can be efficiently evaluated using analytical expressions, enabling larger calculations to be performed.

However, GTO basis sets present certain disadvantages, notably the basis set superposition error (BSSE). BSSE arises when a basis set is non-orthogonal and incomplete, as is the case with GTO basis sets. As the number of atoms increases, the overlap between them results in a more complete local basis set compared to that of a single atom. Consequently, this situation leads to overestimated binding energies, as clusters become over-stabilised.

3.2.2 Periodic Boundary Conditions

For condensed materials, the use of periodic boundary conditions (PBC) can be useful. PBC facilitate the simulation of an infinitely repeating unit cell, which is especially advantageous for ideal and infinite systems, such as crystalline solids.

The use of PBC facilitates the introduction of periodic wavefunctions rather than relying solely on atom-centred wavefunctions. This approach employs Bloch's theorem, where the period of these wavefunctions is determined by the PBC. The period corresponds to the cell length, which can be either a unit cell or a supercell. In the case of CP2K, Γ point calculations are employed, thus supercells are generally utilised, as outlined in 3.2.6.

However, PBC present certain challenges, particularly in selecting the appropriate cell size. When defects are incorporated within a cell, interactions between the periodic defect images occur. These interactions may lead to artifacts within the system. Therefore, it is crucial to ensure that cell sizes are sufficiently large to mitigate these issues.

3.2.3 Plane Wave Basis Set

The plane wave (PW) basis set differs from the Gaussian basis set in that it does not represent the electron density via atomic-centred orbitals; rather it uses periodic waves. This presents advantages such as orthogonal basis sets which are complete, therefore BSSE is not an issue unlike with GTO. Instead, due to the PBC, the PW basis set can use Bloch's theorem to describe electronic wavefunctions as periodic waves:

$$\phi_i(k_{\mathbf{r}}) = \sum_{\mathbf{G}}^{|\mathbf{G}|<G_{max}} c_{i\mathbf{k},\mathbf{G}} \exp(i((\mathbf{k}+\mathbf{G})\cdot\mathbf{r})), \tag{3.12}$$

here, **G** represents the reciprocal lattice vector, while **k** denotes the wave vector. This description therefore uses real space (**r**), and reciprocal space (**k** and **G**).

The electron density can then be described as:

$$n(\mathbf{r}) = \frac{1}{\Omega}\sum_{G} n(\mathbf{G}{+}\mathbf{k})\exp(i\mathbf{G}{+}\mathbf{k}\cdot\mathbf{r}), \tag{3.13}$$

where Ω is the unit cell volume.

Bloch's theorem and the periodic nature of the system make PW basis sets effective for modelling crystalline solids with a repeating unit cell. The use of fast Fourier transform (FFT) methods allows for quick transformations between real and reciprocal space. Moreover, employing PW to describe the periodic potential within a cell enhances the efficiency of calculations for the Hartree potential of a system.

However, the number of PWs to describe an electronic wavefunction at each **k** point can be infinite. To manage this, a cutoff is implemented to exclude plane waves with high kinetic energies, focusing only on those with lower kinetic energies. Although this method introduces some error into the calculations, reliable cutoff values are determined by progressively increasing the cutoffs until the total energies of the system converge to a specified threshold.

3.2.4 Gaussian Plane Wave Basis Sets

The PW and Gaussian basis sets represent electron density in fundamentally different ways, resulting in variations in computational cost. The combination of these methods through Gaussian Plane Wave (GPW) allows for a dual representation of electron density. The primary electron density is represented using the cost-effective Gaussian basis sets, while the Hartree potential is represented more accurately with the auxiliary PW basis. This combined basis set approach enables larger calculations than would be possible with either basis set independently.

The Kohn-Sham DFT equation can be expressed as follows:

$$\begin{aligned} E[\rho] &= T_s[n(\mathbf{r})] + V_{ext}[n(\mathbf{r})] + U_H[n(\mathbf{r})] + E_{XC}[n(\mathbf{r})] \\ = \sum_{\mu\nu} P_{\mu\nu}\phi_\mu(\mathbf{r})| &- \frac{1}{2}\nabla^2|\phi_\nu(\mathbf{r}) + (\sum_{\mu\nu} P_{\mu\nu}\phi_\mu(\mathbf{r})|V_{loc}^{PP}(\mathbf{r})|\phi_\nu(\mathbf{r}) \\ &+ \sum_{\mu\nu} P_{\mu\nu}\phi_\mu(\mathbf{r})|V_{nl}^{PP}(\mathbf{r})|\phi_\nu(\mathbf{r})) + 2\pi\Omega\sum_{\mathbf{G}}\frac{n^*(\mathbf{G})n(\mathbf{G})}{\mathbf{G}^2} \\ &+ \int \exp(XC)(\mathbf{r})d\mathbf{r}. \end{aligned} \tag{3.14}$$

This notation illustrates the contribution of the GTO basis set to both the kinetic energy and the nucleus-electron interaction. Conversely, the PW basis set determines the Hartree term.

The interaction between the nucleus and electrons involves both local pseudopotentials ($V_{loc}^{PP}(\mathbf{r})$) and non-local pseudopotentials ($V_{nl}^{PP}(\mathbf{r})$). A more detailed discussion of the application of pseudopotentials follows.

3.2.5 Pseudopotentials

When all electrons in a system are included in a DFT calculation, the computational cost increases significantly due to the large number of degrees of freedom. Core electrons exhibit rapid oscillations in their wavefunctions, resulting in nodes located close to the nucleus. These nodes and oscillations are difficult to accurately describe with basic basis sets. Furthermore, bonding and reactivity in molecules and materials primarily arise from the valence electrons. As a consequence, substituting core electrons and the nucleus with a pseudopotential is computationally advantageous. This approach eliminates the need for a quantum mechanical description of the core electrons and nucleus, reduces the number of electrons to be considered, and minimises the required basis set.

The pseudopotential relies on the frozen core approximation. Here, the electronic wavefunction can be replaced by an effective potential in the Hamiltonian. To ensure that only the core electrons are modelled, the pseudopotential must ensure that the valence wavefunctions are orthogonal to the core states, so there is no overlap between the core and electron states. The pseudopotential is applied up to a cutoff radius, so will only describe the core electrons. In this region, the potential is smoother than a nuclear potential and has no or fewer nodes in the wavefunction. This allows for both the basis set size and the number of electrons to be reduced, improving efficiency.

In the case of CP2K, Goedecker-Teter-Hutter (GTH) pseudopotentials are employed which can work with the GPW basis set.[81] The pseudopotentials are divided into local and non-local parts. The local potential takes the form:

$$V_{loc}^{PP}(r) = \frac{-Z_{ion}}{r}\mathrm{erf}(\frac{r}{\sqrt{2}r_{loc}})+(exp)[-\frac{1}{2}(\frac{r}{r_{loc}})^2]\times[C_1+C_2(\frac{r}{r_{loc}})^2+C_3(\frac{r}{r_{loc}})^4+C_4(\frac{r}{r_{loc}})^6] \tag{3.15}$$

Where erf is the error function, Z_{ion} is the ionic charge, and r_{loc} is the range of the Gaussian ionic charge distribution. The non-local part is then expressed as

$$V_{nl}^{PP}(\mathbf{r},\mathbf{r}') = \sum_{lm}\sum_{ij}\langle\mathbf{r}|p_i^{lm}\rangle h_{ij}^{l}\langle p_j^{lm}|\mathbf{r}'\rangle. \tag{3.16}$$

Here, the Gaussian-type projectors are used for p_i^{lm}. The parameters of the pseudopotential in this form have been optimized with respect to an all-electron wavefunction.

3.2.6 Gamma Point Calculations

As CP2K employs GTO basis sets as its primary basis in the GPW method, the computational cost can be reduced through the use of Gamma (Γ) point calculations. Γ point calculations ensure that **k** is set to (0,0,0), thereby eliminating reciprocal space complexity and avoiding the need for transformations between real and reciprocal space, which improves computational efficiency. Nonetheless, it remains essential for the band structure of the system being calculated to be accurate. Consequently, supercells are necessary to facilitate the folding of **k** points into the Γ point.

The number of **k** points folding into the Γ point increases linearly with the size of the supercell. This is important for WS_2 due to the complex nature of the band structure, as seen in Figure 2.5. Therefore, larger supercells are needed to ensure that important **k** points that are responsible for the dispersion curves of the band structure are included. In the case of WS_2, the K point for the monolayer and the Q point in the bilayer must be folded into the Γ point. All **k** point calculations were performed using a Monkhorst-Pack grid.[82]

All hybrid DFT calculations were conducted using Γ point calculations, as **k** point sampling for the non-local XC functional had not been fully integrated into CP2K at the time of these calculations.

3.2.7 Auxiliary Density Matrix Method

The auxiliary density matrix method (ADMM) enhances the computational efficiency of hybrid functionals by employing an auxiliary basis set with reduced numerical complexity to compute the non-local Hartree-Fock component. However, this approach may induce errors, as the less comprehensive basis set may not adequately represent the density of the system being analysed. To mitigate this error, a correction is applied based on the difference between the exchange energy calculated using the PBE exchange-correlation functional on the original and the auxiliary basis sets:

$$\begin{aligned} E_x^{HF}[n] &= E_x^{HF}[\hat{n}] + (E_x^{HF}[n] - E_x^{HF}[\hat{n}]) \\ &\approx E_x^{HF}[\hat{n}] + (E_x^{PBE}[n] - E_x^{PBE}[\hat{n}]), \end{aligned} \tag{3.17}$$

where n is the density of the original basis set, $\hat{n}$ is the density with the auxiliary basis set.

3.3 Ab initio Molecular Dynamics

DFT is primarily used as an optimisation method for determining the static ground state of a system. However, this approach does not account for the range of configurations and energy landscapes accessible at finite temperatures, nor does it capture the time evolution of the system.

To address these limitations, *ab initio* molecular dynamics (AIMD) can be employed to simulate the dynamic behaviour of systems over time. AIMD calculates intermolecular forces on the fly using first-principles electronic structure methods, avoiding the need for pre-fitted potentials as used in classical molecular dynamics (CMD). However, the computational cost of AIMD is significantly higher than CMD, limiting its applicability to smaller systems and shorter time scales. Common AIMD methods include Car-Parrinello molecular dynamics and Born-Oppenheimer molecular dynamics (BOMD), with the latter being the focus of this thesis.

In BOMD, the electronic and nuclear motions are decoupled through the Born-Oppenheimer (BO) approximation. This decoupling of nuclear and electronic motion allows BOMD to avoid solving the time-dependent Schrödinger equation for the entire system. Instead, the method propagates nuclear motion by evaluating the forces acting on the nuclei at each time step using the Hellmann-Feynman theorem. At each time step, the system is assumed to be in the electronic ground state, and a SCF method is used to iteratively solve for the electronic wavefunction Ψ_0 that minimises the total energy. Therefore, the force acting on the nuclei is expressed as:

$$M_I \ddot{\mathbf{R}}_I(t) = -\nabla_{\mathbf{R_I}}(E_e(\mathbf{R}) + V_{NN}(\mathbf{R})). \tag{3.18}$$

Where $E_e(\mathbf{R})$ is the electronic energy for a fixed nuclear configuration, and $V_{NN}(\mathbf{R})$

is the nuclei-nuclei Coulomb repulsion, M_I is the mass of the nucleus, and $\ddot{\mathbf{R}}_I(t)$ is the acceleration. The force ($\mathbf{F}_{\mathbf{I}_e}$) from the electronic contribution is given by:

$$\mathbf{F}_{\mathbf{I}_e} = -\nabla_I \min \Psi_0 \langle \Psi_0 | H_e | \Psi_0 \rangle, \tag{3.19}$$

Where H_e is the electronic Hamiltonian. This equation is solved using DFT to get the ground state at the fixed nuclear position. Subsequently, the time evolution of the system is then determined using classical equations of motion.

To update the nuclear positions based on the calculated forces, it is essential to integrate the motion of atoms over time. Integration is performed by discretising time into small timesteps (Δt), during which the positions and velocities of the nuclei are updated. A commonly used approach for this is the velocity-Verlet algorithm (Equations 3.20-3.21), which efficiently propagates nuclear motion using the computed forces.

$$\mathbf{R}_I(t+\Delta t) = \mathbf{R}_I(t) + \boldsymbol{\nu}_I(t)\Delta t + \frac{\mathbf{F}_I(t)}{2M_I}(\Delta t)^2, \tag{3.20}$$

$$\boldsymbol{\nu}_I(t+\Delta t) = \boldsymbol{\nu}_I(t) + \frac{\mathbf{F}_I(t) + \mathbf{F}_I(t+\Delta t)}{2M_I}\Delta t. \tag{3.21}$$

Where R_I is the nuclear position, ν_I is the nuclear velocity. After updating the nuclear positions to $\mathbf{R}_I(t+\Delta t)$, the electronic structure is recalculated. The electronic structure is recalculated at each step via SCF methods, such as DFT. Further details on the BOMD implementation of AIMD can be found in refs[83,84].

3.3.1 NVT ensemble and Thermostats

AIMD simulations can be performed using various statistical ensembles, such as the NPT (constant number of particles, pressure, and temperature) or NVT (constant number of particles, volume, and temperature) ensembles. In this thesis, we focus on the NVT ensemble because it allows precise control of the temperature while maintaining a constant volume, which is suitable for simulating both solid and liquid materials. The temperature control in NVT simulations is achieved through the use of thermostats. Thermostats regulate the temperature by adjusting the velocities of particles, which directly affects the kinetic energy, as described by the relation:

$$T(t) = \frac{2}{3Nk_B}\frac{1}{2}\sum_i m_i \dot{R}_i^2(t), \tag{3.22}$$

where $T(t)$ is the instantaneous temperature at time t, N is the number of degrees of freedom, k_B is the Boltzmann constant. In this case, the temperature is defined as $T = \langle T(t) \rangle$.

In this work, we employ the Nosé-Hoover thermostat, which functions as a heat bath by introducing a friction-like term, ξ, that alters the velocities of particles. The equation of motion in this system is expressed as follows:

$$M_i \frac{d^2\boldsymbol{R}_i}{dt^2} = \boldsymbol{F_i} - \xi M_i \frac{d\boldsymbol{R_i}}{dt}, \tag{3.23}$$

where M_i is the mass of the particle i, $\boldsymbol{R_i}$ is its position, and $\boldsymbol{F_i}$ is its force. The friction-like term, ξ, evolves over time according to the equation:

$$\frac{d\xi}{dt} = \frac{1}{Q}(\frac{K}{K_{target}} - 1). \tag{3.24}$$

Here Q is a parameter that controls the strength of the thermostat coupling, and K_{target} is the target kinetic energy corresponding to the desired temperature. The variable ξ adjusts the velocities of particles to regulate temperature fluctuations, smoothing them over time by scaling the system's velocities accordingly.

3.4 Time Dependent Density Functional Theory

DFT, established by the Hohenberg-Kohn theorem, is a ground-state formalism that cannot inherently account for dynamic phenomena, such as optical transitions, due to its static nature. To address such dynamical processes, Time-Dependent

Density Functional Theory (TDDFT) was introduced by Rünge and Gross as an extension of DFT.[85] TDDFT enables the calculation of the optical absorption spectrum of materials by incorporating time-dependent effects.[86,87]

Unlike traditional DFT, which is grounded in a variational principle optimising the ground-state energy, TDDFT lacks a corresponding variational framework, as its formalism addresses time-evolving systems. There are a number of ways to address this, but here we will focus on the linear response method for solving the time dependent Kohn-Sham (TDKS) equations as CP2K uses this methodology.

In linear-response TDDFT, the system is subjected to a small, time-dependent external perturbation, denoted as $\delta\nu_{ext}(\mathbf{r}, t)$ which induces a change in the electron density $\delta n_{ext}(\mathbf{r}, t)$. The TDKS equations are then linearised to relate the change in the electron density to the perturbing potential via the density response function $\chi(\mathbf{r}, \mathbf{r'}, \omega)$, which characterises how the electron density at position $\mathbf{r}$ and frequency ω responds to a perturbation at position $\mathbf{r'}$. The non-interacting density response function is written as:

$$\delta n(\mathbf{r}, \omega) = \int d^3r_1 d^3r_2 \chi_0(\mathbf{r}, \mathbf{r'}, \omega)\delta\nu_{KS}(\mathbf{r'}, t). \tag{3.25}$$

The non-interacting response function χ_0 is given by:

$$\chi_0(\mathbf{r}, \mathbf{r'}, \omega) = \sum_{i,j} \frac{(f_i - f_j)\psi_i(\mathbf{r})\psi_j^*(\mathbf{r})\psi_j(\mathbf{r'})\psi_i^*(\mathbf{r'})}{\omega - (\epsilon_j - \epsilon_i) + i\eta}, \tag{3.26}$$

here, f are occupation numbers and ϵ are KS orbital energies.

To account for particle-particle interactions, the Dyson equation is employed, which introduces the exchange-correlation kernel f_{XC} to capture these effects. The Dyson equation is written as:

$$\chi(\mathbf{r},\mathbf{r'},\omega) = \chi_0(\mathbf{r},\mathbf{r'},\omega) + \int d^3r_1 d^3r_2 \chi_0(\mathbf{r},\mathbf{r}_1,\omega) f_{XC}(\mathbf{r}_1,\mathbf{r}_2,\omega)\chi(\mathbf{r}_2,\mathbf{r'},\omega). \quad (3.27)$$

To solve the Dyson equation, we reformulate it as an eigenvalue problem using the Casida formalism creating a matrix. This matrix can then be solved by the Tamm-Dancoff Approximation. Further details on this can be found in references[85–87]. While this approximation reduces computational complexity, it may introduce errors in the description of correlated excitations and low-energy states. However, it remains a viable method for accurately capturing neutral excitations at a lower computational cost.

3.5 Nudged Elastic Band

To understand the barriers between different defect configurations and reactions, it is essential to investigate the potential energy surface (PES) of the system. The PES allows for an analysis of the energy required for the transition between initial and final states, enabling the calculation of the reaction barrier. To identify the most feasible route, specifically the minimum energy pathway (MEP) between the two configurations, the nudged elastic band (NEB) method is applied. The NEB begins with a linear interpolation of the positions of the initial and final states, producing a specified number of images along this interpolation; in this work, 7 images were chosen. In the MEP, the forces acting on the atoms are such that any component perpendicular to the pathway is minimised to zero, ensuring the images remain on the path. As a result, the only non-zero force is directed along the MEP, representing the energy gradient that drives the transition. The maximum of this path is the saddle point or transition state. A spring constant is introduced to connect each image into a path. To ensure that the fictitious spring forces between the images do not interfere with the convergence to the MEP, a projection scheme is applied. Specifically, the spring force is constrained to act only along the tangent to the pathway connecting the images, while the perpendicular component of the true force is used to refine the path. This approach effectively decouples the spring forces from the true forces, allowing the spring forces to control the distribution of images along the path without influencing its shape. By minimising the perpendicular component of the true force acting on each image, this method facilitates convergence to the MEP while ensuring an even distribution of images along its length. This results in the force on each image of:

$$\mathbf{F}_{i\|}^{spring} = k(|\mathbf{R}_{i+1} - \mathbf{R}_i| - |\mathbf{R}_i - \mathbf{R}_{i-1}|)\hat{\tau}_i, \tag{3.28}$$

where k is the spring constant and $\hat{\tau}$ is the normalised local tangent at image i.

However, while the NEB method provides a good approximation of the MEP it does not guarantee that the highest energy image will converge to the saddle point, or transition state, which is crucial for accurately determining the energy barrier between the initial and final states. To address this limitation, the climbing-image NEB (CI-NEB) method is employed.[88] In the CI-NEB approach, the highest-energy image along the path is identified and, after a number of ordinary NEB iterations, the force is modified. The parallel component of the true force is inverted, driving the image uphill along the energy surface, while the perpendicular component of the true force ensures it remains on the MEP. This adjustment systematically moves the highest-energy image toward the saddle point, ensuring rigorous convergence while preserving the accuracy of the MEP.

3.6 Practical Interface Considerations

3.6.1 Lattice Mismatch Strain

In solid interfaces, it is common for the materials involved to exhibit different lattice constants, leading to strain at the interface under experimental conditions.[59] This strain can be further intensified in theoretical simulations, particularly when employing methods such as DFT and AIMD using periodic boundary conditions. The limited number of atoms typically included in such calculations tends to exacerbate lattice mismatches and associated strain effects. Strain is defined as:

$$S = \frac{a - a_0}{a_0} \times 100\%, \tag{3.29}$$

where a is the strained lattice parameter, and a_0 is the unstrained lattice parameter.

For this thesis, we are considering an underlying substrate, SiO_2, with WS_2 exfoliated or grown on top. Given that WS_2 is a 2D material with a high degree of flexibility, it is expected to be strained in order to conform to the lattice parameters of the underlying SiO_2 substrate. For the construction of the interface models, we adopt the lattice vectors of the SiO_2 substrate, as depicted in Figure 3.1a. Two distinct approaches can be employed to adapt WS_2 to these lattice vectors: the slab model and the cluster model, illustrated in Figures 3.1b and 3.1c, respectively.

In the slab model, various strategies can be implemented to minimise artificial lattice strain within the computational system. One such approach involves rotating and optimising the alignment of the two materials in a slab configuration, which can reduce lattice mismatch at the interface. However, achieving a significant reduction in strain often necessitates larger simulations, leading to increased computational expense. If the residual strain is not adequately mitigated, it may adversely affect the material properties at the interface. A key advantage of the slab model lies in its ability to simulate the materials as infinite layers through the use of periodic boundary conditions, thereby eliminating artificial edges or self-interaction effects. This approach is particularly valuable for studying bulk properties of WS_2, as it enables a faithful representation of the interface in bulk-like environments.

An alternative approach to modelling the interface is the cluster-based calculation method (Figure 3.1c). In this model, periodic boundary conditions are applied such that it fits the lattice of one material—typically the underlying substrate. The second material, such as WS_2, is modelled as a flake that does not extend to the boundaries of the simulation box, thus creating an isolated cluster. This approach allows for the semiconductor material to be calculated

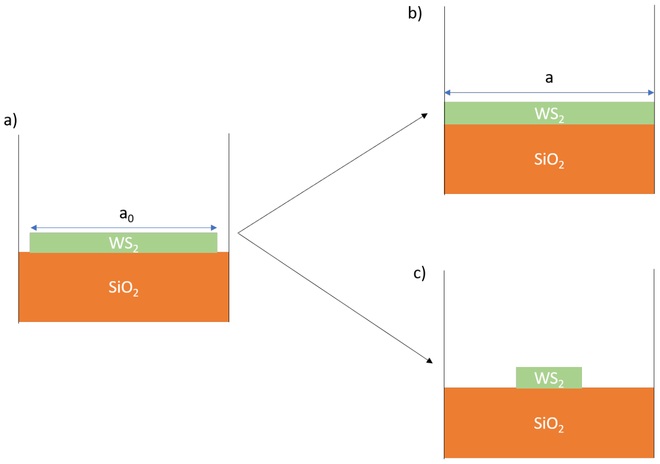

Figure 3.1 Possible models for the SiO_2/WS_2 interface. The black lines indicate the super cell boundaries under periodic boundary conditions. **a**) WS_2 aligned on a SiO_2 substrate without strain, showing a lattice mismatch between WS_2 (a_0) and SiO_2. **b**) Slab model of the interface, where WS_2 is subjected to tensile strain so that its lattice parameter a matches that of SiO_2. **c**) Cluster model of the interface, where a small WS_2 cluster is placed in the centre of the simulation box to prevent interactions with periodic images.

without the imposition of strain. Additionally, the flexibility of the flake geometry facilitates optimisation of the interface by enabling rotation and translation of the flake across the substrate until the system reaches an energy minimum. However, the introduction of edges in the top layer complicates the analysis, as these edge effects may alter the interface properties. Moreover, passivation of the flake edges adds additional complexity to the model. To accurately represent the interface and capture the influence of the flake edges, the size of the cluster must be sufficiently large. Furthermore, due to the periodic boundary conditions, image interactions must be taken into account, requiring a large simulation cell to prevent interactions between flakes in adjacent periodic images.

For the purposes of this work, the slab-based interface model has been selected as the primary method of investigation. The WS_2 unit cell was converted to an orthorhombic cell to reduce strain.

To verify that the orthorhombic cell accurately represents WS_2, the properties of WS_2 in its hexagonal primitive cell were initially examined to establish a reference for the pristine, unstrained system in vacuum using the PBE(D3) XC functional. The band structure for this can be seen in Figure 3.2a.

As expected, a direct band gap of 1.93 eV is calculated.

WS_2 in the orthorhombic cell was then investigated to understand how the change of the unit cell and consequently the Brillouin zone affects the band gap. I note that the number of bands differs based on the number of atoms per unit cell, with hexagonal cells having three atoms and orthorhombic cells having six. The band gap of the orthorhombic unit cell is calculated to be 1.95 eV. As expected, the band gap is also direct; this is seen in Figure 3.2b. The band gap is 0.02 eV higher in the orthorhombic cell than in the hexagonal. This is a minor difference, indicating that the band-gap values will only have a minor error when the cell is changed to an orthorhombic cell.

Finally, the orthorhombic cell was then investigated under strain. To fit the underlying SiO_2 substrate 2.62 % strain (compression) was introduced in the **a** direction and -5.69 % strain (tension) in the **b** direction. The indirect band gap is 2.02 eV, and the direct band gap is 2.04 eV (Figure 3.2c). These two points are close together, both in value and in k-space, so there is a minimal difference between the indirect and direct band gaps. The band gap has a small increase of 0.07 eV compared to the orthorhombic cell and by 0.09 eV compared to the hexagonal cell. Therefore, the introduction of artificial strain into the WS_2 makes the interface structure acceptable.

3.6.2 Averaging Water Configurations

The core issue addressed in this thesis is the influence of confined water at the SiO_2/WS_2 interface. Unlike solid-state crystalline systems, liquid-phase systems exhibit no single global minimum energy. At room temperature, the system changes dynamically, evolving through numerous configurations over time. Consequently, to accurately assess the impact of water at the interface, it is essential to explore multiple configurations and obtain an averaged representation of the interfacial properties.

To achieve this, AIMD is employed, as described in the previous subsection. While the PBE functional was used for the AIMD simulations, it is well known to underestimate band gaps. To address this limitation, single-point

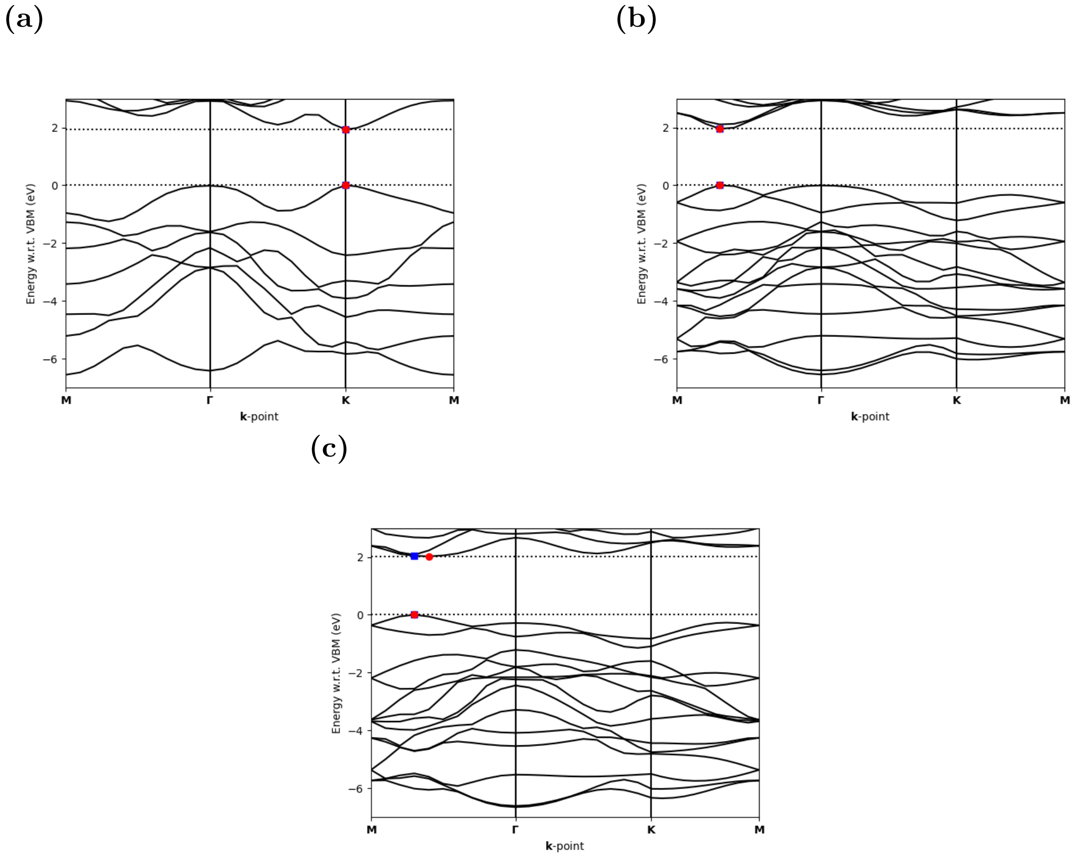

Figure 3.2 WS_2 band structure for: **a)** pristine WS_2 using a primitive hexagonal unit cell; **b)** pristine WS_2 with an orthorhombic unit cell; **c)** strained WS_2 with an orthorhombic unit cell. The red circles indicate the lowest energy difference between the valence and conduction bands. If the lowest energy is an indirect band gap, the direct band gap is shown by a blue square.

energy calculations were performed on snapshots extracted from the AIMD trajectories using PBE0-TC-LRC XC functional, maintaining frozen geometries. These snapshots were taken every 0.5 ps for a 12.5 ps production run, resulting in a total of 26 snapshots, which provided a representative average while allowing sufficient time for water molecule movement between frames. Ideally, a longer interval between snapshots would be preferred to ensure complete decorrelation of configurations; however, the computational limitations inherent in AIMD constrain the achievable timescale.

This methodology section primarily focuses on the theoretical background of the methods. The analysis and application of additional methods are addressed in the methodology sections of the relevant chapter.

Chapter 4

Oxygen Vacancies in α-Cristobalite SiO_2

As outlined in Chapters 1 and 2, SiO_2 is an essential dielectric material in electronic devices. α-cristobalite (α-C), a polymorph of silica, is frequently employed as a substitute for amorphous SiO_2, particularly in computer simulations of SiO_2 surfaces and interfaces.[89–91] However, limited knowledge exists regarding the properties of α-C and its fundamental oxygen defects. Defects present in SiO_2 can influence the performance of electronic devices, as discussed in Chapter 2. Since the α-cristobalite phase of SiO_2 serves as a proxy for amorphous silica surface in my models, understanding the defects within the system can enable us to accurately model potential defects at the interface, leading to a more comprehensive and realistic representation of the interface's functionality.

This chapter will begin with an introduction to α-C, expanding upon the background of oxygen vacancies discussed in Chapter 2. I then use DFT simulations to study the properties of the pristine structure and oxygen vacancies in α-C. The calculated properties of pristine α-C and its oxygen vacancy defects are compared with those of the better-characterised α-quartz (α-Q). My results demonstrate that the positively charged O vacancy in α-C is most stable in the dimer configuration, in contrast to α-Q which favours the puckered configuration.

A back-projected configuration is also predicted in both polymorphs. This work thus offers one of the first in-depth investigations of the properties of oxygen vacancies in α-C.

4.1 Introduction

Oxygen vacancies are among the most basic defects in oxide crystals, and their properties affect and control the performance of oxides in technology. Defects in SiO_2 have long been the focus of many-electron calculations using quantum chemistry[28,34,92] and periodic DFT[2,27,93–95] due to their importance in numerous applications, including microelectronics, catalysis, fibre optics, and dosimetry. These calculations have demonstrated that oxygen vacancies in SiO_2 distinguish themselves from other oxides in at least two accounts: 1) the number of different configurations they adopt, and 2) significant distortions they are capable of exerting on the surrounding lattice. Both of these properties are due to the extraordinary flexibility of the SiO_2 network. Oxygen vacancies in silica are best studied experimentally in α-Q and amorphous SiO_2 (a-SiO_2) where they have been experimentally shown to be stable under many conditions and have at least two (+1 and 0) accessible charge states[25]. It is important to note that I have broadly referred to various types of silica glass and amorphous silica films as a-SiO_2. Although there are subtle differences, these do not affect the discussion.

On the other hand, theoretical calculations have predicted the existence of five charge states of the O vacancy in α-Q and a-SiO_2 (with defect charges ranging +2 ...0 ...-2)[35,95–98], as well as more than eight different geometric configurations for the +1 charge state vacancy in a-SiO_2 (see, refs.[2,28]). When transforming between these charge states and configurations, O vacancies in SiO_2 undergo lattice relaxation with atomic displacements often exceeding 0.5 Å [28], in excess of typical displacements in other oxides (0.1 – 0.3 Å [99]). The abundance of predicted configurations of positively charged vacancies in a-SiO_2 results from different short and medium range order environments surrounding oxygen sites due to disorder.

Quite extraordinary, SiO_2 is one of those materials where some of the experimentally suggested defect configurations have never been verified theoretically (e.g. the so-called E'_δ centre in a-SiO_2[38]) and a large number of theoretically predicted defect configurations and charge states have not yet been identified experimentally. This huge gulf between theory and experiment is in part caused by high energies and instability of some defect configurations and by difficulties in experimental measurements and interpretation. The uncertainty in the verification of theoretical predictions undermines current attempts to employ machine learning to predict defect structures in solids (see ref.[100]) and particularly in amorphous SiO_2[101].

One of the longest controversies concerns the existence of the so-called ”dimer” configuration of the +1 charge state of O vacancy in SiO_2. This simple configuration has been predicted by most theoretical calculations of α-Q and a-SiO_2 but never observed experimentally, despite numerous attempts (see an overview in ref.[38]). This is likely due to the small barrier for its transformation into the more complex dangling bond configuration of O vacancy also known as the ”puckered” configuration (see details in Chapter 2.1.2). Since the existence and stability of both configurations is strongly affected by the short and medium range environment of O sites in SiO_2, one could gain additional insights from investigating these defects in other crystalline SiO_2 polymorphs. However, surprisingly little is known about the properties of O vacancies in other stable silica polymorphs, such as α-C or tridymite. Samples of these polymorphs are much less abundant and often much more contaminated with impurities than those of α-Q.[102,103] Therefore, theoretical calculations are often the only way to shed light on their properties and provide the information required to identify defects in these polymorphs.

4.1.1 Properties of α-cristobalite

Tetragonal α-C has a structure similar to α-Q with rings of the same size in both, but α-C has a much lower density (see Fig. 4.1). It is present in various planetary materials, e.g. lunar and Martian rocks[104] and meteorites.[105] On the Earth, it occurs as a metastable phase in many geological settings, for example as crystals deposited from vapour within the pores of volcanic rocks.[106] Most data on this silica phase have been obtained from geochemical analysis of volcanic rocks where α-C crystals or paracrystals are found with a mixture of silica phases, such as opal-CT.[107–109] Extensive studies on the effect of pressure on α-C have contributed to the understanding of this phase[110–116]. Several earlier computational studies of α-C focused mainly on producing a complete data set of silica polymorphs and lack detailed characterisation of α-C itself.[117–120]

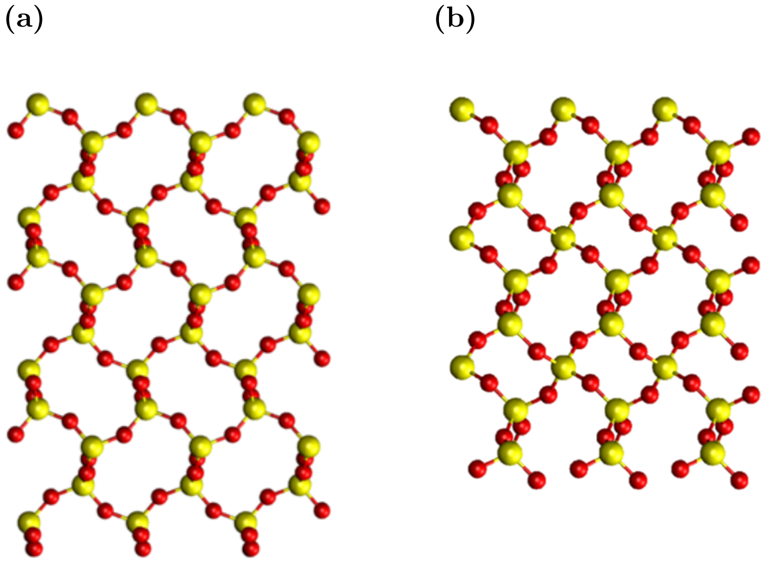

Figure 4.1 Pristine structures of SiO_2 in different phases, viewed along the **a** axis. Yellow atoms correspond to Si, red atoms correspond to oxygen atoms. (**a**) α-cristobalite structure; (**b**) α-quartz structure. Both phases are on the same scale as α-quartz has a smaller unit cell than α-cristobalite.

Quite independently of its geochemical and mineral interest, α-C is popular in theoretical calculations of silica as a mimic of the bulk and surface properties of amorphous silica[91,121,122], as both have very similar densities and structural characteristics (e.g., see discussion in refs.[123]). In particular, Emami *et al.*[124] have shown that the α-C $(10\bar{1})$ surface has a similar silanol group density to a-SiO_2. This makes α-C a good model for the a-SiO_2 surface structure without the need for computationally demanding melt-quench methods to produce theoretical models of a-SiO_2 surface structures. Therefore, interfaces of α-C with water[125,126] and with solids have been calculated extensively.[89–91]

In α-C, all Si positions are equivalent, so the distinction of Si_S and Si_L

cannot be made, as in Chapter 2 Figure 2.3. However, as E' centres will be investigated in both, the Si atom involved in the back bonding must be labelled. To distinguish α-C as separate from the α-Q $\mathrm{Si_S}$ notation, a new labelling is introduced, where Si_A is the Si involved in the back bonding ($\mathrm{Si_L}$ equivalent) and Si_B is the other Si at the oxygen vacancy ($\mathrm{Si_S}$ equivalent). For the sake of comparison, α-Q will also be labelled in the same way, see Fig. 4.2.

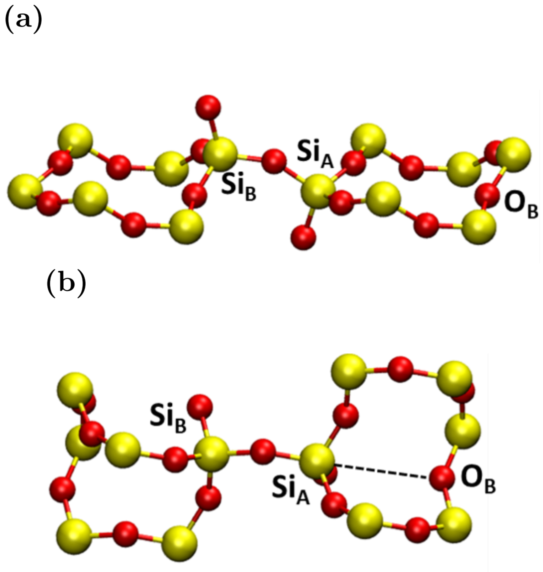

Figure 4.2 Local pristine structures of **a)** α-cristobalite with two connected tetrahedrons and **b)** α-quartz with two connected tetrahedrons with a ring containing back bonding O_B. In α-quartz, Si_A and Si_B are not equivalent, but in α-cristobalite they are equivalent. The Si_A and Si_B notations are therefore used to distinguish the Si atoms in defects which are later introduced to the pristine structure, more detail can be found in the text.

In this work, I focus on calculating properties of O vacancies in α-C, which is a high-temperature and low-pressure silica polymorph. It has a less dense structure than α-Q (see Fig. 4.1) with larger rings close to a-$\mathrm{SiO_2}$ structures. There are no theoretical studies of the O vacancies in α-C. By comparing my results for α-C with those for α-Q and a-$\mathrm{SiO_2}$ I hope to better understand the vacancy structure and guide experimental studies of their identification in α-C. In particular, I am interested in comparing the stable configurations of positively charged O vacancies in both crystals. Furthermore, α-Q serves as a reliable benchmark for assessing the accuracy of the α-C results.

My results demonstrate that the positively charged O vacancy in α-C is most stable in the dimer configuration, whereas α-Q favours the puckered configuration. Additionally, a back-projected configuration is also predicted for both polymorphs. I calculate the optical transition energies and isotropic hyperfine constants for oxygen vacancies in both α-Q and α-C, and I compare my findings with the results of previous studies utilising molecular clusters[92] and experimental data. This work provides one of the first comprehensive analyses of the properties of oxygen vacancies in α-C.

4.2 Methodology

In this Chapter, I compare properties of O vacancies in two SiO_2 polymorphs, α-Q and α-C. Most previous calculations of α-C used molecular cluster models, or local DFT functionals and small periodic cells. In contrast, I use periodic DFT calculations with a hybrid functional and large periodic cells to predict more accurately the structure, electronic, EPR, and optical absorption properties of positively charged, neutral, and negatively charged O vacancies in α-C. These results are compared with those obtained in α-Q and amorphous silica.

Calculations were carried out using DFT implemented in CP2K software package using a Gaussian Plane Wave method.[80] A 324 atom 3×3×3 supercell of α-C and a 260 atom 3×3×3 supercell of α-Q were used. All calculations were carried out at the Γ-point of the Brillouin zone. Double-ζ Gaussian basis sets[127] were used with the GTH pseudopotential.[81] Plane wave cutoffs were set to 650 Ry (8844 eV) with a relative cutoff of 70 Ry (952 eV). The Broyden–Fletcher–Goldfarb–Shanno algorithm (BFGS) was used to minimise the force on the atoms to 0.0001 a.u (0.005 eV) $Å^{-1}$.[128]

PBE was used to optimise the cell parameters and atomic positions in all calculations.[129] The optimised structures from the PBE calculations were then used as input for the calculations with the non-local XC functional PBE0-TC-LRC.[79] These PBE0-TC-LRC calculations had an exchange interaction cutoff of 2 Å and a Hartree-Fock exchange of 25%. To reduce the computational cost of non-local functional calculations, the ADMM was used.[130] The same GTH pseudopotentials and plane wave cutoffs were used in both the PBE and PBE0-TC-LRC calculations.

The defect formation energy $E^f[X^q]$ was calculated using:

$$E^f[X^q] = E_{tot}[X^q] - E_{tot[bulk]} + \sum_i n_i \mu_i + q(E_{VBM} + \mu_e) + E_{corr} \tag{4.1}$$

Where E$^f[X^q]$ represents the formation energy of a defect with charge q, $E_{tot}[X^q]$ i is the total energy of the system containing the defect, while $E_{tot}[bulk]$ denotes the total energy of the pristine (defect-free) system. The term $\sum_i n_i \mu_i$ accounts for the chemical potentials of species added or removed to create the defect, q is the charge state, E_{VBM} represents the energy of the valence band maximum, and μ_e is the Fermi energy, or electron chemical potential. The correction term E_{corr} addresses the finite-size electrostatic errors due to periodic boundary conditions, typically employing the Makov-Payne correction, as outlined in prior literature[131]. Chemical potentials for species were derived from calculations of the same cell size as the defect-containing system.

NEB calculations were performed using the CI-NEB method, as described in Chapter 3.[88]

Optical absorption (OA) energies were calculated using the CP2K implementation of the TD-DFT, which does not include long range correction.[132,133] The truncation cutoff of the PBE0-TC functional was increased, making the function more alike to the PBE0 XC functional.[134] This was used with an enhanced TZVP-MOLOPT-GTH basis set, as the DZVP-MOLOPT-GTH basis sets did not accurately calculate the optical absorption peak energies. The local structure of the defect was re-optimised with these new parameters.

Positively charged vacancies are paramagnetic and are characterised using Electron Paramagnetic Resonance (EPR). This work was done by Thomas R. Durrant. To calculate the hyperfine EPR constants of defects, all-electron calculations were performed using CP2K and a Gaussian and Augmented Plane

Wave basis.[135] For these all electron calculations, pcJ basis sets were employed.[136] The EPR properties were then calculated within the framework of the density functional perturbation theory.[137]

4.3 Results of Calculations

4.3.1 Pristine crystals

First, I compare the properties of α-C and α-Q to understand the underlying structural differences that could contribute to any deviation in the stability of oxygen vacancies. As seen in Table 4.1, the calculated α-C and α-Q structures in this work are close to the experimental values. The space group of α-C is $P4_12_12$ with all lattice angles equalling 90°. α-Q has a right-hand crystallisation $P3_221$ space group with lattice angles α=β=90° and γ=120°.

The band gap width of α-Q has been studied in more detail than for α-C. The early experimental works by Bart *et al.*[138,139] shown a range in band gap values in α-Q of 8.6−9.5 eV, depending on the surface structure of α-Q. The bulk experimental band gap values have been then determined to be 9.65 eV by Garvie *et al.*[140,141] A close value has also been calculated with high-level theories, such as quasi-particle self-consistent GW.[142]

Earlier calculations using the PBE0-TC-LRC XC functional (also used in my work) have predicted the single-electron α-Q band gap at 8.6 eV.[143] Although this value corresponds well to Bart *et al.*[138,139] it is expected to be an underestimate of the bulk SiO_2 value. This underestimate is also seen in my work, with a α-Q band gap of 8.5 eV.

The band gap values for α-C are only known from theoretical work and depend on the XC functional used. Higher-level XC functionals increase the accuracy of the band gap. The highest level theory calculation found in the literature was using a meta-GGA XC functional to produce a single-electron band gap of 8.54 eV,[118] consequently, this value will be used for comparison. Using the PBE0-TC-LRC XC functional I calculated the band gap to be 8.57 eV, similar to the meta-GGA functional. Other lower levels of theory produced band gap values in the range of 5.5−10.3 eV[117,119,144–146].

The geometry of the two phases shows that the Si-O-Si bond angles of α-C are larger than in α-Q. This indicates that α-C has a more open and flexible structure than α-Q, leading to a lower density compared to α-Q. This is seen in Figure 4.1, where the large rings in α-C can be clearly seen. In addition, the Si-O bond lengths of α-C are slightly shorter than in α-Q; this may mean that any distortion introduced into α-C will introduce more strain as the bonds will be perturbed to a greater extent.

The calculated density of α-C (2.35 g/cm^3) and a-SiO$_2$ (2.20 g/cm^3) shows a difference of 0.15 g/cm^3, thus the band gaps are expected to differ with a lower density indicating a lower band gap value, as based on experimental literature.[147] However, El-Sayed *et al.*[148] calculated a band gap value of 8.9 eV for a-SiO$_2$ using the hybrid HSE06 XC functional, while experimental band gap values of a-SiO$_2$ range from 8.9-9.7 eV.[140,149–151]

In summary, a comparison of the calculated α-Q band gap to the experimental and high-level theory data shows that the α-Q band gap is likely underestimated in this work. Therefore, it is assumed that the α-C band gap is also underestimated. The geometries of the two phases are close to previously observed and calculated results. α-C has a less dense structure with large open rings, but the shortened Si-O bonds may mean distortions introduce more strain than with α-Q.

Table 4.1: The structural properties of α-cristobalite and α-quartz compared to the previous experimental and theoretical literature. The geometric structure is also shown, with the band gap separated at the end of the table. All bond lengths and lattice vectors are in Å, all angles are in degrees (°), the density is in g/cm^3, and the band gap is in eV.

Parameter	α-Cristobalite		α-Quartz	
	This Work	Literature Data	This Work	Literature Data
Lattice Vectors				
a=b	5.05	4.97[152]	4.93	4.91[153]
c	7.08	6.93[152]	5.43	5.40[153]
Bond length				
Si$_A$-O	1.604−1.609	1.600−1.607[152]	1.608	1.604[153]
Si$_B$-O	1.604−1.609	1.600−1.607[152]	1.612	1.613[153]
Bond Angles				
O-Si-O	108−111.8	108.1−111.3[154]	109.2−110.5	109.0−109.5[153]
Si-O-Si	150−153	146.6[152]	144.8−145.1	143.7[153]
Density	2.35	2.18−2.37[118,119]	2.41	2.47−2.70[118,119,155]
Band gap	8.57	8.54[118]	8.5	9.65[140]

References[118,119,155] are the results of theoretical calculations.
References[140,152–154] are experimental data.

4.3.2 Oxygen Vacancies

Three charge states of oxygen vacancies were investigated in both α-Q and α-C in different configurations: neutral Si-Si dimer (V_O^0), negative Si-Si dimer (V_O^-), positive Si-Si dimer (E'_{di}), puckered (E'_{puck}) and back-projected (E'_{bp}) configurations. The structures and highest occupied molecular orbitals (HOMOs) of these defects are shown in Figs. 4.3 and 4.4. The short-range geometric parameters of the four configurations are summarised in Tables 4.2-4.3 in conjunction with Figs. 4.3 and 4.4. Below I discuss their geometric, electronic and optical properties in more detail.

4.3.2.1 Geometric structure and stability

Neutral vacancies

Neutral O vacancies in SiO$_2$ are characterised by the formation of a Si–Si bond sharing two electrons, which is accompanied by significant displacement of

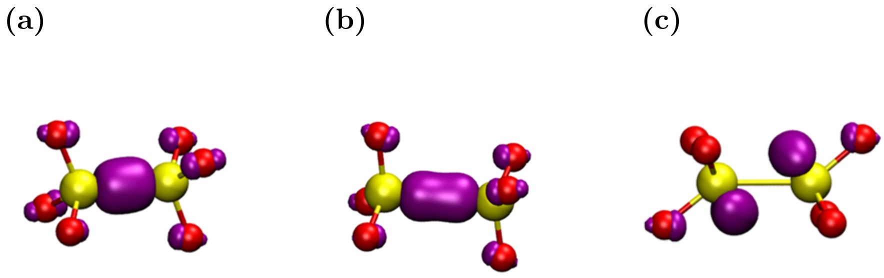

Figure 4.3 Square modulus of the wavefunction of the highest occupied state in the studied dimer oxygen defects in α-C shown in purple, the isosurface shown is $|0.1|$. Yellow atoms are silicon and red atoms are oxygen. (**a**) V_O^0 neutral dimer configuration. (**b**) E'_{di}, positive dimer. (**c**) V_O^-, negative dimer.(**a-c**) are general HOMOs applicable to either α-cristobalite or α-quartz.

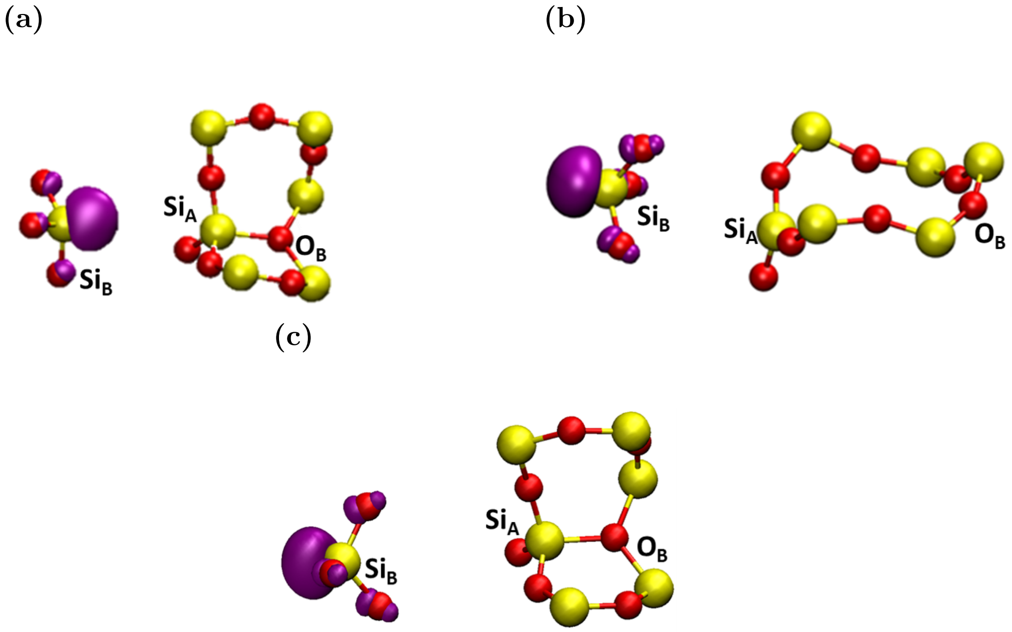

Figure 4.4 Square modulus of the wavefunction of the highest occupied state in the studied oxygen E' defects shown in purple, the isosurface shown is $|0.1|$. Yellow atoms are silicon and red atoms are oxygen. (**a**) E'_{puck}, α-quartz puckered, forward projected; (**b**) E'_{bp}, α-cristobalite, back projected; (**c**) E'_{bp}, α-quartz, puckered, back projected.

two Si atoms in the direction of the vacant O site (see Fig. 4.3a and Tables 4.2-4.3). Comparing to pristine structures, the formation of V_O^0 is accompanied by a decrease in the distance between the two Si atoms by 0.81 Å and 0.69 Å for α-C and α-Q, respectively. The character of electron localisation between the two Si atoms, forming the bond is seen in Fig. 4.3a.

Table 4.2: The formation energies of defects in α-C and the bond length (Å) between the atoms surrounding the oxygen vacancy: Si_A, Si_B, O_B and O surrounding the $\mathrm{Si}_{A/B}$ atoms in α-C. The range $-$ of the $\mathrm{Si}_{A/B}$-O lengths shows that bond lengths slightly differ due to asymmetries in the relaxation around the defect. The atoms and labelling conventions are described in Figs. 4.2, 4.3 and 4.4.

Bond	pristine	V_O^0	E'_{di}	E'_{bp}	V_O^-
Si_A-Si_B	3.11	2.38	2.88	4.59	2.39
Si_A-O_B	5.31	5.54	5.22	4.83	5.63
Si_A-O	1.61	1.61$-$1.63	1.57$-$1.58	1.62$-$1.63	1.67$-$1.70
Si_B-O	1.61	1.62$-$1.63	1.57$-$1.58	1.54$-$1.55	1.67$-$1.71
Formation Energy (eV)	0	5.14	3.67	4.39	12.91

Table 4.3: The formation energies of defects in α-Q and the bond length (Å) between the atoms surrounding the oxygen vacancy: Si_A, Si_B, O_B and O surrounding the $\mathrm{Si}_{A/B}$ atoms in α-Q.

Bond	pristine	V_O^0	E'_{di}	E'_{puck}	E'_{bp}	V_O^-
Si_A-Si_B	3.09	2.41	3.00	4.45	5.38	2.47
Si_A-O_B	3.66	4.10	3.71	1.83	1.84	4.07
Si_A-O	1.61	1.63	1.58	1.62	1.61$-$1.64	1.69$-$1.73
Si_B-O	1.61	1.62	1.57	1.58	1.57$-$1.59	1.66$-$1.68
Formation Energy (eV)	0	5.37	3.59	3.36	3.80	13.14

Positively charged vacancies

Some of the ways of creating positively charged vacancies in SiO_2 are via hole trapping or by electronic excitation and ionisation of neutral vacancies. Both are complex processes that can lead to significant reorganisation of the surrounding lattice due to strong electron-phonon coupling. In static calculations presented here, positive charging of a periodic cell leads to hole trapping on the Si–Si bond and the Si_A-Si_B distance increase compared to the V_O^0 defect by 0.46 Å and 0.59 Å for α-C and α-Q, respectively (see Tables 4.2-4.3). If no further reorganisation occurs, this configuration of the positively charged defect is named E'_{di}. The Si–Si bond is significantly weakened due to the loss of an electron and the consequent reduction in bonding order between the two silicon atoms (see Fig. 4.3b) and due to asymmetry of the lattice structure, more defect configurations are possible.

One such an asymmetric configuration in α-Q was discovered in refs.[34,35] where Si$_A$ in Fig. 4.2b relaxes through the plane of its three back-bonded oxygens and makes a bond with the so-called back oxygen O$_B$, as shown in Fig. 4.4a. This Si atom carries a hole and Si$_B$ carries a strongly localised unpaired electron. This configuration has also been predicted to be stable in some sites of a-SiO$_2$ (see discussion in ref.[36]) and is commonly called the puckered configuration, therefore, I label it as E'_{puck}.

The E'_{puck} configuration has the largest Si$_A$-Si$_B$ distance due to the puckering of Si$_A$ through the plane of O atoms, as seen in Fig. 4.4a, and this distance is close to the literature values[27,28,156]. This configuration is 0.23 eV lower in energy than E'_{di}. The CI-NEB calculated adiabatic barrier between the two configurations is 0.26 eV. Similar results were also found in[40,93]. In particular, the results presented in ref.[40] demonstrate the dependence of the barrier height on the size of the crystal region allowed to relax. The barrier for the reverse process of conversion from E'_{puck} configuration back to the dimer is 0.49 eV, which is in good agreement with previous calculations[27].

The structure of α-C is more symmetric than that of α-Q with Si$_A$ and Si$_B$ being equivalent and O$_B$ further away from them in the corresponding rings (see Fig. 4.2a). Therefore, the E'_{puck} configuration proved to be unstable in α-C. However, I found another stable configuration where the Si$_B$, carrying the unpaired electron, is projected through the plane of its three back-bonded oxygen ions, as shown in Fig. 4.4b. A similar, so-called "back-projected" configuration, E'_{bp}, has been found in DFT calculations of amorphous SiO$_2$[2,157]. I note that in this configuration Si$_A$ carrying the hole relaxes into the plane of its nearest oxygen ions. The energy of the E'_{bp} configuration is 0.83 eV higher than that of the dimer. The NEB calculation to determine a barrier between E'_{di} and E'_{bp} did not fully converge, but the barrier exceeds 1.0 eV. These results suggest that E'_{di} is the dominant configuration of the positively charged O vacancy in α-C. Below, I calculate its optical and EPR characteristics which could be used for identifying it experimentally.

The E'_{bp} configuration is also stable in α-Q (see Fig. 4.4c), but in this case Si_A forms a bond with the back oxygen O_B. Therefore, the energy difference between the more stable E'_{puck} and E'_{bp} configurations is smaller than in α-C at 0.44 eV. Thus, there are at least three different configurations of positively charged vacancy in α-Q. The calculated EPR and optical properties of the E'_{puck} configuration are in agreement with the experimental data for the E'_1 centre in α-Q[35,92] (see also my results below) and this configuration is often associated with this defect. Below I compare the calculated optical and EPR parameters of this and other configurations in α-Q and α-C.

Negatively charged vacancies

The flexibility of the SiO_2 structure suggests that the lattice relaxation could promote trapping of an extra electron by a neutral vacancy, as suggested in earlier calculations[35] and then further investigated in references[96,97]. The results presented here for α-Q and α-C are broadly in line with those previous calculations. The extra electron occupies the anti-bonding state shown in Fig. 4.3c. The Si_A-Si_B distance remains close to that in the neutral vacancy, but the bonds with the nearest O ions are elongated due to repulsion with the extra electron, as shown in Tables 4.2-4.3.

4.3.2.2 Charge Transition Levels

The charge transition levels (CTL) of the O vacancy in α-C and α-Q are compared in Fig. 4.5. In α-C, the E'_{di} centre is the most stable defect at Fermi levels close to the valence band (VB). The transition from E'_{di} to V_O^0 (+1 to 0) occurs at 1.64 eV above the VBM, while the transition from the less stable E'_{bp} occurs at 0.81 eV. The transition from V_O^0 to V_O^- (0 to -1) occurs at 8.34 eV, close to the CBM energy.

On the contrary, the α-Q CTL diagram shows that the E'_{puck}

configuration is the most stable defect near the VB. The +1/0 transition from E'_{puck} to V_O^0 occurs at 2.23 eV above the VBM, whereas the transition from E'_{di} occurs at 1.97 eV. E'_{bp} is less stable than E'_{di}, with a transition at 1.79 eV. The negatively charged V_O^- is more stable in α-Q than in α-C, with a 0/-1 CT at 7.73 eV. The fact that the puckered configuration of the positively charged vacancy is more stable than the dimer configuration agrees with the results of previous calculations in α-Q, e.g. refs.[27,34,35]. However, in α-C positive oxygen vacancies have not been previously investigated, so the contrast in the stability of E'_{di} highlights the differences between α-C and α-Q structures.

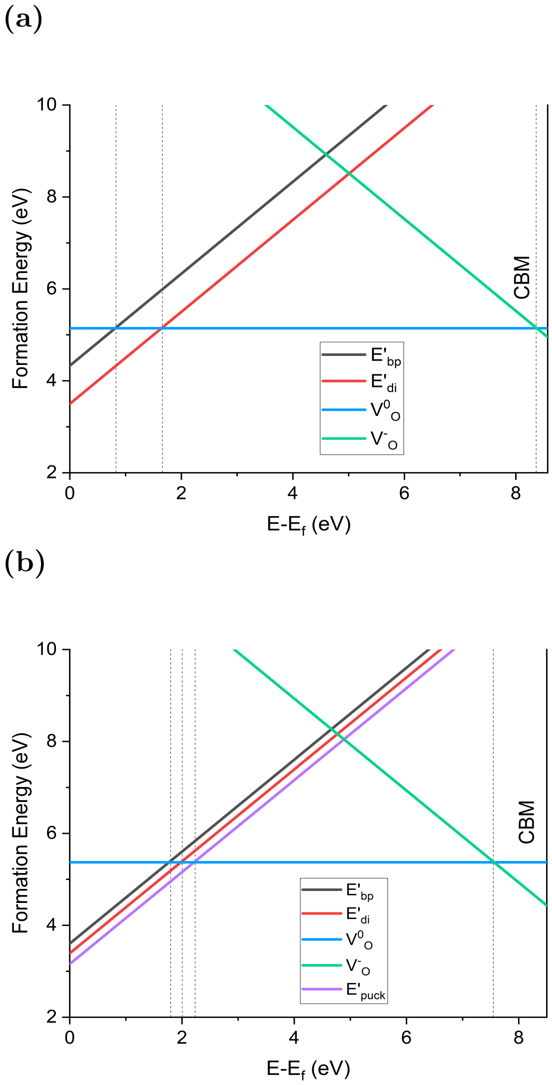

Figure 4.5 Charge transition level diagram of oxygen vacancy defects in (**a**) α-cristobalite and (**b**) α-quartz. 0 eV is the valence band maximum and the graph cuts off at the conduction band minimum. The dotted lines show the charge transition levels between the different charge states.

4.3.2.3 Optical Absorption

To understand how these oxygen vacancy defects affect the observable properties of the two polymorphs, the optical transitions of α-C and α-Q were investigated using TD-DFT. Due to the CP2K implementation of TD-DFT, the results presented in this section were calculated using the PBE0-TC XC functional, in contrast with the other sections where the long-range GGA correction (LRC) was used. PBE0-TC uses a constant fraction of exact exchange in the short range until a specified cut-off distance, at which it sets exact exchange to zero. To check whether the TD-DFT spectra are sensitive to the cut-off used in truncating the exact exchange, apart from using the 2 Å cut-off, I also used the maximum cut-off for each silica phase according to the cell size, 6.4 Å for α-Q and 7.5 Å for α-C, respectively. This ensured that the lack of LRC did not introduce artifacts and also meant that the XC functional is almost identical to the classic PBE0 XC functional.

Table 4.4: Optical absorption of oxygen vacancies calculated using different exact exchange cutoff radii. 2 Å is the cutoff used in geometry optimization. 6.4 Å and 7.5 Å are the highest cutoff points for the phases of α-quartz and α-cristobalite, respectively. Transition types were determined by the state that had the largest contribution to the excitation. In the spin-polarized calculations, i.e. positively charged defects, the α spin channel contributed to a large extent to the transitions. Transition types are notated by the symmetry of the states, the Si. → Si. indicates a promotion into the singly occupied dangling bond on the same Si atom.

Cutoff Radius (Å)	Phase	Defect	Peak energy (eV)	Oscillator Strength	Transition Type
7.5	α-C	V_O^0	7.62	0.22	$\sigma \rightarrow \pi$
			7.72	0.20	
			8.13	0.16	
			8.4	0.13	
		E'_{di}	7.56	0.12	$\sigma \rightarrow \pi$
			7.72	0.11	$\sigma \rightarrow \pi*$
6.4	α-Q	E'_{puck}	6.18	0.12	Si. → deloc. ring
2	α-C	V_O^0	7.86	0.27	$\sigma \rightarrow \pi$
			7.94	0.19	
			8.20	0.13	
			8.48	0.12	
		E'_{di}	6.27	0.15	$\sigma \rightarrow \sigma*$
			7.86	0.12	$\sigma \rightarrow \pi$
	α-Q	E'_{puck}	6.38	0.14	$\text{Si}_B \rightarrow \text{Si}_A$
			6.43	0.12	Si. → deloc. ring

The results shown in Table. 4.4 demonstrate the effect of the cut-off radius on transition energies. I first consider the results for the E'_{puck} configuration in α-Q. In Table 4.4 I only show transitions with oscillator strength exceeding 0.1. The transitions at 6.18 eV for the 6.4 Å cut-off (and at 6.43 eV for the 2.0 Å cut-off) have a strong contribution from the localised orbitals on the Si_B and atoms in the surrounding rings. The unpaired electron mixes with the Si*pd* and O*p* states of the surrounding rings, this forms the bottom of the conduction band. The transition energies are close to the previously calculated values of 5.8-6.1 eV[92,158].

The optical absorption in the 5.8 - 6.0 eV region in SiO_2 is usually associated with the E' centre and is attributed to its E'_{puck} configuration. Experimental optical absorption spectra in α-Q are quite scarce. Guzzi et al.[159]

attribute the 6.08 eV peak measured at 77K to the E'_1 centre in neutron-irradiated α-Q. My results at the 6.4 Å cut-off support this attribution. The nature of electronic excitations responsible for optical absorption of the E'_{puck} centre has been discussed in ref.[160] where it has been proposed that it is caused by electron transfer from Si_B to Si_A carrying the hole. This model has been confirmed by DFT calculations in cluster models[92,158]. However, I observe significant contribution of the charge transfer transition only at the small cut-off. The difference in the nature of excitation with the results of refs.[92,158] can be attributed to the much larger size of the periodic cell and more delocalized nature of the CBM states in my calculations compared to the small cluster calculations in refs.[92,158]. However, I note that most optical transition energies are quite robust with respect to the exchange cut-off value and method of calculation.

Similar trends with respect to the cut-off radius can be seen also for the V_O^0 centre in α-C, the transition energies with the 6.4 Å radius are reduced by about 0.25 eV with respect to those at 2.0 Å. The main transitions at 7.62 and 7.72 eV are in very good agreement with the absorption peak at 7.6 eV[25,159] usually attributed to the ODC(I) defect, where the proposed structure is a relaxed diamagnetic oxygen vacancy with two electrons localised between two silica in α-Q and SiO_2 glass samples.[161–163] The main transition is between the bonding and anti-bonding σ states localised at the Si-Si bond. The strongly localised nature of the bond may explain why the predicted transitions for α -C are so similar to those in α-Q and a-SiO_2, as the long-range structure of the silica may not affect this transition. Two further peaks are seen at 8.2 and 8.48 eV which can be related to those observed experimentally[159] and are due to localised high-energy π defect states in the conduction band.

The calculated transition energies for the E'_{di} configuration in α-C at 7.56 eV and 7.72 eV (see Table. 4.4) overlap strongly with those for V_O^0 but have lower oscillator strengths. Therefore, other data, such as luminescence and EPR spectra will be required for their identification. I note the similarity with F and F^+ centres in MgO and CaO in this respect, where the absorption spectra of these defects also strongly overlap (see e.g. ref.[164]). Below I present the results of my calculations for EPR parameters of E'_{di} and E'_{puck} configurations.

4.3.2.4 EPR parameters

The pseudopotentials used so far in this paper are unsuitable for the calculation of EPR parameters, and instead computationally expensive all-electron (AE) calculations must be performed with an expanded basis set suitable for EPR calculations. This work was conducted by T. R. Durrant. Benchmarking calculations demonstrated that as the quality of the AE basis set was systematically increased, the AE optimised geometry tended to the pseudopotential geometries already obtained. Therefore, the previously calculated defect geometries were maintained, and then an AE calculation of the wave function was performed for these geometries. pcJ basis sets were employed[136], which systematically increase in quality from pcJ-0 to pcJ-2.

Table 4.5: Calculated isotropic hyperfine coupling constants employing the pseudopotential structures and the all-electron wavefunction with the PBE0 functional, as the quality of the pcJ basis sets is systematically improved.

AE basis	α-Quartz (mT)			α-Cristobalite (mT)	
	E'_{di}		E'_{puck}	E'_{di}	
Silica	$\mathrm{Si_A}$	$\mathrm{Si_B}$	$\mathrm{Si_A}$	$\mathrm{Si_A}$	$\mathrm{Si_B}$
pcJ-0	12.29	10.11	42.25	11.16	10.78
pcJ-1	11.14	8.70	38.96	10.44	10.01
pcJ-2	10.26	8.06	37.46	9.55	9.17

The results of these calculations are summarised in Table 4.5. The isotropic hyperfine coupling constants were calculated for the considered defects, which are dominated by Fermi contact interactions and neglect the subtler anisotropic splittings. As can be seen in Table 4.5, there are significant differences in the calculated hyperfine couplings between the two configurations E'_{di} (in α-C and α-Q) and E'_{puck} (in α-Q), due to the differing degree of electronic localisation in the two cases. In the E'_{puck} configuration, the unpaired electron associated with the defect state is localised on a single Si, and hence a strong hyperfine coupling is observed. In contrast, in the E'_{di} configuration in both phases, the defect state is delocalised across two Si atoms, and hence a much weaker coupling is observed. Although there are important structural differences between α-C and α-Q, my results show that they do not significantly affect the resultant EPR parameters. The very minor difference in the calculated values for the two Si atoms in the E'_{di} defect occurs because the introduction of the oxygen vacancy lowers the symmetry and the two Si sites are no longer symmetrically equivalent.

I note that the hyperfine coupling constant obtained here for the E'_{puck} configuration in α-Q is in good agreement with 40.15-42.5 mT attributed to the E'_1 centre[32,165]. These values for the E'_{di} configuration are similar to the 10 mT seen in the literature for E'_δ centre[166] as well as in calculations of dimer vacancy configurations[96]. However, the analysis of experimental EPR spectra of the E'_δ centre in silica glass has concluded that this centre has a more complex structure than the E'_{di} configuration described here and in previous calculations.[37,38] Since E'_{di} is the only stable configuration of positively charged vacancy in α-C, EPR measurements for the positively charged O vacancy in α-C offer a unique opportunity to identify this configuration and verify the theoretical predictions.

4.4 Discussion and Conclusions

Predicting properties of defects in solids is a growing activity involving advanced DFT calculations and increasingly machine learning. Still, the properties of even basic intrinsic defects observed in binary oxides, such as SiO_2, are not fully understood. Creating and proving models of defects in solids is still a major challenge. In this work, I used the O vacancy in α-quartz to calibrate my computational procedure and test previous predictions using less accurate methods. I then compared the structure and properties of O vacancies in two SiO_2 crystalline phases, α-quartz and α-cristobalite, to investigate how the structural difference affects these properties and to find ways to identify the dimer configuration of the positively charged O vacancy. The optical absorption spectra of O vacancies in α-C and α-Q were calculated using TD-DFT and isotropic hyperfine constants were calculated for positively charged configurations to aid in experimental identification.

The results for neutral and negatively charged vacancies are similar in both phases and agree with previous calculations. However, there is a significant difference in the number and relative stability of configurations of positively charged vacancies. I found three configurations in α-Q, with E'_{puck} being the most stable followed by the E'_{di} and E'_{bp} configurations. There are only two stable configurations in α-C, with E'_{di} being much more stable than E'_{bp}. This difference is attributed to the difference in crystal structures and short-range environment of Si atoms in both phases. The back-projected, E'_{bp}, configuration of the positively charged vacancy has been predicted in previous calculations of O vacancies in amorphous SiO_2, but has not been considered in crystalline phases. To the best of my knowledge, it has not been attributed so far to any experimental signal.

The optical and EPR characteristics calculated for the E'_{puck} configuration in α-Q are close to the experimental data for the best-studied E'_1 centre. Periodic cells used in my calculations are much larger than 72-atom cells typically used in the past as well as molecular clusters. They better account for the long-range defect-induced lattice distortions predicted by embedded cluster models[28]. However, the optical transition energies are overestimated with respect to the maxima of absorption spectra observed in α-Q (6.08 eV[159]) and a-SiO_2 (5.8 eV[25]). TD-DFT shows contributions of both charge-transfer excitations and those into the states more localised on one Si and the surrounding atoms into this absorption peak. I note that, although my results in terms of the structure, relative energies, optical and EPR properties are in line with many previous studies of the E'_{puck} configuration in α-Q, the accuracy of these calculations as well as experimental optical measurements should still be improved to make a fully confident attribution.

On the other hand, both the E'_{di} and E'_{bp} configurations have never been experimentally identified in either α-Q or a-SiO_2. By comparison of hyperfine constants, earlier theoretical simulations have associated the E'_{di} configuration with the E'_δ centre observed in a-SiO_2[27]. However, several experimental EPR studies ruled out this attribution[37,38]. The predicted stability of the dimer configuration in α-C may provide an opportunity to finally observe and investigate it using the optical transition energies and hyperfine splittings calculated here.

However, in the pursuit of experimentally validating the E$'$ centres, it is notable that the E'_{di} and E'_{bp} configurations have not yet been identified experimentally in a-SiO_2, despite numerous theoretical predictions. This may suggest that the oxygen vacancy does not serve as the primary precursor for the formation of E' centres. Experiments using field-dependent recombination of holes trapped in thermally grown a-SiO_2 films with injected electrons[167] revealed that the paramagnetic state of the E' centre is not always correlated with the entity bearing the positive charge. It has been suggested that the positive charge is protonic in origin. Consequently, the O_3 ≡Si–H entity in a-SiO_2 has been suggested as a possible E' centre precursor[167], whereupon hole trapping hydrogen dissociates in the form of a proton leaving behind a neutral paramagnetic E' centre, a hypothesis later corroborated by theoretical calculations[168].

To summarise, these results may help defect characterisation in silica phases. They demonstrate how subtle differences in the local structure of silica polymorphs strongly affect the structure and stability of basic intrinsic defects. Although the surface of α-C is a good mimic of that for a-SiO_2, positively charged O vacancies in bulk show significant differences in the structure and relative stability of configurations. This may affect modelling of charge transfer processes at interfaces simulated using α-C.

Chapter 5

$SiO_2/H_2O/WS_2$ Interface Structure

Having established the fundamental properties of α-cristobalite SiO_2 and its defects, I will now focus on the WS_2/SiO_2 interface with confined water present.

As discussed in Chapters 1 and 2, the WS_2/SiO_2 interface is of interest to a variety of research communities due to the electronic properties of WS_2 and the ubiquity of SiO_2 as a dielectric substrate. Due to the hydrophilic nature of silanol groups on the surface of SiO_2, water is difficult to remove at the surface, leading to confined water between WS_2 and SiO_2. Understanding the properties of confined water is important both fundamentally and for their effects on the interfacing materials.

I investigated the structure and dynamics of confined water between WS_2 and SiO_2 using density functional theory and *ab initio* molecular dynamics, comparing it to adsorbed water on the surfaces of WS_2 and SiO_2. The results show that confined water becomes increasingly structured, with its orientation influenced by hydrogen bonding to the silanol groups as well as by the partial reorientation of water molecules to face WS_2 in an H-up configuration. The presence of silanol groups disrupts the hydrogen bonding network of water at monolayer coverage for both confined and unconfined water. For all interfaces explored, changes in both structural and dynamic properties are dependent on the number of water layers present.

5.1 Introduction

Studies and applications of WS_2 and other TMDs often require growth or deposition of thin films of these 2D materials on different substrates[3,15,16]. Insulating substrates, such as Al_2O_3, SiO_2, and h-BN, are often used for potential applications of these heterostructures in microelectronics, sensing and catalysis. From this perspective, understanding how the interaction of TMDs with substrates affects the properties of each material and the performance of the heterostructure is of great interest. In this work, I am particularly focused on the WS_2/SiO_2 interface, but the issues I discuss are common to other TMDs deposited on SiO_2 substrates.

Without special treatment, silica surfaces exposed to humidity are covered by -OH (silanol) groups, resulting in hydrophilicity of the surface and the presence of water at ambient temperatures and pressures[169]. The hydrogen bonding of water to the silanol groups at the silica surface causes the water to reorient and reduce mobility near the surface, although the exact structure of the water is still controversial[170,171]. The deposition of a WS_2 film is likely to trap a certain amount of water between SiO_2 and WS_2 surfaces. The structure and dynamics of this nanoconfined water is the main focus of this study.

The silanol groups on the SiO_2 surface can significantly influence the water structure near the interface, primarily through hydrogen bonding (HBonding) between the silanol groups and water molecules. The density and amount of water at the interface can further affect the structural and dynamic properties of the system. However, the exact structural changes induced by the silanol groups remain a subject of debate in the literature.[172]

Infrared (IR) Attenuated Total Reflection (ATR) studies suggest that, at relative humidity (RH) levels below 50%, water forms ice-like layers that are strongly hydrogen-bonded. Above 50% RH, water transitions to more disordered, liquid-like structures.[170] Theoretical studies using AIMD have also demonstrated that near the silica surface, where silanol groups are present, water forms ice-like layers connected by HBonds.[173,174]

However, heterodyne-detected vibrational sum frequency generation (HD-VSFG) experiments suggest that at 20% RH, nanodroplets begin to form and between 20% and 50% RH, partially liquid water layers emerge, becoming uniform by 90% RH.[171] The formation of these nanodroplets is attributed to preferential interactions between water and silanol groups. Similar results were observed in a separate study using IR-ATR.[175] Further work with non-linear SFG has suggested the formation of two different layers: the binding interfacial layer (BIL), and the diffuse layer (DL). The BIL is tightly hydrogen bonded to the silanol groups, and the diffuse layer is much less structured but does show some reorientation of the water molecules due to stable HBonds formed with the BIL.[176–178] Therefore, one can expect that water is tightly HBonded to the silanol groups on the SiO_2 surface. However, the transition point at which water becomes bulk water is still undefined.

On the other side of the interface, the WS_2 water contact angle (WCA) measurements exhibit considerable variations, ranging from 38.8° to 90° degrees. These variations are influenced by factors such as substrate type, TMD thickness, air exposure, and surface oxidation.[179–186] While these factors substantially impact the hydrophilicity of WS_2, studies of pristine WS_2 indicate that it exhibits mild hydrophilicity, with a WCA of approximately 70°.[179,183] The interaction between TMDs and water is strong enough to support their use in water-sensing devices.[52]

CMD simulations have provided deeper insights into the behaviour of water on TMD surfaces. For example, polygonal water clusters have been observed on MoS_2 and WSe_2 surfaces with bulk water.[187–189] The structuring of water predominantly occurs laterally to promote maximum HBonding among water molecules. When TMDs are exposed to significant amounts of water, CMD simulations predict the dewetting of water on MoS_2. This process leads to the formation of droplets.[190] Further exposure of MoS_2 to liquid water during experiments results in its oxidation to $MoO_3{\cdot}H_2O$, which forms needle-like structures.[185]

Beyond interactions with water at the surface, recent studies have explored water confined between two two-dimensional (2D) sheets to understand the structures and interactions that emerge in these confined environments.[191] The application of 2D materials for the confinement of water has been studied in desalination, focusing on graphene and TMDs MoS_2 and WS_2.[192]

Branching out from 2D material confinement, the choice of confining substrate can significantly influence the structure, reactivity, and properties of water. For example, water confined between Ru and SiO_2 has a reduced activation energy for the oxidation of H_2.[193] Investigations of water confined between graphene and substrates, such as SiO_2 or mica, reveal the formation of ice-like double-layer structures, which allows water to diffuse between layers.[194] Furthermore, graphene and mica display ice-like water layers with a thickness of 3.7 Å, with structural defects in graphene playing a significant role in water adsorption.[191,195] Similar behaviour has been observed in MoS_2/mica systems, where atomic force microscopy (AFM) studies have demonstrated unique frictional properties and morphological deformation of MoS_2 in the presence of silica.[196,197] Water intercalation and the formation of water nanostructures have also been noted in MoS_2/mica interfaces under varying humidity conditions.[198]

However, the impact of SiO_2 substrates that introduce HBonding with confined water has not been thoroughly examined. To our knowledge there has been no previous investigation into the confined water at the SiO_2/WS_2 interface although water can be easily trapped between the two surfaces when the 2D material is mechanically or chemically exfoliated onto SiO_2.[17] Therefore, the SiO_2/WS_2 interface provides a natural platform to investigate the effects of HBonding on confined water. Previous studies of confined water between 2D materials and dielectric oxides have primarily used mica due to its ease of cleavage and low surface roughness. In contrast, SiO_2 has a much rougher surface, making it difficult to study using scanning probes. Therefore, understanding this interface heavily relies on theoretical modelling.

I investigate the structure and dynamics of water between SiO_2 and WS_2 by analysing and comparing the structural and dynamic properties of the

$SiO_2/H_2O/WS_2$, SiO_2/H_2O, and WS_2/H_2O interfaces. I employ AIMD and simulate systems containing one, two, and three layers of water. The water consistently exhibits a long-range structure induced by silanol groups on the SiO_2 surface, while a double-layer structure is observed at the WS_2 interface. At both the WS_2 and SiO_2 interfaces, the hydrogen atoms of water are drawn closer to the surfaces; this effect is amplified with the introduction of confinement. While AIMD offers a higher level of accuracy, it has certain limitations, most notably restricting simulation timescales to picoseconds (ps), compared to the nanosecond (ns) range achievable with CMD. As a result, some dynamic properties may be affected due to the limited sampling. Nonetheless, AIMD provides accurate modelling of the system, serving as a reliable foundation for future studies, such as training machine learning potentials (MLP) or providing a benchmark for other computational methods.

5.2 Methodology

5.2.1 DFT calculations

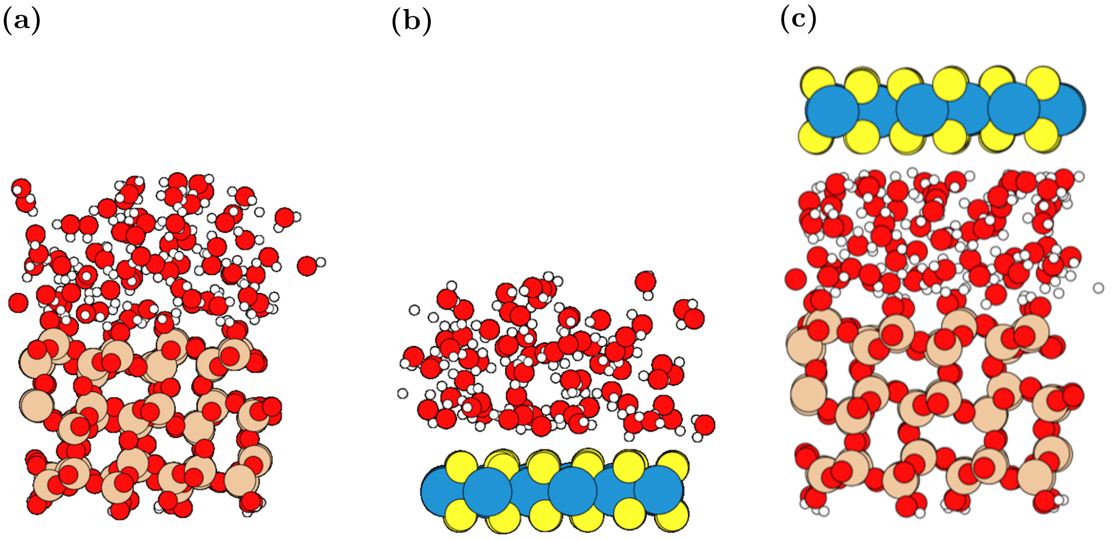

Figure 5.1 Snapshot geometric structures used in this work, with three water layers shown for all interface structures. **a**) Shows the SiO_2/H_2O interface, **b**) shows the WS_2/H_2O interface, and **c**) shows the $SiO_2/H_2O/WS_2$ interface. For every interface, there is an extended vacuum region above and below, not shown in this figure. Colour coding: blue = W, yellow = S, red = O, white = H, beige = Si.

5.2.1.1 Individual Materials

Surfaces of amorphous silica films and silica glasses that can serve as substrates for the deposition or growth of TMDs under normal conditions are known to contain one silanol group per surface Si atom.[19,169] It is commonly accepted that the $(10\bar{1})$ surface of the SiO_2 crystalline phase α-C represents a good mimic of the density and distribution of single silanol groups on an amorphous silica surface[19]. The density of silanol groups on this surface (4.7 OH nm^{-2}) is indeed similar to that of amorphous silica (4.5 OH nm^{-2}), which is predominantly used in device manufacturing. I therefore use α-C as a model substrate in all further calculations. Based on previous simulations of the properties of silica surfaces, I expect that disordered locations of silanol groups characteristic of amorphous substrates will not affect our conclusions[199,200].

5.2.1.2 Constructing the $SiO_2/H_2O/WS_2$ interface

The hydroxylated silica substrate was represented by a 3×2×1 α-C slab, with 12 silanol groups on either side of the slab. With the introduction of a vacuum gap on either side of the cell, its dimensions were 16.9×14.9×60 Å, with the SiO_2 slab $\approx$ 10 Å thick.

To construct the SiO_2/H_2O interface, the water and silica surface were equilibrated separately using CMD simulations, with the cell $\vec{x}$ and $\vec{y}$ dimensions fixed to the size of the silica cell. All CMD calculations were performed by Laura Hargreaves. A 3D periodic cell was then created by attaching the water boxes on either side of the silica slab with the length of the cell along $\vec{z}$ chosen so that, far from the surface, the average water density was 1.00 gcm^{-3}. L. Hargreaves used the standard 12/6 Lennard-Jones potentials with the parameters given by the INTERFACE force field[19] for the Si, O, and H atoms in silica and the TIP4P/2005f[201] forcefield for H and O atoms in water. Geometric mixing rules were applied to describe interactions between water and silica. Using the timestep of 0.5 fs, and T = 298.5 K CMD of this system was run for 10 ns in an NVT and then in an NVE ensemble, followed by another 10 ns CMD run in an NVT ensemble. This allowed us to achieve accurate bulk water densities in the

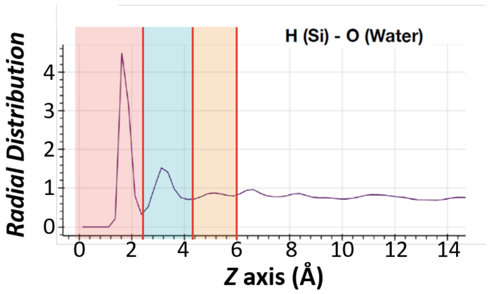

Figure 5.2 RDF between H_t-O_w of $H_2O/SiO_2/H_2O$ from CMD calculations, the distance on the z axis is in Å. Red lines show the cutoff of different layers used in DFT calculations. Red highlight section is 1 layer of water, blue is 2 layers, and orange is 3 layers.

system and reproduce the characteristic layered water structure near the interface[170,202].

This system corresponds to the interface between a thick water layer and a silica surface. However, in deposition experiments, exfoliated TMD layers are deposited on a silica surface exposed to ambient conditions. Based on the data reviewed in ref.[169] it is assumed that, depending on humidity and annealing temperature, the silica surface may have between 1 and 3 adsorbed water layers under such conditions. Based on this insight, L. Hargreaves constructed three SiO_2/H_2O cells with 1, 2 and 3 water layers, respectively. The initial structures of these cells were produced by truncating the equilibrated cell at the troughs of the radial distribution function (RDF) of the water layer as a function of distance from the surface (see Figure 5.2). The third layer, highlighted in orange, does not show a strong peak but resembles the more flat distribution of bulk water; therefore, this was chosen as the closest approximation to bulk water without unnecessarily extending the water for AIMD calculations.

To equilibrate this system, a 100 Å vacuum gap was added to the truncated SiO_2/H_2O systems with 1 - 3 water layers and the same CMD procedure was repeated again, where these systems were equilibrated with an NVT and NVE ensemble for 5 and 10 ns, respectively, at 298.5 K. The adsorbed water layers remain intact on the surface, confirming the reliability of the forcefields used. A detailed description of the structure and dynamic characteristics of this system is provided in reference[203].

To construct the $SiO_2/H_2O/WS2_2$ interface, the bottom layer of water was removed, so the layers of water are only on one side of the SiO_2 slab, and the bottom silica layer was left hydroxylated. This was done to ensure that the resulting 2D slabs with 1, 2 and 3 water layers are amenable for AIMD simulations of the total system.

To accommodate the WS_2 monolayer in these cells, the original WS_2 unit cell was transformed into an orthorhombic cell to ensure a good fit and minimal strain when added to the CMD-optimised SiO_2/H_2O system. The geometry of the 5×3 orthorhombic WS_2 structure was optimised using the PBE0-TC-LRC XC functional and the resulting band gap is given in Table 6.1. As discussed in Chapter 3, The electronic structure of TMDs is known to depend on strain[204–208]. However, introducing strain is inevitable when creating interfaces because of a lattice mismatch between the materials of the heterostructure. I found that the minimum strain between SiO_2 and WS_2 with fewer than 700 atoms in a periodic cell can be achieved when a 5×3 orthorhombic unit cell of WS_2 was rotated 90 ° with respect to the 2×3×1 SiO_2 slab. This leads to 2.62 % strain (compression) in the **a** direction and -5.69 % strain (tension) in the **b** direction of WS_2.

The strained, orthorhombic WS_2 monolayer was then added to the SiO_2/H_2O interface and a vacuum of at least 35 Å was introduced. The geometry of the whole system was optimised using DFT and a PBE-D3(BJ) functional at different WS_2 slab distances from the water surface of H_2O/SiO_2 to increase the efficiency of the calculation.

The optimised structure was then used as the starting geometry for the AIMD calculations in an NVT ensemble maintained at 400 K with a Nosé-Hover thermostat. In these simulations, I used the PBE-D3 functional because it provides a good geometry for WS_2 and SiO_2 although it is known to overbind water.[209–211] The high temperature was chosen because increasing the temperature to 350-400 K was shown to overcome this issue.[212,213] The equilibration time for AIMD was 4 ps, after this time, the system's total energy remained constant. This was followed by the 12.5 ps production runs, examples of snapshot geometries for the three structures are shown in Figure 5.1.

To compare the confined system to both SiO_2/H_2O and WS_2/H_2O, a similar procedure was followed. After CMD equilibration of the SiO_2/H_2O interface, no WS_2 was added. The WS_2/H_2O systems were created by removing the SiO_2 slab from the $SiO_2/H_2O/WS_2$ interfaces. For both interfaces, AIMD was then run using the same methodology as described above. This involved a 4 ps initial run which allowed the water to restructure from the previous configuration, and then a 12.5 ps production run.

5.2.2 Geometric Analysis

Given that water was included in the simulations, the geometric configurations of the system evolve over time. Variations in the positions of water molecules, influenced by factors such as the presence of silanol groups and the number of water molecules, were analysed using the MDAnalysis package.[214,215]

The one-dimensional (1D) density profile calculates the spatial distribution of water molecules. Additionally, further selection criteria can be applied to look at the water hydrogen (H_w) and/or water oxygen (O_w) atoms. The 1D density is defined as:

$$\rho_z(z) = \frac{N_z}{\delta_z \times D_x \times D_y} \tag{5.1}$$

where N_z is the number of molecules, D is the dimension of the cell in the respective direction, and δ_z is the grid spacing which was set to 0.1 Å. The density is calculated for every frame in the trajectory and averaged. The results allow for the investigation of water layering in the z direction and the specific arrangement of H_w and O_w. To enable comparison between the various water layers at each interface, the density was normalised to 1.

The 2D density profile is obtained using a similar method to the 1D profile, where the Cartesian axis is binned into length $\delta_x, \delta_y, \delta_z$. The 2D profile is calculated for each frame using

$$\rho_{xy}(x,y) = \frac{N_{xyz}}{D_z \times \delta_x \times \delta_y} \tag{5.2}$$

and then averaging over the trajectory length. Here N_{xyz} is the number of water molecules within each box and the bins for all δ are 0.1 Å.

The joint probability distribution (JPD) provides a good description of the water orientation by combining the probability of two different angles. The JPD of the water angles was calculated by aggregating two angles into a 2D histogram and normalised to get the probability as the total sum of all bins is one. The OH-OH bond angle, see Figure 5.3, was analysed in this work following the work of Smirnov[178] to ensure that the orientation of water could be determined. Since the distribution of correlated angles may be broad, I will focus on the orientations derived from the midpoint of the distribution, where the probability is highest.

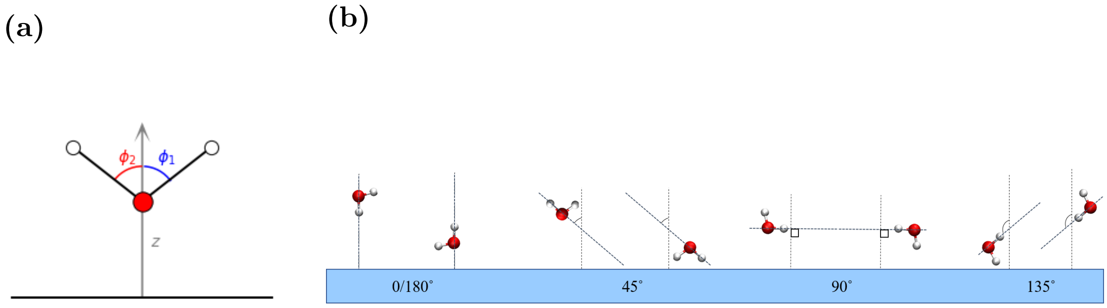

Figure 5.3 Schematics for relative angles of water relative to the surface normal of O-H orientations. **a**) gives the overall calculation of both OH-OH bond angles, and **b**) highlights different OH bond orientations.

Hydrogen bonds between water molecules were characterised based on geometric criteria, specifically the distance and angle between neighbouring molecules. The cutoff distance for HBond formation was defined as 1.2 Å, with a maximum distance between the donor and acceptor oxygen set at 3.0 Å. The cutoff for the O-H-O angle was set to 150 °.

Continuous hydrogen bond lifetimes were analysed using the autocorrelation function[216]:

$$C(t) = \langle \frac{h_{ij}(t_0)h_{ij}(t_0+t)}{h_{ij}(t_0)^2} \rangle, \tag{5.3}$$

where h_{ij} represents the existence of a hydrogen bond between atoms i and j, with $h_{ij} = 1$ if a bond is present and h_{ij}=0 otherwise. At the initial time, $h_{ij}(t_0)$ is equal to one. The calculation is averaged over multiple starting times t_0 to improve statistical reliability.

The HBond lifetimes were calculated by fitting a biexponential curve to the autocorrelation using the form:

$$C(t) = Ae^{-\frac{1}{\tau_1}} + Be^{-\frac{1}{\tau_2}}, \tag{5.4}$$

where A and B are the pre-exponential factors and sum to 1, and both τ_1 and τ_2 are the time constants, and τ_1 is for short-timescale processes and τ_2 is longer timescale processes. This description of the autocorrelation then allows for the HBond lifetime (τ) to be calculated using

$$\tau = \int_0^\infty C(t)dt. \tag{5.5}$$

The mean squared displacement (MSD) of water molecules was computed using the Einstein relation:

$$MSD(r_d) = \langle \frac{1}{N} \sum_{i=1}^{N} |\mathbf{r}_d^i - \mathbf{r}_d^i(t_0)|^2 \rangle_{t_0}, \tag{5.6}$$

where N is the total number of particles in the system, $\mathbf{r}^i$ are the coordinates of each particle, d is the system dimensionality, t_0 is the initial time. From this I can calculate the self-diffusivity:

$$D_r = \frac{\langle \delta r(t)^2 \rangle}{2d}. \tag{5.7}$$

To obtain $\langle \delta r(t)^2 \rangle$ I applied a linear fit to the MSD data.

5.3 Results and Discussion

5.3.1 Static Properties

I begin by calculating the static properties of the system, focusing on the average positions and orientations of water molecules at each interface.

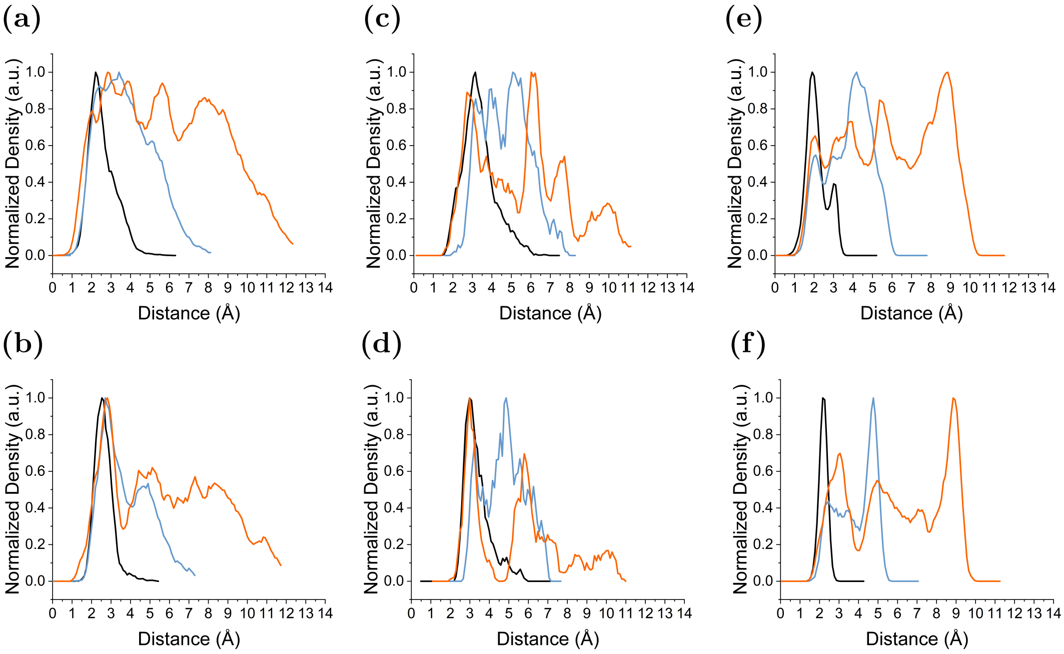

Figure 5.4 1D number density profiles of water for **a,c,e)** hydrogen (H_w) and **b,d,f)** oxygen (O_w). The interfaces shown are: **a,b)** SiO_2/H_2O, **c,d)** WS_2/H_2O, **e,f)** $SiO_2/H_2O/WS_2$. 0 on the x axis corresponds to the top Si atom of the SiO_2 surface for SiO_2/H_2O and $SiO_2/H_2O/WS_2$ interfaces, and the closest sulfur plane for the WS_2/H_2O interface. The different water layers are given by different colours: black: one layer, blue: two layers, orange: three layers.

5.3.1.1 SiO_2/H_2O interface

I first examine the water structure at the SiO_2/H_2O interface. The 1D density profile of water hydrogen (H_w) (Figure 5.4a) shows that all water layers exhibit a distinct initial peak between 2.0-2.4 Å, followed by a water oxygen (O_w) peak at 2.5-2.7 Å Figure 5.4b). The presence of a sharp peak demonstrates significant structuring at the interface, with H_w generally closer to the SiO_2 surface than O_w.

Farther from the surface, the final peak in the three layers is a small O_w peak at 7.3 Å, while the water density continues to 12 Å. This observation indicates a more liquid-like structure of water at greater distances from the silanol-terminated surface. The two distinct regions of water correspond to the BIL (close to the surface, highly structured) and the DL (further from the surface, less structured).

To further investigate the BIL structure of water, the JPD of the SiO_2/H_2O one-layer interface (Figure 5.5a) reveals two distinct correlated angles and using Figure 5.3, I can deduce the orientation of water. The first, most prevalent OH-OH angle is (110 °, 110 °), corresponding to a predominantly flat orientation but exhibits a slight out-of-plane H_w tilt downwards towards SiO_2 the surface. The second peak is at (15 °, 115 °), showing a water molecule with one H_w tilted upwards from the SiO_2 surface (Figure 5.5b).

Overall, these 1D profiles align well with previous studies of silica-water interfaces with similar silanol densities using CMD simulations, confirming that our AIMD results are reliable for reproducing average properties.[178,217,218]

5.3.1.2 $WS2_2/H_2O$ interface

At the WS_2/H_2O interface, the initial O_w and H_w for all systems are centred around 2.8 - 3.2 Å (Figures 5.4c and 5.4d). Therefore, it is expected that the water will be oriented parallel to the surface. However, for all layers, there is a H_w shoulder closer to the surface at 2.0-2.2 Å, so there is a slight preference of H_w to orient toward WS_2 (For precise details, see Table A.1). The WS_2/H_2O one-layer JPD indicates three distinct orientations (Figure 5.5c). The predominant orientation is observed at (90 °, 150 °), where one O-H bond is parallel to the WS_2 surface, while the other H_w points down towards the WS_2. The two alternative orientations are characterised by angles of (90 °, 90 °), where the water molecule is entirely parallel

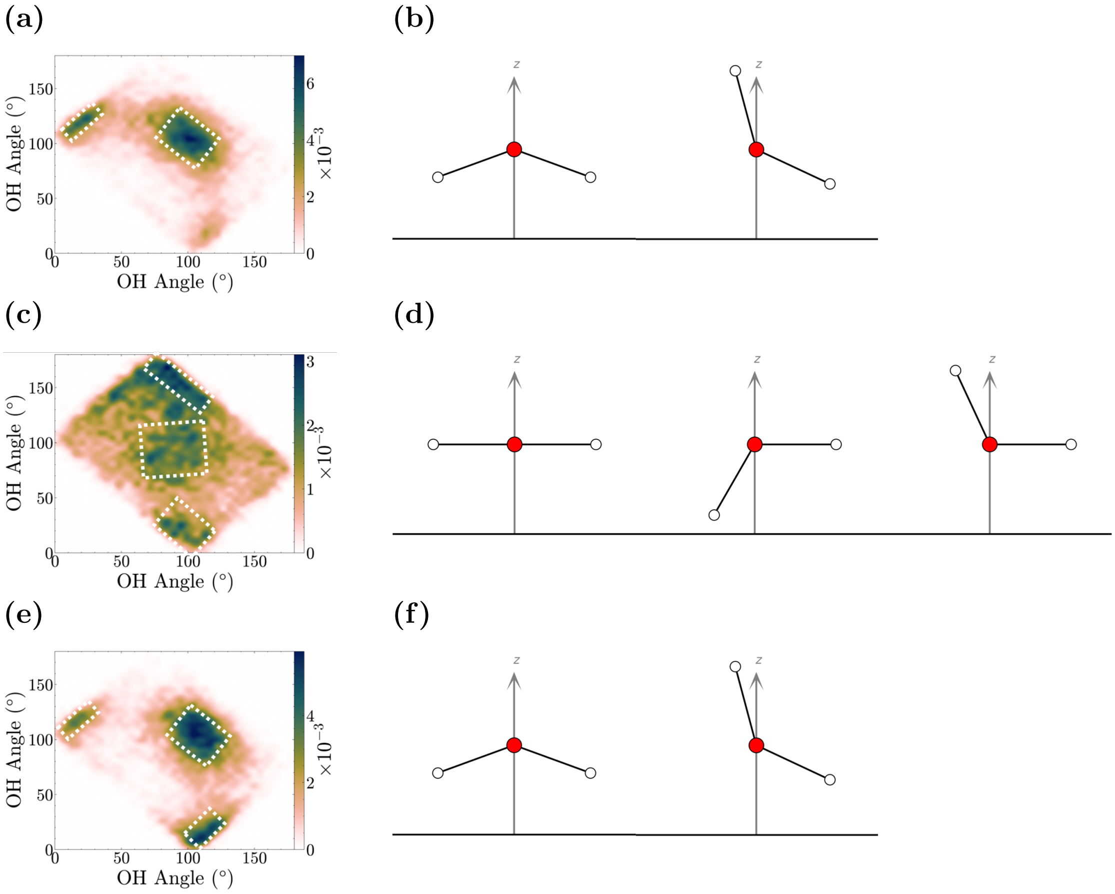

Figure 5.5 The joint probability distribution of OH-OH water angles for **a)** SiO_2/H_2O, **c)** WS_2/H_2O and **e)** $SiO_2/H_2O/WS_2$. The colour bar shows the probability. The right-hand side (**b,d,f**) shows the corresponding water orientations, which are highlighted in the JPD graph; duplicates have been removed for clarity.

to the WS_2 surface, and (90 °, 25 °) where one H_w is tilted away from the WS_2 surface while the other remains parallel (Figure 5.5d). Importantly, the orientation of O-H bonds that are perpendicular to the surface normal can facilitate lateral hydrogen bonding between water molecules. This clustering behaviour, which promotes hydrogen bonding among water molecules, is clearly illustrated for one water layer in Figure 5.6d. The reduced probability density at (90 °, 90 °) relative to other peaks suggests that interactions occur between the WS_2 and H_2O, rather than the water maintaining a flat, cyclic structure.

The two distinct peaks in three water layers for both H_w and O_w are at 2.8-3.0 Å and 5.8-6.1 Å. This indicates that at the surface of WS_2 there is a distinct double layer structure to the water. This is seen to an extent in the two-layer system as well, with peaks at 3.1-3.2 and 4.6-5.2 Å. There is a smaller peak centred around 10 Å for both H_w and O_w in the three-layer system. This may indicate a greater long-range structure at the WS_2/H_2O interface than originally anticipated. These peaks closely correspond to values calculated from AIMD of water on WS_2, MoS_2, and $WeSe_2$, which show peaks at approximately 3, 6, and 10 Å for all three TMDs.[219,220] Similar water structuring at the interface has also been observed for h-BN and graphene.[221]

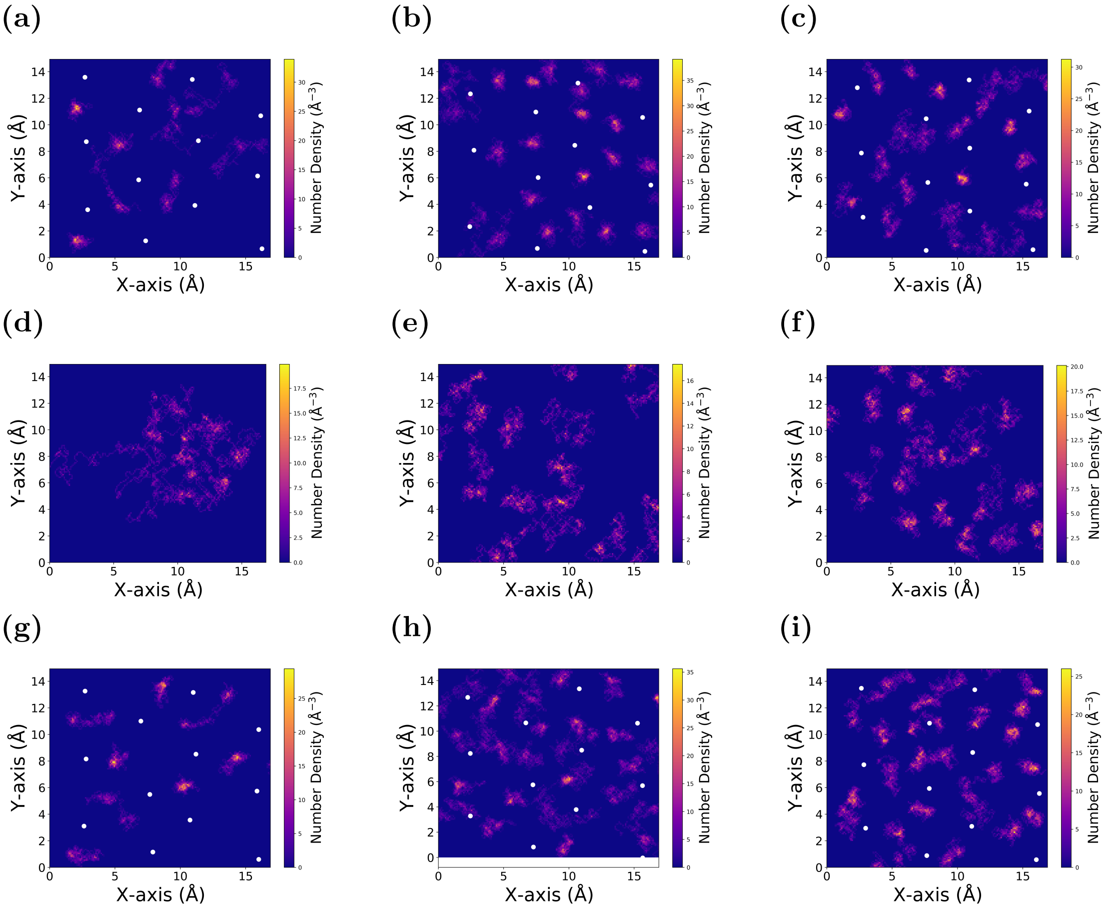

Figure 5.6 The XY 2D number density profiles of water on the underlying substrate. The interfaces are **a-c**) SiO_2/H_2O **d-f**) WS_2/H_2O, and **g-i**) $SiO_2/H_2O/WS_2$. The first column is for 1 water layer, the second column is for 2 water layers within 4 Å of the interface, and the third column is for 3 water layers also within 4 Å of the substrate. For interfaces with SiO_2 present, the average position of silanol group oxygens on the surface are represented by white circles.

5.3.1.3 $SiO_2/H_2O/WS_2$ interface

Finally, I investigate the static properties of the $SiO_2/H_2O/WS_2$ interface. For one layer of water, the H_w and O_w peaks are very sharp (Figures 5.4e-5.4f), indicating strong structuring at the interface, with increased structuring compared to the broader SiO_2/H_2O initial peak. The positions of the most probable orientations in the confined interface closely resemble those observed in the SiO_2/H_2O JPD, indicating that similar orientations are favourable (Figure 5.5e). Notably, the dominant orientation in the confined system at (110 °, 110 °) is also seen in the unconfined SiO_2/H_2O, where the H_w is tilted downward towards the SiO_2 surface. The two additional angles at (115 °, 15 °) and (15 °, 115 °) are equivalent and show the same orientation as in SiO_2/H_2O, with one H_w directed upwards away from the SiO_2 surface (Figure 5.5f).

However, in the two layer system, there is no sharp initial O_w peak observed in the 1D profile, suggesting that either multiple orientations of water are favourable, or that the water is less structured. When I examine the JPD of water 4 Å away from the surface (the BIL), I observe that the localisation of water angles changes for all interfaces. The SiO_2/H_2O interface remains the most consistent across different water layers, indicating that the BIL is tightly bound and less sensitive to changes in additional water (Appendix A Figure A.1). In contrast, for the WS_2/H_2O and $SiO_2/H_2O/WS_2$ interfaces, the JPD differs from that of the one-layer systems. For both interfaces the two-layer water angle is (90 °, 90 °), thus, water is expected to predominantly orient parallel to the underlying substrate. A parallel orientation of water has been observed in a single layer of WS_2/H_2O; however, strong localisation has not been detected within the confined one-layer system. The changes observed in the confined two-layer system may result from the increased availability of water, which facilitates the formation of larger hydrogen bonding networks among the water molecules. This effect is maximised by parallel orientations of water.

Investigating the WS_2/H_2O side of the confined interface, H_w is closer to WS_2 than O_w, as exhibited by the final peaks and shoulders from H_w in Figures 5.4e-5.4f. This is the same behaviour as seen at the unconfined WS_2/H_2O interface, highlighting that WS_2 does have a small impact on the water structure. Further comparison of peak positions between SiO_2/H_2O and $SiO_2/H_2O/WS_2$ reveals that they are aligned quite well, with only minor deviations (Appendix A Table A.1). I observe that the initial peak for one and two water layers is located closer to the SiO_2 surface compared to the SiO_2/H_2O interface. In the case of three water layers, the alignment of the initial peaks in both interfaces becomes comparable, and they also exhibit similar width.

Three water layers shows further change in water structure at the confined system JPD (Appendix A Figure A.3c). This suggests that, while the layering away from the interface resembles that of the SiO_2/H_2O interface, the arrangement of confined water is distinct, showing increased variation in the orientation of water molecules as the number of water layers increases. This difference in water structure is also evident in the 2D profiles in Figure 5.6, where the SiO_2/H_2O water is more localised around the silanol groups compared to the confined water.

Overall, the orientation of confined water is primarily influenced by the SiO_2 surface, with minimal contribution from WS_2. For all interfaces, H_w is oriented toward the substrate, which has been shown to be energetically favourable at both the SiO_2 and WS_2 surfaces.[222] Previous studies on SiO_2 surfaces indicate that the number and type of silanol groups affect the behaviour of water differently. Isolated silanol groups, which are used in our study, typically facilitate water approaching the SiO_2 surface more closely. The confinement of water may exacerbate this, as seen in the 1D density profile and the differences in JPD. HD-VSFG and CMD calculations have demonstrated that water molecules with their hydrogen atoms pointing toward the surface are favoured.[178,223,224] Nevertheless, I acknowledge the possibility of additional orientations, as our sampling is limited due to the AIMD method, potentially resulting in less reliable intensities in the JPD graphs. Previous literature suggests a variety of orientations at the SiO_2 interface.[225]

5.3.2 Dynamic Properties

I now turn to examining the dynamic properties of three interfaces, including hydrogen bonding and water mobility. These dynamic properties may provide insights into the reasons behind the observed structure and orientation of water.

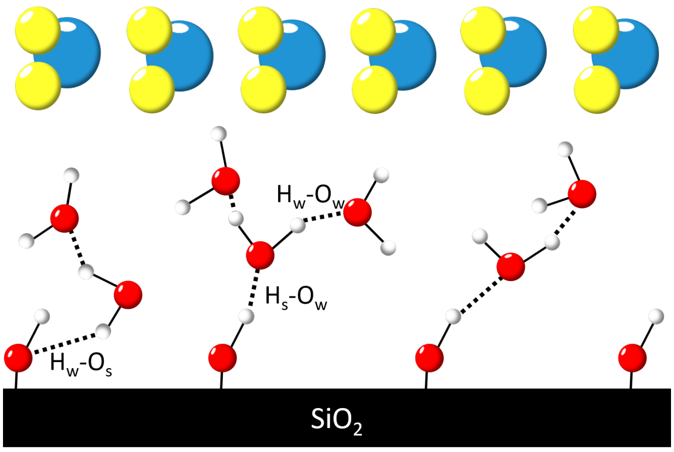

Figure 5.7 Different hydrogen bonding types at the interfaces, highlighting the different hydrogen bonding types between silanol groups and water and water-water hydrogen bonds.

5.3.2.1 SiO_2/H_2O

For the SiO_2/H_2O with a monolayer of water, there is minimal water-water (H_w-O_w) HBonding, with an average of 0.12 HBonds/water molecule (Figure 5.8a). This value is significantly lower than the average number of HBonds formed between silanol oxygen -water hydrogen (O_s-H_w) or water oxygen - silanol hydrogen (O_w-H_s) which are 0.43 and 0.59 HBonds/silanol group, respectively (Figure 5.8b). The MSD analysis of SiO_2/H_2O (Figure 5.9a) shows that the single water layer exhibits the lowest displacement, with a diffusion coefficient (D) of 0.10 Å^2/ps. This indicates that water molecules are strongly bound to the silanol groups, which limits their mobility. Therefore, at monolayer coverage, the silanol groups on the silica surface significantly disrupt the hydrogen bonding network (HBN) of water, a phenomenon also observed in previous CMD studies.[178]

As additional layers of water are introduced, the average number of H_w-O_w HBonds increases, reaching 0.80 HBonds/water molecule for the two-layer system and 1.00 HBonds/water molecule for the three-layer system. Therefore, neither the two- nor the three-layer system achieves a fully saturated HBN.

The lifetimes of HBonds determined by the autocorrelation function show that O_w-H_w HBonds last up to 1.31 (± 0.020) ps in two layers, and 1.21 ps (± 0.004) in three layers (Figure 5.10a). In one layer, the water does not form a sufficient

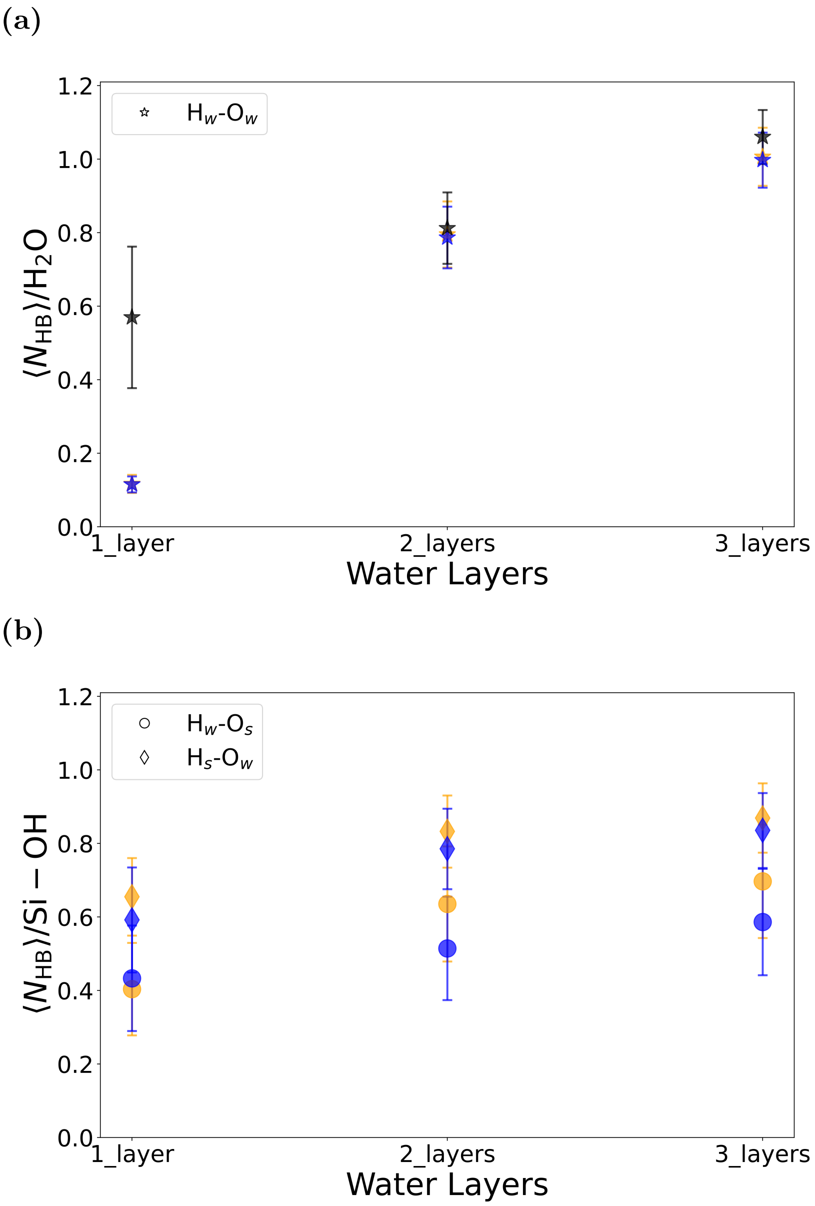

Figure 5.8 Average number of hydrogen bonds for different number of water layers, **a**) Hbonding of water-water and **b**) water to silanol groups HBonding. The HBonds to silanol H_s or O_s are w.r.t the total number of silanol groups, and the H_w-O_w HBonds are w.r.t total number of water molecules. The different interfaces are shown as different colours: blue: SiO_2/H_2O, black: WS_2/H_2O, and orange: $WS_2/H_2O/SiO_2$. It is noted that **a**) has a large overlap between SiO_2/H_2O and $WS_2/H_2O/SiO_2$ markers.

number of HBonds to derive an accurate autocorrelation for the continuous HBond lifetime.

The O_s-H_w HBond has a shorter lifetime of 0.43 (± 0.001) ps in one layer, which increases to 0.75 (± 0.002) ps for two layers and 0.81 (± 0.003) ps for three layers (Figure 5.10b). In contrast, the O_w-H_s lasts significantly longer than any other type of HBond (Figure 5.10c). The HBond lifetimes are 3.47 (± 0.023), 6.12 (± 0.098), and 4.08 (± 0.056) ps for one, two, and three layers, respectively. As shown in the average number of HBonds in Figure 5.8b, there are more O_w-H_s across all water layers. This suggests that these abundant and long-lived hydrogen bonds may contribute to the BIL water observed at the SiO_2 interface.

The mobility of water D increases with the number of water layers, reaching 0.38 (± 7.5 10^{-4}) Å^2/ps for two layers, and 0.58 (± 6.9 10^{-4}) Å^2/ps for three layers. This increased mobility with additional water layers reflects the more liquid-like nature of water located farther from the silica surface, with weaker structuring by silanol groups. This increase in mobility with distance from SiO_2 can be clearly seen in Appendix A Figure A.5a, where less-ordered, distant water layers contribute more significantly to the increased MSD. A similar reduction in mobility due to surface structuring by silanol groups has also been observed in water at the Al_2O_3 interface, as demonstrated by AIMD simulations.[226]

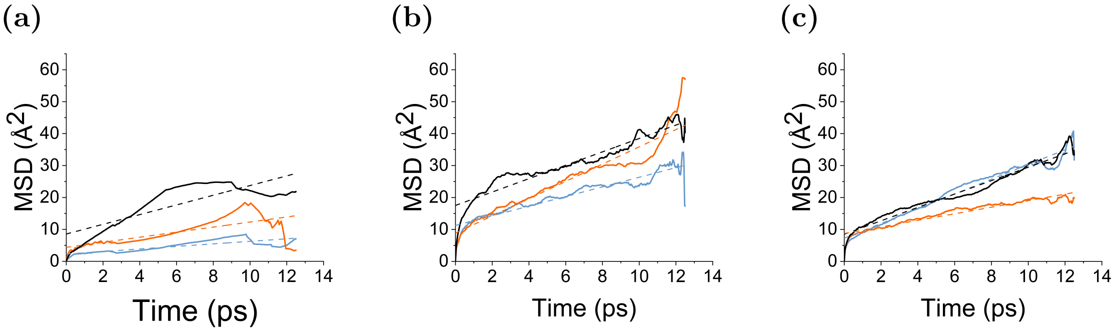

Figure 5.9 2D MSD in the XY direction for all interfaces based on the number of water layers. **a)** 1 layer, **b)** 2 layers, **c)** 3 layers. The different interfaces are shown as different colours: blue: SiO_2/H_2O, black: WS_2/H_2O, and orange: $WS_2/H_2O/SiO_2$. The linear fit of the data is shown by the dashed line corresponding to the material colour.

5.3.2.2 WS_2/H_2O

Investigation of HBonding at the WS_2/H_2O interface reveals that the absence of direct HBonding between WS_2 and H_2O results in an average of 0.57 HBonds /water molecule (Figure 5.8a). The faster decay of HBond lifetimes for WS_2/H_2O, compared to SiO_2/H_2O, is evident in Figure 5.10d. In addition, the HBN at the

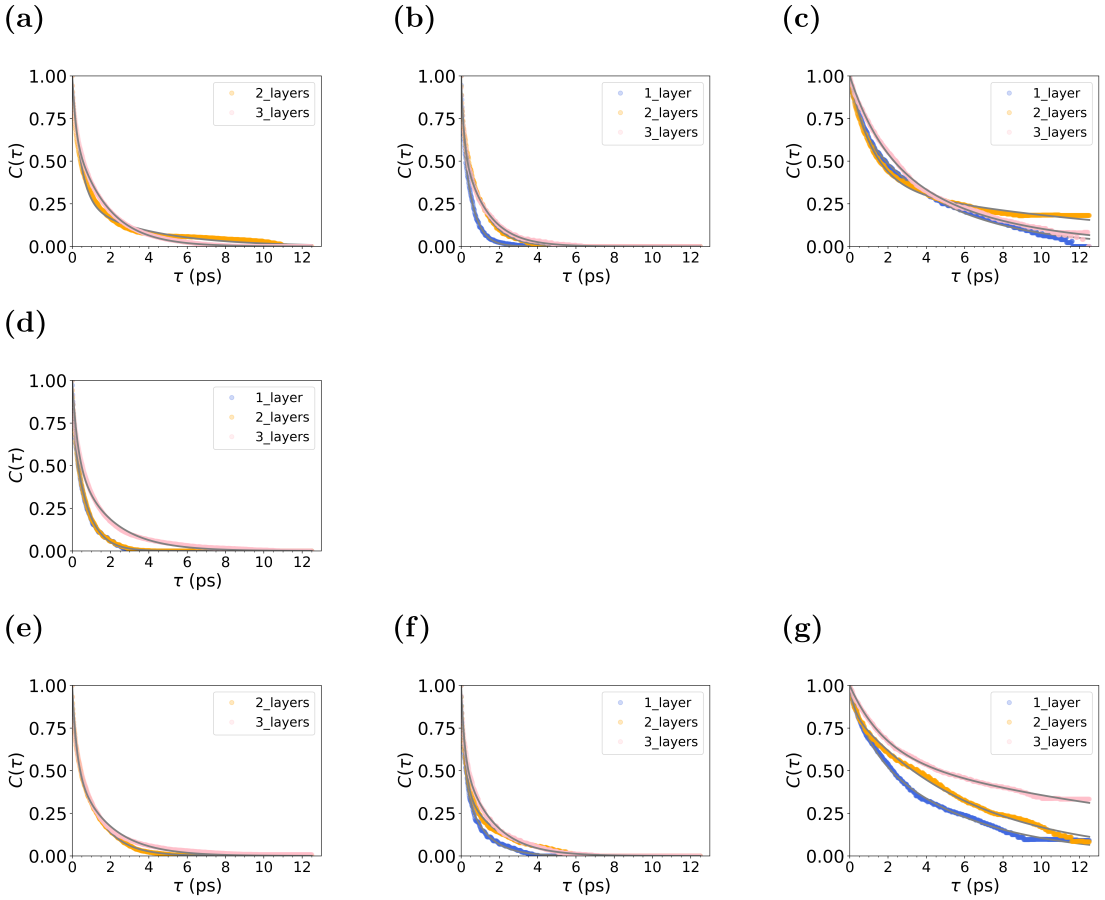

Figure 5.10 Hydrogen bonding autocorrelation for different layers of water in **a-c**) SiO_2/H_2O, **d**) WS_2/H_2O, and **e-g**) $SiO_2/H_2O/WS_2$. The first column (**a,d,e**) is the autocorrelation of water-water hydrogen bonds (O_w – H_w). The second column (**b,f**) is the autocorrelation for water hydrogen and silanol oxygen (O_s – H_w). The final column (**c,g**) is the autocorrelation between water oxygen - silanol group hydrogen bonds (O_w – H_s). The biexponential fit from which the HBond lifetime is derived is shown in grey.

WS_2/H_2O interface exhibits greater fluctuations than at other interfaces (SI Figure A.4b). Therefore, HBonds break more quickly for systems with one and two layers of water, with a lifetime of 0.57 (± 0.003) and 0.59 (± 0.002) ps respectively. The diffusion coefficient for one and two layers was calculated to be 0.38 ($\pm$ 1.8 10^{-3}) Å^2/ps and 0.53 ($\pm$ 1.1 10^{-3}) Å^2/ps, respectively. Overall, clustered water is mobile with HBonds breaking and reforming rapidly.

However, as shown in Figure 5.9a, there is a deviation from the linear fit of the MSD for one layer. Despite the self-diffusion error being low, the accuracy may be compromised due to the limited number of water molecules sampled. This deviation could be due to either the clustered nature of water or the reduced number of water molecules and short timescale, which raises doubts about the exact diffusion coefficient values. This is underscored by the R-squared value for one layer of 0.65, indicating that the fit is not optimal. However, in SI Figure A.5 that the movement of molecules within 4 Å from the WS_2 surface is greater than at any other distance for all water layers, suggesting this may be a common phenomenon at the interface rather than a sampling issue.

For the three-layer system, the HBond lifetimes increase to 1.14 (± 0.010) ps, which is similar to the three layer lifetime in SiO_2/H_2O. The HBonds are retained for longer periods creating a steady HBN, as seen in SI Figure A.4. The MSD at both the WS_2 and SiO_2 interfaces converges (Figure 5.9b-5.9c). This behavior suggests that the water dynamics at three layers resemble more bulk liquid/ a DL than that of a BIL.

5.3.2.3 $SiO_2/H_2O/WS_2$

Similar to the SiO_2/H_2O system, the confined water $SiO_2/H_2O/WS_2$ system shows minimal average H_w-O_w HBonding of 0.12 HBonds/water mols for one water layer (Figure 5.8a). This bonding significantly increases to 0.80 in two layers and 1.01 in three layers. Therefore, the monolayer water HBN is disrupted by the silanol HBonding. The H_w-O_w HBond lifetimes for two layers (0.89 ± 0.002 ps) and three layers (1.06 ± 0.010 ps) are shorter compared to those in the SiO_2/H_2O system, emphasising this disruption (Figure 5.10e).

However, there are 0.13 more H_s-O_w HBonds/silanol group in the confined one layer system compared to the unconfined system (Figure 5.8b). This further confirms the more rigid structure of water seen in the 1D profile of confined water compared to that of unconfined water, as the silanol group interactions are more dominant in the confined one-layer system.

For silanol-water HBonds in the confined system, the lifetimes of HBonds are the smallest for the one-layer system, with O_s-H_w lifetimes lasting 0.57 (± 0.005) ps (Figure 5.10f) and 3.99 (± 0.029) ps for O_w-H_s(Figure 5.10g). Although there is increased HBonding to silanol groups in the confined system, the D of

0.2 ($\pm$1.4 10^{-3}) Å^2/ps for the single water layer is greater than in SiO_2/H_2O. It suggests that this is due to HBond breaking and formation between different silanol groups, reflected in the increased dispersion of water density around these groups in the 2D density profile (SI Figure 5.6). Consequently, monolayer confined water may diffuse more readily between silanol groups.

The O_s-H_w lifetime increases with the number of water layers, reaching 0.88 (± 0.007) ps for two layers and 0.98 (± 0.005) ps for three layers (Figure 5.10f). Similarly, the O_w-H_s lifetimes show a similar trend, with significantly longer lifetimes of 5.30 (± 0.019) ps for two layers and 12.04 (± 0.103) ps for three layers, which approaches the simulation length. It is important to note that in both the SiO_2/H_2O and confined systems, the autocorrelation graphs for O_w-H_s do not exhibit the rapid decay to zero observed in the other hydrogen bond lifetimes. This discrepancy may stem from the increased structuring of water influenced by H_s, which increases the likelihood of water molecules exhibiting longer hydrogen bond lifetimes, thereby complicating the fitting process to a biexponential model. Furthermore, a significant issue is the reduced sampling resulting from the AIMD method, which increases the uncertainty of hydrogen bond lifetime values for O_w-H_s. As a result, these hydrogen bond lifetimes should be regarded with caution due to the accompanying increased error, as previously highlighted.

The MSD of the two layer system shows an unexpected increase in D to 0.68 ($\pm$ 1.4 10^{-3}) Å^2/ps compared to the one layer. Regarding the HBond at the interface for two water layers, I note that the H_w-O_w lifetime in the confined system is shorter than that in the unconfined system by 0.36 ps. Additionally, the two-layer O_w-H_s lifetime is 0.97 ps shorter than in the unconfined system. Consequently, water is breaking HBonds more rapidly in the two layer system which may contribute to the increase in MSD. This phenomenon may also reflect the change in the orientations of water in the confined two-layer system, which are parallel within 4 Å to the surface, as analysed by JPD. The mobility is reduced to 0.27 ($\pm$ 4.6 10^{-4}) Å^2/ps in three-layers. This reduction comes with an increased lifetimes of all types of HBonds in comparison to the SiO_2/H_2O system.

However, the non-linear increase in total displacement between 10-12.5 ps in the two-layer system highlights issues with AIMD. The 12.5 ps time scale restricts the statistical reliability of dynamic data, while the small simulation box diminishes the movement of water molecules, potentially leading to the overrepresentation of anomalous data. These factors can result in longer HBond lifetimes and increased correlation between water molecules impacting the MSD.

Overall, for two and three water layers, the water remains relatively mobile in all systems. This reinforces the conclusion that these layers are not completely rigidly structured (even under confinement) and instead retain the ability to move and reorient.

5.4 Discussion and Conclusions

I used AIMD to provide the first insight into the behaviour of different layers of water at the $SiO_2/H_2O/WS_2$ interface. Currently, there are no experimental measurements available, as these surfaces are challenging to prepare and investigate, unlike mica. The confined water is structured by the SiO_2 silanol groups, which cause the water to form a binding interfacial layer. When silanol groups are present alongside monolayer water, little consistent hydrogen bonding is observed between the water molecules; instead, water is predominantly hydrogen-bonded to the silanol groups. This silanol-water HBonding interaction increases under confinement. In contrast, mica allows for the formation of an ice layer when water is confined with 2D materials, which relies on intact water-water hydrogen bonds. Confined water exhibits increased mobility for one and two water layers compared to SiO_2/H_2O, but decreased mobility for three water layers. Therefore, the water-silanol HBonding interaction is key to the properties of confined water at the SiO_2/WS_2 interface. Furthermore, the relative humidity during sample preparation influences the properties of the water, with increased RH represented by the three layers of water and low RH by the one layer.

The introduction of WS_2 to confine the water results in a slight restructuring of water, with water hydrogen atoms oriented toward the WS_2. However, this effect is minimal when compared to the HBonding interactions with silanol groups. Additional layers of water result in reorientation of water close to the surface for both $SiO_2/H_2O/WS_2$ and WS_2/H_2O interfaces.

To assess the accuracy of our AIMD results, I compare them to relevant values from the literature. I note that the diffusion coefficient calculated for SiO_2/H_2O is greater than in previous CMD work on the cristobalite surface of 0.028 Å^2/ps.[178] To further investigate this difference, I examine the MSD of water based on its position relative to the surface to see if D is reduced to a comparable value due to the HBonding between silanol and water (Appendix A Figure A.5a). The MSD is reduced within 4 Å from the surface, as expected. In the three-layer system, the MSD substantially increases at distances of 8-12 Å from the SiO_2 surface. In order of increasing D, the water within 4 Å is one (0.10 Å^2/ps) $<$ three (0.28 Å^2/ps) $<$ two (0.35 Å^2/ps) water layers. Therefore, I could not identify a reason for the magnitude of difference in D. AIMD may more accurately account for hydrogen bonds, allowing for improved modelling of movement. In contrast, CMD results, obtained over a longer timescale, provide greater statistics, indicating less movement near the SiO_2 surface overall. Thus, additional work is required to accurately determine the MSD of water at the $10\bar{1}$ cristobalite surface. I also note that an elevated temperature of 400K was used in AIMD to mitigate overbinding of water, but this may contribute to increased water mobility.

The continuous lifetimes of HBonds reported in the literature for bulk H_w-O_w range from 0.18-0.7 ps depending on hydroxylation and CMD forcefield.[227–230] In contrast, the lifetimes of silanol-water hydrogen bonds are significantly longer, at 1.73 ps.[227] In our work, the HBond lifetimes are markedly higher than those previously reported; specifically, the lifetime of O_w-H_s is greater than anticipated. However, the shorter lifetimes of O_s-H_w may have some impact, as prior studies have not distinguished between the different types of HBonding. Therefore, averaging of both types of silanol-water HBonds may lead to more comparable HBond lifetimes. Additionally, the water used in our simulations is not bulk, which may contribute to this difference, as the water molecules are not in the same environment in regards to the O_w-H_w HBonds. However, I may also attribute this discrepancy to the short timescale of the AIMD calculations, which cannot be performed on the same nanosecond timescale as CMD. Consequently, less dynamic data can be analysed and averaged.

The bulk water D has been calculated to be between 0.172 and 0.591 Å^2/ps, based on both CMD simulations and experimental literature.[178,231–235] Our diffusion coefficients are at the higher end of this literature range for all interface systems, except for the confined water two-layer interface which exceeds the range. The WS_2/H_2O interface with three layers of water presents the most comparable result to bulk water. This system is less influenced by silanol groups and features only O_w-H_w hydrogen bonds. The D of 0.58 Å^2/ps remains within the literature range, suggesting that water mobility may be accurately represented in the AIMD simulation. However, as previously highlighted, future work to extend the time scale of the simulations may offer improved insight into the water dynamics of the system.

Chapter 6

$SiO_2/H_2O/WS_2$ Interface Electronic Properties

Having established the structural properties of water at the $WS_2/H_2O/SiO_2$ interface and highlighted the role of confinement, I will now examine the electronic properties of this interface. This investigation aims to elucidate the impact of water on device functionality by exploring the band alignment between all three materials. Additionally, this research will focus on the interactions between WS_2 and confined H_2O. This interaction has not been previously studied, whereas the interaction between SiO_2 and confined H_2O is expected to be primarily influenced by the hydrogen bonds between water and silanol groups, as observed at the SiO_2/H_2O interface, which has been previously explored in literature.[236,237]

It was found that the presence of 1-3 water layers does not significantly affect the band alignment between SiO_2 and WS_2 and the electronic properties of the WS_2 monolayer. However, in-gap states caused by the dynamic rearrangement of water molecules could cause a reduction of electron and hole mobility in the WS_2 layers. This work provides new insights into the impact of water on the electronic properties of WS_2 under different environmental conditions.

6.1 Introduction

Experimental investigations have provided compelling evidence for the presence of confined water under ambient conditions on the surface of TMDs and silica[17]. However, as discussed in Chapter 5, there is more experimental data on the properties of water confined on mica surfaces than at SiO_2 surfaces.[68] In particular, there is evidence for charging and discharging of MoS_2 and WS_2 on mica by intercalating water films[238]. Studies of MoS_2 on sapphire have shown the ease at which water is intercalated between the materials resulting in changes in conductivity where water is present.[61] The interface of MoS_2 and SiO_2 has had some insight from CMD and experiment.[239] However, the electronic properties of WS_2 on silica substrates with water present remains unexplored.

I aim to look at both sides of the coin: how confinement affects water and how the presence of water affects the properties of WS_2 film. I investigate theoretically the electronic properties of 1-3 layers of water confined between a WS_2 monolayer and a hydroxylated silica surface. This represents a broad case of strongly hydrophilic – weakly hydrophilic water confinement[68] and is of interest for applications in transistor technology where $WS_2/SiO_2/Si$ heterostructures produced by exfoliation and various growth methods have been extensively explored[240–242].

In particular, one of the important characteristics that affects the applicability of TMDs in transistors is the band offset between the TMD valence and conduction bands and those of a gate dielectric. The band offset between amorphous silica and TMDs has been explored by internal photoemission (IPE) as a function of the TMD synthesis method (growth versus exfoliation)[243]. The observed variations in the band offset between MoS_2 VBM and SiO_2 CBM have been attributed to the presence of water confined between the SiO_2 and MoS_2 as a result of the deposition process. A DFT study has shown that the VBM and CBM fluctuate over time due to the movement of liquid water, highlighting the impact of the geometry of water on the electronic properties of the interface.[244] However, IPE studies of WS_2 on SiO_2 as a function of the synthesis method[241] found no significant change in band offset. The DFT and XPS studies have further confirmed a straddling band alignment between WS_2 and SiO_2.[245] Other experiments using photoluminescence (PL) indicate that subtle interactions between water and TMDs may cause the existence of trap states[52].

Despite these advances, it is still unclear how the water present at the TMD/H_2O/SiO_2 interface affects the electronic properties of each material and whether the electronic properties of the confined water depend on the number of water layers and their interaction with confining surfaces. From a practical perspective of the applications of TMDs in devices, important questions remain: (i) How the presence of water layers affects the adhesion of SiO_2 substrate with WS_2 film. (ii) Whether the presence of water affects the average band alignment between materials. (iii) Can fluctuations of water molecules affect electron mobility in WS_2.

Here I investigate the properties of WS_2/H_2O/SiO_2 heterostructures with different numbers of water layers using DFT and AIMD. This approach enables us to capture how the behaviour of WS_2 can change at different humidity conditions and to calculate the electronic structure and band offsets in the entire heterostructure. The results demonstrate that the interaction between the WS_2, water and SiO_2 layer, on average, results in a type I or the so-called straddling band alignment where the band gap of WS_2 is completely contained within the much wider band gaps of SiO_2 and water (see also ref.[246]). Although perturbed, this band alignment is similar to the rigid band alignment. Thus, the presence of water does not significantly affect the band offset between SiO_2 and WS_2 and the electronic properties of the WS_2 monolayer. However, investigating individual water configurations showed the formation of localised, short-lived, in-gap states between H_2O and WS_2, which may affect the electron and hole conductivity in WS_2 layer. This study provides an atomistic insight into the structure and properties of confined water at the WS_2/silica interface, contributing to the understanding of the impact of water on the electronic properties of WS_2 under different environmental conditions.

6.2 Methodology

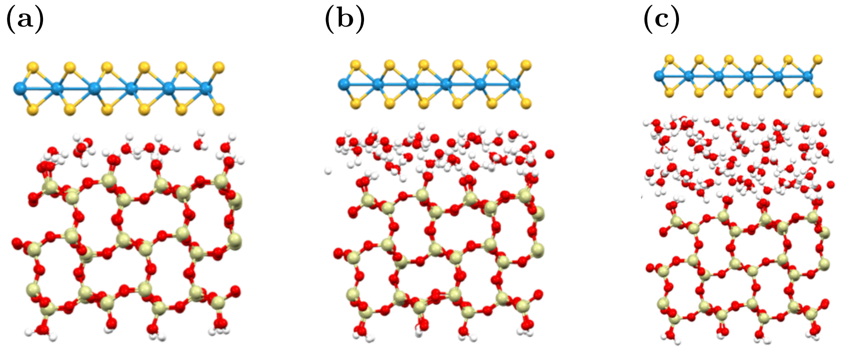

Figure 6.1 Snapshot geometric structures of the $SiO_2/H_2O/WS_2$ interfaces with **a)** 1 layer of water; **b)** 2 layers of water; **c)** 3 layers of water. Color coding: blue = W, yellow = S, red = O, white = H, beige = Si.

The details of the calculation setup are provided in Chapter 5.2

I start by testing our methods on individual perfect materials. The 3×3×3 extension of the α-C bulk structure, the 6×6 cell of the WS_2 monolayer and the 3×3×3 extension of the I_h bulk ice were calculated with DFT using the CP2K code[80]. The double-ζ Gaussian basis set[127] with the Goedecker-Teter-Hutter pseudopotential[81] was used in all calculations. I used the PBE0-TC-LRC XC functional[79] and ADMM[130,247] to speed up the calculations. As this chapter focuses on the electronic parameters of the interface, I will provide an in-depth analysis of the selection and implications of the PBE0-TC-LRC XC functional.

The PBE0-TC-LRC functional uses a constant fraction of exact exchange in the short range until a specified cut-off distance, R_c, at which it sets exact exchange to zero. In this work the truncation radius $R_c = 2$ $\AA$ and the fraction of Hartree-Fock (HF) exact exchange $\alpha = 25$ %. I note that the amount of HF exchange was not optimised to reproduce band gaps of the wide bandgap insulators H_2O and SiO_2 because the interface consists of three materials with different dielectric constants and different amounts of exchange will be needed to accurately describe each material. Therefore, optimising the amount of exchange for one material at the expense of the others is not feasible. Standard PBE0-TC-LRC accurately describes the band gap of WS_2 in both the pristine

Table 6.1: Experimental and calculated values of band gap and conduction band minimum w.r.t vacuum level. The data for liquid water from this work shown in the table are obtained from 3 layers of water geometry optimized without any interface present.

Reference	Material	Band Gap (eV)	V_0 (eV)
Literature Values	α-Quartz SiO_2[140]	9.65	–
	amorphous SiO_2[250,251]	8.95	-0.75
	WS_2[252]	2.4	-3.91−3.93
	Ice Ih[253]	9.4	-0.9
	Liquid Water[253]	9.0	-1.0
This Work	α-C SiO_2 Slab	8.2	-0.6
	Liquid Water	7.65	-0.53
	hexagonal WS_2	2.47	-2.34
	orthorhombic WS_2	2.34	-3.89
	bulk α-C	8.57	–
	bulk Ice Ih	8.39	–

hexagonal and orthorhombic phases. The dispersion interaction was included using the D3(BJ) correction[79,130,248].

The calculated geometric structures of the three perfect systems are in good agreement with experiment. The properties of the bulk α-C are discussed in more detail in ref.[249] and the dependence of the properties of WS_2 layers on the computational parameters is discussed in ref.[4]. The calculated Kohn-Sham and experimental band gaps and positions of the CBM relative to the vacuum level (V_0) of perfect materials are summarised in Table 6.1.

The interface was then constructed by using CMD equilibrated SiO_2/H_2O provided by L. Hargreaves. Then an orthorhombic WS_2 cell was introduced to confine the water. AIMD calculations using a PBE-D3(BJ) XC functional were then performed with an initial run of 4 ps, before the production run was performed for 12.5 ps, as described in detail in Chapter 5. Examples of snapshot geometries for the three structures are shown in Figure 6.1.

Snapshots of the AIMD system were taken every 0.5 ps, and single-point energy calculations using the PBE0-TC-LRC + D3 XC functional and a dipole correction were performed for the 26 snapshots.[254] The geometric structures captured in these snapshots were not re-optimised with PBE0-TC-LRC to keep the non-0K configurations of water, but the hybrid functional provided a better description of the band gap and, consequently, the band alignment.

To better understand and provide comparison to how WS_2 interacts with water without the presence of SiO_2, WS_2/H_2O systems were created by removing the SiO_2 slab from the $SiO_2/H_2O/WS_2$ interfaces. AIMD was then run using the same methodology as described above. This involved a 4 ps initial run which allowed the water to restructure from the previous configuration, and then a 12.5 ps production run with snapshots taken every 0.5 ps with a single-point calculation PBE0-TC-LRC + D3. I note that the water did not evaporate at this interface at 400 K.

6.2.0.1 Snapshot Analysis

In total, 26 snapshots of the AIMD trajectory were analysed and averaged. To calculate the band alignment of the system, a reference value is required. Previous work investigating the band alignment of water and semiconductors have used averaged electrostatic profiles referenced to the vacuum level with average bulk potentials used to align conduction bands to determine band alignment.[255] However, in my work, the small amount of water used means that the bulk water potential could not be easily determined. Therefore, the local density of states (LDoS) was used to determine the band alignment.

Band alignment at material interfaces is commonly calculated using the rigid band alignment or electron affinity model. In this approach, the VBM and CBM of each material are computed independently and aligned to a common energy reference, typically the vacuum level, the average Hartree potential, or the standard hydrogen electrode. This allows for direct comparison of band positions across materials at the interface and estimation of interfacial properties.[256–258] In this work, the vacuum level is used as the reference due to the use of slab models, where this potential is easily defined.

However, the rigid band model neglects interfacial effects, such as molecular orientation and local dipole variations, particularly in liquid-phase systems, which can induce band bending.[259,260] Consequently, an explicit interfacial model is more accurate for capturing these effects.

For explicit band alignment models, the vacuum level remains the standard reference in slab models. Alignment can be achieved by comparing the average Hartree potential or by referencing the eigenstates in the density of states (DoS) to the vacuum energy. However, for bulk materials, this method is more challenging, often requiring the use of a specific redox potential as a reference. The water redox potential is frequently chosen due to its well-characterised value and relevance in electrochemical systems such as water splitting.

Despite providing more accurate results, the explicit model introduces complexities such as artificial strain, as discussed in Section 3.6.1.

The alignment of the bands in the $SiO_2/H_2O/WS_2$ heterostructure was determined by averaging the LDoS with the vacuum level as a reference. The average LDoS was spatially resolved along the z axis, perpendicular to the interface. The energy resolution of the states was 0.1 eV, with a 0.5 $\AA$ smearing applied to the spatial resolution using a Gaussian and previously reported methodology.[261]

The dynamic nature of the interface introduces variability in the electronic states across different time snapshots, complicating the determination of the local band gap. As a result, the density of states associated with dynamic eigenstates is reduced due to the temporal averaging. The local VBM and CBM were identified by analysing the density of states within the averaged LDoS. A threshold-based approach was employed to define the local VBM and CBM, where the states were considered only if their LDoS contribution exceeded a predefined cutoff value, corresponding to a specific state density.

This threshold was used to modulate the sensitivity to detect the local CBM and VBM, allowing the capture of subtle variations in the alignment of the band that may arise from the dynamic interaction between water molecules and the WS_2 surface. The higher threshold of 0.5 provided average values, revealing larger band gaps for SiO_2 and H_2O, while the lower threshold of 0.1 offered greater sensitivity to spatially dependent interactions between WS_2 and H_2O. The impact of these threshold values and their implications for band alignment will be discussed in detail in the Results and Discussion section.

The inverse participation ratio (IPR) was calculated from the snapshots to quantify the degree of localization of the eigenstates. The IPR methodology, previously detailed in the literature[262–266] uses atom-centred base sets in CP2K to assess the localisation of eigenstates. The IPR values range from 1, representing highly localized states, to 0, indicating completely delocalized states.

The adhesion energy was calculated as:

$$E_{adhes} = \frac{1}{AN_{SS}} \sum_{n=1}^{N_{SS}} [E_{(XY)_n} - (E_{(X)_n} + E_{(Y)_n})], \tag{6.1}$$

Where, A is the surface area, E_{XY} is the energy of the entire interface, and E_X and E_Y are the total energies of the individual materials at the interface separately calculated from the same snapshot geometry, n is the number of a snapshot and N_{SS} is the total number of snapshots. In some literature, a factor of $\frac{1}{2}$ is added to account for the two surfaces at an interface. However, since most papers do not include this term, I have excluded it for easier comparison.

Average adhesion energy calculations for interfaces involving water use snapshots from an AIMD trajectory. In contrast, for the WS_2/SiO_2 interface, a single optimized geometry is used; therefore, this adhesion energy is not averaged.

Charge transfer and electrostatic interaction at the $H_2O/WS_2/SiO_2$ interface were calculated using the Bader charge, which was calculated using the code developed by the Henkelman group.[267]

Bader charges were calculated for each snapshot of the $SiO_2/H_2O/WS_2$ interface to determine the charge transfer between WS_2 and H_2O. The Bader charges of WS_2 and H_2O/SiO_2 were computed based on the geometry of each snapshot from the $SiO_2/H_2O/WS_2$ interface. The average change in charge, resulting from the formation of the interface, was then determined for each atom of interest. In this work, I focused on the interfacial atoms, specifically W and S from WS_2, H and O from H_2O (denoted as H_w and O_w, respectively), and the silanol groups interacting with water on the silica surface, labelled as O_t and H_t. This gave the general formula for change in charge for each atom as:

$$\Delta q = \frac{1}{N_{SS}} \sum_{n=1}^{N_{SS}} q_{(XY)_n} - q_{(X)_n} - q_{(Y_n)}. \tag{6.2}$$

Here, q is the Bader charge of the atom, n is the snapshot number, and N_{SS} is the number of snapshots of the AIMD trajectory. XY is the charge on the atom in the entire interface, and X and Y are the Bader charges from the atom in the individual materials at the interface.

6.3 Results and Discussion

6.3.1 Adhesion energy

I start by calculating the binary interfaces to compare them with the previous literature. The low adhesion energy between WS_2 and several water layers seen in Table 6.2 shows that water is physisorbed on WS_2. For the $SiO_2/H_2O/WS_2$ interface, similar to the WS_2/H_2O interfaces, adhesion energy increases with the number of water layers; however, the confined system exhibits a significantly higher adhesion strength. This mild physisorption is expected as experimental evidence shows that WS_2 is mildly hydrophilic.[184,185,268–272] Similar trends have been reported for graphene/H_2O/SiO_2 systems, though the adhesion energy for graphene is slightly lower, as graphene is more hydrophobic than WS_2[273,274]. It is observed that the adhesion energy stabilizes at three water layers at the $SiO_2/H_2O/WS_2$ interface. This indicates that beyond a certain distance, additional water molecules contribute negligibly to the energy gain due to the limited interaction with the WS_2 surface. This suggests that the interaction between WS_2 and H_2O is short-range, being dominated by van der Waals (vdW) forces.

Atomic force microscopy (AFM) measurements performed on the

Table 6.2: Average adhesion energy of WS_2 interface, and average adsorption energy with respect to the number of water layers present at the interface.

Interface	Water Layers	Adhesion Energy (Jm^{-2})
WS_2/H_2O	1	-0.0531 (± 0.005)
	2	-0.146 (± 0.008)
	3	-0.164 (± 0.010)
$WS_2/H_2O/SiO_2$	1	-0.188 (± 0.011)
	2	-0.196 (± 0.005)
	3	-0.194 (± 0.007)
WS_2/SiO_2	0	-0.250

MoS_2/SiO_x system provide a relevant comparison.[271] In these experiments, at a temperature of -15 °C, where it was expected that water would be confined at the interface, the adhesion energy was measured at 0.152 Jm^{-2}, which is comparable to the adhesion energies reported in Table 6.2. The rise in temperature and, thus, the reduction in the amount of interfacial water resulted in an increase in the adhesion energy. This agrees with the increase in adhesion energy when water is removed leaving only the hydroxylated SiO_2 slab and WS_2 in contact also observed in my work (see Table 6.2).

6.3.2 Rigid band alignment

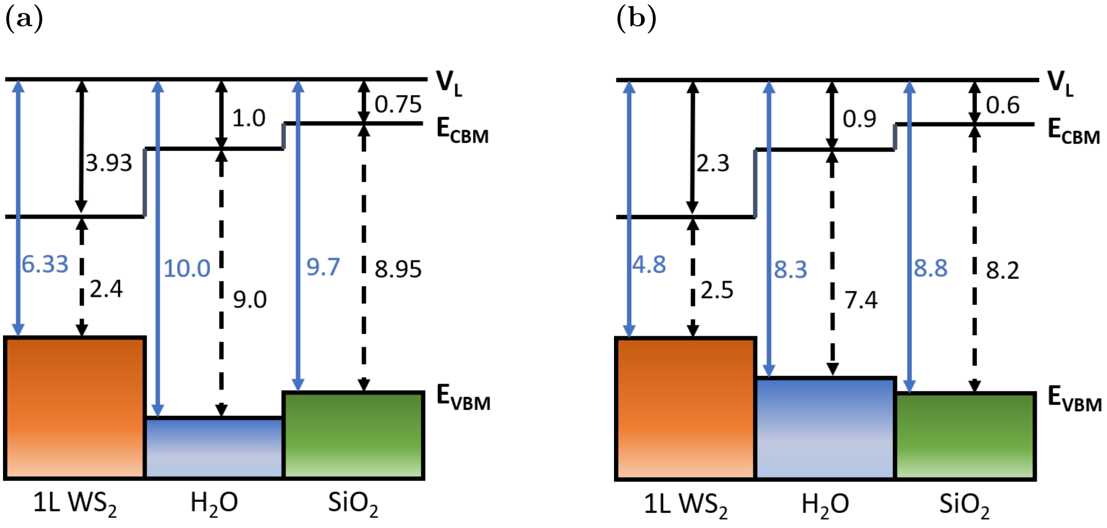

Figure 6.2 The rigid band alignment of the $WS_2/H_2O/SiO_2$ interface with reference to the vacuum level (V_L), shown for **a)** experimental values from the literature and **b)** values calculated in this work using the PBE0-TC-LRC functional (see Table 6.1 for detailed comparison and references).

To understand the electronic structure of the interface, I first calibrate my results to known values and create a rigid band alignment (RBA) diagram. This popular method is based on the bulk characteristics of individual systems. I can then compare the results with a more realistic system where interactions at interfaces may change this alignment.

In my study, the vacuum level serves as the common reference point for the RBA across all materials. To align the materials to this reference, two key values are required for each material: the CBM relative to the vacuum level (V_0), which corresponds to the electron affinity, and the band gap. V_0 ensures that all materials are aligned consistently with respect to the vacuum level, thereby providing a uniform reference for comparing electronic properties across different materials.

The experimental values for the RBA are collated in Table 6.1. Unlike the α-C phase used in this study, the amorphous and alpha-quartz phases of SiO_2 have been well studied and, therefore, have more accurate band gap values in the literature. The bulk band gaps calculated in my work are compared with the literature values for α-C and ice I_h to understand how the chosen XC functional affects electronic properties. The previously calculated α-C is close to the experimental value of amorphous SiO_2, with only a slight underestimation; see Table 6.1. For ice I_h, the band gap is underestimated by 1.01 eV. As discussed in the methodology section, this is due to the 25% HF exchange used in this work.

The parameters for the RBA based on the data calculated in this work, seen in Figure 6.2b, are obtained using slab models where the band gap is reduced with respect to the bulk value. To understand how the SiO_2 band gap can change due to the small slab thickness used in the simulations, I refer to the work on SiO_2 films, where the experimental band gap was determined to be 6.7 eV[275], which is much smaller than my slab value. I ascribe this to the difference in the film structure and to the presence of the interface with Ru in the experimental measurements.

The choice of XC functional and the amount of water lead to underestimating the water band gap too, which changes the offset between water and silica compared to the bulk experimental values; see Figure 6.2b. However, the description of water and silica as dielectrics and WS_2 with a straddling band alignment is consistent. The calculated V_0 values match fairly well with the values in the literature, so I expect the CBM alignment to be fairly accurate.

6.3.3 Average band offset

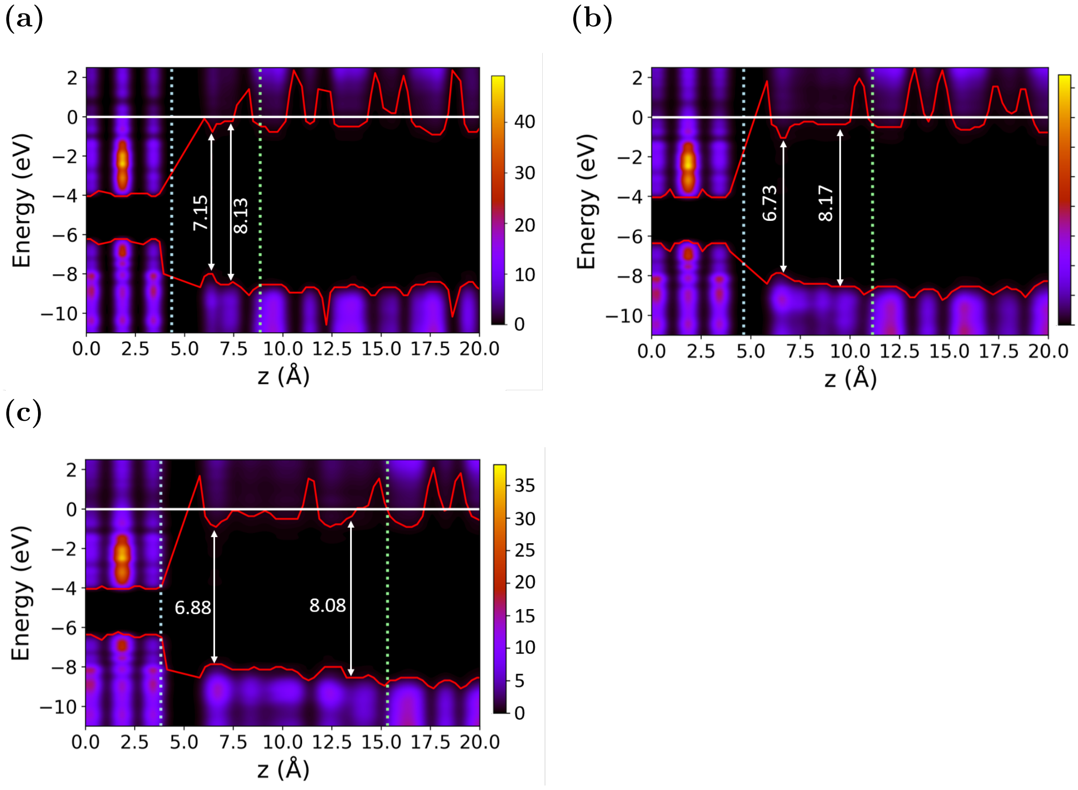

Figure 6.3 The band alignment derived from the local density of states (LDoS) at the $SiO_2/H_2O/WS_2$ interface, applying a threshold cutoff of 0.5. Red lines indicate the VBM and CBM at the interface. The colour map represents the LDoS in arbitrary units, illustrating the atomic contributions to the eigenstates across the energy spectrum. The blue dotted line marks the termination of WS_2, while the green dashed line indicates the start of the SiO_2 slab. Arrows denote the band gaps of water in contact with WS_2 and SiO_2, with corresponding values in eV. The white line at 0 eV corresponds to the vacuum level. **a)** 1 layer of water, **b)** 2 layers of water, **c)** 3 layers of water.

The band alignment in the system of interacting layers was examined using the averaged LDoS projected on atoms along the axis perpendicular to the interface slabs. The local VBM and CBM were identified by analysing the eigenvalues below and above the Fermi level, respectively. For a state to be considered the VBM or

CBM at a particular position within the stack, the averaged density of states of the atoms contributing to that state must exceed a specified threshold. This approach enables the LDoS to be adjusted, either to resolve finer features or to increase the threshold for a clearer LDoS representation.

In Figure 6.3, a threshold of 0.5 was applied, representing a relatively high cutoff. Here, significant variations in the local VBM and CBM are observed, particularly within the SiO_2 slab. Due to the crystalline nature of SiO_2, the atomic positions exhibit minimal average displacement, resulting in a noticeable "layering" along the z-direction: when there are no atoms contributing substantially to the LDoS, the electron density falls below the threshold. It is also noted that the

Further notable drops occur at the WS_2/H_2O interface, where water does not form bonds with WS_2, leading to a small gap at the structure. A similar effect is observed at the SiO_2/H_2O interface, although the VBM and CBM drop is less pronounced, as water is drawn closer to the SiO_2 surface through hydrogen bonding with silanol groups. A clearer figure showing the alignment of the position of the averaged atoms with respect to LDoS can be seen in Appendix B Figure B.2.

In contrast to RBA, the introduction of interfaces between SiO_2 and water leads to a reduction in their respective band gaps, which decrease to $7.25 - 7.5$ eV. This suggests that the electronic properties of the system are altered by the presence of these interfaces, as demonstrated in Figures 6.3a- 6.3c. Although the band gap of WS_2 also decreases by 0.16 eV, the variation in its band gap is minimal when water is introduced, which aligns well with previous findings on WS_2 band alignment.[241,244] Previous studies have reported differences in the band gap and band offsets in MoS_2/WS_2 systems in contact with water. These variations have been attributed to factors such as structural perturbations, dipole changes, and electron density overlap, which may collectively explain the observed reduction in the band gap.[188,189,220]

For all layers of water, the offset of the WS_2 and SiO_2 bands and the WS_2 band gap remain consistent, with a valence band offset (VBO) of 1.91-2.18 eV and a conduction band offset (CBO) of 3.14 eV, see Table 6.3. To understand the offset results calculated in this work, I compare them with the experimental values, as seen in Table 6.3. The experimental literature shows a consistent straddling band alignment. Still, the offset varies depending on the experimental technique used, with IPE showing much larger VBO and smaller CBO compared to XPS. My results are more consistent with the XPS values. However, the VBO is consistently underestimated due to the reduced band gap in SiO_2, as previously discussed.

The most accurate measure of band alignment should be coming from IPE, where the alignment of the WS_2 VBM to the SiO_2 CBM is measured directly when the two materials form an interface. This alignment has been experimentally determined to be 3.8 eV.[242] In contrast, my calculations yield a value of 5.32 eV. One factor influencing the band alignment of WS_2/SiO_2 may be the conditions under which WS_2 was measured, such as: the presence of dopants which will impact the work function of WS_2, the formation of adsorbate layers on the WS_2 surface, or the charging of WS_2 layers under photon excitation.[276,277] I also note that the ionization energy of WS_2, obtained from the averaged projected density of states (PDoS) of my system (Appendix B Figure B.1), is approximately 6 eV, which falls within both experimental and theoretical ranges. Furthermore, I note that the LDoS V_0 values for all water layers in Figure 6.3 are ≤ 1 eV, consistent with the experimental values, indicating that the CBO in this work is accurately described. Finally, the WS_2 V_0 for IPE is 2.3 eV (with SiO_2 V_0 equal to 0.9 eV), smaller than literature values in Table 6.4, further highlighting experimental conditions as a significant factor.

However, I must also consider that the difference of 1.52 eV between my results and IPE may arise from my choice of XC functional, since my calculated SiO_2 band gap is underestimated by 1.67 eV compared to the value used in the IPE study. The discrepancy in band gap can also be highlighted by comparing the PEEM and IPE studies in Table 6.3, where varying band-gap assumptions impact band-offset outcomes. Here, the CBO and VBO influenced by the assumption of an 8.9 eV band gap for SiO_2 in IPE versus a 9.7 eV band gap in PEEM.

Table 6.3: Average electronic properties of the $WS_2/H_2O/SiO_2$ system in eV. The CBO and VBO are shown for the calculated and measured in the literature values between SiO_2 and WS_2.

System	Band Gap	Average CBO	Average VBO
rigid	2.34	2.42	2.86
1 layer*	2.18	3.14	2.18
2 layers	2.18	3.14	1.91
3 layers	2.18	3.14	1.91
HSE06[245]	2.24	2.58	3.17
XPS and STS[6,245]	2.38	2.70	3.97
IPE†[241,242]	n/a	≈ 1.4	5.1
PEEM‡[278]	n/a	3.3	4.0

*From LDoS calculations using a 0.5 threshold.

†IPE used a 8.9 eV SiO_2 bandgap, we have applied a 2.4 eV WS_2 bandgap.

‡PEEM used a 9.7 eV SiO_2 band gap.

Table 6.4: The literature values of ionization potential (IP), work function (WF), and V_0 of WS_2 in eV.

Method	Ionisation Energy	Work Function	V_0	Synthesis/ Method	Substrate
IPE*[242]	4.55-4.9	–	–	MBE / MOCVD	SiO_2/Si
UPS[279]	–	4.95	–	hydro thermal, powder	water (nanoflower)
I_D-V_G†[280]	6.9	4.6	4.5	exfoliation	SiO_2/p+ Si
PEEM[281]	5.74	–	–	CVD	SiO_2/p+ Si
KPFM[252]	5.48	4.75–4.13	3.91–3.93	CVD, exfoliation	Au & Al
G_0W_0[8]	6.09	4.85	3.6	SOC	–

*The IPE technique values have been extrapolated using SiO_2 V_0 to be between $0.75 - 0.9$ eV.

† The I_D-V_G ionization potential is extrapolated with WS_2 band gap equal to 2.4 eV.

6.3.4 Water band gap

The structure of the nanoconfined water layer is determined by the interaction with the confining surfaces. I investigated how this confinement affects the water's band gap. Understanding water's properties is particularly challenging because of the influence of nuclear quantum effects (NQE), which still remains controversial (see discussion in refs.[253,282]). I used the results of Bischoff et al.[253] as a reference.

The band gap of the confined water at the $SiO_2/H_2O/WS_2$ interface was determined using LDoS, as shown in Figure 6.3. In particular, local variations in the VBM and CBM are influenced by the proximity of the surfaces of WS_2 and SiO_2. For all water layers, the band gap of H_2O decreases near the WS_2 surface but increases as it approaches the SiO_2 surface. At the SiO_2 interface, the band gap is similar to that of bulk I_h phase. This increase of the band gap results in minimal band offset between H_2O and SiO_2, caused by the strong hydrogen bonding between H_2O and the SiO_2 surface, which induces structuring of the water molecules near the interface. The reduction in the band gap near the WS_2 surface is hypothesized to arise from the formation of in-gap states between H_2O and WS_2 discussed in detail below.

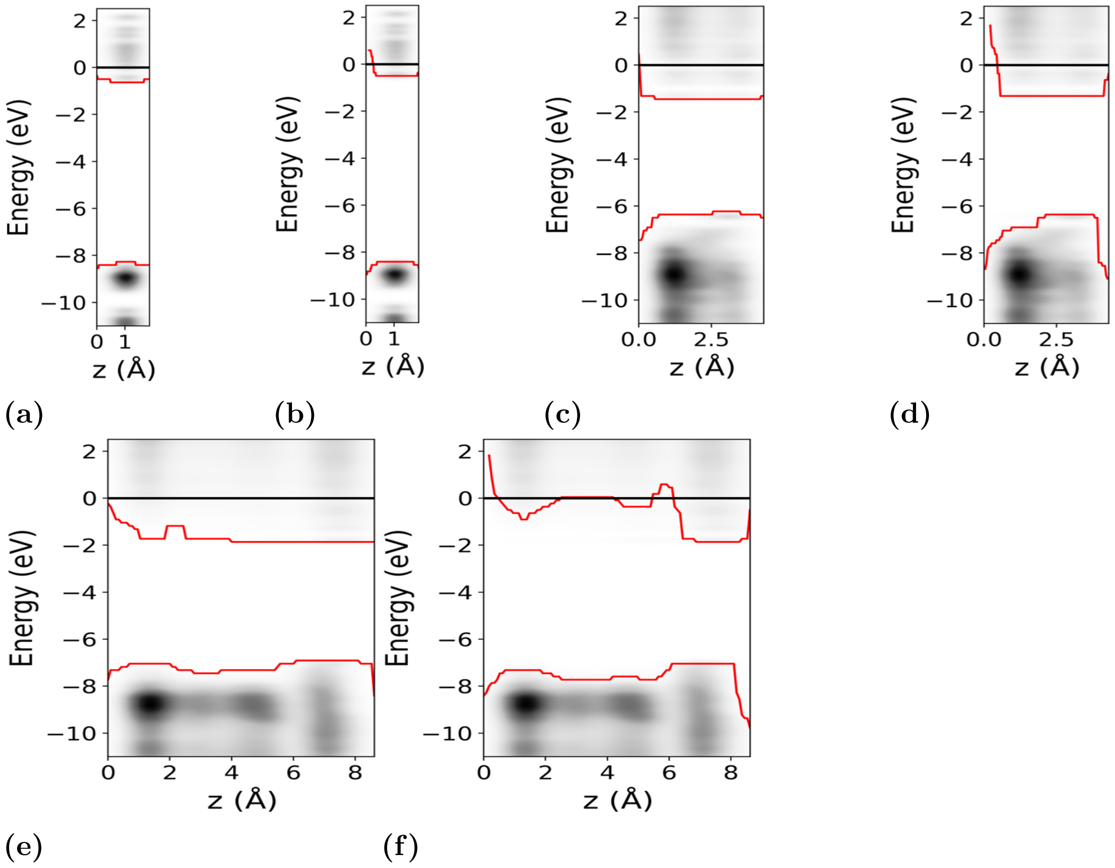

(a) **(b)** **(c)** **(d)**

(e) **(f)**

Figure 6.4 LDoS of water layers: **a,b**) 1 layer, **c,d**) 2 layers, and **e,f**) 3 layers, from averaging AIMD snapshots with a threshold of **a,c,e**) 0.1, and **b,d,f**) 0.5.

To assess the effects of confining surfaces on the water electronic structure, I analysed changes in the water band gap upon removal of the interface. This was done using geometric structures of water extracted from interface snapshots, calculating the band gap for each configuration, and averaging the results. For a single layer of water the average band gap (8.12 eV) remains relatively unchanged compared to the confined system. However, for two (5.19 eV) and three (5.34 eV) layers of water, a significant reduction in the band gap is observed when the interfaces are removed. The LDoS in Figure 6.4 shows that, depending on the threshold value used, there is some spatial dependence of the band gap close to where the SiO_2 surface was. This indicates that the change in band gap is caused by the impact of broken hydrogen bonding at the interface. The rearrangement of water molecules by surface silanol groups leads to a change in the dipole moment, which in turn affects the system's overall dipole when the interface is removed.

Overall, the pronounced changes in the water band gap under confinement, compared to those in the unconfined case, underscore the strong interactions between water and the confining materials, specifically the hydrogen bonding between water and silanol groups.

6.3.5 Work function shift

It is also interesting to see how the presence of water and SiO_2 layers affect the work function of WS_2. Previous studies have shown that thermalised water can alter the work function of metals over time, depending on the orientation of the water molecules and the resulting dipole interactions with the metal surface.[283,284] The work function changes at interfaces are linked to factors such as reduced electron spillover into the vacuum and surface roughness.[285] The shift in work function can be significant, with the literature reporting changes ($\Delta\phi$) of up to 1.4 eV in systems such as MgO/Ag.[286,287]

I find that the confined water interface shifts the WS_2 work function ($\Delta\phi$) on average by -0.10 (±0.15), -0.20 (±0.20), and -0.26 (±0.23) eV for 1, 2, and 3 layers of water, respectively, which is notably smaller compared to typical values for metal oxide/metal or metal/water interfaces.

To assess the impact of water confinement, I compared the $\Delta\phi$ values at the $WS_2/H_2O/SiO_2$ interface with those for the WS_2/H_2O system. The WS_2/H_2O interface was calculated using the same methodology, with an AIMD calculation and 25 snapshots analysed to get an average. The calculated $\Delta\phi$ values for 1, 2, and 3 water layers in the WS_2/H_2O system are -0.10 (±0.14), +0.021 (±0.14), and -0.097 (±0.21) eV, respectively. This comparison shows that for two and three water layers, the magnitude of $\Delta\phi$ is significantly reduced in the WS_2/H_2O system compared to the confined $WS_2/H_2O/SiO_2$ interface. However, for a monolayer of water, the $\Delta\phi$ values are comparable between both interfaces. These results suggest that, while the interaction between WS_2 and H_2O is generally weak, the introduction of confinement notably enhances this interaction. Additionally, it is noted that the work function values of WS_2 are likely to vary with relative humidity, which should be considered in experimental measurements.

6.3.6 Effects of water fluctuations

My AIMD results show that water remains mobile in the confined state and thus reorientates. These dipole fluctuations can affect the electronic structure of the heterostructure by introducing some short-lived states, as discussed for water/metal interfaces[284]. Adsorption of water has been shown to significantly affect electron and hole conduction of WS_2 nanotubes[288] and it has been suggested that adsorbed water can act as trapping and scattering centres for free carriers.

Confined water interface states at the H_2O and WS_2 interface were analysed by examining the time evolution of the PDoS from simulation snapshots. The degree of localisation of in-gap states was analysed by calculating the inverse participation ratio spectrum. Several of the states have high IPR values, indicating greater electron localisation, as seen in Figure 6.5 for one of the snapshots. Similar states form in many snapshots, but the energies of the localised states vary significantly. The molecular orbital corresponding to the peak with the highest IPR in Figure 6.5a (c) is illustrated in Figure 6.5c. This and PDoS analysis revealed the creation of electronic states with significant contributions from both water molecules and WS_2 valence band states in PDoS. These fluctuations highlight the effect of the water configurations and consequent dipole changes on the interfacial electronic properties. Across all water layers, the formation of short-lived in-gap states was observed in the region between the

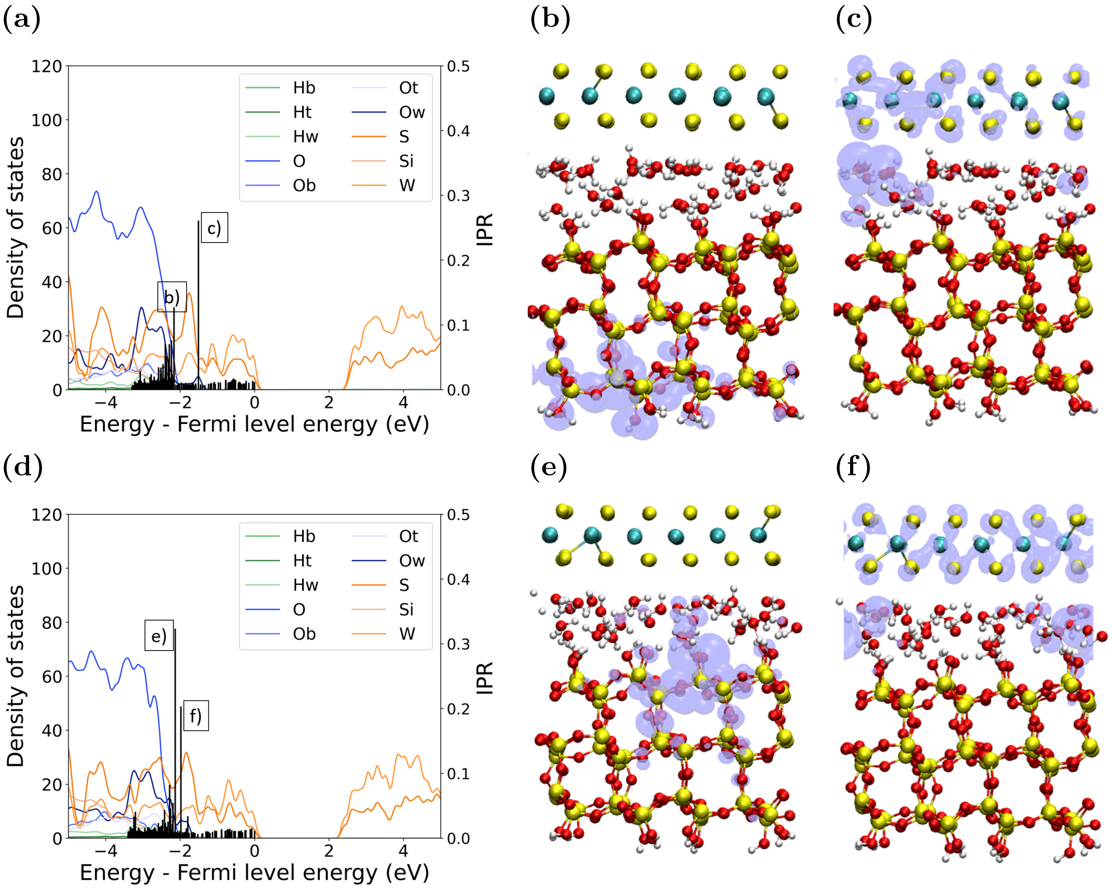

Figure 6.5 IPR Analysis of two snapshots in the two layer system at **a-c)** 5.5 ps, and **d-f)** 8ps. **a**) and **d**) show the IPR spectrum imposed on the PDoS of the snapshots, with the two largest IPR peaks labelled according to the relevant wfn, i.e. **b**) corresponds to label b in **a**). The Molecular Orbitals shown in **b,c,e,f**) are with isosurface: 0.01.

VBM of WS_2 and that of H_2O. These transient in-gap states became more frequent with increasing water layer thickness and are typically lasting less than 500 fs.

However, more in-gap states are present, as seen by peak b in Figure 6.5a. This peak corresponds to a state localised on the bottom silanol groups of the silica slab (Figure 6.5b). This highlights the slab nature of the SiO_2 used in this work as although the slab is passivated by the silanol groups, there are still localised states forming due to the termination of the bottom surface. I also highlight further states that can form at different snapshots, with peak e in Figure 6.5d showing greater localisation than in f, despite e (Figure 6.5e) showing a state between SiO_2 and water instead of between WS_2 and water (Figure 6.5f).

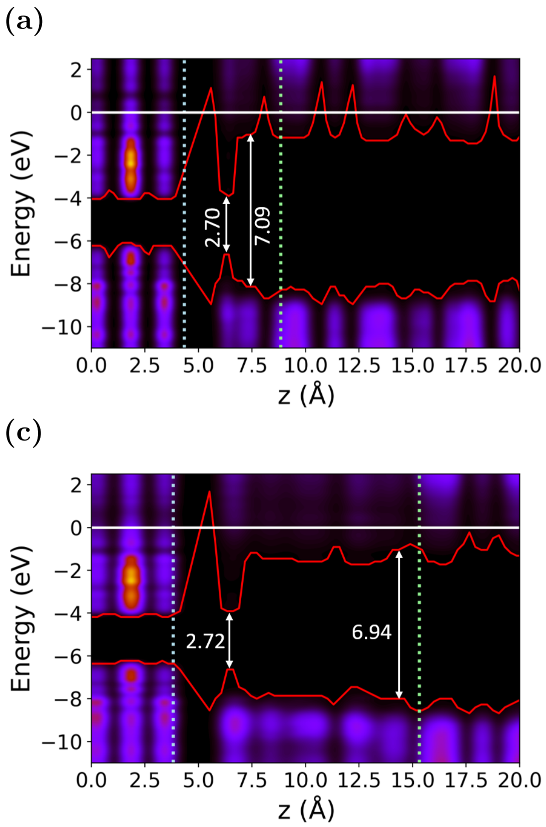

Figure 6.6 The band alignment with a 0.1 cutoff threshold at the $SiO_2/H_2O/WS_2$ interface, red lines show the VBM and CBM of the interface, the surface on the right indicates the contribution of the atoms to the eigenstate at each energy. The diagram on the left is a scaled diagram of the average interface position. **a)** 1 layer of water, **b)** 2 layers of water, **c)** 3 layers of water.

Comparing the position of peak c (-1.51 eV) in Figure 6.5a and peak f (-1.98 eV) in Figure 6.5d, I see that the energy has shifted by 0.47 eV. Therefore, although these water in gap states are present in different snapshots, the energy fluctuates. The number and variety of localised states at this interface could impact the conduction of WS_2 via the WS_2-water states, but also via additional states formed between the SiO_2 surface and water which may lead to charge moving away from the WS_2.

To investigate the effect of these dynamic processes on band offsets, I reduced the LDoS cut-off threshold to 0.1, thereby increasing the sensitivity of band alignment, as shown in Figure 6.6. The resulting band alignment at the H_2O and WS_2 interface reveals a minimal offset near the WS_2 surface across all water layers. This reduced band offset is spatially confined, occurring primarily in the water molecules interfacing with the WS_2 surface, while water molecules farther away from WS_2 exhibit a wider band gap. Furthermore, there is no observed offset between SiO_2 and the water adjacent to it.

To further examine the interaction at the WS_2 and H_2O interface, I analysed the charge transfer between WS_2 and H_2O at the $WS_2/H_2O/SiO_2$ interface. As seen in Figure 6.7, the charge transfer increases with increasing number of water layers, with the charge transfer spatially dependent in both water and WS_2. The largest magnitude of charge transfer is seen closest to the WS_2 in all models. This aligns with previous band alignment diagrams, showing the spatial dependence of the water valence band aligned with WS_2 close to the interface. The average charge transfer shows that the order of magnitude of the change is small, indicating that this is only a small electrostatic interaction. This is in contrast to the hypothesis suggested by Serron *et al.*[61] that changes in conductivity at the interface is due to charge transfer. However, in this system, I only consider pristine WS_2 and SiO_2, so any defects that might contribute to charge transfer are not present. Additionally, the systems investigated are not charged or have an applied bias, which may change the magnitude of charge transfer at the interface.

This charge transfer exhibits a similar spatial dependence on the water layers, as shown in Figure 6.7. Although the overall magnitude of charge transfer remains relatively small due to spatial averaging, these results indicate an interfacial interaction between water and WS_2.

It is noted that electron and hole scattering on these dynamic localized states could be a mechanism responsible for the reduction of conductivity in WS_2 nanotubes observed in ref.[288]. Similar scattering mechanisms in 2D transistors have been recently considered in ref.[289]. The difference in electron transport properties of single-layer WS_2 on SiO_2 measured in air and vacuum has been attributed to the presence of water and oxygen gas, but is difficult to disentangle into components[290].

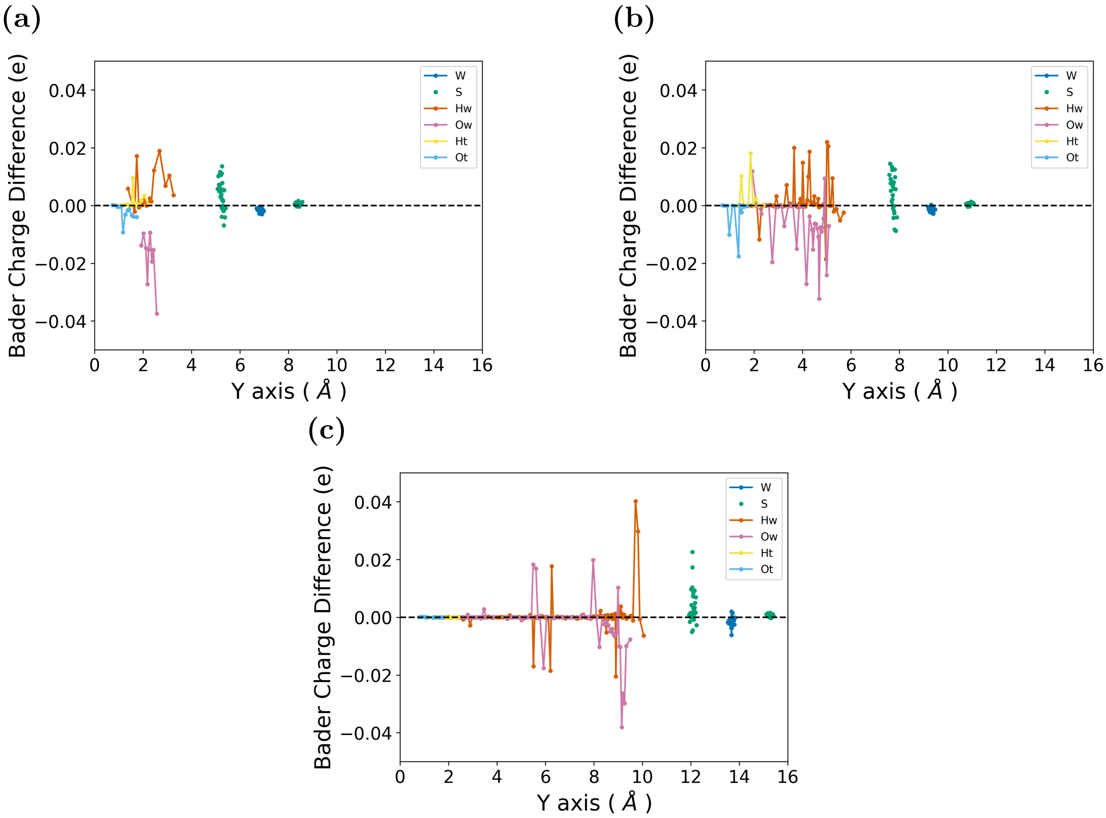

Figure 6.7 Average Bader charge difference between water and WS_2 at the $SiO_2/H_2O/WS_2$ interface. The Positions of the atoms are averaged over snapshots of the AIMD run. **a)** 1 layer of water, **b)** 2 layers of water, **c)** 3 layers of water. H_w and O_w is the water hydrogen and oxygen, respectively. H_t and O_t are the silanol groups hydrogen and oxygen.

6.4 Conclusions

This work offers an insight into the impact of confined water within the $WS_2/H_2O/SiO_2$ heterostructure, exploring different numbers of water layers using DFT and *ab initio* molecular dynamics. The adhesion between WS_2 and water layers is dominated by weak hydrophilic interactions. The structuring of water does not induce significant shifts in the band alignment at the interface compared to the rigid band alignment. This is confirmed by electronic structure calculations that demonstrate that the interaction between WS_2, water, and SiO_2, on average, results in a type I or the so-called straddling band alignment, in agreement with previous IPE measurements[243]. The band gap of WS_2 is completely contained within the much wider band gaps of SiO_2 and water. The presence of water does not also significantly affect the average band offset between SiO_2 and WS_2 and the electronic properties of the WS_2 monolayer. The work function of WS_2 shifts by 0.1 - 0.26 eV with the introduction of confined water with the extent of the shift depending on the number of water layers. Localized short-lived in-gap states identified at the confined water interface between H_2O/WS_2 surfaces may affect the electron and hole conductivity in WS_2 layers. To understand the importance of this effect, carrier mobility measurements in WS_2 at water freezing temperatures and above room temperature will be useful. More studies are needed to understand the impact of confined water under experimental conditions in realistic WS_2 systems that include interface defects.

Chapter 7

WS_2 Oxidation

The pristine interface discussed in the previous two chapters offers valuable insight into the interactions at the $WS_2/H_2O/SiO_2$ interface. However, in realistic systems, defects will be present in both WS_2 and SiO_2. It has been reported that the interaction between water and WS_2 defects can lead to oxidation of WS_2,[291,292] while the edges of WS_2 can facilitate the hydrogen evolution reaction with H_2O.[293] Therefore, this chapter will focus on the interaction of water with WS_2 defects and edges. I will begin with a comprehensive review of the oxidation of TMDs, as there is currently a lack of consensus regarding the oxidation process in the literature. Furthermore, this review will examine the role of oxygen, which has been more extensively studied, in contrast to the limited literature available on the role of water. Subsequently, I will present my results, which take initial steps toward understanding the mechanism of water dissociation at the WS_2 edges and defects.

My investigation of the interaction between defects at the WS_2 surface and H_2O found that the interaction with point defects results in an increase in the adsorption energy of H_2O and, in some cases, leads to the spontaneous dissociation of H_2O. This dissociation initiates oxidation by leaving behind W–OH groups, which can further dissociate to form W–O. This process may also facilitate the hydrogen evolution reaction (HER) by generating protons as W–O forms. The key factors influencing H_2O dissociation include exposure of both tungsten and sulphur atoms with dangling bonds in the defect, as well as sufficiently large defects so that water can interact with atoms inside the defect. An examination of the edges focused on spontaneous dissociation, as this occurs without a reaction barrier and thus has the highest reaction rate. Our analysis showed that water at the tungsten zigzag (W-ZZ) edge was physisorbed and did not undergo spontaneous dissociation. However, spontaneous oxidation at the W-ZZ edge occurred upon exposure to O_2 molecules. When both H_2O and O_2 were introduced, oxidation occurred, facilitated by H_2O dissociation via a Grotthuss-like mechanism, where protons are transferred between H_2O and O_2 molecules. A higher concentration of water and oxygen molecules led to increased dissociation of both molecules, enhancing oxidation at both edge types.

Investigation of water at the armchair edge, which exposes more sulphur, showed that water could spontaneously dissociate if two or more water molecules were arranged in configurations that optimised the S-H interaction.

7.1 Introduction

TMDs are susceptible to oxidation under ambient conditions, which changes their electronic and optoelectronic properties, such as band gap and PL spectra.[70,294,295] Additionally, structural changes in the TMD result from oxidation; in particular, XO_3 formation is a well-known product, where X is the transition metal from the TMD.

Oxidation can be desirable; applications in the hydrogen evolution reaction report that oxidation can increase the hydrogen production rate.[296,297] Moreover, there are reports of TMDs being selectively oxidised to form a dielectric oxide layer that exhibits a good lattice match with the TMD.[74,298,299] This selective oxidation may lead to advantageous future applications, as it occurs to a limited depth and reduces the presence of impurities, such as water, at the interface.

However, oxidation of TMDs is not always favourable. The alteration of properties due to oxidation can pose challenges for devices requiring stability and intrinsic n-type doping of TMDs. Consequently, unexpected oxidation can introduce additional variables, such as variations in surface roughness when analysing WS_2 on SiO_2.[17] Moreover, if oxidation is not characterised prior to measurements, it may result in inconsistent and misleading outcomes.

The complexity of various conditions that induce oxidation has led to the proposal of many potential mechanisms and causes.[73,185,295,300] Understanding this process is crucial for selectively facilitating or preventing oxidation through optimised storage and experimental conditions. This understanding would enable TMDs to be utilised in devices without the risk of oxidation. Current reviews offer a comprehensive overview of the landscape;[301] however, the literature has not established a consensus on oxidation products or mechanisms.

7.1.1 Oxidation Areas

To understand the oxidation mechanism, we first need to understand where oxidation occurs. Experimental studies have shown that oxidation occurs only in specific areas of TMDs.

The edges of TMDs oxidise more rapidly than any other defect site, with oxidation predominantly occurring in these regions. The consensus within the literature is that increased oxidation is due to the under-coordinated nature and exposed geometry of these edge metal atoms.[302] The type of edge also dictates how quickly oxidation occurs, see Figure 7.1. Edges with 100% metal atoms (metal zigzag edges), both in theory and in experiments, have the highest rates of oxidation.[74,303,304] On the other hand, 100% S/Se zigzag edges are resistant to oxidation.[305] Therefore, if the edge can be controlled in synthesis, the oxidation of TMDs could be suppressed or stimulated depending on the required functionality.

For HER catalysis, 50% sulphur edges have been found to have optimal hydrogen binding energies.[306] However, the interaction of water with edges to produce hydrogen has been insufficiently studied, but the role of water has been highlighted to impact the energetics hydrogen interaction with TMDs as part of HER catalysis.[307,308]

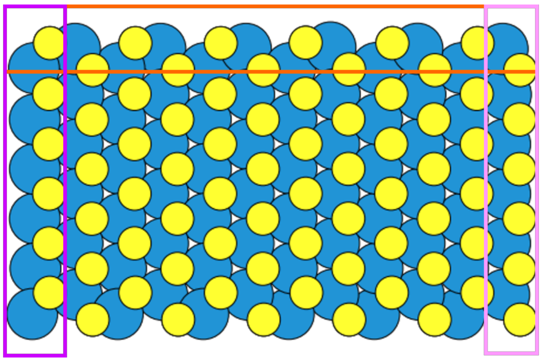

Figure 7.1 The Different edges of the TMD WS_2. The tungsten zigzag edge is highlighted in purple, the sulphur zigzag edge is highlighted in pink, and finally the armchair edge is highlighted in orange.

Generally, the pristine basal plane of TMDs is resistant to oxidation and, under ambient conditions, does not oxidise rapidly. However, oxidation can begin at defects in the basal plane, with initial oxidation occurring at defect sites before being propagated through the system. Sulphur vacancies are the most common defect attributed to TMD oxidation. It is proposed that the resulting exposed metal ions can interact with surrounding O_2 or H_2O molecules.[309,310] These sites have a reduced barrier for forming metal-O bonds from O_2.[311] However, the reaction barriers for this oxidation process vary significantly in the literature. Taking the example of MoS_2 oxidation with O_2, experimental values vary between $0.9 - 1.5$ eV, while the theoretical barriers range from $0.8 - 5$ eV, revealing the complexity of the oxidation process.[294,312]

It has also been observed that in MoS_2, V_{MoS_2} vacancies (a vacancy where one unit of MoS_2 has been removed) can significantly lower the barrier for H_2O dissociation at the defect site. The first hydrogen dissociation reaction can occur with an extremely low reaction barrier of only 0.08 eV. When water is fully dissociated, the total energy of the system stabilises between 2.85 eV and 3.39 eV, in comparison to the pristine defect.[309,313] This is significant as Peto *et al.* have calculated the native defect density to be $1{\times}10^{11}$ to $1{\times}10^{12}$ cm^{-2} in MoS_2 using STM, this increases to $3{\times}10^{12}$ to $2{\times}10^{13}$ cm^{-2} over a month under ambient conditions; it should be noted that this also includes light exposure.[70]

The final area addressed in this review is the boundary between the flakes. Grain boundaries are typically seen when a TMD is grown using methods such as CVD.[314,315] It is understood that grain boundaries and edge sites are initially oxidised before the basal plane.[300] In TMDs, it is generally understood that there is a high concentration of mirror twin boundaries (MTB). The role of MTB in oxidation has found that it is a favourable area to anchor OH groups and shows favourable adsorption energies of O_2 molecules, this has been confirmed both experimentally and theoretically.[291,292]

7.1.2 Factors Influencing TMD Oxidation

Defects and edges in TMDs serve as sites for oxidation; however, the environmental conditions in which the TMD is maintained significantly influence the oxidation rate of these areas.

Experimental studies have found that an increase in humidity leads to a faster oxidation rate.[185,295] However, the mechanism by which this increased oxidation occurs has not yet been fully elucidated. In the work of Lei *et al.*[316], the formation of OH radicals is proposed to act as a key intermediate leading to oxidation. Kinetic Monte Carlo studies have shown that the surface termination of MoS_2 dictates the adsorption energy and dissociation of water, with (001) surfaces having up to 90% coverage with OH groups after a 1000 ns trajectory with water.[317] The role of OH groups has also been discussed in experimental work, with OH groups forming sulphuric acid and leading to products such as $MoO_x(OH)_n$.[318,319]

The photooxidation of TMDs was first discussed by Kotsakidis *et al.*[73], this experimental work highlighted the degradation of MoS_2 under ambient laboratory light for a year. The light-induced oxidation was further confirmed by measuring the PL spectrum of MoS_2 under laser irradiation over time, during which three distinct photooxidation regimes were identified.[320] In WSe_2, photooxidation was observed under white light and humid conditions, resulting in the formation of cracks either randomly or along grain boundaries.[321] The authors posit that light generates $O_2^{-\bullet}$ radicals, which facilitate cracking. Furthermore, the authors suggested that the cracking along grain boundaries may also be attributed to strain induced by water droplets located between the substrate and the TMD.

Temperature also plays a critical role, with higher temperatures increasing the oxidation and etching rate.[322] However, these high temperatures are well above room temperature, with 200 °C the lowest temperature required to see changes.[323]

Finally, we note that the underlying substrate can play a significant role, as highlighted by Kang *et al.*[324]. They proposed that the dielectric screening of the substrate influences the oxidation of WS_2. SiO_2 substrates were shown to increase oxidation compared to WS_2 grown on suspended graphene and WS_2/graphene/SiO_2.

7.1.3 Propagation and Products of Oxidation

As discussed in the previous section, theoretical studies have shown that edges and defect sites are favourable for oxidation. However, it is not understood how oxidation penetrates through the layers and occurs across the surface of TMDs. Experimentally, various products have been observed, yet only a few have had a verified formation mechanism attributed to them. The propagation of oxidation is currently debated within the literature, with different mechanisms proposed for distinct environmental conditions.

Some studies suggest that hydrogen plays a role in forming S-H groups, leading to the propagation of sulphur vacancies and consequent oxidation.[325] Experimental work by Afanasiev *et al.*[318] has also shown that sulphuric acid is produced when water is present through the formation of S-H groups. From this, they have proposed that the initial S-H surface groups are transformed into $S_2{}^{2-}$ bridges and OH species. Sulfate species are then formed, and these species go on to form H_2SO_4 or large molecules containing molybdenum such as $Mo_2O_5HSO_4$.

Theoretical studies of the oxidation of TMDs with water show that the barrier to water dissociation at the 100% and 50% metal edges of MoS_2 is very small. The barrier is lowest when more Mo is exposed, with the lowest barrier calculated at 0.54 eV with 100% Mo edges.[304] Furthermore, AIMD calculations at 300 K demonstrate that water dissociation occurs at the 100% Mo edge, suggesting that this process can take place at room temperature.

Further work on the mechanism for oxidation propagation with water using DFT, suggested that water dissociation results in an OH group bound to the Mo atom and an H^+ atom bound to the S atom.[309] The OH^- group subsequently dissociates, leaving the O atom still attached to the Mo atom. This is thought to be due to the donation of electrons from Mo to water O. However, this work finds that the edges are not active enough to split water; instead, vacancies are most effective for dissociation due to a strong interaction with water. This finding contradicts experimental observations that edges rapidly oxidise and the previously discussed theoretical work, raising further questions about the role of water dissociation in TMD oxidation. Experimental studies using AFM[185,311,322,326,327] have shown that molybdenum oxide protrusions form after oxidation. In the case of ref.[185], MoS_2 was oxidised through submersion in bulk water at room temperature. In contrast, ref.[311] demonstrates that protrusions develop when the basal plane mode is activated by H_2O_2 or light illumination at room temperature. Despite these observations, there has been no elucidation of the mechanism underlying the formation of these oxide protrusions.

The presence of water increases the variety of products observed, with the increased stability of sulphuric acid particularly noted at temperatures ≤ 300 °C.[319] This was also evident in experimental findings, which showed that the flakes disappeared and exhibited reduced roughness with the introduction of water vapour.[301] This is believed to be due to the formation of volatile $MoO_2(OH)_2$ and H_2SO_4.

XPS has also confirmed the formation of sulphuric acid. MoS_2 flakes, which were left to oxidise in air, displayed no peaks corresponding to MoS_2 in the XPS analysis; instead, only sulphuric acid was detected.[318] Additionally, the XPS data revealed the presence of three oxidation states of Mo: IV,V, and VI, indicating the formation of various oxidation products. Experimental evidence further suggests the presence of water confined between the TMD and the substrate, leading to increased oxidation in areas where the water is trapped.[17,328]

It is also observed that the oxidation of the grain boundary is influenced by humidity; specifically, 40% RH is insufficient to induce oxidation, whereas an increase to 65% RH results in observable oxidation. This is postulated due to the presence of OH radicals.[315] However, the complete mechanism by which water catalyses oxidation remains unexplored, and the variety of potential products complicates the analysis of these mechanisms.

The final point to consider regarding H_2O-based oxidation is that some experimental studies indicate that oxidation does not take place in the presence of water alone, without O_2.[295] The thermodynamic equilibrium of MoS_2 in the presence of oxygen is different when exposed to oxygen and water vapour simultaneously. This results in the formation of distinct products based on the molecules present, with variations in products also occurring with changes in temperature.[319]

Therefore, to understand the role of H_2O as a potential catalyst for TMD oxidation, it is essential to also understand the mechanism of O_2 oxidation. Focusing on the role of O_2, *ab-initio* based work suggests that oxygen molecules initially interact with the metal atom at sulphur vacancy defects.[329] The adsorbed O_2 molecules then interact with the sulphur atoms nearby, eventually removing SO or SO_2 groups from the surface of MoS_2, eventually leading to a metal-O bond.

The removal of SO_x species has been investigated using AIMD and CMD, with x being an integer between zero and three. At elevated temperatures, typically exceeding 1500 K, the removal of SO_x can occur spontaneously.[310,330] Additionally, the desorption of SO_x has been examined using temperature desorption spectroscopy (TPD)[331]. TPD peaks appear at 400 °C and 650 °C, which are attributed to SO_2. At temperatures of $\geq$ 800 °C, TPD yields peaks associated with S, showing the diversity of oxidation products. These peaks at elevated temperatures can be rationalised by the different intermediates formed during the desorption of SO_2.[310,329] However, the high temperature required for desorption suggests that SO_x desorption is unlikely to occur under ambient conditions.

7.1.4 Summary

In conclusion, WS_2 is susceptible to oxidation at the grain boundaries, edges, or defects in the material when exposed to air.[300,315,332] Prolonged exposure to air increases oxidation, with higher temperatures and humidity further accelerating the oxidation rate. The presence of water at the substrate interface and within the TMD has also been linked to the oxidation of the TMD film.[185] Water is hypothesised to contribute to oxidation by dissociating into hydrogen and hydroxyl groups, potentially leading to the formation of sulphuric acid or oxidised transition metal complexes.

However, the mechanism underlying this oxidation has been poorly understood. The wide range of conditions that can lead to oxidation, along with the diverse array of resultant products, makes this process difficult to model. Furthermore, there is no consensus in the literature regarding whether water directly oxidises TMDs; instead, it may catalyse or facilitate their oxidation in the presence of oxygen.

Therefore, in this chapter, I investigate the interaction between water and defects, as well as edges in WS_2. I will examine the effect of introducing multiple water molecules at the edges of WS_2 to understand how these interactions influence the water dissociation. Furthermore, I will explore whether the simultaneous introduction of oxygen and water affects oxidation by adding both O_2 and H_2O to the edges of WS_2. These calculations illuminate how water splitting and subsequent oxidation can occur at defects and edges, with the presence of both sulphur and tungsten facilitating the spontaneous dissociation of water. Moreover, the presence of both O_2 and H_2O at the edge of WS_2 promotes H_2O dissociation via a proton hopping mechanism that resembles the Grotthuss mechanism. Furthermore, these initial results provide further evidence that increasing the concentrations of H_2O and O_2 promotes oxidation.

7.2 Methodology

A 10×10 cell of monolayer hexagonal WS_2 with a 60 $\mathring{A}$ vacuum was optimised using PBE-D3(BJ) XC functional with CP2K, employing double ζ Gaussian basis sets and GTH pseudopotentials. The adsorption of a water molecule on top of the WS_2 surface was calculated by performing a geometry optimisation of the full system with PBE-D3(BJ) XC functional.

Defects were subsequently introduced into the WS_2. The introduction of defects results in the displacement of atoms, with varying defect energy levels observed depending on the choice of XC functional, as demonstrated in ref.[4]. This study justifies the selection of the PBE(D3), as the defect geometries are generally similar to those calculated with the PBE0-TC-LRC XC functional, although differences in their electronic properties are noted. Considering our investigation of oxidation mechanisms, the less computationally intensive PBE(D3) functional is suitable for accurately describing the defects and water geometry without necessitating expensive calculations.

For the edges calculated in this work, a 6×6 orthorhombic WS_2 cell was optimised with a width of 60 $\mathring{A}$ in both the z and x directions for the zigzag edge, and in the z and y directions for the armchair edge. This ensured that only one direction had a continuous WS_2 cell, thereby forming a large nanoribbon. The directions were chosen based on the edge type, which requires different cutting on pristine WS_2, see Figure 7.1. Water was added to the edge and the whole system was then optimised. When oxygen was introduced, each O_2 molecule was calculated in a triplet state.

The Bader charges were calculated using the code by the Henklemann group[88]. The average Bader charges for pristine WS_2 were determined to be +1.2 e on tungsten, while that of sulphur was -0.6 e.

Adsorption energy was calculated using:

$$E_{ads} = \frac{1}{N}((E_{(Nmol)} + E_{(WS_2)}) - E_{(WS_2,Nmol)}), \tag{7.1}$$

where N is the total number of molecules, E_{Nmol} is the total energy of the molecule(s) optimised in a vacuum, which can be either H_2O or O_2. This approach was undertaken to consider the hydrogen bonds present in water, which must be disrupted in order to facilitate interaction with the defect. The impact of using different E_{Nmol} values is discussed in Appendix C, and illustrated with Figure C.1. Finally, $E_{(WS_2,Nmol)}$ is the total energy of the system with N molecules adsorbed on WS_2. The positive value of E_{ads} corresponds to exothermic adsorption.

The total energy change was calculated to determine whether water dissociation is thermodynamically favourable using:

$$\Delta E_{tot} = E_{initial} - E_{final}. \tag{7.2}$$

Here, $E_{initial}$ is the total energy of the system before any interaction, with molecular reference energies calculated as described for adsorption energy. In the case where a single molecular species is present, the reference energy is that of the isolated molecule. When multiple molecular species are present, $E_{initial}$ includes both the pre-adsorbed species on WS_2 and the energy of the second, non-adsorbed molecular species. A more detailed discussion can be found in Section 7.3.5.3. E_{final} is the total energy of the system after interaction, where dissociation of at least one molecule has occurred.

Notably, Equation 7.2 is formulated with the initial and final energies reversed compared to the conventional definition i.e. the heat of reaction. This choice allows us to describe energy changes from the perspective of the surrounding environment: energy gain for exothermic reactions and energy loss for endothermic reactions. This convention facilitates direct comparison with adsorption energy values. I also note that the entropic contribution is neglected; this may impact some of the total energy changes when multiple molecular species are present.

This study does not examine activation energy (E_a, Figure 7.2) due to the computational cost of performing the required NEB calculations. However, in cases such as Figure 7.2c, the entire reaction path can be inferred from geometry optimisation when no reaction barrier is present or when the barrier is sufficiently low to be overcome by force relaxation in the simulation.

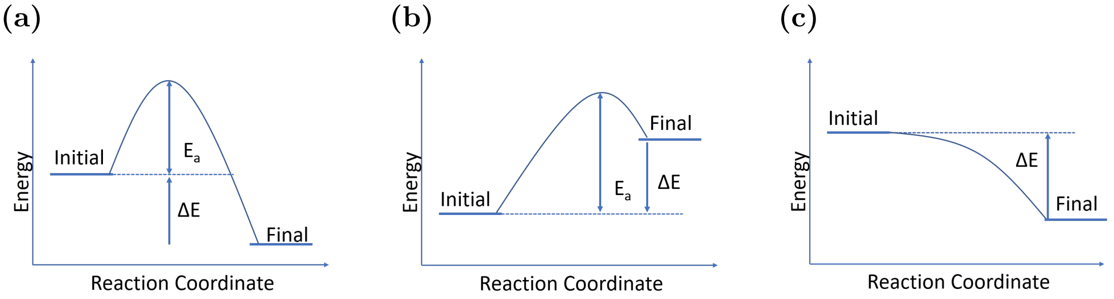

Figure 7.2 Figure describing the two possible reaction mechanisms **a**) exothermic and **b**) endothermic. The total energy change between initial and final systems is shown by ΔE, and the activation energy is shown by E_a. **c**) Shows an exothermic reaction pathway without a barrier, where spontaneous reactions will occur.

7.3 Results and Discussion

7.3.1 Water Molecule on Pristine WS_2

The geometry of a system with one water molecule on the surface of a pristine 10×10 monolayer of WS_2 was optimised. Four initial configurations were explored: both hydrogen atoms faced the surface, one hydrogen atom faced the surface, the oxygen atom faced the surface, or the water molecule lay parallel to the WS_2 surface (Figure 7.3). It was determined that, regardless of the initial configuration, the most stable arrangement of the water molecule occurred with both hydrogen atoms directed towards the WS_2 surface, at a distance of 2.49 $\mathring{A}$ from the top sulphur layer to the hydrogen atoms. The energy gain for the adsorption of water in this configuration was 0.23 eV; therefore, at room temperature, molecules from a gas phase can desorb rapidly.

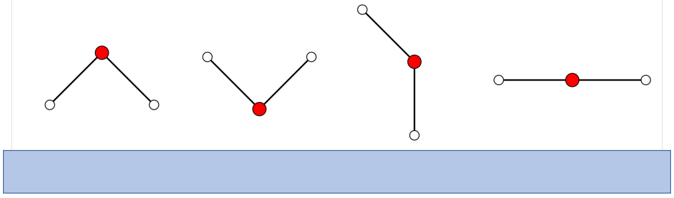

Figure 7.3 Initial orientations of water on top of the WS_2 substrate before geometry optimisation.

7.3.2 Introduction to Point Defects

As discussed in the Introduction, the pristine basal plane is resistant to oxidation; instead, defects can act as initial sites of oxidation. Therefore, we investigate point defects, including a single sulphur vacancy V_S, as well as double and triple sulphur vacancies. The double vacancies investigated have vacancies either: adjacent (V_{2S}^{A}), located at the same site but on different sulphur planes (V_{2S}^{P}), or separated by one sulphur atom (V_{2S}^{S}). Triple sulphur vacancies were also examined, where the vacancies may be clustered in a triangle (V_{3S}^{T}), arranged in a line (V_{3S}^{L}), or consist of two adjacent vacancies with an additional vacancy separated by a sulphur atom in a line (V_{3S}^{LS}). Finally, a vacancy created by removing a WS_2 unit (V_{WS_2}) was investigated. All these defects can be seen in Figure 7.4.

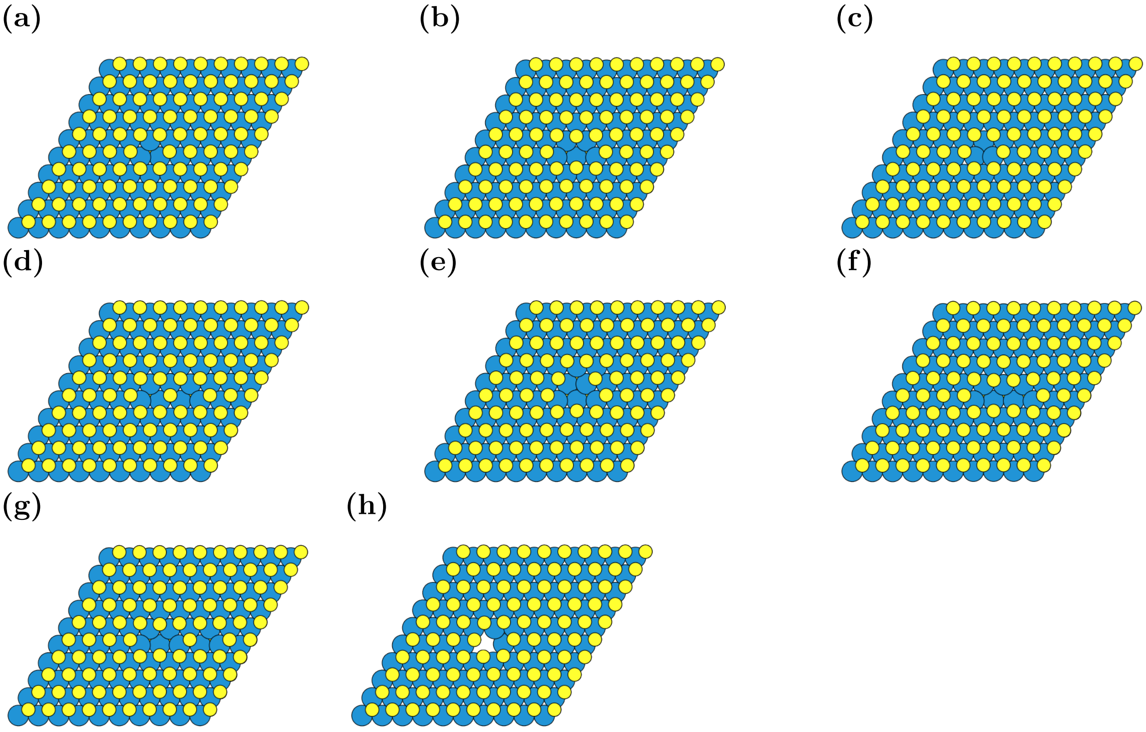

Figure 7.4 Images of the sulphur vacancies used in this work. **a**) is a mono vacancy (V_S) **b-d**) are di vacancies: **b**) sulphur vacancies are adjacent (V_{2S}^{A}), **c**) vacancies are on opposite planes (V_{2S}^{P}), and **d**) Sulphur vacancies are separated by a sulphur atom (V_{2S}^{S}). **e-h**) are tri vacancies: **e**) has sulphur vacancies clustered into a triangle (V_{3S}^{T}), **f**) sulphur vacancies are in a line (V_{3S}^{L}), **g**) Sulphur vacancies are separated by a sulphur atom (V_{3S}^{LS}). Defect **h**) has a WS_2 vacancy, resulting in a hole in the WS_2 monolayer (V_{WS_2}).

For all defects, charge redistribution predominantly occurs on the tungsten atoms in the sulphur vacancy (Figure 7.5), the sulphur atom exhibits minimal charge alteration (Appendix C Figure C.3).

When exposed by sulphur vacancies, the Bader charge on tungsten decreases when compared to pristine WS_2 ($+1.2$ e). The most significant reductions observed on an individual tungsten atom are in V_{3S}^{T} ($+0.79$ e), V_{3S}^{L} ($+0.89$ e), and V_{2S}^{P} ($+0.76$ e) defects. The increase in electron localisation on tungsten atoms results from the removal of sulphur, which leaves a dangling bond on tungsten. The valence electron that would have bonded with sulphur instead remains localised on tungsten, increasing its susceptibility to oxidation through W-O bond formation.[333]

7.3.3 Interaction of Defects with One Water Molecule

The interaction of water with defects is crucial to understanding the role of water in oxidation. Initially, we examine how a single water molecule interacts with different defect sites. To calculate the interactions of water with defect sites, the initial water orientations selected were the same as in Figure 7.3. The geometry of the system was then optimised, and the most stable configuration of the water was then used to calculate the adsorption energy. To model the dissociation of water, the molecule was separated into hydrogen and hydroxyl species, and the geometry of the dissociated water at the WS_2 surface was optimised.

7.3.3.1 Adsorption of Water

The energy gain from the adsorption of water molecules at all defect sites exceeds the adsorption energy of water on the pristine surface (Figure 7.6a). The adsorption energy of water across all defects remains fairly consistent, ranging from 0.28 to 0.3 eV and increases at the V_{3S}^{T} site to 0.42 eV. In the case of the V_{3S}^{T} defect, the optimal configuration is when water lies parallel to the surface, inside the defect (see Figure 7.6b). This parallel orientation at the defect site results in the water molecule being positioned closer to the WS_2, with the plane of the molecule located 0.6 $\mathring{A}$ above the upper sulphur plane and 2.2 $\mathring{A}$ above the tungsten plane inside the V_{3S}^{T} defect.

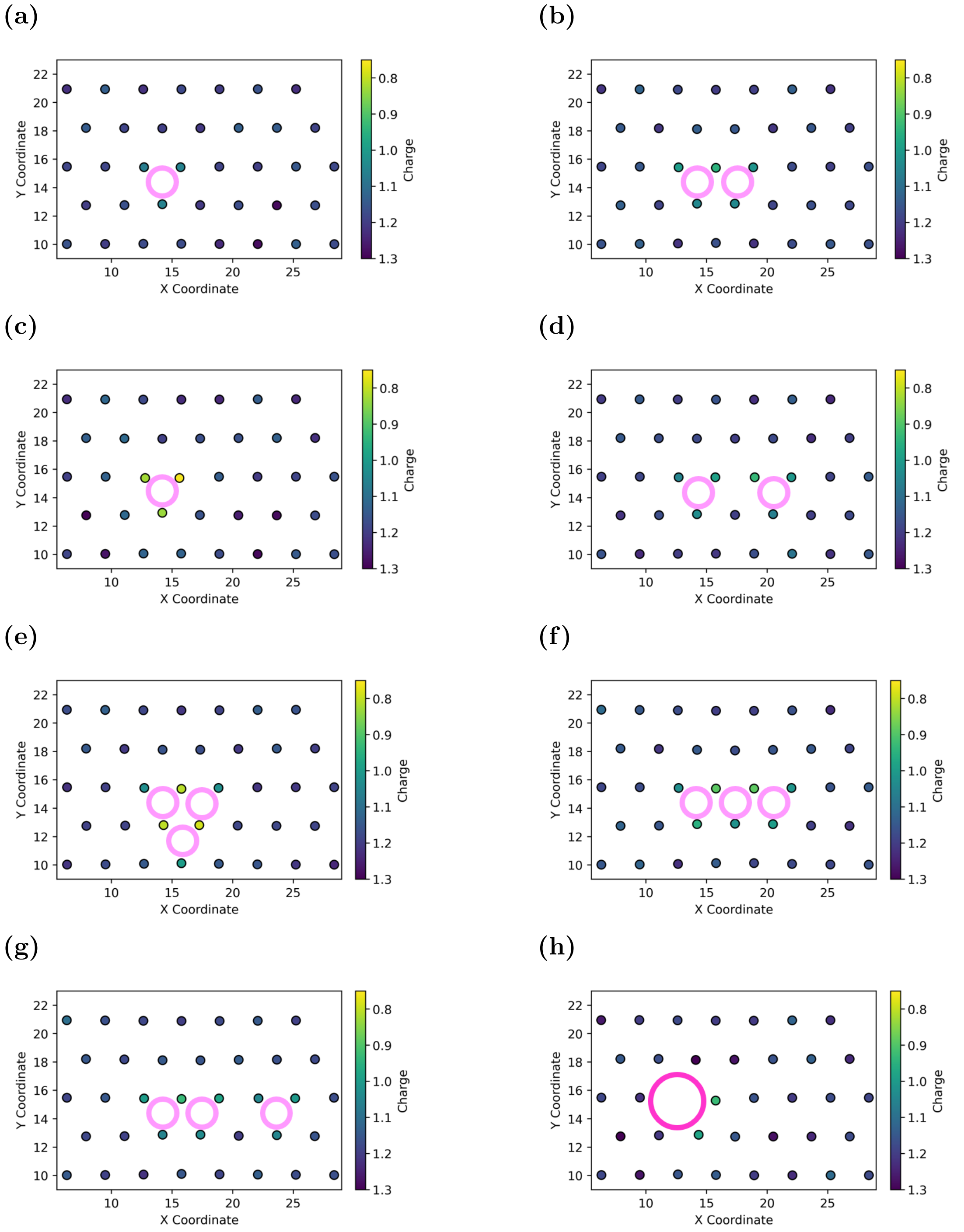

Figure 7.5 Bader charges on tungsten surrounding the vacancies used in this work. **a)** V_S, **b)** V_{2S}^A, **c)** V_{2S}^P, **d)** V_{2S}^S, **f)** V_{3S}^T, **e)** V_{3S}^L, **g)** V_{3S}^{LS}, **h)** V_{WS_2}. Corresponding structures are found in Figure 7.4. Sulphur vacancies are shown by light pink circles, and the WS_2 vacancy is shown by a dark pink circle.

The smallest Bader charge on W in V_{3S}^T (Figure 7.5e) is +0.79 e at the defect site, which may promote favourable adsorption. Furthermore, the steric hindrance associated with the defect is relevant, as the V_{3S}^T defect is the only defect providing sufficient space for H_2O to lie parallel to the defect site.

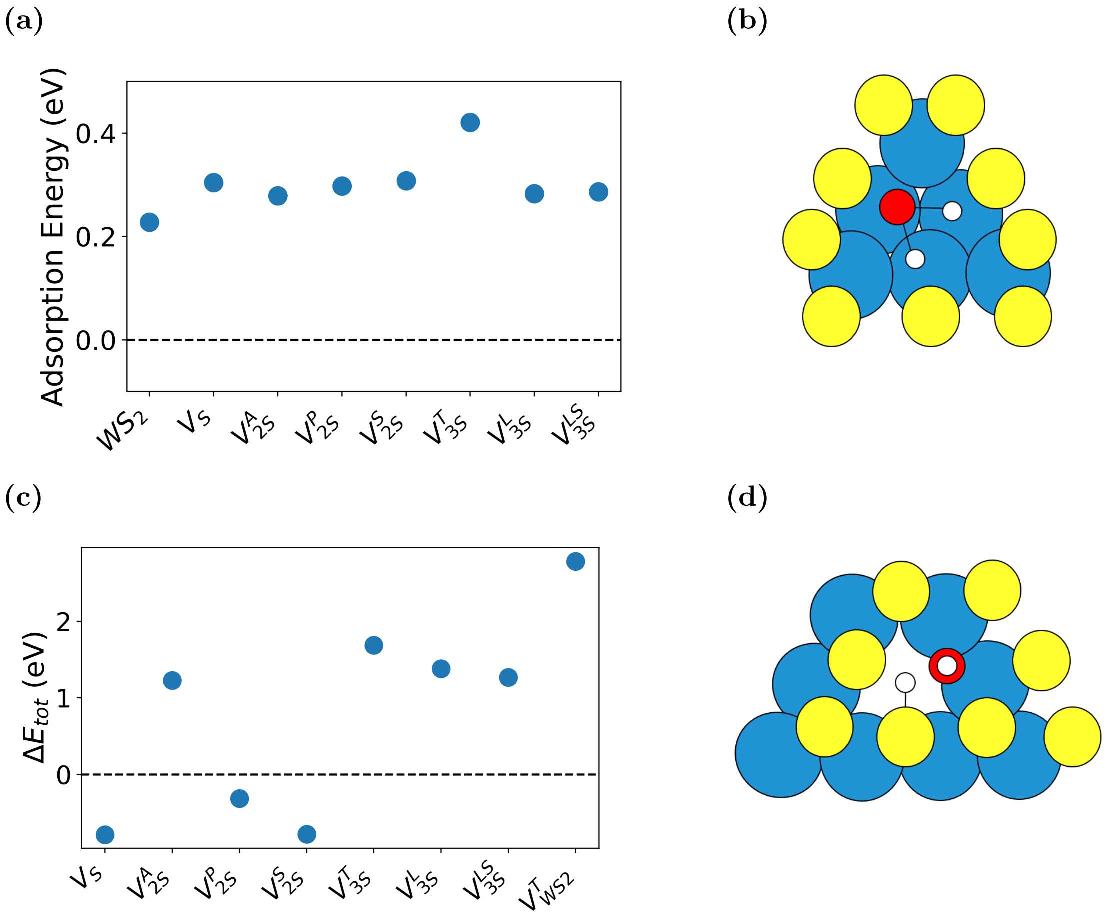

Figure 7.6 a) The adsorption energy of a single water molecule above different defect complexes on the surface of WS_2. **b)** Diagram of the position of water inside the V_{3S} defect site. **c)** The total energy change from the dissociation of water at defect sites. **d)** Diagram of the water dissociated at the $V^{T}_{WS_2}$ defect.

7.3.3.2 Dissociation of Water

In this section, I examine the total energy change associated with the dissociation of water at specific defects, with the aim of determining whether the dissociation process is thermodynamically favourable. However, due to the prohibitive cost of calculating all the barriers for water dissociation, the activation energy (reaction barrier) is not calculated.

At V_S, V^P_{2S}, and V^S_{2S} the most stable configuration of dissociated water corresponds to the formation of W-OH bonds at the defect site, accompanied by the generation of a S-H group. However, the corresponding total energy change at these defects shows that dissociation is thermodynamically unfavourable, with E_{tot} of -0.79, -0.31, and -0.78 eV, respectively. This occurs despite the V^P_{2S} defect exposing tungsten with a minimum Bader charge of +0.75 e. This reduction of tungsten is associated with increased oxidation of WS_2. Consequently, it can be concluded that the ΔE_{tot} for water dissociation is affected by steric hindrance at the defect sites. When a single sulphur atom is removed, the limited space restricts water's ability to interact strongly with the defect site.

The defects with at least two adjacent sulphur vacancies exhibit positive ΔE_{tot} for water dissociation. ΔE_{tot} for V_{3S}^{LS} water dissociation is 1.27 eV, comparable to that of V_{2S}^{A}, which is 1.23 eV. This similarity is expected, as both sites have two adjacent sulphur vacancies where water is adsorbed. As the distances between the sulphur vacancies of tri-vacancy defects decrease, the ΔE_{tot} increases. This trend is illustrated by V_{3S}^{L}, where the total energy gain of water dissociation is 1.38 eV, and it further increases at V_{3S}^{T} to 1.69 eV, where the distances between the sulphur vacancies are minimised. The most stable configuration for water dissociation in these defects involves the formation of one W-OH bond and a W-H bond with a nearby exposed tungsten atom that also has a dangling bond.

The largest total energy change from water dissociation on a defect site is with the V_{WS_2} defect, which is 2.79 eV. It is important to note that water adsorption on V_{WS_2} was not observed in Figure 7.6a, as water spontaneously dissociates. In the case of V_{WS_2}, the hydrogen atom forms a S-H group with an exposed sulphur atom with a dangling bond, as illustrated in Figure 7.6d.

This S-H formation contrasts with the tri-vacancy defects. This distinction is significant, as prior studies have indicated that only exposed tungsten plays a key role in oxidation via O_2.[302] Additionally, at the V_{WS_2} defect site, the exposed tungsten atoms have Bader charges exceeding +0.93 e, with this value representing the minimum charge among them (Figure 7.5h). This charge is higher than that of other defects, such as V_{3S}^{L}, suggesting that the tungsten charge may be less critical for H_2O dissociation than for O_2 oxidation. Consequently, the greater energy gains associated with S-H formation indicate that water dissociation can be more affected by sulphur availability than by tungsten alone.

The dissociation of water at the V_{WS_2} defect passivates the dangling S and W bonds, resulting in the formation of W-OH groups, akin to the formation of silanol groups on the surface of SiO_2 from ambient water.[169] This passivation could lead to protection from further oxidation; however, the experimental evidence indicating that increased humidity correlates with increased oxidation rates suggests that this is unlikely.[185,295] Instead, it is postulated that the interaction with S-H could influence water dissociation and promote oxidation, as discussed by Afanasiev.[318] Previous DFT studies have reported a total energy change of 2.85 eV with MoS_2, highlighting the similar interaction of water with different TMDs.[309]

7.3.4 Larger Defects: Holes and 2D defects

As discussed, the strongest interaction between water and WS_2 occurs when both tungsten and sulphur are exposed with dangling bonds and steric hindrance is minimised. This facilitates the interaction between H_2O and available sulphur atoms, promoting H_2O dissociation. The V_{WS_2} defect highlighted that spontaneous dissociation is possible; therefore, I investigated the dissociation of water on larger defects using the same methodology as with the point defects. Defects, specifically holes in WS_2, consisting of $V_{2(WS_2)}$ and $V_{3(WS_2)}$ were examined to determine if water dissociation is more favourable with increased availability of both sulphur and tungsten. Subsequently, one-dimensional defects were explored, including a line defect of sulphur vacancies (V_{10S_2}) and another line defect featuring both tungsten and sulphur vacancies ($V_{10(WS_2)}$), as illustrated in Figure 7.7.

Investigating the interaction of water with defects by optimising the geometry of water on the defects, we observe that the large $V_{2(WS_2)}$ and $V_{3(WS_2)}$ defects do not spontaneously dissociate water, in contrast to the smaller V_{WS_2} defect. Instead, the water at the $V_{2(WS_2)}$ and $V_{3(WS_2)}$ defects exhibit significantly greater adsorption energies of 2.25 eV and 2.07 eV, respectively. This substantial increase in adsorption energy can be attributed to the water molecules fitting into the defect, resulting in O-W and S-H distances of 2.1 $\AA$ and 2.2 $\AA$,

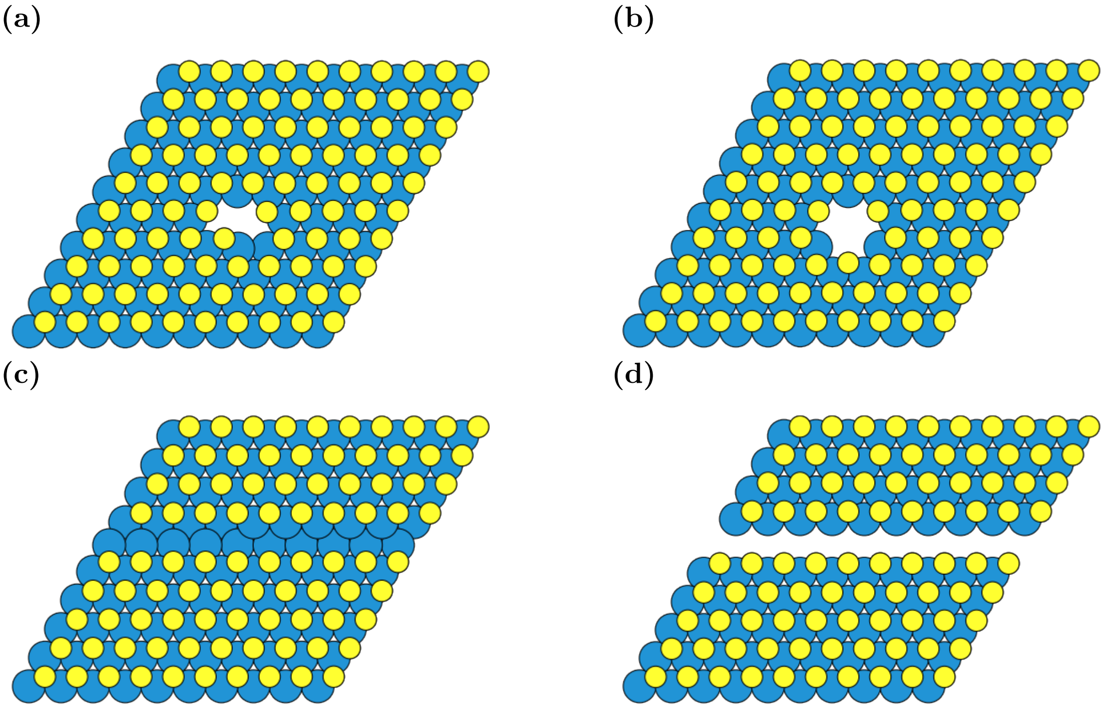

Figure 7.7 Images of the large defect sites: **a)** $V_{2(WS_2)}$, and **b)** $V_{3(WS_2)}$, and 2D defects **c)** V_{10S_2}, and **d)** $V_{10(WS_2)}$.

respectively (Figure 7.8). In contrast, the W-S bond length is 2.35-2.45 $\mathring{A}$, indicating the formation of a chemical bond between W and O. This is consistent with the high adsorption energy, even in the absence of dissociation. However, at $V_{3(WS_2)}$ the adsorption energy is smaller than that at $V_{2(WS_2)}$. This difference could result from the strain in the water molecule caused by increasing the H-O-H angle from 110.4° to 117.2°, while an unstrained water molecule has a H-O-H angle of 104.1°. The increased angle in $V_{3(WS_2)}$ allowed the water molecule to interact with two exposed sulphur atoms in the defect, see Figure 7.8. It is also noted that in both defects, the O-H bond increases to 1.01-1.02 $\mathring{A}$ compared to pristine water O-H bond of 0.97 $\mathring{A}$.

The dissociation of water at the $V_{2(WS_2)}$ and $V_{3(WS_2)}$ defects, while not spontaneous, is thermodynamically favourable. The total energy change for the water dissociation at $V_{2(WS_2)}$ and $V_{3(WS_2)}$ defects are 2.64 eV and 2.52 eV, respectively, and W-OH and S-H bonds are formed. When water is completely dissociated into W-O and 2×S-H, the dissociation energies increase to 2.82 eV for $V_{2(WS_2)}$ and 2.72 eV for $V_{3(WS_2)}$. However, if no S-H bonds are produced in the $V_{3(WS_2)}$ during dissociation into W-OH and W-H, ΔE_{tot} is only 1.65 eV. This underscores the significance of S-H bond formation in stabilising the dissociation of water.

Similar to the $V_{2(WS_2)}$ and $V_{3(WS_2)}$ defects, the V_{10S_2} 1D defect (Figure 7.7c) does not exhibit spontaneous water dissociation. Instead, it shows weak water adsorption on the surface, with an adsorption energy of 0.28 eV, consistent with previously calculated smaller line defects. Notably, V_{10S_2} has the lowest tungsten Bader charge among all WS_2 defects studied, with an average of +0.68 *e* for the most negatively charged line of exposed tungsten, and +0.74 *e* for the second exposed line of tungsten (see Appendix C, Figure C.4c). Therefore, it is concluded that, when V_S are arranged in a line, they do not strongly adsorb water due to steric hindrance that prevents water from getting close enough to interact with exposed tungsten or sulphur.

In contrast, the $V_{10(WS_2)}$ defect (Figure 7.7d) facilitates the spontaneous complete dissociation of H_2O into O and 2 H atoms through the formation of two S-H bonds and one W-O bond; this has ΔE_{tot} equal to 4.02 eV. The complete dissociation of water is not seen in any other defect explored and is attributed to $V_{10(WS_2)}$ having the largest exposure of both sulphur and tungsten atoms.

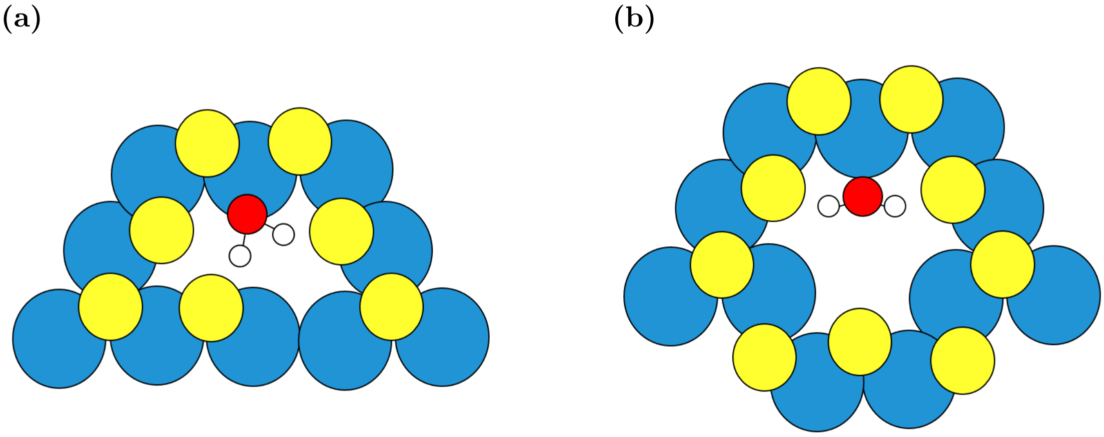

Figure 7.8 The adsorption of water to the **a)** $V_{2(WS_2)}$, and **b)** $V_{3(WS_2)}$ defect sites.

7.3.5 Interaction of Water and Oxygen with WS_2 Edges

As previously discussed in the literature review, the regions of WS_2 most susceptible to oxidation are the edges. Hence, we further explore WS_2 oxidation via the interaction of H_2O with WS_2 edges.

The first edge investigated was the tungsten zigzag (W-ZZ) edge, which oxidises more rapidly due to the high percentage of exposed tungsten. These strips of unpassivated tungsten exhibit metallic behaviour. Following this, the armchair edge, characterised by an equal exposure of 50% tungsten and 50% sulphur atoms, was investigated.

The edges explored here are expected to be chemically active. Consequently, it is anticipated that these edges may be passivated under experimental conditions, depending on the specific environment in which they are situated. However, this work is focused on understanding the chemical reactivity of these edges, with particular emphasis on their interaction with water; therefore, it is assumed that these edges have not yet undergone passivation.

7.3.5.1 Interaction of Water Molecules with W-ZZ Edge

The interaction of water with the W-ZZ edge was examined using 1, 2, and 8 water molecules to assess how the interaction varies with molecular coverage. Eight molecules were chosen as this quantity is sufficient to fully cover the edge surface.

First, a single water molecule was optimised on the W-ZZ edge following the configurations described in Figure 7.3. The lowest energy configuration was identified as O_w facing the edge, interacting directly with tungsten. When a second water molecule was introduced, it was positioned to form a hydrogen bond with the first molecule and was then optimised, allowing for the evaluation of hydrogen bonding effects.

For the eight-molecule system, water molecules were distributed across the length of the edge and were positioned at least 3 $\mathring{A}$ away from the surface, and were subsequently geometrically optimised. 3 $\mathring{A}$ was chosen as it was above the equilibrium distance between water and pristine WS_2, so any extra energy from artificially placing the water molecules near the edge would be reduced. This static geometry optimisation does limit the number of configurations, as with only eight water molecules, the potential configurations are numerous, and even molecular dynamic techniques would struggle to explore every configuration. Consequently, we opted for a static geometry optimisation to obtain a feasible water configuration at the surface; however, it is important to emphasise that this represents only one possible configuration among many.

Water adsorption at the edge is significantly stronger than at point defects, with adsorption energies of 1.18, 0.92, and 0.52 eV for 1, 2, and 8 water molecules, respectively. The large magnitude of adsorption energy indicates that the water is chemisorbed to the surface. The decreasing adsorption energy with increasing coverage is expected, as not all water molecules interact directly with exposed tungsten. Instead, hydrogen bonding between water molecules occurs.

However, the adsorption energy for one water molecule at the edge is smaller than at $V_{2(WS_2)}$ or $V_{3(WS_2)}$ defects, emphasising the role of S–H interactions in enhancing water adsorption on WS_2. Nevertheless, the adsorption energy at the edge remains high, suggesting that H_2O is likely to remain physisorbed at room temperature.

No spontaneous water dissociation was observed at the W-ZZ edge. When a water molecule was manually dissociated into hydroxyl and hydrogen species and then optimised, the total energy change was found to be 3.23 eV, indicating that the dissociation products are more stable at the edge than at the defect sites. Further manual dissociation of hydroxyl resulting in one oxygen and two hydrogen atoms resulted in an even greater energy stabilisation of 4.87 eV. This suggests that while water dissociation at the edge is thermodynamically favourable, the lack of exposed sulphur prevents spontaneous oxidation, as observed at the $V_{10(WS_2)}$ defect. As a result, the W-ZZ edge is expected to exhibit a lower water dissociation rate compared to the $V_{(WS_2)}$ and $V_{10(WS_2)}$ defects.

7.3.5.2 Interaction of Oxygen Molecules with W-ZZ Edge

As oxygen is considered the primary molecule to facilitate oxidation, O_2 molecules were introduced in their triplet state at the edge to investigate the oxidation process.

The optimisation of O_2 molecules only at the W-ZZ edge resulted in the spontaneous dissociation of O_2, leading to the formation of two W-O bonds per oxygen molecule. The total energy change for this dissociation is 9.93 eV for one molecule and 19.48 eV (9.74 eV/O_2) for two molecules underscore the large energy gain from this dissociation, illustrating why the edges of WS_2 are susceptible to oxidation. In comparison, the ΔE_{tot} for one O_2 molecule at defect sites V_{3S}^{L} is 7.77 eV in its triplet state.[333] While this is significant, the W-ZZ edge not only exhibits greater energy gain and spontaneous dissociation of O_2, but also has a larger cross-section than basal plane defects. These significant energy gains indicate that unpassivated exposed tungsten will be rapidly oxidised by nearby oxygen, corroborating findings from earlier literature.[74,303,304]

However, energy dissipation poses a challenge, as the large energy gains from oxidation exceed what can be managed solely by phonons dissipating the energy as heat. Although some energy is expended in the creation of edges and defects, this alone cannot account for the substantial exothermic oxidation reaction. It has been suggested that the significant energy release could assist in the desorption of molecules, such as SO_2,[329] or that electron-hole pairs may form.[334] It is also noted that, although the W-ZZ edges have been seen experimentally using scanning transmission electron microscopy (STEM), light atoms, such as hydrogen will not be seen in these images, although they could have passivated the tungsten if the TMD is not in ultra high vacuum (UHV). This could result in reduction of ΔE_{tot} for O_2 dissociation.[335,336] However, investigating this energy dissipation falls outside the scope of this work.

7.3.5.3 Interactions of both Oxygen and Water Molecules with W-ZZ Edge

To investigate how both O_2 and H_2O can contribute to oxidation, both water and oxygen were introduced to the W-ZZ edge. The adsorption and dissociation energies were calculated, where the sum of the WS_2 system with pre-adsorbed molecules and the additional species in vacuum was compared to the total energy of the optimised configuration with all adsorbed species. An example of this is:

$$\Delta E = (E_{(WS_2+2H_2O)} + E_{(2O_2)}) - E_{(WS_2+2H_2O+2O_2)}. \tag{7.3}$$

To simulate a realistic adsorption process, the additional molecules ($2O_2$ in this example) were initially positioned at least 4 $\mathring{A}$ away from the WS_2 edge. This positioning ensured that the additional molecules were sufficiently distanced from the WS_2 edge, so any interactions were with the adsorbed species.

I begin by considering the previously described scenario where oxygen is already present and has oxidised the edge of the WS_2, with either one, two, three, or six O_2 molecules. Focusing on the models with one or two oxygen molecules initially present, both exhibit the same adsorption and dissociation mechanisms when a single water molecule is introduced. Upon approaching the W-O bonds, the water molecule dissociates, with a H^+ atom transferring to a neighbouring W-O oxygen, while the OH^- group binds with the exposed tungsten. See Figure 7.9a for an illustration of this mechanism. This results in the formation of two W-OH groups, with ΔE_{tot} of 2.23 eV for one O_2 molecule and 1.98 eV (0.99 eV/O_2) for two O_2 molecules.

When an additional water molecule is introduced near the W-OH group and the system undergoes geometry optimisation, the hydrogen atoms of the water molecules can 'hop' between different water molecules. This process involves breaking an O-H bond in one water molecule while forming a new O-H bond with a neighbouring water molecule; therefore, hydrogen can transfer, or hop, between water molecules. As a result, the water molecule closest to the edge dissociates: one hydrogen transfers to the second water molecule, which in turn transfers a hydrogen to the oxidised tungsten edge. Figure 7.9b illustrates this process. This mechanism is analogous to the Grotthuss mechanism for proton diffusion in bulk water. As a result, ΔE_{tot} is 2.51 eV for one O_2 molecule and 1.99 eV (0.96 eV/O_2) for two O_2 molecules, respectively.

However, when a different water configuration was tested, where water molecules are positioned away from the oxidised edge before geometry optimisation (Figure 7.9), only the adsorption of water on the exposed tungsten occurs. This results in a small adsorption energy of 0.2 eV and 0.1 eV for one and two H_2O molecules, respectively. In a realistic scenario with water vapour present, dissociation will depend on the frequency of interactions between water molecules and the edge, as well as the rate of collisions near the oxidised edge.

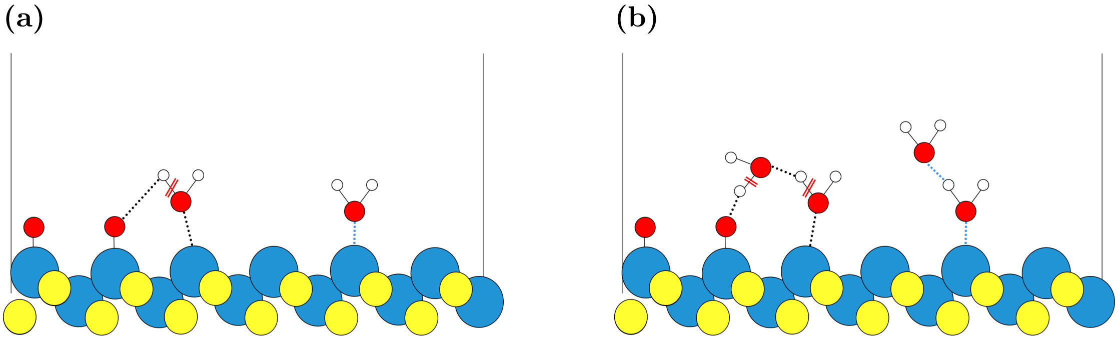

Figure 7.9 Schematic of the two interaction mechanisms of water and a partially oxidised edge when water is close to the oxidised edge (left) or further away (right). The illustration is of **a**) one water molecule and **b**) two water molecules. Black dotted lines show the bonds being formed, and the double red line shows the bonds broken. Light blue dotted lines show non-bonding, stabilising interactions. The grey lines represent the periodic boundary conditions of the simulation.

Therefore, we investigated the scenario where water molecules are initially present at the edge, followed by the introduction of O_2 molecules. When one H_2O molecule and one O_2 molecule are present, water dissociates, forming a W–OH bond and H^+. Simultaneously, the O_2 molecule interacts with the exposed tungsten atom and incorporates the dissociated proton, leading to the formation of a W–OOH group. This configuration exhibits ΔE_{tot} of 4.92 eV. Since a single H_2O molecule dissociates in the presence of only one O_2 molecule, adding additional O_2 molecules to a single H_2O was not considered.

When multiple water molecules are present alongside O_2, the resulting products and mechanisms differ. For two water molecules, one H_2O molecule can interact with the edge, while the second forms a hydrogen bond with the first. Proton transfer occurs via a coordinated movement: the first water molecule donates a H^+ to the second, which in turn donates one of its hydrogens to a nearby O_2 molecule. This proton hopping process results in the formation of a W–OH group and a O_2H molecule. The W-OH group can then donate another hydrogen to O_2H, producing H_2O_2 and W–O. The overall total energy change is 4.01 eV.

The introduction of a second O_2 molecule leads to two distinct outcomes depending on its placement. When positioned further from the water molecules, the mechanism mirrors the earlier case with one O_2 and two H_2O molecules, resulting in the formation of W–OH and H_2O_2. The second O_2 molecule only interacts with exposed tungsten, contributing to a total energy gain of 7.30 eV. However, when the second O_2 molecule is introduced closer to the water molecules, complete dissociation occurs for both H_2O molecules and one O_2 molecule. Proton hopping facilitates the formation of H_2O and H_2O_2 from the two O_2 molecules and three W-O bonds from the dissociated molecules, resulting in a significant total energy gain of 12.18 eV. Addition of a third O_2 molecule results in O_2 adsorbed to tungsten, leading to a total energy gain of 11.82 eV.

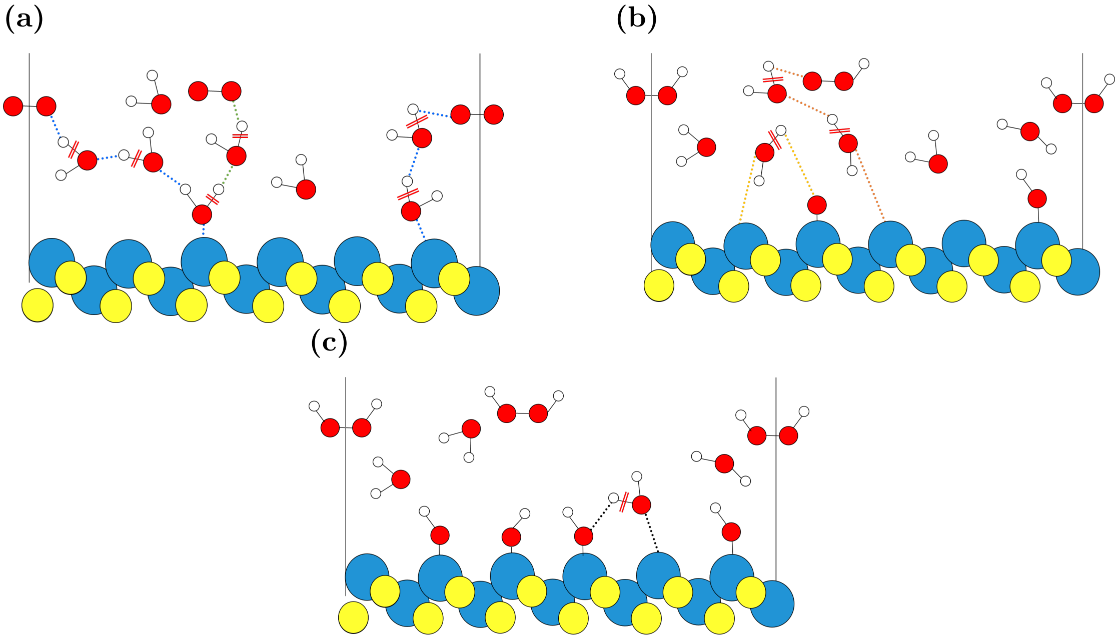

Figure 7.10 Schematic of the interaction mechanism involving eight water molecules and two oxygen molecules with the W-ZZ edge is illustrated, but it is not drawn to scale. Dashed lines are drawn to represent bond formation, and red double lines show bond breaking. The colour of the dashed lines in **a**) green signifies the first step, and blue the second. In **b**) orange is the third step, followed by yellow. The final part of the mechanism is shown in **c**) with black as the final step.

In the case of eight H_2O molecules with one O_2 at the W-ZZ edge, the mechanism resembles those observed with two H_2O molecules. H_2O_2 forms, but the complete dissociation of one water molecule does not occur. Instead, two W–OH groups are produced, as additional water molecules participate in the proton hopping mechanism, facilitating hydrogen transfer to O_2. This process results in a total energy gain of 4.97 eV. When a second O_2 molecule is introduced, proton diffusion and rearrangement through the proton hopping mechanism result in the formation of two H_2O_2 molecules and four W–OH groups. The oxidation mechanism is illustrated in Figure 7.10, highlighting the complexity of the molecular interactions and the multi-stage process essential for enabling water dissociation through coordinated proton movement. For the interested reader, further comparison of the geometry of the water at two different snapshots from the geometry optimisation and corresponding Bader charges can be seen in Appendix C Figure C.5. The total energy gain increases to 10.6 eV.

Figure 7.11 Geometry of the interaction of eight water molecules and three oxygen molecules with the W ZZ edge. **a**) The initial configuration and **b**) the final configuration.

The addition of a third O_2 molecule further facilitates water dissociation, yielding a ΔE_{tot} of 22.66 eV. This process leads to the complete dissociation of two H_2O molecules and two O_2 molecules. The dissociated components form four W–OH groups, three W–O groups, and one H_2O_2 molecule, with remaining water molecules adsorbed near the edge. The formation of these products is the result of the proton hopping mechanism, similar to that seen in Figure 7.10. The final structure is illustrated in Figure 7.11b. The large total energy gain observed for the eight H_2O and three O_2 system is similar in magnitude to the oxidation of the W-ZZ edge with three or six O_2 molecules, underscoring the favourable oxidation of the W-ZZ edge.

Overall, the increase in oxidation rates with rising relative humidity is postulated to be more closely associated with the dissociation of water molecules than with the dissociation of O_2 at the W-ZZ edges of WS_2. When water is initially present, the introduction of O_2 resulted in the spontaneous dissociation of H_2O molecules in all water configurations. Furthermore, it is observed that an increase in the number of water and oxygen molecules promotes the oxidation of tungsten at the W-ZZ edges. This oxidation process involving water is facilitated by a proton hopping mechanism. However, the reactions and products of dissociation may differ depending on the configuration of the adsorbates, as molecules must be sufficiently close to interact before dissociation can take place. Additionally, it is noted that there are numerous pathways for proton diffusion, evidenced by the variety of products generated even in these small-scale simulations.

7.3.5.4 The Armchair Edge

Following the examination of the W-ZZ edge, the armchair edge was investigated to assess the impact of sulphur exposure on water dissociation. The methods utilised to investigate the W-ZZ edge were also applied to the armchair edge, with one, two and eight water molecules explored and the configurations decided with the same techniques.

The optimised configuration of a single water molecule adsorbed at the armchair edge involves the H_2O adsorbed side-on to the edge to facilitate both W-O and S-H interactions. The water molecule did not spontaneously dissociate; however, it demonstrated a higher adsorption energy of 1.56 eV compared to the 1.18 eV observed at the W-ZZ edge. This difference can be attributed to the S-H interaction at the armchair edge.

The introduction of two water molecules can result in the dissociation of water; however, this process is contingent upon the initial configuration of the molecules. When the water molecules are hydrogen bonded to each other, one molecule can interact with exposed tungsten. However, it is the positioning of the second water that determines if spontaneous water dissociation occurs. If the two hydrogen atoms of the second water molecule interact with two exposed sulphur atoms, this water can stabilise H_3O^+, thereby facilitating the dissociation of the first H_2O molecule. This stabilisation of H_3O^+ can be seen in the increase in sulphur Bader charge to -0.7 *e* (Appendix C Figure C.6). However, in the absence of interactions between the second water molecule and exposed sulphur, spontaneous dissociation does not occur. The energy difference between the two final configurations is only 0.07 eV, with a total energy gain of 2.05 eV for the adsorbed configuration and 2.12 eV for the dissociation configuration.

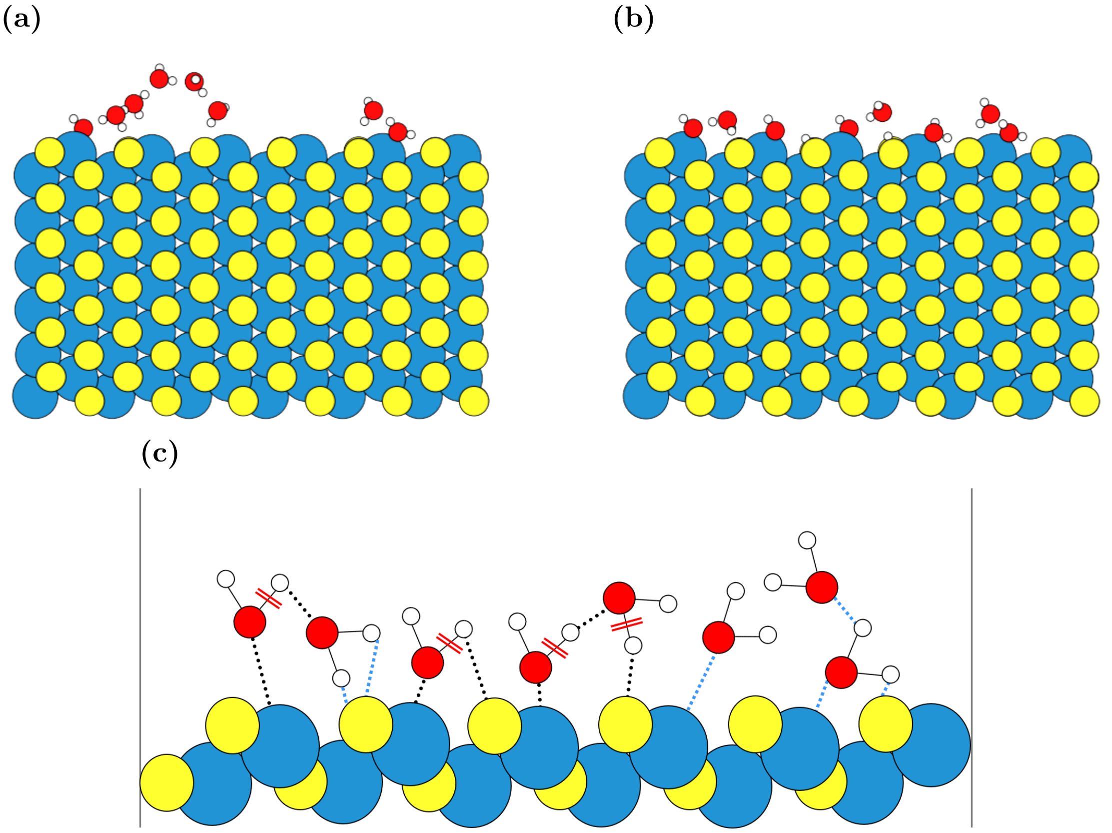

Figure 7.12 The final configuration of eight water molecules interacting with the armchair edge. The initial configuration was either in **a**) clustered groups, or **b**) a line covering the entire edge. **c**) Schematic of the mechanism for water dissociation of water in a line, the dashed blue lines represent stabilising interactions which do not involve chemical bonds i.e. hydrogen bonds.

The introduction of eight water molecules, however, demonstrates spontaneous water dissociation. The extent of this spontaneous water dissociation is influenced by the configuration of water at the edge. When water is more clustered, as illustrated in Figure 7.12a, one water molecule dissociates, resulting in an overall total energy gain of 4.39 eV.

Conversely, when the water molecules are spread across the armchair edge, allowing multiple interactions at the edge, three water molecules dissociate, as shown in Figure 7.12b. This process, again, occurs via proton hopping, as seen in

Figure 7.12c. Here, H^+ migrates between water molecules, leading to the formation of a H_3O^+ molecule and S-H groups. The H_3O^+ molecule produced is stabilised by interactions with two H atoms and nearby sulphur atoms, as described with two water molecules. Moreover, one water molecule can spontaneously dissociate even in the absence of another H_2O molecule nearby. I theorise that this is due to the charge change on the adjacent sulphur atom which increases to stabilise H_3O^+ (Appendix C Figure C.6). This allows for the water O_w to form a bond with tungsten and consequently dissociate. The overall total energy gain, in this case, is 8.41 eV.

The primary focus of investigating the armchair edge is to understand the interaction of water with exposed sulphur. Therefore, I will only briefly outline the interactions involving oxygen molecules and the interactions between oxygen and water molecules.

Adding one or two O_2 molecules to the armchair edge did not result in any spontaneous dissociation. Instead, the O_2 molecules are adsorbed with adsorption energies of 2.59 eV for one molecule and 2.6 eV for two molecules. This contrast with the W-ZZ edge underscores the influence of tungsten charge on oxidation via O_2. The W-ZZ edge experiences a larger change in Bader charge of $+0.91\ e$ at the edge tungsten atoms, whereas the armchair edge tungsten atoms have a reduced Bader charge of $+1.20\ e$. Nevertheless, given the substantial water adsorption energies, O_2 is expected to passivate tungsten dangling bonds, suggesting that O_2 should remain adsorbed at the armchair edge.

The impact of water and oxygen molecules interacting with the armchair edge was examined using one and two molecules of each species. My results show that when an O_2 molecule interacts with a tungsten atom adjacent to H_2O, it can facilitate water dissociation through proton transfer. This mechanism is analogous to those described in relation to the W-ZZ edge, emphasising the role of H^+ movement in facilitating the oxidation of WS_2.

Therefore, the armchair edge highlights that the spontaneous dissociation of water follows a different mechanism than that of O_2. This dissociation of water depends on the availability of exposed sulphur and tungsten atoms. Consequently, I propose that this could facilitate the oxidation of edges and defects that have dangling sulphur bonds, which O_2 is unable to oxidise independently. This mechanism could significantly influence the propagation of oxidation throughout the TMD flake and account for the increase in oxidation with elevated relative humidity.

7.3.6 Adsorption and Total Energy Change Comparison

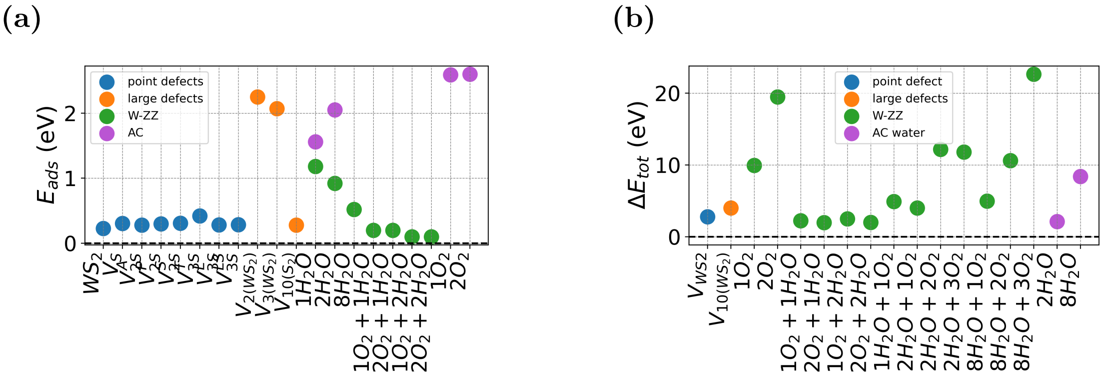

Figure 7.13 Comparison of **a**) adsorption energies of H_2O and/or O_2 at defects and edges where no spontaneous dissociation occurred. **b**) Total energy change for all cases of spontaneous dissociation of either O_2 or H_2O. The x-axis represents either point defects and large defects (examined with a single H_2O molecule) or the molecules studied at WS_2 edges. The specific edge type is indicated in the legend, with colours distinguishing between each edge.

In this chapter, I have examined how exposing tungsten and sulphur influences the adsorption energy of water molecules. As shown in Figure 7.13a, large defects such as $V_{2(WS_2)}$ and $V_{3(WS_2)}$, along with armchair edges, exhibit the highest water adsorption energies. The adsorption energy of water at the W-ZZ edge is consistently lower than that at the armchair edge, reinforcing the role of S-H interactions in enhancing the adsorption energy. However, the highest adsorption energies are observed for O_2 at the armchair edge, indicating that the W-O interactions with O_2 are stronger than the combined W-O and S-H interactions with H_2O.

To further assess these interactions, we compare the total energy change in Figure 7.13b when spontaneous dissociation occurs. The W-ZZ edge shows the largest ΔE_{tot}, with the highest values for one and two O_2 molecules occurring without water. This suggests that water is not essential for oxidation at the W-ZZ edges. Furthermore, while the armchair edge with $8H_2O$ shows an increase in ΔE_{tot}, it remains lower than the $8H_2O + O_2$ combination at the W-ZZ edge. These findings support the experimental evidence that exposed tungsten is more readily oxidised under ambient conditions.

7.4 Conclusions

Overall, I have demonstrated that water adsorption energy increases at defect sites, with notably larger adsorption energies calculated for defect sites that allow for S-H interactions. Furthermore, it has been found that water dissociation is thermodynamically favourable only at defect sites where there is enough space for water to interact with the exposed atoms in the defect. Water more easily dissociates into a stable configuration when both tungsten and sulphur are exposed with dangling bonds. This configuration facilitates the formation of W-O and S-H interactions.

The W-ZZ edges of WS_2 are particularly susceptible to oxidation by O_2, which occurs spontaneously with a significant energy gain, indicating that it is a highly exothermic reaction. However, water at the W-ZZ edge does not dissociate spontaneously. To investigate this further, both O_2 and H_2O were introduced to the edges. When O_2 was added first, resulting in an oxidised edge, water could dissociate spontaneously if it interacted with a tungsten atom next to a W-O group. Conversely, if water is present initially, the subsequent addition of O_2 initiates water dissociation through a Grotthuss-like mechanism, leading to the formation of W-OH groups. The resulting proton subsequently reacts with nearby O_2 molecules, forming products such as H_2O_2 and H_2O. The specific products formed are influenced by the molecular configuration and the number and type of molecules present.

At the armchair edge, spontaneous water dissociation is observed in the presence of two or more water molecules. The interaction between S and H facilitates this dissociation, with water dissociating via a H^+ hopping mechanism.

However, the extent of water dissociation is influenced by the configuration of the water molecules. It is, therefore, hypothesised that water dissociating at defect sites or edges, leading to the formation of S-H bonds, may enable oxidation in areas that O_2 alone cannot oxidise. More work is needed to elucidate this mechanism, with further steps required focusing on the reported formation of H_2SO_4. However, I believe these results represent a promising foundation for understanding the oxidation process at WS_2.

It has to be noted that I have only explored a few possible configurations of water and/or oxygen at the edges of WS_2. Therefore, it is anticipated that additional mechanisms will be present when studying a wider range of molecules and configurations. Future studies could explore oxidation mechanisms in greater detail by considering more molecular configurations over longer timescales. This could be achieved using large-scale but computationally expensive AIMD simulations or machine learning approaches, such as machine-learnt density functional tight binding or potentials. These methods will be discussed in the following chapter.

Additionally, while this work has presented comprehensive thermodynamic data on water dissociation, future research could investigate the kinetics of this dissociation, particularly at defects that do not exhibit spontaneous dissociation of oxygen and water. This could reveal additional oxidation routes beyond those that occur spontaneously, as examined in this study. Such investigations would enhance our understanding of the defects that contribute to the oxidation of WS_2.

Chapter 8

Exploring Alternative Methods

As was noted in the previous chapters, both the characterisation of the $WS_2/H_2O/SiO_2$ interface and the description of oxidation face a common challenge of traditional *ab-initio* methods: the required timescale of simulations and size of the interfaces required for accurate descriptions are unfeasible. One potential solution to bridge the gap between required timescales and calculation accuracy is to employ machine learning for the characterisation of these interfaces and interactions, using training data derived from accurate simulations using DFT. In this chapter, I discuss the implementation of machine learning to optimise density functional tight binding (DFTB) parameters, as DFTB can be orders of magnitude faster than DFT while still providing valuable electronic information that may be lacking in other machine learning approaches. The results presented in this chapter represent an initial exploration of applicability of ML-DFTB to characterise the $WS_2/H_2O/SiO_2$ interface and should not be regarded as a complete study.

8.1 Introduction

The use of machine learning (ML) in atomistic modelling has surged in recent years. Various ML approaches have been employed, including neural networks (NN) and machine learning potentials (MLP) that serve as substitutes for conventional potentials in CMD.[337] General-purpose MLPs are currently under development, which would allow for their application across a range of materials without the need for extensive training.[338] These advancements have facilitated significant increases in computational speed, as well as in the size and timescales of simulated systems. This progress is particularly appealing to the materials community, given that previously established accurate methodologies such as AIMD are often limited by high computational costs.

However, current MLPs, while effective for evaluating structural properties, have inherent limitations. Most MLPs do not provide information on the electronic structure; instead, they rely on 'black box' methods or CMD-like potentials for material descriptions. Furthermore, many MLPs find it challenging to accurately capture electrostatic interactions or subtle forces, such as van der Waals forces and hydrogen bonds. In this context, the use of DFTB presents an appealing alternative, as its increased computational efficiency over DFT allows for the modelling of larger systems over longer timescales. By implementing machine learning to describe repulsive potentials and confinement parameters, DFTB can achieve simulation accuracy comparable to DFT while also providing electronic information. I had the pleasure of collaborating with the groups of Christoph Scheurer and Chiara Panosetti at the Fritz-Haber Institute of the Max Planck Society to initiate this work. They have been pioneers in the application of machine learning for DFTB parameterisation.[339–342]

8.2 Methodology

8.2.1 Theory

To provide a clearer context for the application of ML DFTB, I will first introduce the theory of DFTB, followed by an overview of the machine learning techniques that will be utilised.

8.2.1.1 Density Functional Tight Binding

To begin, I will provide a succinct introduction to the theory underlying DFTB, emphasising the parameters which will be optimised through machine learning.

For a more in-depth understanding of the method, see the references[343,344] which offer thorough explanations.

DFTB is a semi-empirical approach to molecular modelling, derived from a similar foundation as DFT. The primary distinction between DFT and DFTB is the tight-binding approximation, which posits that electrons are closely bound to the nucleus of an atom. As a result, they experience minimal perturbation from surrounding atoms. This allows DFTB to employ a minimal basis set, thus significantly reducing computational time.

To understand how DFTB functions, we start by reformulating the DFT description of total energy (Equation 3.2). Using the Harris-Foulkes method, we can rearrange this formulation to emphasise the role of one-particle energies:

$$E[n(r)] = \sum_i f_i \epsilon_i - \frac{1}{2} \int V_H[n] n(r) dr - \int V_{XC}[n] n(r) dr + E_{XC}[n] + E_{II}. \quad (8.1)$$

Where f_i is the coefficient, ϵ_i is the Kohn-Sham energy level, V_H is the Hartree potential, V_{XC} is the exchange correlation potential, and E_{II} is the nuclear-nuclear repulsion energy. This formulation allows us to separate the so-called band structure energy (E$_{bs}$) as the term $\sum_i f_i \epsilon_i$. The rest of the terms are then approximated as a single repulsive energy (E$_{rep}$).

The tight-binding aspect of DFTB can be utilised, where it is assumed that atomistic descriptions of electron density (n_0) are applicable. This leads to the overall equation:

$$E[n(r)] = E_{bs}[n_0] + E_{rep}[n_0]. \quad (8.2)$$

This is based on the original implementation of DFTB, where no self-consistent charge (SCC) was implemented. This was improved with the introduction of small density fluctuations (δn) to the second and third order (DFTB2/3) to get:

$$E[n(r)] = E_{bs}[n_0, \delta n] + E_{coul}[\delta n] + E_{rep}[n_0], \quad (8.3)$$

where $E_{coul}[\delta n]$ is the screened Coulomb interaction between the atomic partial charges and a Hubbard-like on-site term for the energy of the partially charged atom.

In this overview of DFTB, I will now focus on the role of the confinement potential and the repulsive potential, as these are the two parameters optimised by ML.

The band structure energy reflects the single-particle energy levels, with wavefunctions represented as the linear combination of pseudo-atomic valence orbitals. The atomic valence orbitals originating from free atoms tend to be too diffuse. To address this, a confinement potential (V_{conf}) is introduced into the Hamiltonian, resulting in a more compact basis set. Optimising this confinement potential is essential to obtain an accurate representation of the orbital wavefunctions.

The potential can be defined in several ways, including power potentials and the Woods-Saxon potential. In this study, we will concentrate on power potentials because of their ease of use. They are characterised by the following functional form[345]:

$$V_{conf} = \left(\frac{r}{r_0}\right)^S . \tag{8.4}$$

Here, r_0 is conventionally around twice the covalent radius of the atom, and S is employed to regulate the functional form. These confining parameters can be optimised to modify the potential function, thereby improving the accuracy of the electronic parameterisation.

The confining parameters are calculated for each atomic valence orbital. Upon the application of the confinement potential, the overlap integral between different orbitals is calculated and stored in the Slater-Koster file (skf). Additionally, the Hamiltonian matrix element, which includes both kinetic energy and potential contributions between orbitals, is recorded in the skf. This skf for each atom-atom interaction is not recalculated; rather, it is utilised to provide overlap and Hamiltonian matrices for subsequent DFTB calculations, so only the electron density needs to be optimised through SCF cycles. The ability to avoid recalculating these parameters significantly decreases the computational time of DFTB compared to DFT; however, it is essential that they are accurately tabulated from the outset.

In this work, the Particle Swarm Optimisation is employed to automate the optimisation of confinement parameters.[346,347] This is particularly important in this work, as no confinement parameters have been produced for the interaction at the $WS_2/H_2O/SiO_2$ interface.

The second parameterisation required is that of the repulsive energy. Here, we simplify the complex terms given in Equation 8.1 into a single repulsive energy based on pairwise distance potential ($V_{rep}(R_{IJ})$):

$$\begin{aligned} E_{rep}[n_0] &= E_{XC}[n_0] + E_{II} - \frac{1}{2}\int\int \frac{n_o(r)n_0(r')}{|r-r'|}dr - \int V_{XC}[n_0]n(r)dr \\ &= \frac{1}{2}\sum_{I}\sum_{I\neq J} V_{rep}(R_{IJ}). \end{aligned} \tag{8.5}$$

This simplified approximation considers short-ranged, atom-pairwise contributions based on atomic distances, while also addressing the complex physics involved in the exchange-correlation functional. Due to the intricate physics it must encompass, a fitting procedure is necessary to formulate the repulsive potential, based on the difference between a DFT total energy and the combined E_{BS} and E_{coul} terms from DFTB. Historically, this fitting procedure has not been automated and has required substantial effort to generate parameterisation sets tailored for specific systems.[348]

Machine learning can significantly enhance this fitting process; Gaussian Process Regression (specifically implemented with GPrep in my work)[342] can utilise DFT training data to produce the V_{rep} functional force by minimising the root mean square error (RMSE) of the energy and forces of DFTB compared to DFT calculations.[339,341] This procedure must follow from the PSO optimisation

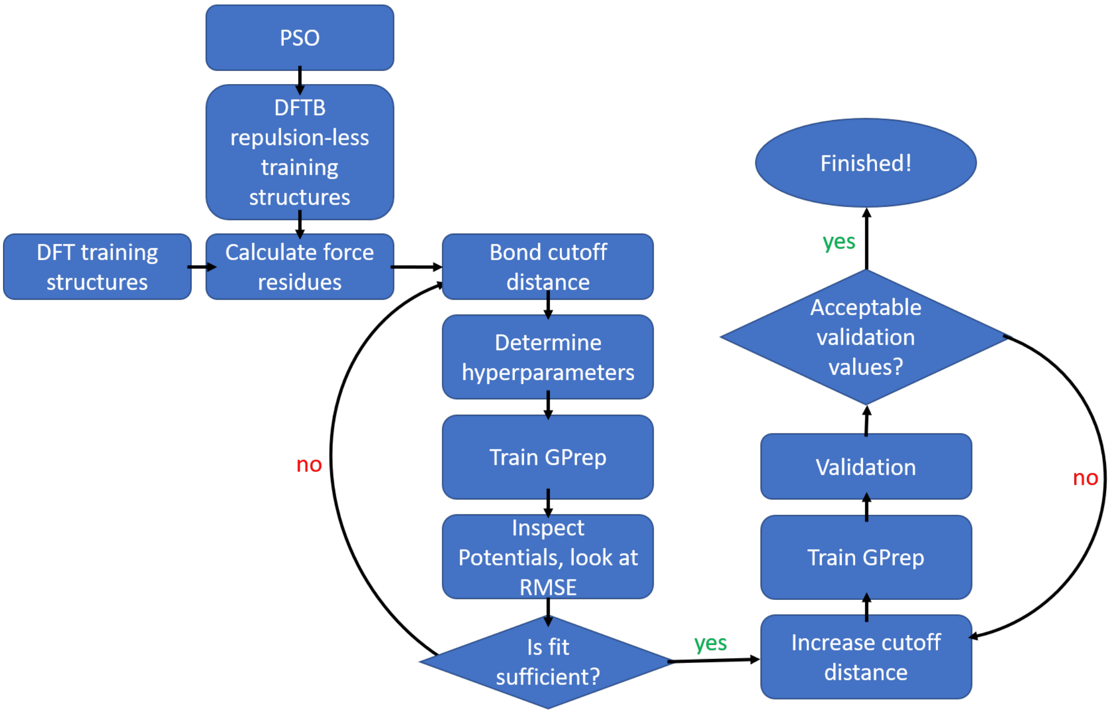

Figure 8.1 Process for training the V_{rep} functional using GPrep

of the confinement parameters as the confinement potential is integral to the correct description of E_{BS}.

The general workflow for training the DFTB repulsive potential with machine learning is shown in Figure 8.1. The GPrep training flow can require multiple iterations to ensure accurate training, so that the trained parameters result in a reliable description of repulsive potential behaviour.

8.2.1.2 Particle Swarm Optimization

Particle Swarm Optimisation (PSO) is a population-based optimisation technique inspired by the collective behaviour of swarms.[349] It explores a multi-dimensional parameter space through a set of particles, each assigned an initial position and velocity. The particles adaptively traverse the search space, influenced by both their own historical best positions and the best positions found by other particles in the swarm. This collaborative approach improves the ability to locate the global optimum.

In the context of DFTB confinement potential optimisation, PSO is utilised to refine the V_{conf} parameters. The objective is to minimise the deviation between the reference DFT band structure and the band structure predicted by DFTB. This optimisation process is governed by a cost function that quantifies the discrepancy and is minimised to guide the particles towards optimal parameter values.

8.2.1.3 Gaussian Process Regression

I will briefly describe the method of Gaussian Process Regression (GPR). The methodology employed in this work, specifically GPRep, is detailed in references[341,342] which are the primary sources of information for this section.

GPR is a versatile machine learning technique for modelling functions based on a covariance kernel. By employing probabilistic principles, it provides a flexible and robust framework for constructing accurate predictive models. In this context, GPR has been chosen to model V_{rep} due to its capacity to capture complex, non-linear relationships between inputs and outputs, even when the functional form of V_{rep} is not known. When applying GPR implemented with GPrep to describe the repulsive potential, we use the following form:

$$V_{rep}(R) = \sum_{I,J \epsilon \{\mathbf{X}\}} \alpha_{IJ} \cdot k(R, R_{IJ}). \tag{8.6}$$

In this context, α_{IJ} represents the regression coefficients, while $k(R, R_{IJ})$ denotes the kernel function. This formulation depicts V_{rep} as a linear combination of kernel functions, summed across all atom-atom pairs within the set of reference structures $\mathbf{X}$.

In this study the squared exponential kernel was used:

$$k^{SE}(R, R_{IJ}) = \exp(\frac{-|R - R_{IJ}|^2}{\theta}), \tag{8.7}$$

where θ is a hyperparameter related to length scale. Small values of θ indicate that the kernel function approaches zero unless the $R - R_{IJ}$ distance is minimal. Increasing θ enables the inclusion of more distant inputs, resulting in a smoother potential form.

Accurately describing V_{rep} requires a cutoff, as the repulsive potential in DFTB is short-ranged, reflecting the method's tight-binding nature, which restricts significant interactions to neighbouring atoms. To characterise this cutoff, a damping factor is introduced:

$$k^{damp}(R, R') = \exp(-\beta R) f_{cut}(R) k^{SE}(R, R'), \tag{8.8}$$

here, β the hyperparameter enforces a smooth decay of the function over distance.

The loss function utilised in GPrep is expressed as:

$$L = \sum_{I,J \epsilon \{\mathbf{X}\}} (t_{IJ} - V_{rep}(R_{IJ}))^2 + \sigma ||\alpha||^2. \tag{8.9}$$

This includes a final hyperparameter σ, which represents the noise present in the data. While we are fitting to DFT data, which is generally anticipated to be noise-free, this parameter can act as an indicator of the accuracy of the DFTB model. t_{IJ} denotes the reference values for the repulsive potential, while α is a coefficient that incorporates the covariance kernel, σ, and the reference values t_{IJ}.

8.2.2 Implementation

Given our goal to train the DFTB data using band structure, we selected the Quantum Espresso (QE)[350,351] code over CP2K for generating our training data for PSO. The plane wave basis sets in QE offer a more accurate representation of the band structure. A PBE XC functional was used with a 4×4×4 k-point Monkhorst-Pack grid for all QE calculations. The PSO used 64 particles and was iterated 20 times to reach a convergence in the cost function. In the case of oxygen, $3d$ orbitals were also included, as these could be used during oxidation as water molecules dissociate. To check the PSO data produced, DFTB was implemented using DFTB+ software,[352] with the same k-point density as the reference QE DFT calculations. A Fermi filling with an electronic temperature of 0.001 hartree (approximately 316 K) was employed. It is also noted here, that Hubbard values were kept fixed as to those tabulated in reference[345].

Force residues were calculated using the PSO-optimised skf files for DFTB, with the repulsive potential set to zero. Subsequently, the differences in force and energy were calculated and utilised as training data for GPrep using:

$$E_{rep} = E_{DFT} - E_{DFTB}. \tag{8.10}$$

A substantial training dataset was created from snapshots of the AIMD trajectories conducted in this thesis: WS_2/H_2O, $SiO_2/H_2O/WS_2$, SiO_2/H_2O as well as smaller trajectories involving confining water between SiO_2 slabs ($SiO_2/H_2O/SiO_2$) and between WS_2 sheets ($WS_2/H_2O/WS_2$). This extensive dataset was anticipated to effectively represent water interactions when interfaced with SiO_2 and WS_2, as well as when confined between these materials. Various phases of SiO_2, WS_2, and ice were included to provide data on optimal bond distances. Further refinement of the bond distances was accomplished by incorporating individual molecules into the training data, where bonds were either elongated or compressed to investigate the energy landscape. This ensures that the repulsive potential could accommodate larger repulsions resulting from atoms in close proximity. All training data was generated using DFT with CP2K, employing the PBE(D3) XC functional. The training data was then pruned, so that any data with forces greater than 35 eV/$\AA$ were removed, making training more efficient and removing any unfeasible configurations. The resulting bond distance training data can be seen in Appendix D, Figures D.1-D.2.

The GPrep optimisation was initially conducted with a small cutoff of 5 $\AA$ to determine the hyperparameters. The cutoff signifies the threshold beyond which training bond data is excluded. Within the training set of bond distance, individual start and end cutoffs were chosen for each atom-atom interaction based on the distribution of bond distances so that training time could be reduced. Optimal hyperparameters were identified by selecting a range of values and re-training the repulsion potentials until a minimal RMSE was achieved. Once the hyperparameters were optimised, the entire dataset was retrained using these values, and the potentials were subsequently reviewed. When all potentials accurately represented repulsive behaviour at small distances and exhibited no interaction at longer distances, the hyperparameters were accepted, and the cutoff was increased to $8\mathring{A}$ to train the final potential. The bond distance distributions for 8 $\mathring{A}$ cutoff are seen in Figures D.1-D.2, and the selected atom-atom cutoffs are shown in Table D.2. The identified optimal hyperparameters were 0.8, 1.5, and 0.02 for β, θ, and σ, respectively.

Validation data was generated using DFT with CP2K, employing the PBE(D3) XC functional. The dataset included 9 snapshots from an extended $SiO_2/H_2O/WS_2$ interface. This interface contained 738 atoms in a 10×3×1 supercell, which featured one layer of water. This was accomplished using the same AIMD process described in Chapter 5.

8.3 Results and Discussion

8.3.1 Confinement Potential Training

We begin by training the confinement parameters essential for modelling the $WS_2/H_2O/SiO_2$ interface. This process requires consideration of the interactions between O, H, Si, W, and S atoms, as outlined in section 8.2.1.1. An example of this consideration is the parameterisation of O-H interactions, which must encompass interactions both in liquid water and as part of a silanol group. For band structure calculations, only E_{BS} is required, and thus the E_{rep} term is excluded, leading to the repulsive potential being set to zero for the PSO optimisation.

The confinement parameters are trained using materials that effectively capture the interactions at the $WS_2/H_2O/SiO_2$ interface. I classify the training sets into WSOH and SiOH, reflecting the materials included in each set. There is limited interaction between SiO_2 and WS_2; thus, the Si-W or Si-S interactions do not necessitate a detailed description.

The SiOH training set contained: bulk α-C, α-C compressed by 0.01%,

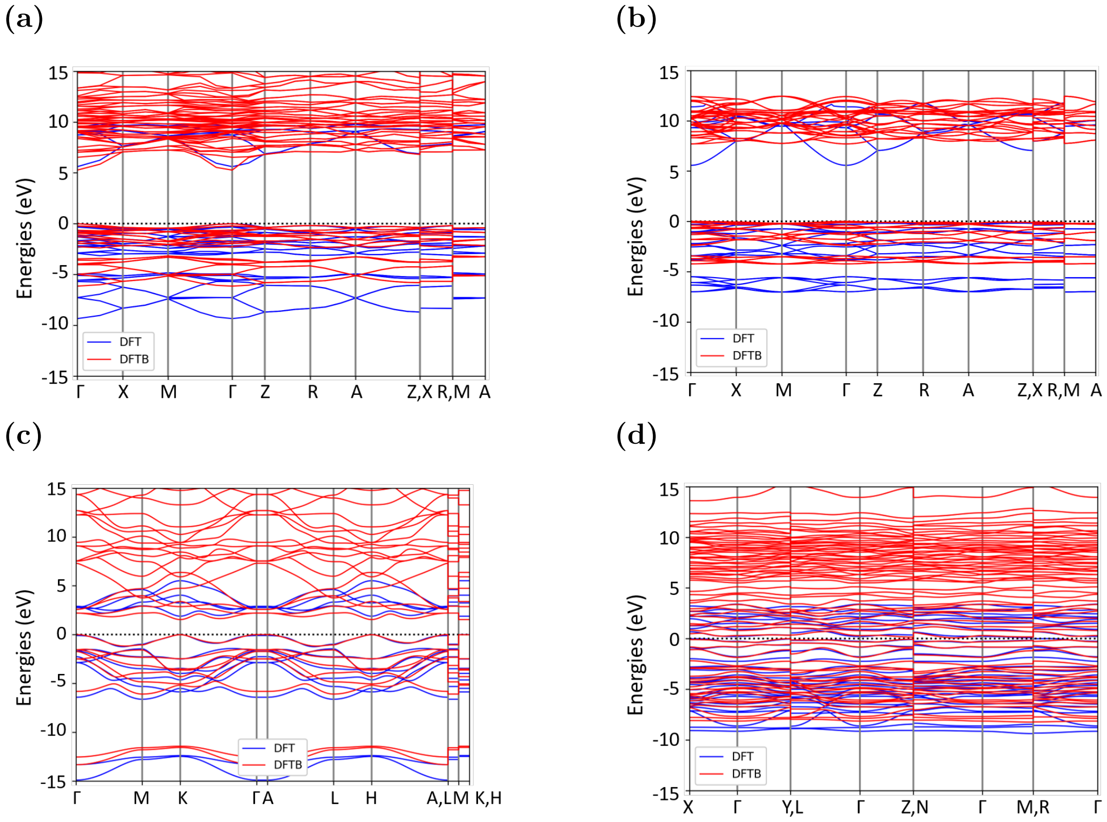

Figure 8.2 Fit of the training set from DFTB electronic parameterisation (red line) compared to PBE DFT band structure (blue line). **a-b)** is from our work with the SiOH training set, **a**) is the α-cristobalite phase of SiO_2 and **b**) is the ice VIII phase. **c-d**) is from the WSOH set where **c**) is 1H-WS_2 and **d**) is $WO_3{\cdot}H_2O$.

$(10\bar{1})$ α-C slab containing silanol groups, and ice XI and ice VIII phases of H_2O. The confinement potential from this training set describes both α-C and the ice VIII phase well (Figure 8.2a-8.2b). The α-C band structure is particularly well characterised, yielding accurate descriptions of the CB and VB. In contrast, the ice VIII phase demonstrates an accurate VB but presents a less satisfactory description of the CB dispersion.

The resulting skf files were then tested with a validation data set containing α-Q and the ice III phase of water, as shown in Figure 8.3. The α-Q showed that the VB has been accurately described by the PSO fitted confinement potential. However, the CB was much too high in energy, resulting in an unrealistic band gap of 16 eV (Figure 8.3a). However, similar parameterisation is seen for the Siband-1-1 parameter set, a commonly used parameterisation of DFTB for SiO_2 with silanol groups (Figure 8.3b). In fact, the band gap using the PSO confinement is slightly more accurate than the Siband-1-1 so the parameterisation may still be acceptable.

The ice III phase also experienced the same band gap overestimation (Figure 8.3c), but the CB dispersion further from the CBM aligns closely to that of the DFT CB. However, the VB of ice III is more accurately described by the Siband-1-1 parameters, although the band gap overestimation issue is also present (Figure 8.3d).

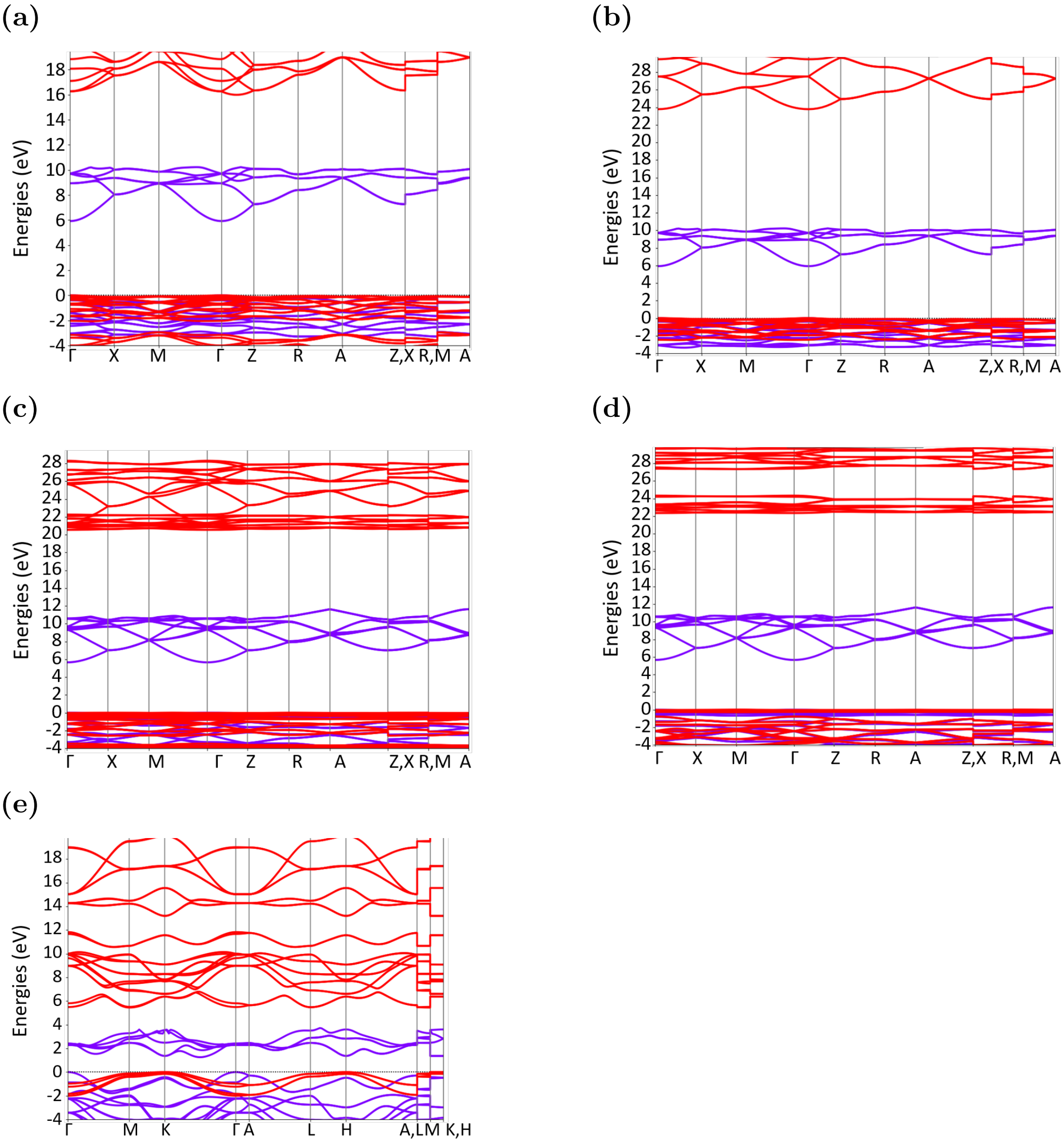

Figure 8.3 Validation of the DFTB electronic parameterisation (red line) against the PBE DFT band structure (purple line). **a,b)** Results for α-quartz SiO_2: **a)** derived from our work using the SiOH training set, and **b)** from the widely-used DFTB parameterisation Siband-1-1. **c,d** Band structure comparison for ice III: **c)** from the SiOH training set, and **d)** from Siband-1-1. **e**) Validation of the 2H-WS_2 phase from the WSOH training set.

The WSOH training set included the following materials: H_2SO_4, $WO_3{\cdot}H_2O$, 3T-WS_2, and 1H-WS_2. Figures 8.2c-8.2d demonstrate that the parameters effectively characterise the 1H-WS_2 and $WO_3{\cdot}H_2O$ materials, suggesting that the interactions between the monolayer WS_2 and H_2O are likely to be reliable.

However, validation tests using a 2H-WS_2 PBE band structure from QE revealed low fitting accuracy (Figure 8.3e). The band structure obtained from the PSO parameterisation of 2H-WS_2 is inadequately described, with the band gap overestimated by $\approx$3 eV, and the dispersion of the band structure is incorrect compared to DFT. This discrepancy is particularly significant as it does not show the transition to an indirect band gap with a bilayer of WS_2, with the Q point becoming the CBM. Consequently, it is not anticipated that the current electronic parameterisation is transferable. Nonetheless, due to time constraints and the satisfactory description of the monolayer, the parameters were retained for further GPrep training. For the O-H, O-O, and H-H interactions, we will utilise the skf files from the SiOH training set parameterisation, as it encompasses the water ice phases as well as description of SiO_2 with silanol groups present.

Overall, the description of band gaps and band structure has shown that the confinement potentials are currently not transferable to other materials not included in the training set. The difficulties encountered by both the WSOH and SiOH PSO-optimised skf in accurately replicating the validation sets highlight the necessity of expanding the training set and improving parameterisation accuracy. Alternatively, another approach could involve exploring different methods for optimising the confinement potential. Potential strategies may include modifying the function that describes the confinement potential, for example, by employing the Woodman-Sax potential, or by incorporating additional parameters for optimisation, such as the Hubbard parameter.

8.3.2 Repulsive Potential Fitting

The training process for the DFTB potential using GPrep is illustrated in Figure 8.1. The methodologies for PSO and hyperparameter fitting have been previously

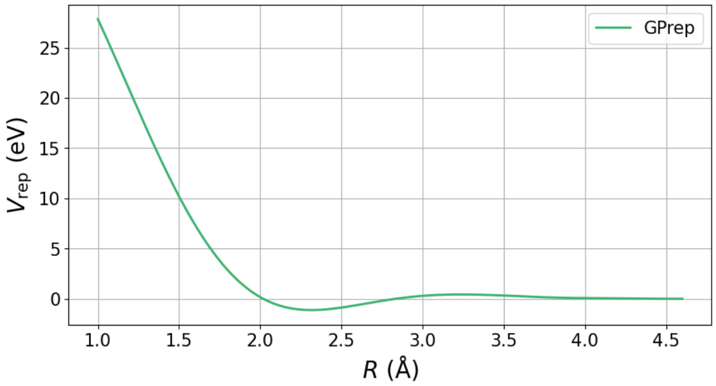

Figure 8.4 The functional form of the W-O repulsive potential calculated using GPrep.

outlined in Section 8.2.2. After hyperparameter training, the cutoff distance was increased from 5 $\AA$ to 8 $\AA$ and the GPrep potential was retrained.

The repulsive potential for each atom interaction, calculated through this process, is presented in Appendix D Figures D.3-D.4. The expected repulsion is evident at short distances for all atom-atom interactions. Moreover, the potential fitting reveals more nuanced interactions, as demonstrated by the W-O potential in Figure 8.4 which shows a more intricate fitting of the repulsive potential. A minimum is observed at 2.2 $\AA$, indicating that the repulsive potential includes previously unaccounted interactions between the two atoms, such as subtle vdW interactions. This enhancement is expected to enable the DFTB results to align more closely with those obtained from PBE(D3) DFT.

8.3.3 Validation

The fitted repulsive potentials successfully exhibited the expected repulsive behaviour for each atom-atom interaction. Following this, we validated the generated skfs against DFT data. For this validation, we utilised 9 extended one-layer $SiO_2/H_2O/WS_2$ AIMD snapshots, each consisting of 738 atoms. These snapshots were excluded from the original training set to ensure unbiased evaluation. Single-point energy DFTB calculations were performed on the validation data, and the forces obtained from DFT and DFTB were compared, as compiled in Figure 8.5.

The RMSE of the force comparison was 0.87 eV/$\AA$, demonstrating successful training and a strong correspondence between DFTB and DFT forces. This alignment is further supported by the validation set data, which adheres to a linear trend, as illustrated by the black line in Figure 8.5, indicating a robust correlation between the DFTB and DFT results.

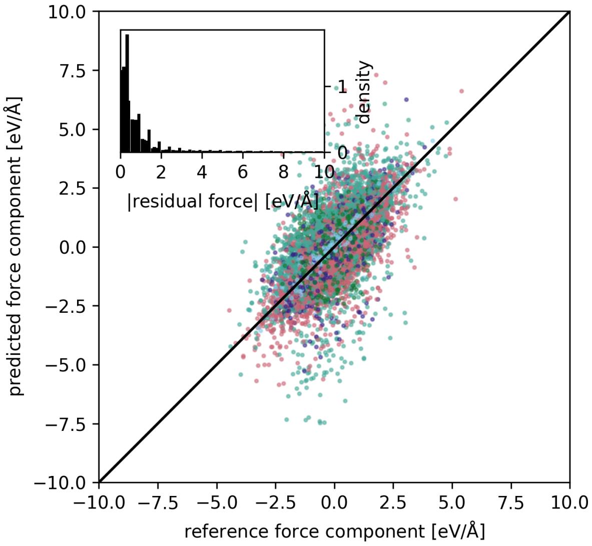

Figure 8.5 Forces acting on the atoms from snapshots of the extended one layer $WS_2/H_2O/SiO_2$ interface compared using DFTB (y axis) to that of DFT (x axis). The different atoms are specified by colour: green is S, dark blue is W, teal is Si, H is light blue, and O is pink.

Encouraged by the positive validation results, I assessed the usability of the ML-optimised DFTB parameters in dynamics simulations. Specifically, NVT AIMD simulations were performed at 300 K with a 0.5 fs time step, starting from a three-layer $WS_2/H_2O/SiO_2$ interface snapshot (Figure 8.6a). Over the course of the 34 fs simulation, excessive expansion of water was observed within the confined region, suggesting that the ML-trained parameters were insufficient for capturing the properties of confined water accurately (Figure 8.6b). However, the α-C slab and WS_2 maintained their correct phases as expected. These findings highlight the need for future ML training efforts to focus primarily on accurately describing water, to enable a thorough investigation of confined water behaviour in these systems.

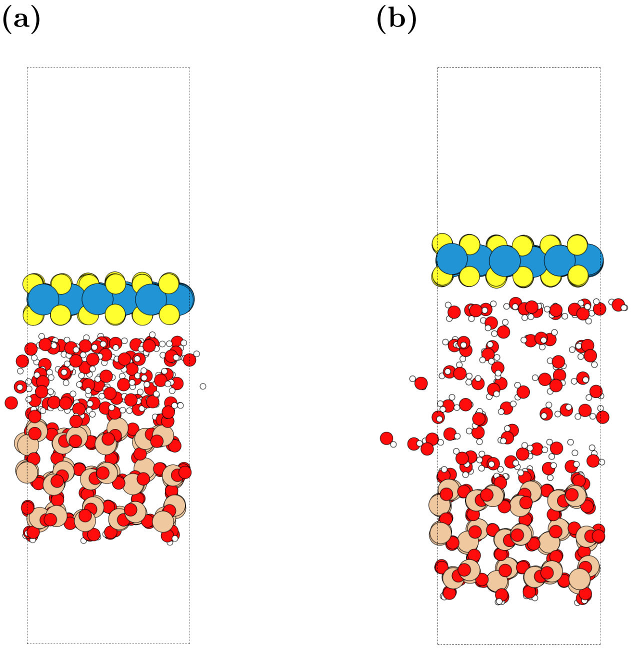

Figure 8.6 **a**) The initial snapshot used with the DFTB ML parameters, **b**) the interface after 35 femtoseconds of DFTB ML AIMD run time.

8.4 Conclusions

Although this initial attempt to utilise machine learning for the development of more accurate DFTB parameters did not yield precise results, it holds potential for improvement with additional time and data in the future. The primary challenge in this interface is the accurate description of water to prevent unrealistic evaporation or expansion rates. Furthermore, the band structure generated by PSO-trained confinement potentials requires further refinement. This can be achieved by either optimising the parameters with additional training data or modifying the approach by adjusting the confinement potential function, or incorporating further parameters. Unfortunately, due to time constraints, I was unable to explore the use of machine learning further. Future work resolving these issues could enhance our understanding of the interactions and dynamics at the confined water interface, which could ultimately lead to a more comprehensive elucidation of the oxidation process through DFTB AIMD calculations.

Chapter 9

Conclusions

The aim of this thesis was to investigate the impact of water on the SiO_2/WS_2 interface. I began by examining the oxygen vacancy defects within α-cristobalite SiO_2, as it serves as a good model for amorphous silica surface, and the defects present in it are not well characterised. The investigation of positively charged oxygen vacancies revealed that the dimer configuration which forms Si-Si bonds (E'_{di}) is the most stable in α-cristobalite. Furthermore, a positive oxygen vacancy stabilised by puckering to form a Si-O bond (E'_{puck}) was not stable in α-cristobalite, although it is the most stable configuration in the α-quartz phase. This disparity was attributed to the differences of crystal structures and the short-range environment of Si atoms in both phases. This research provided valuable insights into the properties of defects in crystalline SiO_2 and the reasons why some defect configurations develop favourably while others do not. Understanding the fundamental defect properties of α-cristobalite SiO_2 is significant; however, incorporating oxygen vacancies into the $SiO_2/H_2O/WS_2$ interface would enhance our understanding of the impact of defects at interfaces. While this study primarily focused on bulk SiO_2, it is important to note that surface defects play a more prominent role in charge trapping within interfacial systems. Therefore, further research should investigate surface defects, as they could greatly influence the interaction of materials at interfaces.

I subsequently focused on the $SiO_2/H_2O/WS_2$ interface. It was demonstrated that the confinement of water at this interface alters both the structure and dynamic behaviour of water in comparison to unconfined scenarios at the SiO_2/H_2O and WS_2/H_2O interfaces. The SiO_2 silanol groups significantly influence the structuring of water, both in confined and unconfined conditions. This effect was particularly notable in one-layer systems, where fewer water-water hydrogen bonds were observed in contrast to the increased number of silanol-water hydrogen bonds. This work provided the first insights into the behaviour of confined water at this interface; however, many questions remain unanswered. In particular, the timescale of the simulations limits the reliability of these results, and discrepancies between these findings and some CMD results indicate that further research is necessary to fully understand the behaviour of water at these interfaces.

I then examined the electronic properties at the confined water interface, revealing that, on average, water did not significantly impact the band offset between SiO_2 and WS_2. However, the work function of WS_2 shifted when confined water was present. It was found that increasing the number of water layers increased the average magnitude of the work function shift. Short-lived, localised in-gap states were detected between the two materials for some water configurations or with increased sensitivity introduced by a threshold value for determining band alignment, caused by fluctuations in the water configuration. These in-gap states could impact the hole conductivity in WS_2 layers. Nevertheless, there is potential for improvement in the analysis of band alignment, as the current practice of selecting threshold values has not been exhaustively investigated, which limits its transferability between different systems. Overall, this work serves as a promising first step in the initial exploration of a complex interface.

To further investigate the interaction of WS_2 with H_2O, we introduce defects to WS_2. The size of the defect influences the interaction between water and the defect site, as larger defects allow for greater interaction between water and the exposed atoms with dangling bonds. Exposure to both tungsten and sulphur dangling bonds resulted in the largest adsorption energies due to W-O and S-H interactions. These interactions can promote the spontaneous dissociation of water molecules. This was further investigated at the edge of WS_2. At the W-ZZ edge, it was found that water would not spontaneously dissociate. However, when O_2 was introduced, protons from water could migrate between molecules, facilitating the dissociation of H_2O. When an armchair edge was introduced, spontaneous water dissociation was observed if enough water molecules were present in configurations that enabled S-H interactions. This research has enhanced our understanding of the role of H_2O in the oxidation of WS_2. However, this study is somewhat limited as it relies solely on thermodynamic data and does not provide reaction barriers of reactions that do not occur spontaneously. Therefore, understanding the extent to which other defects play a role in oxidation remains challenging. Furthermore, the static nature of these calculations means that only a small sample of water configurations has been assessed. There may be additional potential mechanisms that have not been captured in this study. Overall, this research provides various defect-water interactions that have not been previously explored, and the proton hopping mechanism for water oxidation has not been reported in the literature, making this a valuable first step in understanding the mechanisms behind the oxidation of TMDs.

However, a limitation of this thesis is the timescale of the simulations performed and the size of periodic cells modelling interfaces. Consequently, the exploration of ML trained DFTB repulsive potentials and confinement parameters was addressed in Chapter 8. While the results presented are still quite rudimentary and require further training, they offer a framework for future exploration of the $WS_2/H_2O/SiO_2$ interface. Moreover, the oxidation study could be utilised as a training set to further refine the potentials, facilitating an examination of the oxidation process over a longer timescale with a greater number of molecules involved.

In conclusion, this Thesis has provided valuable insights into a previously unexamined interface, which holds significant implications for both academia and industry. Future work to build upon this initial research should include the introduction of SiO_2 surface defects, the exploration of the oxidation of TMDs in the presence of confined water, and enhancement of the timescale and size of the modelled interface. To improve the timescale and size of the model, I suggest that incorporating machine learning could be a crucial step and have provided initial results for the use of ML trained DFTB.

Bibliography

[1] B. Radisavljevic, A. Radenovic, J. Brivio, V. Giacometti, and A. Kis, "Single-layer MoS_2 transistors," *Nature Nanotechnology*, vol. 6, pp. 147–150, 2011.

[2] L. Giacomazzi, A. Martin-Samos, L.and Boukenter, Y. Ouerdane, S. Girard, and N. Richard, "EPR parameters of E' centers in v-SiO_2 from first-principles calculations," *Physical Review B*, vol. 90, no. 15, p. 014108, 2014.

[3] C. Lan, C. Li, J. C. Ho, and Y. Liu, "2d WS_2: From Vapor Phase Synthesis to Device Applications," *Advanced Electronic Materials*, vol. 7, p. 2000688, 2021.

[4] D. Kieczka, T. Durrant, K. Milton, K. E. J. Goh, M. Bosman, and A. Shluger, "Defects in WS_2 monolayer calculated with a nonlocal functional: any difference from GGA?," *Electronic Structure*, vol. 5, no. 2, p. 024001, 2023.

[5] F. A. Rasmussen and K. S. Thygesen, "Computational 2d materials database: electronic structure of transition-metal dichalcogenides and oxides," *The Journal of Physical Chemistry C*, vol. 119, no. 23, pp. 13169–13183, 2015.

[6] H. M. Hill, A. F. Rigosi, K. T. Rim, G. W. Flynn, and T. F. Heinz, "Band Alignment in MoS_2/WS_2 Transition Metal Dichalcogenide Heterostructures Probed by Scanning Tunneling Microscopy and Spectroscopy," *Nano Letters*, vol. 16, no. 8, pp. 4831–4837, 2016. PMID: 27298270.

[7] B. Pielić, D. Novko, I. S. Rakić, J. Cai, M. Petrović, R. Ohmann, N. Vujiˇ cić, M. Basletić, C. Busse, and M. Kralj, "Electronic Structure of

Quasi-Freestanding WS_2/MoS_2 Heterostructures," *ACS Applied Materials & Interfaces*, vol. 13, no. 42, pp. 50552–50563, 2021. PMID: 34661383.

[8] H.-G. Kim and H. J. Choi, "Thickness dependence of work function, ionization energy, and electron affinity of Mo and W dichalcogenides from DFT and GW calculations," *Physical Review B*, vol. 103, p. 085404, Feb 2021.

[9] J. Ping, Z. Fan, M. Sindoro, Y. Ying, and H. Zhang, "Recent Advances in Sensing Applications of Two-Dimensional Transition Metal Dichalcogenide Nanosheets and Their Composites," *Advanced Functional Materials*, vol. 27, no. 19, p. 1605817, 2017.

[10] A. Mirzaei, M. Alizadeh, H. R. Ansari, M. Moayedi, Z. Kordrostami, H. Safaeian, M. H. Lee, T. Kim, J. Kim, H. W. Kim, and S. S. Kim, "Resistive gas sensors for the detection of NH_3 gas based on 2d WS_2, WSe_2, MoS_2, and $MoSe_2$: a review," *Nanotechnology*, vol. 35, p. 332002, may 2024.

[11] Q. Deng, Z. Li, R. Huang, P. Li, H. Gomaa, S. Wu, C. An, and N. Hu, "Research progress of transition-metal dichalcogenides for the hydrogen evolution reaction," *Journal Material Chemistry A*, vol. 11, pp. 24434–24453, 2023.

[12] D. Jiang, Z. Liu, Z. Xiao, Z. Qian, Y. Sun, Z. Zeng, and R. Wang, "Flexible electronics based on 2d transition metal dichalcogenides," *Journal Material Chemistry A*, vol. 10, pp. 89–121, 2022.

[13] M. Chhowalla, D. Jena, and H. Zhang, "Two-dimensional semiconductors for transistors," *Nature Review Materials*, vol. 1, no. 1, p. 16052, 2016.

[14] K. O'Brien, C. Naylor, C. Dorow, and et al., "Process integration and future outlook of 2d transistors," *Nature Communications*, vol. 14, p. 6400, 2023.

[15] J. Kim, T. Ko, E. Okogbue, and et al., "Centimeter-scale Green Integration of Layer-by-Layer 2d TMD vdw Heterostructures on Arbitrary Substrates by Water-Assisted Layer Transfer," *Scientific Reports*, vol. 9, p. 1641, 2019.

[16] G. Xue, B. Qin, C. Ma, P. Yin, C. Liu, and K. Liu, "Large-Area Epitaxial Growth of Transition Metal Dichalcogenides," *Chemical Reviews*, vol. 0, pp. 9785–9865, 2024.

[17] S. Palleschi, G. D'Olimpio, P. Benassi, M. Nardone, R. Alfonsetti, G. Moccia, M. Renzelli, O. A. Cacioppo, A. Hichri, S. Jaziri, A. Politano, and L. Ottaviano, "On the role of nano-confined water at the 2D/SiO_2 interface in layer number engineering of exfoliated MoS_2 via thermal annealing," *2D Materials*, vol. 7, 2020.

[18] D. J. Late, B. Liu, H. S. S. R. Matte, V. P. Dravid, and C. N. R. Rao, "Hysteresis in Single-Layer MoS_2 Field Effect Transistors," *ACS Nano*, vol. 6, no. 6, pp. 5635–5641, 2012. PMID: 22577885.

[19] F. S. Emami, V. Puddu, R. J. Berry, V. Varshney, S. V. Patwardhan, C. C. Perry, and H. Heinz, "Force Field and a Surface Model Database for Silica to Simulate Interfacial Properties in Atomic Resolution," *Chemistry of Materials*, vol. 26, pp. 2647–2658, 2014.

[20] L. Lin, P. Sherrell, Y. Liu, W. Lei, S. Zhang, H. Zhang, G. G. Wallace, and J. Chen, "Engineered 2d Transition Metal Dichalcogenides—A Vision of Viable Hydrogen Evolution Reaction Catalysis," *Advanced Energy Materials*, vol. 10, no. 16, p. 1903870, 2020.

[21] R. C. Longo, R. Addou, K. Santosh, J.-Y. Noh, C. M. Smyth, D. Barrera, C. Zhang, J. W. Hsu, R. M. Wallace, and K. Cho, "Intrinsic air stability mechanisms of two-dimensional transition metal dichalcogenide surfaces: basal versus edge oxidation," *2D Materials*, vol. 4, no. 2, p. 025050, 2017.

[22] G. D. Wilk, R. M. Wallace, and J. M. Anthony, "High-K gate dielectrics: Current status and materials properties considerations," *Journal of Applied Physics*, vol. 89, pp. 5243–5275, 05 2001.

[23] C. Zhao, X. Wang, and W. Wang, "High-κ dielectric and metal gate," in *CMOS Past, Present and Future*, pp. 69–103, Elsevier Ltd., 2018.

[24] A. Hiraiwa, T. Saito, A. Daicho, and H. Kawarada, "Accuracy assessment of sheet-charge approximation for Fowler-Nordheim tunneling into charged insulators," *Journal of Applied Physics*, vol. 114, p. 134501, 10 2013.

[25] L. Skuja, "Optically active oxygen-deficiency-related centers in amorphous silicon dioxide," *Journal of Non-Crystalline Solids*, vol. 239, no. 1, pp. 16–48, 1998.

[26] D. L. Griscom, "Trapped-electron centers in pure and doped glassy silica: A review and synthesis," vol. 357, pp. 1945–1962, 4 2011.

[27] P. E. Blöchl, "First-principles calculations of defects in oxygen-deficient silica exposed to hydrogen," *Physical Review B*, vol. 62, no. 10, pp. 6158–6179, 2000.

[28] P. V. Sushko, S. Mukhopadhyay, A. S. Mysovsky, V. B. Sulimov, A. Taga, and A. Shluger, "Structure and properties of defects in amorphous silica: New insights from embedded cluster calculations," *Journal of Physics Condensed Matter*, vol. 17, no. 21, p. S2115, 2005.

[29] H. Imai, K. Arai, H. Hosono, and Y. Abe, "Two types of oxygen-deficient centers in synthetic silica glass," *Physical Review B*, vol. 38, pp. 12773–12775, 1988.

[30] R. A. Weeks, "Paramagnetic resonance of lattice defects in irradiated quartz," *Journal of Applied Physics*, vol. 27, no. 11, pp. 1376–1381, 1956.

[31] R. A. Weeks, R. H. Magruder, and A. Stesmans, "Review of some experiments in the 50 year saga of the E$'$ center and suggestions for future research," *Journal of Non-Crystalline Solids*, vol. 354, pp. 208–216, 1 2008.

[32] R. I. Mashkovtsev and Y. Pan, "Nature of paramagnetic defects in alpha-quartz: Progresses in the first decade of the 21st century," in *New Developments in Quartz Research: Varieties, Crystal Chemistry and Uses in Technology*, pp. 66–104, 2013.

[33] R. I. Mashkovtsev, A. I. Nepomnyashchikh, A. P. Zhaboedov, and A. S. Paklin, “EPR study of the E' defects in optical glasses and cristobalite,” *Epl*, vol. 133, no. 1, p. 14003, 2021.

[34] F. J. Feigl, W. B. Fowler, and K. L. Yip, “Oxygen Vacancy Model for the E'-center in SiO_2,” *Solid State Communications*, vol. 14, no. 3, pp. 225–229, 1974.

[35] J. K. Rudra and W. B. Fowler, “Oxygen vacancy and the ${E'}_1$ center in crystalline SiO_2,” *Physical Review B*, vol. 35, no. 15, pp. 8223–8230, 1987.

[36] S. Mukhopadhyay, P. V. Sushko, A. M. Stoneham, and A. L. Shluger, “Modeling of the structure and properties of oxygen vacancies in amorphous silica,” *Physical Review B*, vol. 70, no. 19, p. 195203, 2004.

[37] G. Buscarino, S. Agnello, F. Gelardi, and A. Parlato, “Electron paramagnetic resonance investigation on the hyperfine structure of the ${E'}_\delta$ center in amorphous silicon dioxide,” *ournal of Non-Crystaliine Solids*, vol. 353, pp. 518–521, 2007.

[38] M. Jivanescu, A. Stesmans, and V. V. Afanas’ev, “Multifrequency ESR analysis of the E'_δ defect in a-sio_2,” *Physical Review B*, vol. 83, no. 9, p. 094118, 2011.

[39] W. B. Fowler and A. H. Edwards, “Theory of defects and defect processes in silicon dioxide,” *J. Non-Cryst. Sol.*, vol. 222, pp. 33–41, 1997.

[40] A. S. Mysovsky, P. V. Sushko, S. Mukhopadhyay, A. H. Edwards, and A. L. Shluger, “Calibration of embedded-cluster method for defect studies in amorphous silica,” *Physical Review B*, vol. 69, no. 8, p. 085202, 2004.

[41] C. Lan, C. Li, J. C. Ho, and Y. Liu, “2D WS_2: From Vapor Phase Synthesis to Device Applications,” *Advanced Electronic Materials*, vol. 7, pp. 1–36, 7 2021.

[42] D. Voiry, A. Goswami, R. Kappera, C. D. C. C. E. Silva, D. Kaplan, T. Fujita, M. Chen, T. Asefa, and M. Chhowalla, “Covalent functionalization

of monolayered transition metal dichalcogenides by phase engineering," *Nature Chemistry*, vol. 7, pp. 45–49, 1 2015.

[43] Q. H. Wang, K. Kalantar-Zadeh, A. Kis, J. N. Coleman, and M. S. Strano, "Electronics and optoelectronics of two-dimensional transition metal dichalcogenides," *Nature nanotechnology*, vol. 7, no. 11, pp. 699–712, 2012.

[44] A. F. Rigosi, H. M. Hill, K. T. Rim, G. W. Flynn, and T. F. Heinz, "Electronic band gaps and exciton binding energies in monolayer $Mo_xW_{1-x}S_2$ transition metal dichalcogenide alloys probed by scanning tunneling and optical spectroscopy," *Physical Review B*, vol. 94, 8 2016.

[45] H. G. Kim and H. J. Choi, "Thickness dependence of work function, ionization energy, and electron affinity of Mo and W dichalcogenides from DFT and GW calculations," *Physical Review B*, vol. 103, 2 2021.

[46] M. Samadi, N. Sarikhani, M. Zirak, H. Zhang, H.-L. Zhang, and A. Z. Moshfegh, "Group 6 transition metal dichalcogenide nanomaterials: synthesis, applications and future perspectives," *Nanoscale Horizons*, vol. 3, no. 2, pp. 90–204, 2018.

[47] H. M. Hill, A. F. Rigosi, K. T. Rim, G. W. Flynn, and T. F. Heinz, "Band alignment in MoS_2/WS_2 transition metal dichalcogenide heterostructures probed by scanning tunneling microscopy and spectroscopy," *Nano letters*, vol. 16, no. 8, pp. 4831–4837, 2016.

[48] K. T. Munson, R. Torsi, S. Mathela, M. A. Feidler, Y.-C. Lin, J. A. Robinson, and J. B. Asbury, "Influence of Substrate-Induced Charge Doping on Defect-Related Excitonic Emission in Monolayer MoS_2," *The Journal of Physical Chemistry Letters*, vol. 15, no. 31, pp. 7850–7856, 2024. PMID: 39052863.

[49] S. Wang, A. Robertson, and J. H. Warner, "Atomic structure of defects and dopants in 2d layered transition metal dichalcogenides," *Chem. Soc. Rev.*, vol. 47, pp. 6764–6794, 2018.

[50] C. S. Lau, S. Das, I. A. Verzhbitskiy, D. Huang, Y. Zhang, T. Talha-Dean, W. Fu, D. Venkatakrishnarao, and K. E. Johnson Goh, "Dielectrics

for Two-Dimensional Transition-Metal Dichalcogenide Applications," *ACS Nano*, vol. 17, no. 11, pp. 9870–9905, 2023. PMID: 37257134.

[51] W. Zhu, T. Low, H. Wang, P. Ye, and X. Duan, "Nanoscale electronic devices based on transition metal dichalcogenides," *2D Materials*, vol. 6, p. 032004, jun 2019.

[52] C. Lan, C. Li, Y. Yin, and Y. Liu, "Large-area synthesis of monolayer WS_2 and its ambient-sensitive photo-detecting performance," *Nanoscale*, vol. 7, no. 14, pp. 5974–5980, 2015.

[53] S. Wang, Y. Rong, Y. Fan, M. Pacios, H. Bhaskaran, K. He, and J. H. Warner, "Shape evolution of monolayer MoS_2 crystals grown by chemical vapor deposition," *Chemistry of Materials*, vol. 26, pp. 6371–6379, 11 2014.

[54] Y. Shi, H. Li, and L.-J. Li, "Recent advances in controlled synthesis of two-dimensional transition metal dichalcogenides via vapour deposition techniques," *Chem. Soc. Rev.*, vol. 44, pp. 2744–2756, 2015.

[55] K. Chen, R. Ghosh, X. Meng, A. Roy, J.-S. Kim, F. He, S. C. Mason, X. Xu, J.-F. Lin, D. Akinwande, *et al.*, "Experimental evidence of exciton capture by mid-gap defects in CVD grown monolayer $MoSe_2$," *npj 2D Materials and Applications*, vol. 1, no. 1, p. 15, 2017.

[56] Y. Shi, W. Zhou, A.-Y. Lu, W. Fang, Y.-H. Lee, A. L. Hsu, S. M. Kim, K. K. Kim, H. Y. Yang, L.-J. Li, *et al.*, "van der Waals epitaxy of MoS_2 layers using graphene as growth templates," *Nano letters*, vol. 12, no. 6, pp. 2784–2791, 2012.

[57] Q. Ji, Y. Zhang, T. Gao, Y. Zhang, D. Ma, M. Liu, Y. Chen, X. Qiao, P.-H. Tan, M. Kan, *et al.*, "Epitaxial monolayer MoS_2 on mica with novel photoluminescence," *Nano letters*, vol. 13, no. 8, pp. 3870–3877, 2013.

[58] D. Dumcenco, D. Ovchinnikov, K. Marinov, P. Lazic, M. Gibertini, N. Marzari, O. L. Sanchez, Y.-C. Kung, D. Krasnozhon, M.-W. Chen, *et al.*, "Large-area epitaxial monolayer MoS_2," *ACS nano*, vol. 9, no. 4, pp. 4611–4620, 2015.

[59] L. Su, Y. Yu, L. Cao, and Y. Zhang, "Effects of substrate type and material-substrate bonding on high-temperature behavior of monolayer WS_2," *Nano Research*, vol. 8, pp. 2686–2697, 2015.

[60] Y. Zhang, Y. Zhang, Q. Ji, J. Ju, H. Yuan, J. Shi, T. Gao, D. Ma, M. Liu, Y. Chen, *et al.*, "Controlled growth of high-quality monolayer WS_2 layers on sapphire and imaging its grain boundary," *ACS nano*, vol. 7, no. 10, pp. 8963–8971, 2013.

[61] J. Serron, A. Minj, V. Spampinato, A. Franquet, Y. Rybalchenko, M.-E. Boulon, S. Brems, H. M. Silva, Y. Shi, B. Groven, R. Villarreal, T. Conard, P. van der Heide, and T. Hantschel, "Conductivity Enhancement in Transition Metal Dichalcogenides: A Complex Water Intercalation and Desorption Mechanism," *ACS Applied Materials & Interfaces*, vol. 15, no. 21, pp. 26175–26189, 2023. PMID: 37194926.

[62] Y. Huang, E. Sutter, N. N. Shi, J. Zheng, T. Yang, D. Englund, H.-J. Gao, and P. Sutter, "Reliable exfoliation of large-area high-quality flakes of graphene and other two-dimensional materials," *ACS nano*, vol. 9, no. 11, pp. 10612–10620, 2015.

[63] X. Wang, K. Kang, K. Godin, S. Fu, S. Chen, and E.-H. Yang, "Effects of solvents and polymer on photoluminescence of transferred WS_2 monolayers," *Journal of Vacuum Science I& Technology B*, vol. 37, no. 5, 2019.

[64] D. Ma, J. Shi, Q. Ji, K. Chen, J. Yin, Y. Lin, Y. Zhang, M. Liu, Q. Feng, X. Song, X. Guo, J. Zhang, Y. Zhang, and Z. Liu, "A universal etching-free transfer of MoS_2 films for applications in photodetectors," *Nano Research*, vol. 8, pp. 3662–3672, 10 2015.

[65] Z. Q. Xu, Y. Zhang, S. Lin, C. Zheng, Y. L. Zhong, X. Xia, Z. Li, P. J. Sophia, M. S. Fuhrer, Y. B. Cheng, and Q. Bao, "Synthesis and Transfer of Large-Area Monolayer WS_2 Crystals: Moving Toward the Recyclable Use of Sapphire Substrates," *ACS Nano*, vol. 9, pp. 6178–6187, 6 2015.

[66] H. Yu, M. Liao, W. Zhao, G. Liu, X. J. Zhou, Z. Wei, X. Xu, K. Liu, Z. Hu, K. Deng, S. Zhou, J. A. Shi, L. Gu, C. Shen, T. Zhang, L. Du, L. Xie, J. Zhu,

W. Chen, R. Yang, D. Shi, and G. Zhang, "Wafer-Scale Growth and Transfer of Highly-Oriented Monolayer MoS_2 Continuous Films," *ACS Nano*, vol. 11, pp. 12001–12007, 12 2017.

[67] F. Zhang, C. Erb, L. Runkle, X. Zhang, and N. Alem, "Etchant-free transfer of 2D nanostructures," *Nanotechnology*, vol. 29, 1 2018.

[68] P. Bampoulis, K. Sotthewes, E. Dollekamp, and B. Poelsema, "Water confined in two-dimensions: Fundamentals and applications," *Surface Science Reports*, vol. 73, pp. 233–264, 2018.

[69] H. R. Corti, G. A. Appignanesi, M. C. Barbosa, J. R. Bordin, C. Calero, G. Camisasca, M. D. Elola, G. Franzese, P. Gallo, and A. Hassanali, "Structure and dynamics of nanoconfined water and aqueous solutions," *The European Physical Journal E*, vol. 44, p. 136, 2021.

[70] J. Pető, T. Ollár, P. Vancsó, Z. I. Popov, G. Z. Magda, G. Dobrik, C. Hwang, P. B. Sorokin, and L. Tapasztó, "Spontaneous doping of the basal plane of MoS_2 single layers through oxygen substitution under ambient conditions," *Nature chemistry*, vol. 10, no. 12, pp. 1246–1251, 2018.

[71] M. Chhowalla, D. Jena, and H. Zhang, "Two-dimensional semiconductors for transistors," *Nature Reviews Materials*, vol. 1, no. 11, pp. 1–15, 2016.

[72] H. Yoo, K. Heo, M. H. R. Ansari, and S. Cho, "Recent Advances in Electrical Doping of 2d Semiconductor Materials: Methods, Analyses, and Applications," *Nanomaterials*, vol. 11, no. 4, 2021.

[73] J. C. Kotsakidis, Q. Zhang, A. L. V. D. Parga, M. Currie, K. Helmerson, D. K. Gaskill, and M. S. Fuhrer, "Oxidation of Monolayer WS_2 in Ambient Is a Photoinduced Process," *Nano Letters*, vol. 19, pp. 5205–5215, 8 2019.

[74] M. Yamamoto, S. Dutta, S. Aikawa, S. Nakaharai, K. Wakabayashi, M. S. Fuhrer, K. Ueno, and K. Tsukagoshi, "Self-Limiting Layer-by-Layer Oxidation of Atomically Thin WSe_2," *Nano Letters*, vol. 15, no. 3, pp. 2067–2073, 2015. PMID: 25646637.

[75] A. Nagy, "Density Functional Theory and Application to Atoms and Molecules," *Physics Reports*, vol. 298, no. 1, pp. 1–79, 1998.

[76] P. Geerlings, F. De Proft, and W. Langenaeker, "Conceptual Density Functional Theory," *Chemical Reviews*, vol. 103, no. 5, pp. 1793–1874, 2003. PMID: 12744694.

[77] K. Burke and L. O. Wagner, "DFT in a nutshell," *International Journal of Quantum Chemistry*, vol. 113, no. 2, pp. 96–101, 2013.

[78] K. Capelle and V. L. Campo, "Density functionals and model Hamiltonians: Pillars of many-particle physics," *Physics Reports*, vol. 528, no. 3, pp. 91–159, 2013. Density functionals and model Hamiltonians: Pillars of many-particle physics.

[79] M. Guidon, J. Hutter, and J. VandeVondele, "Robust periodic Hartree-Fock exchange for large-scale simulations using Gaussian basis sets," *Journal of Chemical Theory and Computation*, vol. 5, no. 11, pp. 3010–3021, 2009.

[80] J. Vandevondele, M. Krack, F. Mohamed, M. Parrinello, T. Chassaing, and J. Hutter, "Quickstep: Fast and accurate density functional calculations using a mixed Gaussian and plane waves approach," *Computer Physics Communications*, vol. 167, no. 2, pp. 103–128, 2005.

[81] S. Goedecker, M. Teter, and J. Hutter, "Separable dual-space Gaussian pseudopotentials," *Physical Review B*, vol. 54, no. 3, pp. 1703–1710, 1996.

[82] H. J. Monkhorst and J. D. Pack, "Special points for Brillonin-zone integrations," *Physical Review B*, vol. 13, no. 12, pp. 5188–5192, 1976.

[83] C. Ribaldone and S. Casassa, "Born–Oppenheimer Molecular Dynamics with a Linear Combination of Atomic Orbitals and Hybrid Functionals for Condensed Matter Simulations Made Possible. Theory and Performance for the Microcanonical and Canonical Ensembles," *Journal of Chemical Theory and Computation*, vol. 20, no. 9, pp. 3954–3975, 2024. PMID: 38648566.

[84] R. Iftimie, P. Minary, and M. E. Tuckerman, “Ab initio molecular dynamics: Concepts, recent developments, and future trends,” *Proceedings of the National Academy of Sciences*, vol. 102, no. 19, pp. 6654–6659, 2005.

[85] E. Runge and E. K. U. Gross, “Density-Functional Theory for Time-Dependent Systems,” *Phys. Rev. Lett.*, vol. 52, pp. 997–1000, Mar 1984.

[86] K. Burke, J. Werschnik, and E. K. U. Gross, “Time-dependent density functional theory: Past, present, and future,” *The Journal of Chemical Physics*, vol. 123, p. 062206, 08 2005.

[87] M. Iannuzzi, T. Chassaing, T. Wallman, and J. Hutter, “Ground and excited state density functional calculations with the Gaussian and augmented-plane-wave method,” *Chimia*, vol. 59, no. 7-8, pp. 499–499, 2005.

[88] G. Henkelman, B. P. Uberuaga, and H. Jónsson, “Climbing image nudged elastic band method for finding saddle points and minimum energy paths,” *Journal of Chemical Physics*, vol. 113, pp. 9901–9904, 2000.

[89] T. R. Shan, B. D. Devine, S. R. Phillpot, and S. B. Sinnott, “Molecular dynamics study of the adhesion of Cu/SiO_2 interfaces using a variable-charge interatomic potential,” *Physical Review B*, vol. 83, p. 115327, 2011.

[90] C. Tang and L. Cai, “The effect of surface heterogeneity between α-quartz and α-cristobalite on adsorption behaviors toward Cu^{2+} solution,” *Colloids and Surfaces A: Physicochemical and Engineering Aspects*, vol. 609, no. October 2020, p. 125651, 2021.

[91] K. Nagao, B. Neaton, and W. Ashcroft, “First-principles study of adhesion at Cu/SiO_2 interfaces,” *Physical Review B*, vol. 68, no. 12, p. 125403, 2003.

[92] G. Pacchioni, G. Ierano, and A. M. Márquez, “Optical absorption and nonradiative decay mechanism of E$'$ center in silica,” *Physical Review Letters*, vol. 81, no. 2, pp. 377–380, 1998.

[93] M. Boero, A. Pasquarello, J. Sarnthein, and R. Car, “Structure and Hyperfine Parameters of E_1' Centers in α-quartz and in Vitreous SiO_2,” *Physical Review Lett.*, vol. 78, pp. 887–890, Feb 1997.

[94] Z.-Y. Lu, C. J. Nicklaw, D. Fleetwood, R. D. Schrimpf, and S. Pantelides, “Structure, Properties, and Dynamics of Oxygen Vacancies in Amorphous SiO_2,” *Physical Review Letters*, vol. 89, no. 28, p. 285505, 2002.

[95] D. J. Chadi, “Negative-U property of the oxygen vacancy defect in SiO_2 and its implication for the E′ center in α-quartz,” *Applied Physics Letters*, vol. 83, no. 3, pp. 437–439, 2003.

[96] P. V. Sushko, S. Mukhopadhyay, A. M. Stoneham, and A. L. Shluger, “Oxygen vacancies in amorphous silica: Structure and distribution of properties,” *Microelectronic Engineering*, vol. 80, pp. 292–295, 2005.

[97] A. Kimmel, P. Sushko, A. Shluger, and G. Bersuker, “Positive and Negative Oxygen Vacancies in Amorphous Silica,” *ECS Transactions*, vol. 19, pp. 3–17, 2009.

[98] M. S. Munde, D. Z. Gao, and A. L. Shluger, “Diffusion and aggregation of oxygen vacancies in amorphous silica,” *Journal of Physics: Condensed Matter*, vol. 29, no. 24, p. 245701, 2017.

[99] M. V. Ganduglia-Pirovano, A. Hofmann, and J. Sauer, “Oxygen vacancies in transition metal and rare earth oxides: Current state of understanding and remaining challenges,” *Surface Science Reports*, vol. 62, no. 6, pp. 219–270, 2007.

[100] M. Arrigoni and G. K. H. Madsen, “Evolutionary computing and machine learning for discovering of low-energy defect configurations,” *npj Computational Materials*, vol. 7, p. 71, Feb 2021.

[101] D. Milardovich, M. Jech, D. Waldhoer, A.-M. B. El-Sayed, and T. Grasser, “Machine Learning Prediction of Defect Structures in Amorphous Silicon Dioxide,” *IEEE 51st European Solid-State Device Research Conference (ESSDER2021)*, pp. 239–242, Feb 2021.

[102] Z. Qiao, Q. Liu, S. Zhang, and Y. Wu, “The mineralogical characteristics between opaline silica in bentonite and α-cristobalite,” *Solid State Sciences*, vol. 96, p. 105948, 10 2019.

[103] M. Önal, S. Kahraman, and Y. Sarikaya, "Differentiation of α-cristobalite from opals in bentonites from Turkey," *Applied Clay Science*, vol. 35, pp. 25–30, 1 2007.

[104] M. Kayama, H. Nagaoka, and T. Niihara, "Lunar and martian silica," *Minerals*, vol. 8, no. 7, p. 8070267, 2018.

[105] A. J. Brearley and R. H. Jones, *Chondritic meteorites*, vol. 36 of *Reviews in Mineralogy*, pp. 3.1–3.398. 1998.

[106] C. I. Schipper, W. D. Rickard, D. W. Reddy, Steven M.and Saxey, J. M. Castro, D. Fougerouse, Z. Quadir, C. Conway, D. J. Prior, and K. Lilly, "Volcanic SiO_2-cristobalite: A natural product of chemical vapor deposition," *American Mineralogist*, vol. 105, no. 3, pp. 510–524, 2020.

[107] D. K. Smith, "Opal, cristobalite, and tridymite: Noncrystallinity versus crystallinity, nomenclature of the silica minerals and bibliography," *Power Diffraction*, vol. 13, no. 1, pp. 2–19, 1998.

[108] V. Correcher, J. Garcia-Guinea, M. A. Bustillo, and R. Garcia, "Study of the thermoluminescence emission of a natural α-cristobalite," *Radiation Effects and Defects in Solids*, vol. 164, no. 1, pp. 59–67, 2009.

[109] S. Dağlar, N. D. Kahya, G. Ustunisik, and M. Onal, "Thermal Crystallization Kinetics of an Opal-like Biogenic Silica," *silicon*, vol. 14, p. 7211–7217, 2022.

[110] P. Dera, J. D. Lazarz, V. B. Prakapenka, M. Barkley, and R. T. Downs, "New insights into the high-pressure polymorphism of SiO_2 cristobalite," *Physics and Chemistry of Minerals*, vol. 38, no. 7, pp. 517–529, 2011.

[111] M. A. Salvadó, P. Pertierra, A. Morales-García, J. M. Menéndez, and J. M. Recio, "Understanding chemical changes across the α-cristobalite to stishovite transition path in silica," *Journal of Physical Chemistry C*, vol. 117, no. 17, pp. 8950–8958, 2013.

[112] J. B. Parise, A. Yeganeh-Haeri, D. J. Weidner, J. D. Jorgensen, and M. A. Saltzberg, "Pressure-induced phase transition and pressure dependence of

crystal structure in low (α) and Ca/Al-doped cristobalite," *Journal of Applied Physics*, vol. 75, no. 3, pp. 1361–1367, 1994.

[113] D. Hatch and S. Ghose, "The $\alpha - \beta$ phase transition in cristobalite, SiO_2," *Physics and Chemistry of Minerals*, vol. 17, no. 6, pp. 554–562, 1991.

[114] N. Garg and S. M. Sharma, "Classical molecular dynamical simulations of high pressure behavior of alpha cristobalite (SiO_2)," *Journal of Physics Condensed Matter*, vol. 19, no. 45, 2007.

[115] A. Cernok, K. Marquardt, R. Caracas, E. Bykova, G. Habler, H. P. Liermann, M. Hanfland, M. Mezouar, E. Bobocioiu, and L. Dubrovinsky, "Compressional pathways of α-cristobalite, structure of cristobalite X-I, and towards the understanding of seifertite formation," *Nature Communications*, vol. 8, p. 15647, 2017.

[116] H. Shelton, T. Bi, E. Zurek, J. Smith, and P. Dera, "The Ideal Crystal Structure of Cristobalite X-I: A Bridge in SiO_2 Densification," *Journal of Physical Chemistry C*, vol. 122, no. 30, pp. 17437–17446, 2018.

[117] E. Güler, G. Uğur, Uğur, and M. Güler, "A theoretical study for the band gap energies of the most common silica polymorphs," *Chinese Journal of Physics*, vol. 65, no. January, pp. 472–480, 2020.

[118] R. Warmbier, F. Mohammed, and A. Quandt, " Optical and other material properties of SiO_2 from ab initio studies ," *Optical Engineering*, vol. 53, no. 7, p. 071808, 2014.

[119] C. Sevik and C. Bulutay, "Theoretical study of the insulating oxides and nitrides: SiO_2, GeO_2, Al_2O_3, Si_3N_4, and Ge_3N_4," *Journal of Materials Science*, vol. 42, no. 16, pp. 6555–6565, 2007.

[120] Y. N. Xu and W. Y. Ching, "Electronic and optical properties of all polymorphic forms of silicon dioxide," *Physical Review B*, vol. 44, no. 20, pp. 11048–11059, 1991.

[121] T. Akiyama, K. Kawamoto, H. Kageshima, M. Uematsu, K. Nakamura, and T. Ito, "A first-principles study of O_2 incorporation and its diffusion

in compressively strained high-density silicon oxides," *Thin Solid Films*, vol. 508, no. 1-2, pp. 311–314, 2006.

[122] A. Rimola, D. Costa, M. Sodupe, J. F. Lambert, and P. Ugliengo, "Silica surface features and their role in the adsorption of biomolecules: Computational modeling and experiments," *Chemical Reviews*, vol. 113, no. 6, pp. 4216–4313, 2013.

[123] L. Huang and J. Kieffer, "Amorphous-amorphous transitions in silica glass. I. Reversible transitions and thermomechanical anomalies," *Physical Review B*, vol. 69, p. 224203, 2004.

[124] F. S. Emami, V. Puddu, R. J. Berry, V. Varshney, S. V. Patwardhan, C. C. Perry, and H. Heinz, "Erratum: Force Field and a Surface Model Database for Silica to Simulate Interfacial Properties in Atomic Resolution ," *Chemistry of Materials*, vol. 26, no. 1, p. 2647–2658, 2016.

[125] J. Yang, S. Meng, L. Xu, and E. G. Wang, "Water adsorption on hydroxylated silica surfaces studied using the density functional theory," *Physical Review B*, vol. 71, no. 3, p. 035413, 2005.

[126] E. Valencia, "Calculation of the adsorption potential energy of water vapour on α-cristobalite," *Journal of the Chemical Society, Faraday Transactions*, vol. 90, no. 17, pp. 2555–2559, 1994.

[127] J. Vandevondele and J. Hutter, "Gaussian basis sets for accurate calculations on molecular systems in gas and condensed phases," *Journal of Chemical Physics*, vol. 127, no. 11, p. 114105, 2007.

[128] B. G. Pfrommer, M. Côté, S. G. Louie, and M. L. Cohen, "Relaxation of crystals with the quasi-newton method," *Journal of Computational Physics*, vol. 131, no. 1, pp. 233–240, 1997.

[129] J. P. Perdew, K. Burke, and M. Ernzerhof, "Generalized gradient approximation made simple," *Physical Review Letters*, vol. 77, no. 18, pp. 3865–3868, 1996.

[130] M. Guidon, J. Hutter, and J. Vandevondele, "Auxiliary density matrix methods for Hartree-Fock exchange calculations," *Journal of Chemical Theory and Computation*, vol. 6, no. 8, pp. 2348–2364, 2010.

[131] S. T. Murphy and N. D. Hine, "Anisotropic charge screening and supercell size convergence of defect formation energies," *Physical Review B*, vol. 87, no. 9, p. 094111, 2013.

[132] M. Iannuzzi, T. Chassaing, T. Wallman, J. Hutter, and J. Hutter, "Ground and Excited State Density Functional Calculations with the Gaussian and Augmented-Plane-Wave Method," *Chimia*, vol. 59, pp. 499–503, 2005.

[133] J. Strand, S. K. Chulkov, M. B. Watkins, and A. L. Shluger, "First principles calculations of optical properties for oxygen vacancies in binary metal oxides," *Journal of Chemical Physics*, vol. 150, p. 044702, 1 2019.

[134] C. Adamo and V. Barone, "Toward reliable density functional methods without adjustable parameters: The PBE0 model," *Journal of Chemical Physics*, vol. 110, pp. 6158–6170, 4 1999.

[135] G. Lippert, J. Hutter, and M. Parrinello, "The Gaussian and augmented-plane-wave density functional method for ab initio molecular dynamics simulations," *Theoretical Chemistry Accounts*, vol. 103, no. 2, pp. 124–140, 1999.

[136] F. Jensen, "The optimum contraction of basis sets for calculating spin–spin coupling constants," *Theoretical Chemistry Accounts*, vol. 126, no. 5, pp. 371–382, 2010.

[137] V. Weber, M. Iannuzzi, S. Giani, J. Hutter, R. Declerck, and M. Waroquier, "Magnetic linear response properties calculations with the Gaussian and augmented-plane-wave method," *The Journal of chemical physics*, vol. 131, no. 1, p. 014106, 2009.

[138] F. Bart, J. Gautier, and M. Henriot, "$(01\bar{1}0)$ α-quartz Surface: a LEED, XANES and ELS Study," *Surface Science*, vol. 274, pp. 317–328, 1992.

[139] F. Bart, M. Gautier, F. Jollet, and J. Duraud, “Electronic structure of the (0001) and $(10\bar{1}0)$ quartz surfaces and of their defects as observed by reflection electron energy loss spectroscopy (reels),” *Surface Science*, vol. 306, pp. 342–358, 1994.

[140] L. Garvie, P. Rez, J. Alvarez, and P. Buseck, “Interband transitions of crystalline and amorphous SiO_2: An electron energy-loss spectroscopy (eels) study of the low-loss region,” *Solid state communications*, vol. 106, no. 5, pp. 303–307, 1998.

[141] L. A. J. Garvie, P. Rez, J. R. Alvarez, P. R. Buseck, A. J. Craven, and R. Brydson, “Bonding in α-quartz (sio_2): A view of the unoccupied states,” *American Mineralogist*, vol. 85, pp. 732–738, 2000.

[142] G. Kresse, M. Marsman, L. E. Hintzsche, and E. Flage-Larsen, “Optical and electronic properties of Si_3N_4 and α-SiO_2,” *Physical Review B*, vol. 85, p. 045205, 1 2012.

[143] A. M. El-Sayed, M. B. Watkins, V. V. Afanas’ev, and A. L. Shluger, “Nature of intrinsic and extrinsic electron trapping in SiO_2,” *Physical Review B*, vol. 89, p. 125201, 2014.

[144] S. Maj, “Energy gap and density in SiO_2 polymorphs,” *Physics and Chemistry of Minerals*, vol. 15, no. 3, pp. 271–273, 1988.

[145] Y. P. Li and W. Y. Ching, “Band structures of all polycrystalline forms of silicon dioxide,” *Physical Review B*, vol. 31, no. 4, pp. 2172–2179, 1985.

[146] E. Gnani, S. Reggiani, R. Colle, and M. Rudan, “Band-Structure Calculations Of SiO_2 by Means of Hartree-Fock and density-functional techniques,” *IEEE Transactions on Electron Devices*, vol. 47, no. 10, pp. 1795–1803, 2000.

[147] R. L. Mozzi and B. E. Warren, “Structure of Vitreous Silica,” *Journal of Applied Crystallography*, vol. 2, no. 4, pp. 164–172, 1969.

[148] A. M. El-Sayed, M. B. Watkins, A. L. Shluger, and V. V. Afanas’ev, “Identification of intrinsic electron trapping sites in bulk amorphous silica

from ab initio calculations," *Microelectronic Engineering*, vol. 109, pp. 68–71, 2013.

[149] T. DiStefano and D. Eastman, "The Band Edge of Amorphous SiO_2 by Photoinjection and Photoconductivity Measurements," *Solid State Communications*, vol. 9, pp. 2259–2261, 1971.

[150] V. J. Nithianandam and S. E. Schnatterly, "Soft-x-ray emission and inelastic electron-scattering study of the electronic excitations in amorphous and crystalline silicon dioxide," *Physical Review B*, vol. 38, pp. 5547–5553, 1998.

[151] Z. A. Weinberg, G. W. Rubloff, and E. Bassous, "Transmission, photoconductivity, and the experimental band gap of thermally grown SiO_2 films," *Physical Review B*, vol. 19, pp. 3107–3117, 1979.

[152] S. Lee and H. Xu, "Using powder XRD and pair distribution function to determine anisotropic atomic displacement parameters of orthorhombic tridymite and tetragonal cristobalite," *Acta Crystallographica Section B: Structural Science, Crystal Engineering and Materials*, vol. 75, pp. 160–167, 4 2019.

[153] W. H. Baur, "In search of the crystal structure of low quartz," *Zeitschrift fur Kristallographie*, vol. 224, pp. 580–592, 2009.

[154] J. J. Pluth, J. V. Smith, and J. Faber, "Crystal structure of low cristobalite at 10, 293, and 473 K: Variation of framework geometry with temperature," *Journal of Applied Physics*, vol. 57, pp. 1045–1049, 1985.

[155] O. L. Anderson and E. Schreiber, "The Relation between Refractive Index and Density of Minerals Related to the Earth's Mantle," *Journal of geophysical research*, vol. 70, no. 6, pp. 1463–1471, 1965.

[156] N. Capron, S. Carniato, A. Lagraa, G. Boureau, and A. Pasturel, "Local density approximation and generalized gradient approximation calculations for oxygen and silicon vacancies in silica," *Journal of Chemical Physics*, vol. 112, no. 21, pp. 9543–9548, 2000.

[157] S. Mukhopadhyay, P. V. Sushko, A. H. Edwards, and A. L. Shluger, "Calculation of relative concentrations of E$'$ centres in amorphous silica," *Journal of Non-Crystalline Solids*, vol. 345-346, pp. 703–709, 2004.

[158] K. Raghavachari, D. Ricci, and G. Pacchioni, "Optical properties of point defects in SiO_2 from time-dependent density functional theory," *Journal of Chemical Physics*, vol. 116, no. 2, pp. 825–831, 2002.

[159] M. Guzzi, F. Piot, G. Spinolo, A. Vedda, C. B. Azzoni, and A. Paleari, "Neutron irradiation effects in quartz: Optical absorption and electron paramagnetic resonance," *Journal of Physics: Condensed Matter*, vol. 4, no. 44, pp. 8635–8648, 1992.

[160] D. Griscom and W. B. Fowler, "Electron-transfer model for E$'$-center optical absorption in SiO_2," in *The Physics of MOS Insulators. Proceedings of the International Topical Conference on the Physics of MOS Insulators, Pergamon Press*, pp. 97–101, 1980.

[161] A. N. Trukhin, "Radiation processes in oxygen-deficient silica glasses: Is ODC(I) a precursor of E$'$-center?," *Journal of Non-Crystalline Solids*, vol. 352, no. 28-29, pp. 3002–3008, 2006.

[162] D. L. Griscom, "Optical properties and structure of defects in silica glass," *Journal of the Ceramic Society of Japan*, vol. 99, no. 1154, pp. 923–942, 1991.

[163] H. Hosono, Y. Abe, H. Imagawa, H. Imai, and K. Arai, "Experimental evidence for the Si-Si bond model of the 7.6-eV band in SiO_2 glass," *Physical Review B*, vol. 44, no. 21, pp. 12043–12045, 1991.

[164] B. Henderson, Y. Chen, and W. A. Sibley, "Temperature Dependence of Luminescence of F' and F Centers in CaO," *Physical Review B*, vol. 6, no. 10, pp. 4060–4068, 1972.

[165] B. D. Perlson and J. A. Weil, "Electron paramagnetic resonance studies of the E$'$ centers in alpha-quartz," *Canadian Journal of Physics*, vol. 86, no. 7, pp. 871–881, 2008.

[166] L. Zhang and R. G. Leisure, “The E'_δ and triplet-state centers in x-irradiated high-purity amorphous SiO_2,” *Journal of Applied Physics*, vol. 80, pp. 3744–3749, 10 1996.

[167] V. Afanas’ev and A. Stesmans, “Charge state of paramagnetic E' centre in thermal SiO_2 layers on silicon,” *Journal of Physics: Condensed Matter*, vol. 12, p. 2285–2290, 2000.

[168] S. Ling, A.-M. El-Sayed, F. Lopez-Gejo, M. B. Watkins, V. V. Afanas’ev, and A. L. Shluger, “A computational study of Si–H bonds as precursors for neutral E_0 centres in amorphous silica and at the Si/SiO_2 interface,” *Microelectronic Engineering*, vol. 109, p. 310–313, 2013.

[169] L. Zhuravlev, “The surface chemistry of amorphous silica. Zhuravlev model,” *Colloids and Surfaces A: Physicochemical and Engineering Aspects*, vol. 173, no. 1-3, pp. 1–38, 2000.

[170] D. B. Asay and S. H. Kim, “Evolution of the adsorbed water layer structure on silicon oxide at room temperature,” *Journal of Physical Chemistry B*, vol. 109, pp. 16760–16763, 2005.

[171] S.-H. Urashima, T. Uchida, and H. Yui, “A hydrogen-bonding structure in self-formed nanodroplets of water adsorbed on amorphous silica revealed via surface-selective vibrational spectroscopy,” *Physical Chemistry Chemical Physics*, vol. 22, no. 46, pp. 27031–27036, 2020.

[172] L. Chen and L. Qian, “Role of interfacial water in adhesion, friction, and wear—a critical review,” *Friction*, vol. 9, no. 1, pp. 1–28, 2021.

[173] F. Musso, P. Mignon, P. Ugliengo, and M. Sodupe, “Cooperative effects at water–crystalline silica interfaces strengthen surface silanol hydrogen bonding. An ab initio molecular dynamics study,” *Physical Chemistry Chemical Physics*, vol. 14, no. 30, pp. 10507–10514, 2012.

[174] Á. Cimas, F. Tielens, M. Sulpizi, M.-P. Gaigeot, and D. Costa, “The amorphous silica–liquid water interface studied by ab initio molecular

dynamics (aimd): local organization in global disorder," *Journal of Physics: Condensed Matter*, vol. 26, no. 24, p. 244106, 2014.

[175] L. Chen, X. He, H. Liu, L. Qian, and S. H. Kim, "Water Adsorption on Hydrophilic and Hydrophobic Surfaces of Silicon," *The Journal of Physical Chemistry C*, vol. 122, no. 21, pp. 11385–11391, 2018.

[176] S. Pezzotti, D. R. Galimberti, and M.-P. Gaigeot, "Deconvolution of BIL-SFG and DL-SFG spectroscopic signals reveals order/disorder of water at the elusive aqueous silica interface," *Physical Chemistry Chemical Physics*, vol. 21, pp. 22188–22202, 2019.

[177] S. Pezzotti, D. R. Galimberti, Y. R. Shen, and M.-P. Gaigeot, "Structural definition of the BIL and DL: a new universal methodology to rationalize non-linear $\chi(2)(\omega)$ SFG signals at charged interfaces, including $\chi(3)(\omega)$ contributions," *Physical Chemistry Chemical Physics*, vol. 20, pp. 5190–5199, 2018.

[178] K. S. Smirnov, "Structure and sum-frequency generation spectra of water on neutral hydroxylated silica surfaces," *Physical Chemistry Chemical Physics*, vol. 23, pp. 6929–6949, 2021.

[179] B. K. Choi, I. H. Lee, J. Kim, and Y. J. Chang, "Tunable Wetting Property in Growth Mode-Controlled WS_2 Thin Films," *Nanoscale Research Letters*, vol. 12, no. 1, 2017.

[180] Z. Peng, R. Yang, M. A. Kim, L. Li, and H. Liu, "Influence of O_2, H_2O and airborne hydrocarbons on the properties of selected 2D materials," *RSC Advances*, vol. 7, no. 43, pp. 27048–27057, 2017.

[181] H. Rokni and W. Lu, "Direct measurements of interfacial adhesion in 2D materials and van der Waals heterostructures in ambient air," *Nature Communications*, vol. 11, no. 1, 2020.

[182] M. R. Uhlig, D. Martin-Jimenez, and R. Garcia, "Atomic-scale mapping of hydrophobic layers on graphene and few-layer MoS_2 and WSe_2 in water," *Nature communications*, vol. 10, no. 1, p. 2606, 2019.

[183] P. K. Chow, E. Singh, B. C. Viana, J. Gao, J. Luo, J. Li, Z. Lin, A. L. Elías, Y. Shi, Z. Wang, M. Terrones, and N. Koratkar, "Wetting of mono and few-layered WS_2 and MoS_2 films supported on Si/SiO_2 substrates," *ACS Nano*, vol. 9, no. 3, pp. 3023–3031, 2015.

[184] J. Ma, Z. G. Yu, and Y. W. Zhang, "Tuning deep dopants to shallow ones in 2d semiconductors by substrate screening: The case of X S (x = Cl, Br, I) in MoS_2," *Physical Review B*, vol. 95, pp. 1–6, 2017.

[185] X. Zhang, F. Jia, B. Yang, and S. Song, "Oxidation of Molybdenum Disulfide Sheet in Water under in Situ Atomic Force Microscopy Observation," *Journal of Physical Chemistry C*, vol. 121, pp. 9938–9943, 2017.

[186] M. Khalkhali, H. Zhang, and Q. Liu, "Effects of Thickness and Adsorption of Airborne Hydrocarbons on Wetting Properties of MoS_2: An Atomistic Simulation Study," *The Journal of Physical Chemistry C*, vol. 122, no. 12, pp. 6737–6747, 2018.

[187] M. Foroutan, S. M. Fatemi, and M. Darvishi, "Formation and stability of water clusters at the molybdenum disulfide interface: a molecular dynamics simulation investigation," *Journal of Physics: Condensed Matter*, vol. 30, p. 415001, sep 2018.

[188] Z. Cao, M. Harb, S. M. Kozlov, and L. Cavallo, "Structural and Electronic Effects at the Interface between Transition Metal Dichalcogenide Monolayers (MoS_2, WSe_2, and Their Lateral Heterojunctions) and Liquid Water," *International Journal of Molecular Sciences*, vol. 23, no. 19, 2022.

[189] Y. Zhang, "Photocatalytic activity of MoS_2 with water monolayers: Global optimization," *The Journal of Chemical Physics*, vol. 157, p. 184703, 11 2022.

[190] B. Wang, R. K. Kalia, A. Nakano, and P. D. Vashishta, "Dewetting of monolayer water and isopropanol between MoS_2 nanosheets," *Scientific Reports*, vol. 8, no. 1, p. 16704, 2018.

[191] Q. Li, J. Song, F. Besenbacher, and M. Dong, “Two-Dimensional Material Confined Water,” *Accounts of Chemical Research*, vol. 48, no. 1, pp. 119–127, 2015. PMID: 25539031.

[192] G. Liu, W. Jin, and N. Xu, “Two-Dimensional-Material Membranes: A New Family of High-Performance Separation Membranes,” *Angewandte Chemie International Edition*, vol. 55, no. 43, pp. 13384–13397, 2016.

[193] M. J. Prieto, H. W. Klemm, F. Xiong, D. M. Gottlob, D. Menzel, T. Schmidt, and H.-J. Freund, “Water Formation under Silica Thin Films: Real-Time Observation of a Chemical Reaction in a Physically Confined Space,” *Angewandte Chemie International Edition*, vol. 57, no. 28, pp. 8749–8753, 2018.

[194] M. J. Lee, J. S. Choi, J.-S. Kim, I.-S. Byun, D. H. Lee, S. Ryu, C. Lee, and B. H. Park, “Characteristics and effects of diffused water between graphene and a SiO_2 substrate,” *Nano Research*, vol. 5, pp. 710–717, 2012.

[195] K. Xu, P. Cao, and J. R. Heath, “Graphene visualizes the first water adlayers on mica at ambient conditions,” *Science*, vol. 329, no. 5996, pp. 1188–1191, 2010.

[196] D. Lee, H. Lee, H. Lee, and J. Y. Park, “Nanotribological Effect of Water Layers Intercalated between Exfoliated MoS_2 and Mica,” *The Journal of Physical Chemistry C*, vol. 124, no. 31, pp. 16902–16907, 2020.

[197] H. Lee, H. Jeong, J. Suh, W. H. Doh, J. Baik, H.-J. Shin, J.-H. Ko, J. Wu, Y.-H. Kim, and J. Y. Park, “Nanoscale Friction on Confined Water Layers Intercalated between MoS_2 Flakes and Silica,” *The Journal of Physical Chemistry C*, vol. 123, no. 14, pp. 8827–8835, 2019.

[198] A. Rauf, A. Schilo, N. Severin, I. M. Sokolov, and J. P. Rabe, “Non-monotonous Wetting of Graphene–Mica and MoS_2–Mica Interfaces with a Molecular Layer of Water,” *Langmuir*, vol. 34, no. 50, pp. 15228–15237, 2018.

[199] L. Giordano, P. V. Sushko, G. Pacchioni, and A. L. Shluger, “Electron

Trapping at Point Defects on Hydroxylated Silica Surfaces," *Physical Review Letters*, vol. 99, p. 136801, 2007.

[200] F. Federici Canova, M. Mizukami, T. Imamura, K. Kurihara, and A. L. Shluger, "Structural stability and polarisation of ionic liquid films on silica surfaces," *Physical Chemistry Chemical Physics*, vol. 17, pp. 17661–17669, 2015.

[201] M. A. González and J. L. Abascal, "A flexible model for water based on TIP4P/2005," *The Journal of chemical physics*, vol. 135, no. 22, 2011.

[202] M. Sulpizi, M.-P. Gaigeot, and M. Sprik, "The Silica–Water Interface: How the Silanols Determine the Surface Acidity and Modulate the Water Properties," *Journal of Chemical Theory and Computation*, vol. 8, pp. 1037–1047, 2012.

[203] L. Hargreaves, "Computational Modelling of Molecular Adsorption on Oxide Surfaces at Different Coverages," *PhD Thesis*, vol. UCL, no. 26, p. pp. 221, 2024.

[204] M. A. U. Absor, H. Kotaka, F. Ishii, and M. Saito, "Strain-controlled spin splitting in the conduction band of monolayer WS_2," *Physical Review B*, vol. 94, 9 2016.

[205] B. Amin, T. P. Kaloni, and U. Schwingenschlögl, "Strain engineering of WS_2, WSe_2, and WTe_2," *RSC Advances*, vol. 4, no. 65, pp. 34561–34565, 2014.

[206] R. Chaurasiya, A. Dixit, and R. Pandey, "Strain-mediated stability and electronic properties of WS_2, Janus WSSe and WSe_2 monolayers," *Superlattices and Microstructures*, vol. 122, pp. 268–279, 10 2018.

[207] H. J. Conley, B. Wang, J. I. Ziegler, R. F. Haglund, S. T. Pantelides, and K. I. Bolotin, "Bandgap engineering of strained monolayer and bilayer MoS_2," *Nano Letters*, vol. 13, pp. 3626–3630, 8 2013.

[208] S. Deng, L. Li, and M. Li, "Stability of direct band gap under mechanical strains for monolayer MoS_2, $MoSe_2$, WS_2 and WSe_2," *Physica E: Low-Dimensional Systems and Nanostructures*, vol. 101, pp. 44–49, 7 2018.

[209] B. Santra, J. Klimeš, A. Tkatchenko, D. Alfè, B. Slater, A. Michaelides, R. Car, and M. Scheffler, "On the accuracy of van der Waals inclusive density-functional theory exchange-correlation functionals for ice at ambient and high pressures," *The Journal of Chemical Physics*, vol. 139, no. 15, 2013.

[210] J. Schmidt, J. VandeVondele, I.-F. W. Kuo, D. Sebastiani, J. I. Siepmann, J. Hutter, and C. J. Mundy, "Isobaric-Isothermal Molecular Dynamics Simulations Utilizing Density Functional Theory: An Assessment of the Structure and Density of Water at Near-Ambient Conditions," *The Journal of Physical Chemistry B*, vol. 113, no. 35, pp. 11959–11964, 2009. PMID: 19663399.

[211] M. J. Gillan, D. Alfè, and A. Michaelides, "Perspective: How good is DFT for water?," *The Journal of Chemical Physics*, vol. 144, p. 130901, 04 2016.

[212] T. A. Pham, T. Ogitsu, E. Y. Lau, and E. Schwegler, "Structure and dynamics of aqueous solutions from PBE-based first-principles molecular dynamics simulations," *The Journal of Chemical Physics*, vol. 145, p. 154501, 10 2016.

[213] P. Schienbein and J. Blumberger, "Nanosecond solvation dynamics of the hematite/liquid water interface at hybrid DFT accuracy using committee neural network potentials," *Physical Chemistry Chemical Physics*, vol. 24, no. 25, pp. 15365–15375, 2022.

[214] Richard J. Gowers, Max Linke, Jonathan Barnoud, Tyler J. E. Reddy, Manuel N. Melo, Sean L. Seyler, Jan Domański, David L. Dotson, Sébastien Buchoux, Ian M. Kenney, and Oliver Beckstein, "MDAnalysis: A Python Package for the Rapid Analysis of Molecular Dynamics Simulations," in *Proceedings of the 15th Python in Science Conference* (Sebastian Benthall and Scott Rostrup, eds.), pp. 98 – 105, 2016.

[215] N. Michaud-Agrawal, E. J. Denning, T. B. Woolf, and O. Beckstein, "MDAnalysis: a toolkit for the analysis of molecular dynamics simulations," *Journal of computational chemistry*, vol. 32, no. 10, pp. 2319–2327, 2011.

[216] R. J. Gowers and P. Carbone, "A multiscale approach to model hydrogen bonding: The case of polyamide," *The Journal of Chemical Physics*, vol. 142, p. 224907, 06 2015.

[217] D. Argyris, N. R. Tummala, A. Striolo, and D. R. Cole, "Molecular structure and dynamics in thin water films at the silica and graphite surfaces," *The Journal of Physical Chemistry C*, vol. 112, no. 35, pp. 13587–13599, 2008.

[218] D. Argyris, D. R. Cole, and A. Striolo, "Hydration structure on crystalline silica substrates," *Langmuir*, vol. 25, no. 14, pp. 8025–8035, 2009.

[219] S. Li, K. Liu, J. c. v. Klimeš, and J. Chen, "Understanding the wetting of transition metal dichalcogenides from an ab initio perspective," *Physical Review Research*, vol. 5, p. 023018, Apr 2023.

[220] X. Wen, X.-T. Fan, X. Jin, and J. Cheng, "Band Alignment of 2d Material–Water Interfaces," *The Journal of Physical Chemistry C*, vol. 127, no. 8, pp. 4132–4143, 2023.

[221] A. T. Sose, E. Mohammadi, P. F. Achari, and S. A. Deshmukh, "Determination of Accurate Interaction Parameters between the Molybdenum Disulfide and Water to Investigate Their Interfacial Properties," *The Journal of Physical Chemistry C*, vol. 126, no. 4, pp. 2013–2022, 2022.

[222] Y.-W. Chen, I.-H. Chu, Y. Wang, and H.-P. Cheng, "Water thin film-silica interaction on α-quartz (0001) surfaces," *Physical Review B*, vol. 84, p. 155444, Oct 2011.

[223] Y. Berro, M. Badawi, F. El Haj Hassan, M. Kassir, and F. Tielens, "Water-silanol interactions on the amorphous silica surface: A dispersion-corrected DFT investigation," *Journal of Molecular Liquids*, vol. 320, p. 114496, 2020.

[224] K. Kobayashi and A. Firoozabadi, "Water Film Structure and Wettability of Different Quartz Surfaces: Hydrogen Bonding Across Various Cutting Planes," *Langmuir*, vol. 40, no. 9, pp. 4635–4645, 2024. PMID: 38377565.

[225] A. Myalitsin, S.-h. Urashima, S. Nihonyanagi, S. Yamaguchi, and T. Tahara, "Water Structure at the Buried Silica/Aqueous Interface Studied by Heterodyne-Detected Vibrational Sum-Frequency Generation," *The Journal of Physical Chemistry C*, vol. 120, no. 17, pp. 9357–9363, 2016.

[226] R. Réocreux, T. Jiang, M. Iannuzzi, C. Michel, and P. Sautet, "Structuration and Dynamics of Interfacial Liquid Water at Hydrated γ-alumina Determined by ab Initio Molecular Simulations: Implications for Nanoparticle Stability," *ACS Applied Nano Materials*, vol. 1, no. 1, pp. 191–199, 2018.

[227] D. Argyris, D. R. Cole, and A. Striolo, "Dynamic Behavior of Interfacial Water at the Silica Surface," *The Journal of Physical Chemistry C*, vol. 113, no. 45, pp. 19591–19600, 2009.

[228] J. Padró, L. Saiz, and E. Guàrdia, "Hydrogen bonding in liquid alcohols: a computer simulation study," *Journal of Molecular Structure*, vol. 416, no. 1, pp. 243–248, 1997. Hydrogen Bonding - Experimental and Theoretical Studies.

[229] M. Antipova and V. Petrenko, "Hydrogen bond lifetime for water in classic and quantum molecular dynamics," *Russian Journal of Physical Chemistry A*, vol. 87, pp. 1170–1174, 2013.

[230] E. Guàrdia, J. Martí, L. García-Tarrés, and D. Laria, "A molecular dynamics simulation study of hydrogen bonding in aqueous ionic solutions," *Journal of Molecular Liquids*, vol. 117, no. 1, pp. 63–67, 2005. Routes from Local Order to Large Scale Cooperativity.

[231] M. Bouhadja and A. A. Skelton, "Dynamical Properties of Water and Ions at the Quartz (101)–water Interface at a Range of Solution Conditions: A Classical Molecular Dynamics Study," *The Journal of Physical Chemistry C*, vol. 122, no. 3, pp. 1535–1546, 2018.

[232] K. Krynicki, C. D. Green, and D. W. Sawyer, "Pressure and temperature dependence of self-diffusion in water," *Faraday Discussions of the Chemical Society*, vol. 66, pp. 199–208, 1978.

[233] R. Mills, "Self-diffusion in normal and heavy water in the range 1-45 °," *The Journal of Physical Chemistry*, vol. 77, no. 5, pp. 685–688, 1973.

[234] P. Mark and L. Nilsson, "Structure and dynamics of the TIP3P, SPC, and SPC/E water models at 298 K," *The Journal of Physical Chemistry A*, vol. 105, no. 43, pp. 9954–9960, 2001.

[235] W. S. Price, H. Ide, and Y. Arata, "Self-diffusion of supercooled water to 238 K using PGSE NMR diffusion measurements," *The Journal of Physical Chemistry A*, vol. 103, no. 4, pp. 448–450, 1999.

[236] P. Ugliengo, V. Saunders, and E. Garrone, "Silanol as a model for the free hydroxyl of amorphous silica: ab-initio calculations of the interaction with water," *Journal of Physical Chemistry*, vol. 94, no. 6, pp. 2260–2267, 1990.

[237] B. M. Lowe, C.-K. Skylaris, and N. G. Green, "Acid-base dissociation mechanisms and energetics at the silica–water interface: An activationless process," *Journal of Colloid and Interface Science*, vol. 451, pp. 231–244, 2015.

[238] H. Li, S. Kovalchuk, A. Kumar, D. Liang, B. D. Frank, H. Lin, N. Severin, K. I. Bolotin, S. Kirstein, and J. P. Rabe, "Evidence for Charging and Discharging of MoS_2 and WS_2 on Mica by Intercalating Molecularly Thin Liquid Layers," *physica status solidi (a)*, vol. 221, p. 2300302, 2024.

[239] H. Lee, H. Jeong, J. Suh, W. H. Doh, J. Baik, H.-J. Shin, J.-H. Ko, J. Wu, Y.-H. Kim, and J. Y. Park, "Nanoscale Friction on Confined Water Layers Intercalated between MoS_2 Flakes and Silica," *The Journal of Physical Chemistry C*, vol. 123, no. 14, pp. 8827–8835, 2019.

[240] Q. Fu, W. Wang, L. Yang, J. Huang, J. Zhang, and B. Xiang, "Controllable synthesis of high quality monolayer WS_2 on a SiO_2/Si substrate by chemical vapor deposition," *RSC Advances*, vol. 5, pp. 15795–15799, 2015.

[241] G. Delie, D. Chiappe, I. Asselberghs, C. Huyghebaert, I. Radu, S. Banerjee, B. Groven, S. Brems, and V. V. Afanas'ev, "Processing Stability of Monolayer WS_2 on SiO_2," *Nano Express*, vol. 2, p. 024004, 2021.

[242] G. Delie, P. M. Litwin, G. C. Abad, S. J. McDonnell, D. Chiappe, and V. V. Afanasiev, “Variability of band alignment between WS_2 and SiO_2: Intrinsic versus extrinsic contributions,” *Journal of Vacuum Science I& Technology A*, vol. 40, p. 062201, 09 2022.

[243] V. V. Afanas’ev, D. Chiappe, M. Perucchini, M. Houssa, C. Huyghebaert, I. Radu, and A. Stesmans, “Impact of MoS_2 layer transfer on electrostatics of MoS_2/SiO_2 interface,” *Nanotechnology*, vol. 30, 2 2019.

[244] D. Kang, X. Kong, V. Michaud-Rioux, Y. C. Chen, Z. Mi, and H. Guo, “Electronic structure of aqueous two-dimensional photocatalyst,” *npj Computational Materials*, vol. 7, 12 2021.

[245] C. Zhou, H. Zhu, W. Yang, Q. Lin, T. Zheng, L. Yang, and S. Lan, “Interfacial properties of 2d WS_2 on SiO_2 substrate from X-ray photoelectron spectroscopy and first-principles calculations,” *Frontiers of Physics*, vol. 17, no. 5, p. 53500, 2022.

[246] W. Hu and J. Yang, “Two-dimensional van der Waals heterojunctions for functional materials and devices,” *Journal Material Chemistry C*, vol. 5, pp. 12289–12297, 2017.

[247] D. Wing, J. Strand, T. Durrant, A. L. Shluger, and L. Kronik, “Role of long-range exact exchange in polaron charge transition levels: The case of MgO,” *Physical Review Materials*, vol. 4, no. 8, p. 083808, 2020.

[248] S. Grimme, J. Antony, S. Ehrlich, and H. Krieg, “A consistent and accurate ab initio parametrization of density functional dispersion correction (dft-d) for the 94 elements H-Pu,” *Journal of Chemical Physics*, vol. 132, 2010.

[249] K. L. Milton, T. R. Durrant, T. R. Cobos Freire, and A. L. Shluger, “Difference in Structure and Electronic Properties of Oxygen Vacancies in α-quartz and α-cristobalite Phases of SiO_2,” *Materials*, vol. 16, p. 1382, 2 2023.

[250] A. Ohta, M. Ikeda, K. Makihara, and S. Miyazaki, “Evaluation of energy

distribution of filled defects of Si oxide thin films from total photoelectron yield spectroscopy," *Microelectronic Engineering*, vol. 178, pp. 85–88, 2017.

[251] A. Ohta, T. Imagawa, N. Taoka, M. Ikeda, K. Makihara, and S. Miyazaki, "Energy band diagram for SiO_2/Si system as evaluated from UPS analysis under vacuum ultraviolet with variable incident photon energy," *Japanese journal of applied physics.*, vol. 60, no. SA, 2021.

[252] P. A. Markeev, E. Najafidehaghani, Z. Gan, K. Sotthewes, A. George, A. Turchanin, and M. P. de Jong, "Energy-Level Alignment at Interfaces between Transition-Metal Dichalcogenide Monolayers and Metal Electrodes Studied with Kelvin Probe Force Microscopy," *Journal of Physical Chemistry C*, vol. 125, pp. 13551–13559, 2021 JUN 24 2021.

[253] T. Bischoff, I. Reshetnyak, and A. Pasquarello, "Band gaps of liquid water and hexagonal ice through advanced electronic-structure calculations," *Physical Review Res.*, vol. 3, p. 023182, Jun 2021.

[254] L. Bengtsson, "Dipole correction for surface supercell calculations," *Physical Review B*, vol. 59, pp. 12301–12304, May 1999.

[255] N. G. Hörmann, Z. Guo, F. Ambrosio, O. Andreussi, A. Pasquarello, and N. Marzari, "Absolute band alignment at semiconductor-water interfaces using explicit and implicit descriptions for liquid water," *npj Computational Materials*, vol. 5, no. 1, p. 100, 2019.

[256] A. Klein, "Energy band alignment at interfaces of semiconducting oxides: A review of experimental determination using photoelectron spectroscopy and comparison with theoretical predictions by the electron affinity rule, charge neutrality levels, and the common anion rule," in *Thin Solid Films*, vol. 520, pp. 3721–3728, 3 2012.

[257] A. Alkauskas and A. Pasquarello, "Band-edge problem in the theoretical determination of defect energy levels: The O vacancy in ZnO as a benchmark case," *Physical Review B - Condensed Matter and Materials Physics*, vol. 84, 9 2011.

[258] M. Berg, K. Keyshar, I. Bilgin, F. Liu, H. Yamaguchi, R. Vajtai, C. Chan, G. Gupta, S. Kar, P. Ajayan, T. Ohta, and A. D. Mohite, "Layer dependence of the electronic band alignment of few-layer MoS_2 on SiO_2 measured using photoemission electron microscopy," *Physical Review B*, vol. 95, 6 2017.

[259] G. Bramley, M. T. Nguyen, V. A. Glezakou, R. Rousseau, and C. K. Skylaris, "Reconciling Work Functions and Adsorption Enthalpies for Implicit Solvent Models: A Pt (111)/Water Interface Case Study," *Journal of Chemical Theory and Computation*, vol. 16, pp. 2703–2715, 4 2020.

[260] V. Tripkovic, M. E. Björketun, E. Skúlason, and J. Rossmeisl, "Standard hydrogen electrode and potential of zero charge in density functional calculations," *Physical Review B - Condensed Matter and Materials Physics*, vol. 84, 9 2011.

[261] D. Veksler, G. Bersuker, M. B. Watkins, and A. Shluger, "Activation of electrically silent defects in the high-k gate stacks," in *2014 IEEE International Reliability Physics Symposium*, pp. 5B.3.1–5B.3.7, 2014.

[262] J. Strand, M. Kaviani, V. V. Afanas'ev, J. G. Lisoni, and A. L. Shluger, "Intrinsic electron trapping in amorphous oxide," *Nanotechnology*, vol. 29, no. 12, p. 125703, 2018.

[263] R. J. Bell and P. Dean, "Atomic vibrations in vitreous silica," *Discussion Faraday Society*, vol. 50, pp. 55–61, 1970.

[264] J. Dong and D. A. Drabold, "Band-tail states and the localized-to-extended transition in amorphous diamond," *Physical Review B*, vol. 54, pp. 10284–10287, Oct 1996.

[265] M. Unge and T. Christen, "Electron and hole mobility edges in polyethylene from material simulations," *Chemical Physics Letters*, vol. 613, pp. 15–18, 2014.

[266] D. A. Drabold, U. Stephan, J. Dong, and S. M. Nakhmanson, "The structure of electronic states in amorphous silicon," *Journal of Molecular Graphics and Modelling*, vol. 17, no. 5, pp. 285–291, 1999.

[267] W. Tang, E. Sanville, and G. Henkelman, “A grid-based Bader analysis algorithm without lattice bias,” *Journal of Physics: Condensed Matter*, vol. 21, no. 8, p. 084204, 2009.

[268] B. K. Choi, I. H. Lee, J. Kim, and Y. J. Chang, “Tunable Wetting Property in Growth Mode-Controlled WS_2 Thin Films,” *Nanoscale Research Letters*, vol. 12, 2017.

[269] P. K. Chow, E. Singh, B. C. Viana, J. Gao, J. Luo, J. Li, Z. Lin, A. L. Elías, Y. Shi, Z. Wang, M. Terrones, and N. Koratkar, “Wetting of mono and few-layered WS_2 and MoS_2 films supported on Si/SiO_2 substrates,” *ACS Nano*, vol. 9, pp. 3023–3031, 3 2015.

[270] Z. Peng, R. Yang, M. A. Kim, L. Li, and H. Liu, “Influence of O_2, H_2O and airborne hydrocarbons on the properties of selected 2d materials,” *RSC Advances*, vol. 7, pp. 27048–27057, 2017.

[271] H. Rokni and W. Lu, “Direct measurements of interfacial adhesion in 2d materials and van der Waals heterostructures in ambient air,” *Nature Communications*, vol. 11, 2020.

[272] M. R. Uhlig, D. Martin-Jimenez, and R. Garcia, “Atomic-scale mapping of hydrophobic layers on graphene and few-layer MoS_2 and WSe_2 in water,” *Nature Communications*, vol. 10, 12 2019.

[273] W. Gao, P. Xiao, G. Henkelman, K. M. Liechti, and R. Huang, “Interfacial adhesion between graphene and silicon dioxide by density functional theory with van der Waals corrections,” *Journal of Physics D: Applied Physics*, vol. 47, p. 255301, may 2014.

[274] C. Li, X. Yang, and Y. Guo, “DFT simulation of interfacial interaction of graphene/SiO_2 composites,” *Materials Science in Semiconductor Processing*, vol. 150, p. 106964, 2022.

[275] L. Lichtenstein, M. Heyde, S. Ulrich, N. Nilius, and H.-J. Freund, “Probing the properties of metal–oxide interfaces: silica films on Mo and Ru supports,” *Journal of Physics: Condensed Matter*, vol. 24, p. 354010, aug 2012.

[276] M. G. Bianchi, F. Risplendi, M. Re Fiorentin, and G. Cicero, "Engineering the Electrical and Optical Properties of WS_2 Monolayers via Defect Control," *Advanced Science*, vol. 11, no. 4, p. 2305162, 2024.

[277] I. Shlyakhov, J. Chai, M. Yang, S. J. Wang, V. V. Afanas'ev, M. Houssa, and A. Stesmans, "Band alignment at interfaces of synthetic few-monolayer MoS_2 with SiO_2 from internal photoemission," *APL Materials*, vol. 6, p. 026801, 11 2017.

[278] S. Ulstrup, R. J. Koch, D. Schwarz, K. M. McCreary, B. T. Jonker, S. Singh, A. Bostwick, E. Rotenberg, C. Jozwiak, and J. Katoch, "Imaging microscopic electronic contrasts at the interface of single-layer WS_2 with oxide and boron nitride substrates," *Applied Physics Letters*, vol. 114, no. 15, 2019.

[279] T. P. Nguyen, K. S. Choi, S. Y. Kim, T. H. Lee, H. W. Jang, Q. Van Le, and I. T. Kim, "Strategy for controlling the morphology and work function of W_2C/WS_2 nanoflowers," *Journal of Alloys and Compounds*, vol. 829, p. 154582, 2020.

[280] J. Kim, A. Venkatesan, N. A. N. Phan, Y. Kim, H. Kim, D. Whang, and G. Kim, "Schottky Diode with Asymmetric Metal Contacts on WS_2," *Advanced electronic materials*, vol. 8, no. 3, 2022.

[281] K. Keyshar, M. Berg, X. Zhang, R. Vajtai, G. Gupta, C. K. Chan, T. E. Beechem, P. M. Ajayan, A. D. Mohite, and T. Ohta, "Experimental Determination of the Ionization Energies of $MoSe_2$, WS_2, and MoS_2 on SiO_2 Using Photoemission Electron Microscopy," *ACS Nano*, vol. 11, no. 8, pp. 8223–8230, 2017. PMID: 28723073.

[282] M. L. Berrens, A. Kundu, M. F. Calegari Andrade, T. A. Pham, G. Galli, and D. Donadio, "Nuclear Quantum Effects on the Electronic Structure of Water and Ice," *The Journal of Physical Chemistry Letters*, vol. 15, no. 26, pp. 6818–6825, 2024.

[283] S. Schnur and A. Groß, "Properties of metal–water interfaces studied from first principles," *New Journal of Physics*, vol. 11, p. 125003, dec 2009.

[284] A. Groß, “Challenges for ab initio molecular dynamics simulations of electrochemical interfaces,” *Current Opinion in Electrochemistry*, vol. 40, p. 101345, 2023.

[285] S. Ling, M. B. Watkins, and A. L. Shluger, “Effects of atomic scale roughness at metal/insulator interfaces on metal work function,” *Physical Chemistry Chemical Physics*, vol. 15, no. 45, pp. 19615–19624, 2013.

[286] S. Prada, L. Giordano, G. Pacchioni, and J. Goniakowski, “Reprint of “theoretical description of metal/oxide interfacial properties: The case of MgO/Ag(001)”,” *Applied Surface Science*, vol. 396, pp. 1850–1854, 2017.

[287] S. Ling, M. B. Watkins, and A. L. Shluger, “Effects of Oxide Roughness at Metal Oxide Interface: MgO on Ag(001),” *The Journal of Physical Chemistry C*, vol. 117, no. 10, pp. 5075–5083, 2013.

[288] C. Zhang, Z. Ning, Y. Liu, T. Xu, Y. Guo, A. Zak, Z. Zhang, S. Wang, R. Tenne, and Q. Chen, “Electrical transport properties of individual WS_2 nanotubes and their dependence on water and oxygen absorption,” *Applied Physics Letters*, vol. 101, p. 113112, 09 2012.

[289] Y.-T. Lee, Y.-T. Huang, S.-P. Chiu, R.-T. Wang, T. Taniguchi, K. Watanabe, R. Sankar, C.-T. Liang, W.-H. Wang, S.-S. Yeh, and J.-J. Lin, “Determining the Electron Scattering from Interfacial Coulomb Scatterers in Two-Dimensional Transistors,” *ACS Applied Materials & Interfaces*, vol. 16, no. 1, pp. 1066–1073, 2024. PMID: 38113538.

[290] D. Ovchinnikov, A. Allain, Y.-S. Huang, D. Dumcenco, and A. Kis, “Electrical Transport Properties of Single-Layer WS_2,” *ACS Nano*, vol. 8, no. 8, pp. 8174–8181, 2014.

[291] T. Joseph, M. Ghorbani-Asl, M. Batzill, and A. V. Krasheninnikov, “Water dissociation and association on mirror twin boundaries in two-dimensional $MoSe_2$: insights from density functional theory calculations,” *Nanoscale Adv.*, vol. 3, pp. 6992–7001, 2021.

[292] Y. Rong, K. He, M. Pacios, A. W. Robertson, H. Bhaskaran, and J. H. Warner, "Controlled Preferential Oxidation of Grain Boundaries in Monolayer Tungsten Disulfide for Direct Optical Imaging," *ACS Nano*, vol. 9, no. 4, pp. 3695–3703, 2015. PMID: 25870912.

[293] J. Lin, Z. Peng, G. Wang, D. Zakhidov, E. Larios, M. J. Yacaman, and J. M. Tour, "Enhanced Electrocatalysis for Hydrogen Evolution Reactions from WS_2 Nanoribbons," *Advanced Energy Materials*, vol. 4, no. 10, p. 1301875, 2014.

[294] S. Kc, R. C. Longo, R. M. Wallace, and K. Cho, "Surface oxidation energetics and kinetics on MoS_2 monolayer," *Journal of Applied Physics*, vol. 117, no. 13, 2015.

[295] H. Zhang, J. R. Dunklin, O. G. Reid, S. J. Yun, S. U. Nanayakkara, Y. H. Lee, J. L. Blackburn, and E. M. Miller, "Disentangling oxygen and water vapor effects on optoelectronic properties of monolayer tungsten disulfide," *Nanoscale*, vol. 12, pp. 8344–8354, 2020.

[296] G. Ye, Y. Gong, J. Lin, B. Li, Y. He, S. T. Pantelides, W. Zhou, R. Vajtai, and P. M. Ajayan, "Defects Engineered Monolayer MoS_2 for Improved Hydrogen Evolution Reaction," *Nano Letters*, vol. 16, no. 2, pp. 1097–1103, 2016. PMID: 26761422.

[297] Z. Wang, Q. Li, H. Xu, C. Dahl-Petersen, Q. Yang, D. Cheng, D. Cao, F. Besenbacher, J. V. Lauritsen, S. Helveg, and M. Dong, "Controllable etching of MoS_2 basal planes for enhanced hydrogen evolution through the formation of active edge sites," *Nano Energy*, vol. 49, pp. 634–643, 2018.

[298] Y. Y. Wang, S. M. Huang, K. Yu, J. Jiang, Y. Liang, B. Zhong, H. Zhang, G. F. Kan, S. F. Quan, and J. Yu, "Atomically flat HfO_2 layer fabricated by mild oxidation HfS_2 with controlled number of layers," *Journal of Applied Physics*, vol. 127, p. 214303, 06 2020.

[299] S. Lai, S. Byeon, S. K. Jang, J. Lee, B. H. Lee, J.-H. Park, Y.-H. Kim, and S. Lee, "HfO_2/HfS_2 hybrid heterostructure fabricated via controllable

chemical conversion of two-dimensional HfS_2," *Nanoscale*, vol. 10, no. 39, pp. 18758–18766, 2018.

[300] J. Gao, B. Li, J. Tan, P. Chow, T. M. Lu, and N. Koratkar, "Aging of Transition Metal Dichalcogenide Monolayers," *ACS Nano*, vol. 10, pp. 2628–2635, 2 2016.

[301] R. Szoszkiewicz, "Local interactions of atmospheric oxygen with MoS_2 crystals," *Materials*, vol. 14, no. 20, p. 5979, 2021.

[302] J. Martincová, M. Otyepka, and P. Lazar, "Is Single Layer MoS_2 Stable in the Air?," *Chemistry – A European Journal*, vol. 23, no. 53, pp. 13233–13239, 2017.

[303] U. Ukegbu and R. Szoszkiewicz, "Microscopic kinetics of heat-induced oxidative etching of thick MoS_2 crystals," *The Journal of Physical Chemistry C*, vol. 123, no. 36, pp. 22123–22129, 2019.

[304] K. K. Ghuman, S. Yadav, and C. V. Singh, "Adsorption and Dissociation of H_2O on Monolayered MoS_2 Edges: Energetics and Mechanism from ab Initio Simulations," *The Journal of Physical Chemistry C*, vol. 119, no. 12, pp. 6518–6529, 2015.

[305] S. S. Grønborg, K. Thorarinsdottir, L. Kyhl, J. Rodriguez-Fernández, C. E. Sanders, M. Bianchi, P. Hofmann, J. A. Miwa, S. Ulstrup, and J. V. Lauritsen, "Basal plane oxygen exchange of epitaxial MoS_2 without edge oxidation," *2D Materials*, vol. 6, no. 4, p. 045013, 2019.

[306] P. Lazar and M. Otyepka, "Role of the Edge Properties in the Hydrogen Evolution Reaction on MoS_2," *Chemistry – A European Journal*, vol. 23, no. 20, pp. 4863–4869, 2017.

[307] W. Li, G. Liu, J. Li, Y. Wang, L. Ricardez-Sandoval, Y. Zhang, and Z. Zhang, "Hydrogen evolution reaction mechanism on 2H-MoS_2 electrocatalyst," *Applied Surface Science*, vol. 498, p. 143869, 2019.

[308] C. Tsai, K. Chan, J. K. Nørskov, and F. Abild-Pedersen, "Theoretical insights into the hydrogen evolution activity of layered transition metal

dichalcogenides," *Surface Science*, vol. 640, pp. 133–140, 2015. Reactivity Concepts at Surfaces: Coupling Theory with Experiment.

[309] C. Ataca and S. Ciraci, "Dissociation of H_2O at the vacancies of single-layer MoS_2," *Physical Review B*, vol. 85, p. 195410, May 2012.

[310] L. M. Farigliano, P. A. Paredes-Olivera, and E. M. Patrito, "Initial Steps of Oxidative Etching of MoS_2 Basal Plane Induced by O_2," *The Journal of Physical Chemistry C*, vol. 124, no. 24, pp. 13177–13186, 2020.

[311] N. Xu, L. Shi, X. Pei, W. Zhang, J. Chen, Z. Han, P. Samorì, J. Wang, P. Wang, Y. Shi, *et al.*, "Oxidation kinetics and non-marcusian charge transfer in dimensionally confined semiconductors," *Nature Communications*, vol. 14, no. 1, p. 4074, 2023.

[312] R. Rao, A. E. Islam, P. M. Campbell, E. M. Vogel, and B. Maruyama, "In situ thermal oxidation kinetics in few layer MoS_2," *2D Materials*, vol. 4, no. 2, p. 025058, 2017.

[313] Z. Yang, S. Bhowmick, F. G. Sen, and A. T. Alpas, "Microscopic and atomistic mechanisms of sliding friction of MoS_2: Effects of undissociated and dissociated H_2O," *Applied Surface Science*, vol. 563, p. 150270, 2021.

[314] S. Chen, J. Gao, B. M. Srinivasan, G. Zhang, M. Yang, J. Chai, S. Wang, D. Chi, and Y.-W. Zhang, "Revealing the grain boundary formation mechanism and kinetics during polycrystalline MoS_2 growth," *ACS applied materials & interfaces*, vol. 11, no. 49, pp. 46090–46100, 2019.

[315] T. H. Ly, M. hui Chiu, M. yang Li, J. Zhao, D. J. Perello, M. O. Cichocka, and L. Y. E. T. Al, "in CVD-Grown Monolayer Transition Metal Dichalcogenides," pp. 11401–11408, 2014.

[316] D. Lei, Z. Wu, Y. Zhang, Y. Zhang, J. Zhang, J. Xue, X. Peng, and Y. Wang, "New insight into the inevitable oxidation-dissolution behavior of MoS_2 at humid environments: Unexpected persistent generation of hydroxyl radicals," *Separation and Purification Technology*, vol. 332, p. 125800, 2024.

[317] R. Wang, X. Wang, Z. Zuo, S. Ni, J. Dai, and D. Wang, "Adsorption Equilibrium and Mechanism and of Water Molecule on the Surfaces of Molybdenite (MoS_2) Based on Kinetic Monte-Carlo Method," *Molecules*, vol. 27, no. 24, 2022.

[318] P. Afanasiev and C. Lorentz, "Oxidation of Nanodispersed MoS_2 in Ambient Air: The Products and the Mechanistic Steps," *The Journal of Physical Chemistry C*, vol. 123, no. 12, pp. 7486–7494, 2019.

[319] T. N. Walter, F. Kwok, H. Simchi, H. M. Aldosari, and S. E. Mohney, "Oxidation and oxidative vapor-phase etching of few-layer MoS_2," *Journal of Vacuum Science I& Technology B*, vol. 35, 01 2017. 021203.

[320] H. M. Oh, G. H. Han, H. Kim, J. J. Bae, M. S. Jeong, and Y. H. Lee, "Photochemical reaction in monolayer MoS_2 via correlated photoluminescence, Raman spectroscopy, and atomic force microscopy," *ACS nano*, vol. 10, no. 5, pp. 5230–5236, 2016.

[321] A. Ben-Smith, S. H. Choi, S. Boandoh, B. H. Lee, D. A. Vu, H. T. T. Nguyen, L. A. Adofo, J. W. Jin, S. M. Kim, Y. H. Lee, *et al.*, "Photo-oxidative Crack Propagation in Transition Metal Dichalcogenides," *ACS nano*, 2024.

[322] W. L. Spychalski, M. Pisarek, and R. Szoszkiewicz, "Microscale Insight into Oxidation of Single MoS_2 Crystals in Air," *The Journal of Physical Chemistry C*, vol. 121, no. 46, pp. 26027–26033, 2017.

[323] M. Yamamoto, T. L. Einstein, M. S. Fuhrer, and W. G. Cullen, "Anisotropic Etching of Atomically Thin MoS_2," *The Journal of Physical Chemistry C*, vol. 117, no. 48, pp. 25643–25649, 2013.

[324] K. Kang, K. Godin, Y. D. Kim, S. Fu, W. Cha, J. Hone, and E. H. Yang, "Graphene-Assisted Antioxidation of Tungsten Disulfide Monolayers: Substrate and Electric-Field Effect," *Advanced Materials*, vol. 29, 2017.

[325] R. A. Roshini and E. S. Kannan, "Physical effects of passivation and creation of sulphur vacancy in MoS_2 nanoparticles," *Materials Research Express*, vol. 6, p. 115045, 9 2019.

[326] S. Sovizi, S. Tosoni, and R. Szoszkiewicz, "MoS_2 oxidative etching caught in the act: formation of single (MoO_3)n molecules," *Nanoscale Adv.*, vol. 4, pp. 4517–4525, 2022.

[327] M. Kolíbal, K. Bukvišová, L. Kachtík, A. Zak, L. Novák, and T. Šikola, "Formation of Tungsten Oxide Nanowires by Electron-Beam-Enhanced Oxidation of WS_2 Nanotubes and Platelets," *The Journal of Physical Chemistry C*, vol. 123, no. 14, pp. 9552–9559, 2019.

[328] J. Li, S. Hu, S. Wang, H. Kang, Z. Chen, S. Zhao, Y. Zhang, Y. Sui, and G. Yu, "The degradation of CVD-grown MoS_2 domains in atmospheric environment," *Materials Letters*, vol. 290, p. 129421, 2021.

[329] L. M. Farigliano, P. A. Paredes-Olivera, and E. M. Patrito, "Oxidative etching of S-vacancy defective MoS_2 monolayer upon reaction with O_2," *Phys. Chem. Chem. Phys.*, vol. 23, pp. 10225–10235, 2021.

[330] M. H. Rahman, E. H. Chowdhury, and S. Hong, "High temperature oxidation of monolayer MoS_2 and its effect on mechanical properties: A ReaxFF molecular dynamics study," *Surfaces and Interfaces*, vol. 26, p. 101371, 2021.

[331] S. Li, T. Nishimura, M. Maruyama, S. Okada, and K. Nagashio, "Experimental verification of SO_2 and S desorption contributing to defect formation in MoS_2 by thermal desorption spectroscopy," *Nanoscale Advances*, vol. 5, no. 2, pp. 405–411, 2023.

[332] "Understanding the Independent and Interdependent Role of Water and Oxidation on the Tribology of Ultrathin Molybdenum Disulfide (mos_2)," *Advanced Materials Interfaces*, vol. 6, pp. 1–9, 2019.

[333] D. Kieczka, F. Bussolotti, T. D. Maddumapatabandib, M. Bosman, A. Shluger, A. Regoutz, and K. E. J. Goh, "Unveiling Surface Dynamics: In Situ Oxidation of Defective WS_2," *submitted*, 2024.

[334] C. Carbogno, A. Groß, J. Meyer, and K. Reuter, *O_2 Adsorption Dynamics at Metal Surfaces: Non-adiabatic Effects, Dissociation and Dissipation*, pp. 389–419. Berlin, Heidelberg: Springer Berlin Heidelberg, 2013.

[335] X. Sang, X. Li, W. Zhao, J. Dong, C. M. Rouleau, D. B. Geohegan, F. Ding, K. Xiao, and R. R. Unocic, "In situ edge engineering in two-dimensional transition metal dichalcogenides," *Nature communications*, vol. 9, no. 1, p. 2051, 2018.

[336] W. Fu, M. John, T. D. Maddumapatabandi, F. Bussolotti, Y. S. Yau, M. Lin, and K. E. Johnson Goh, "Toward Edge Engineering of Two-Dimensional Layered Transition-Metal Dichalcogenides by Chemical Vapor Deposition," *ACS Nano*, vol. 17, no. 17, pp. 16348–16368, 2023. PMID: 37646426.

[337] O. T. Unke, S. Chmiela, H. E. Sauceda, M. Gastegger, I. Poltavsky, K. T. Schütt, A. Tkatchenko, and K.-R. Müller, "Machine Learning Force Fields," *Chemical Reviews*, vol. 121, no. 16, pp. 10142–10186, 2021. PMID: 33705118.

[338] I. Batatia, P. Benner, Y. Chiang, A. M. Elena, D. P. Kovács, J. Riebesell, X. R. Advincula, M. Asta, M. Avaylon, W. J. Baldwin, and et al., "A foundation model for atomistic materials chemistry," *arXiv preprint arXiv:2401.00096*, 2023.

[339] C. Panosetti, S. B. Anniés, C. Grosu, S. Seidlmayer, and C. Scheurer, "DFTB Modeling of Lithium-Intercalated Graphite with Machine-Learned Repulsive Potential," *The Journal of Physical Chemistry A*, vol. 125, no. 2, pp. 691–699, 2021. PMID: 33426892.

[340] S. Anniés, C. Panosetti, M. Voronenko, D. Mauth, C. Rahe, and C. Scheurer, "Accessing Structural, Electronic, Transport and Mesoscale Properties of Li-GICs via a Complete DFTB Model with Machine-Learned Repulsion Potential," *Materials*, vol. 14, no. 21, 2021.

[341] C. Panosetti, Y. Lee, A. Samtsevych, and C. Scheurer, "Black box vs gray box: Comparing GAP and GPrep-DFTB for ruthenium and ruthenium oxide," *The Journal of Chemical Physics*, vol. 158, p. 224115, 06 2023.

[342] C. Panosetti, A. Engelmann, L. Nemec, K. Reuter, and J. T. Margraf, "Learning to Use the Force: Fitting Repulsive Potentials in Density-Functional Tight-Binding with Gaussian Process Regression," *Journal of*

Chemical Theory and Computation, vol. 16, no. 4, pp. 2181–2191, 2020. PMID: 32155065.

[343] P. Koskinen and V. Mäkinen, "Density-functional tight-binding for beginners," *Computational Materials Science*, vol. 47, no. 1, pp. 237–253, 2009.

[344] F. Spiegelman, N. Tarrat, J. Cuny, L. Dontot, E. Posenitskiy, C. Martí, A. Simon, and M. Rapacioli, "Density-functional tight-binding: basic concepts and applications to molecules and clusters," *Advances in Physics: X*, vol. 5, no. 1, p. 1710252, 2020. PMID: 33154977.

[345] M. Wahiduzzaman, A. F. Oliveira, P. Philipsen, L. Zhechkov, E. van Lenthe, H. A. Witek, and T. Heine, "DFTB Parameters for the Periodic Table: Part 1, Electronic Structure," *Journal of Chemical Theory and Computation*, vol. 9, no. 9, pp. 4006–4017, 2013. PMID: 26592396.

[346] C.-P. Chou, Y. Nishimura, C.-C. Fan, G. Mazur, S. Irle, and H. A. Witek, "Automatized Parameterization of DFTB Using Particle Swarm Optimization," *Journal of Chemical Theory and Computation*, vol. 12, no. 1, pp. 53–64, 2016. PMID: 26587758.

[347] R. Eberhart and J. Kennedy, "A new optimizer using particle swarm theory," in *MHS'95. Proceedings of the Sixth International Symposium on Micro Machine and Human Science*, pp. 39–43, 1995.

[348] M. Elstner, "The SCC-DFTB method and its application to biological systems," *Theoretical Chemistry Accounts*, vol. 116, pp. 316–325, 2006.

[349] D. Freitas, L. G. Lopes, and F. Morgado-Dias, "Particle swarm optimisation: a historical review up to the current developments," *Entropy*, vol. 22, no. 3, p. 362, 2020.

[350] P. Giannozzi, S. Baroni, N. Bonini, M. Calandra, R. Car, C. Cavazzoni, D. Ceresoli, G. L. Chiarotti, M. Cococcioni, I. Dabo, *et al.*, "QUANTUM ESPRESSO: a modular and open-source software project for quantum

simulations of materials," *Journal of physics: Condensed matter*, vol. 21, no. 39, p. 395502, 2009.

[351] P. Giannozzi, O. Andreussi, T. Brumme, O. Bunau, M. B. Nardelli, M. Calandra, R. Car, C. Cavazzoni, D. Ceresoli, M. Cococcioni, *et al.*, "Advanced capabilities for materials modelling with Quantum ESPRESSO," *Journal of physics: Condensed matter*, vol. 29, no. 46, p. 465901, 2017.

[352] B. Hourahine, B. Aradi, V. Blum, F. Bonafe, A. Buccheri, C. Camacho, C. Cevallos, M. Deshaye, T. Dumitrică, A. Dominguez, *et al.*, "DFTB+, a software package for efficient approximate density functional theory based atomistic simulations," *The Journal of chemical physics*, vol. 152, no. 12, 2020.

Appendix A

A.1 JPD 4$\mathring{A}$ From the Surface

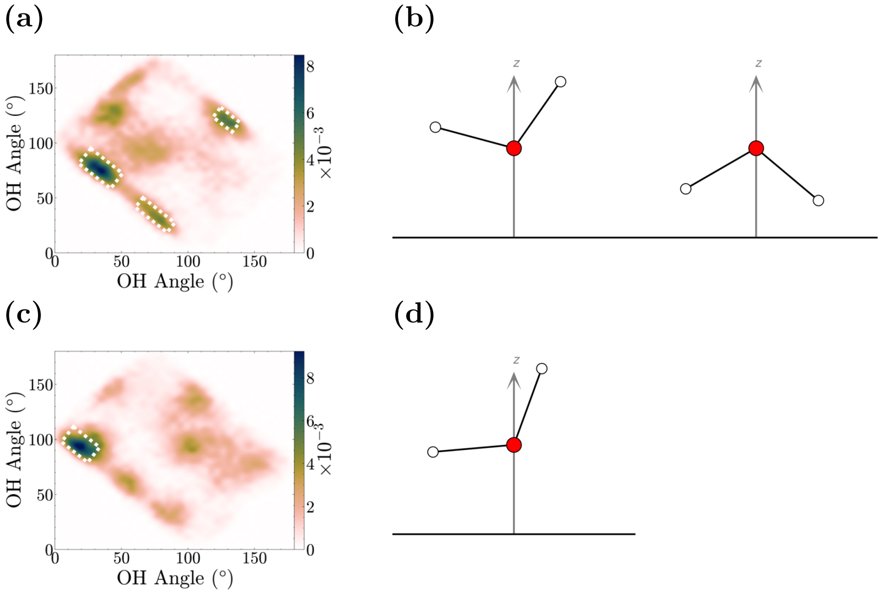

Figure A.1 The probability distribution for water molecules 4 $\mathring{A}$ away from the SiO_2 surface at the SiO_2/H_2O interface. Water angles for **a-b)** two layers, and **c-d)** three layers of water. The first column (**a,c**) is the OH-OH angle for each system, the right-hand side (**b,d**) is the predicted orientations of water from the respective JPD graphs. The colour bar shows the probability.

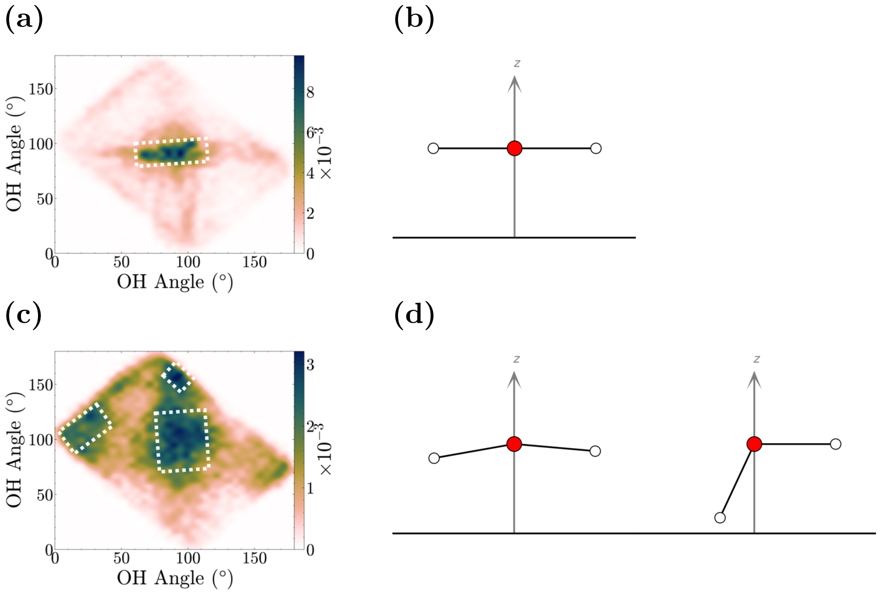

Figure A.2 The probability distribution for water molecules 4 Å away from the WS_2 surface at the WS_2/H_2O interface. Water angles for **a-b)** two layers, and **c-d)** three layers of water. The first column (**a,c**) is the OH-OH angle for each system, the right-hand side (**b,d**) is the predicted orientations of water from the respective JPD graphs. The colour bar shows the probability.

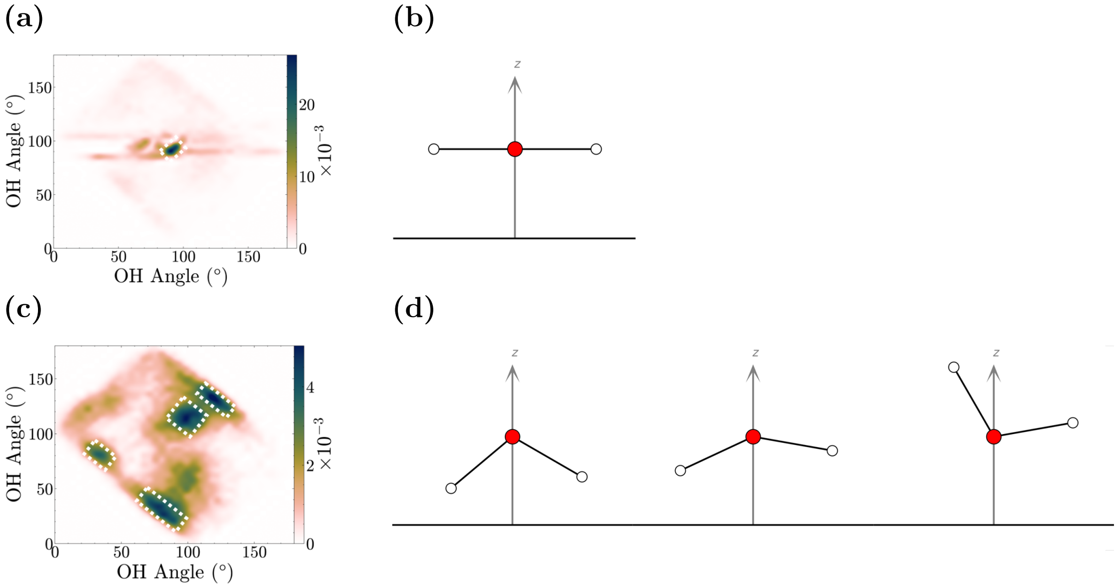

Figure A.3 The probability distribution for water molecules 4 Å away from the SiO_2 surface at the $SiO_2/H_2O/WS_2$ interface. Water angles for **a-b)** two layer, and **c-d)** three layers of water. The first column (**a,c**) is the OH-OH angle for each system, the right-hand side (**b,d**) is the predicted orientations of water from the respective JPD graphs. The colour bar shows the probability.

A.2 1D Density Profile Peaks

Table A.1: Peak positions of the 1D density profile ($\mathring{A}$) with shoulders given in brackets. The zero point from which the peaks originate corresponds to the top of the SiO_2 surface for SiO_2/H_2O and $SiO_2/H_2O/WS_2$ interfaces, and the closest sulfur plane for the WS_2/H_2O interface. Broad peaks are denoted with ^{b}.

Interface	No. Water Layers	Water Atom	P^1	P^2	P^3	P^4	P^5
SiO_2/H_2O	One	H_w	2.2 (3.2)				
		O_w	2.5				
	Two	H_w	2.4	4.0 (5.2)			
		O_w	2.7	4.7			
	Three	H_w	2.0	2.8	3.9	5.6	8.0
		O_w	(2.2) 2.7	5.5	7.3^b		
WS_2/H_2O	One	H_w	(2.2) 3.1				
		O_w	3.0				
	Two	H_w	(2.2) 3.1	4.0	5.2		
		O_w	3.2	4.6			
	Three	H_w	(2.0) 2.8	6.1	7.6	10.0^b	
		O_w	3.0	(5.2) 5.8 (7.0)	10.0^b		
$SiO_2/H_2O/WS_2$	One	H_w	1.9	3.0			
		O_w	2.2				
	Two	H_w	2.0	4.3 (5.5)			
		O_w	2.4^b	4.7			
	Three	H_w	2.0	3.6	5.5	(7.8) 8.8 (9.6)	
		O_w	(2.2) 2.8	4.9	7.2	8.9	

A.3 HBonds Over Time

The evolution of H_w-O_w HBonds over time indicates that at interfaces with SiO_2, HBonding is minimal for a single water layer. In the confined system, no HBonding is detected after 9 ps when using the geometric criteria. This highlights the reduced significance of H_w-O_w HBonds in water properties at one-layer coverage.

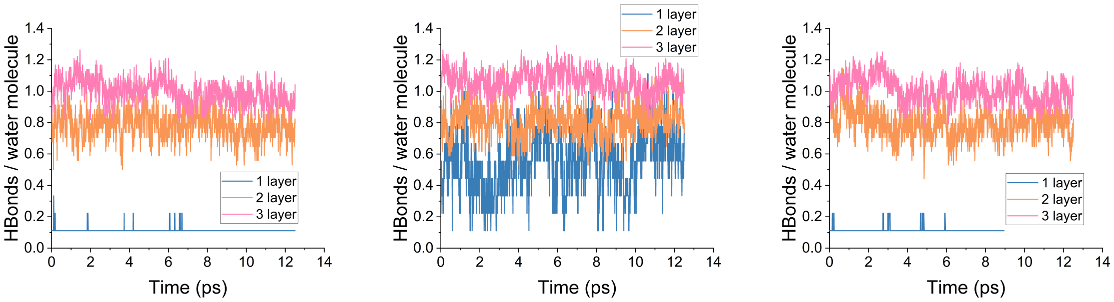

(a) **(b)** **(c)**

Figure A.4 Hydrogen bonding over time of **a)** SiO_2/H_2O, **b)**WS_2/H_2O, and **c)**$WS_2/H_2O/SiO_2$.

A.4 MSD by Distance to Surface

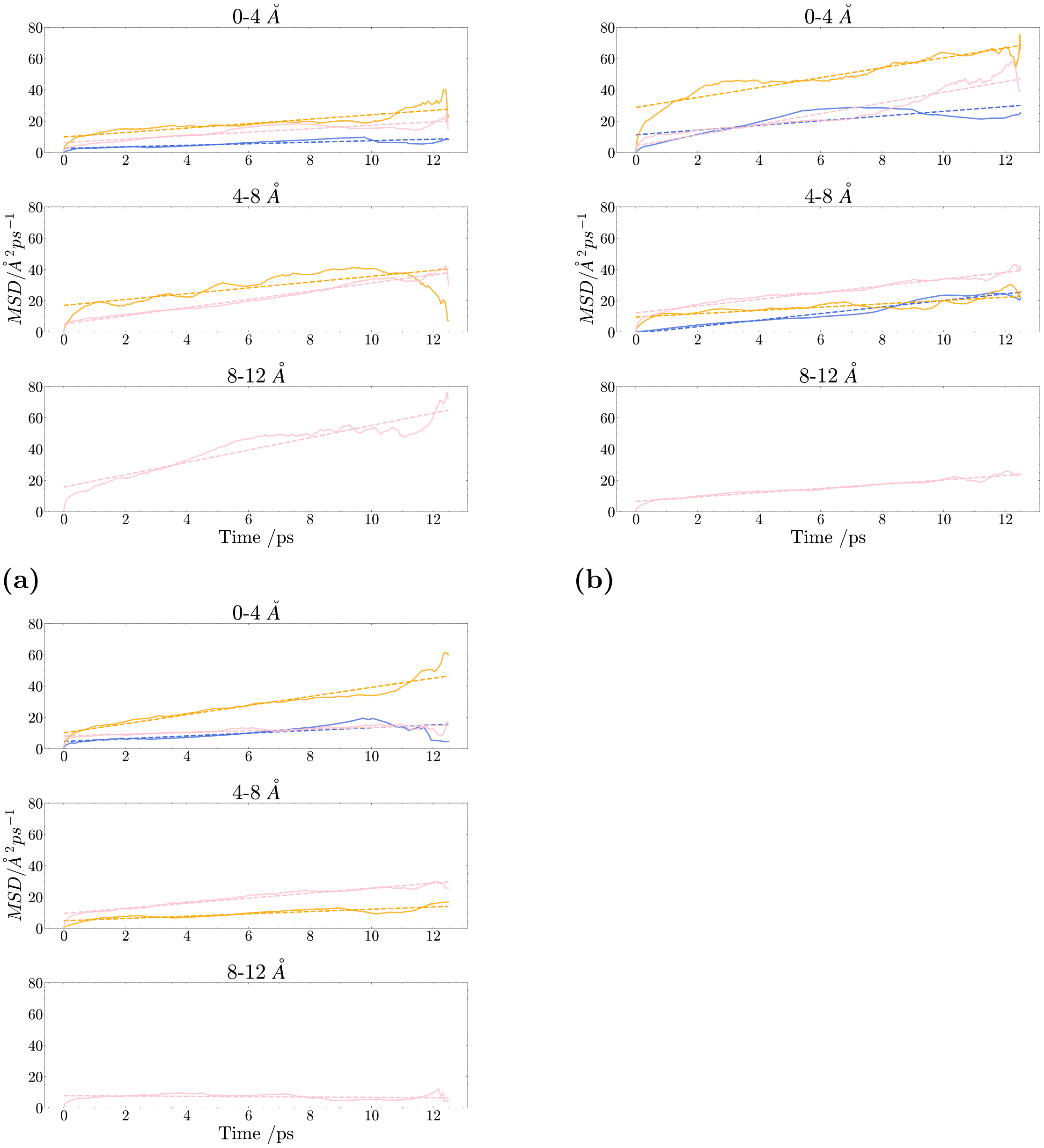

(a)

(b)

(c)

Figure A.5 XY MSD for all interfaces split into the water distance from surface, the interface layers here are described by the water molecule density. **a)** SiO_2/H_2O,**b)** WS_2/H_2O and, **c)** $SiO_2/H_2O/WS_2$. The different water layers are given by the colours: one-layer: blue, two-layers: orange, three-layers: pink.

Appendix B

B.1 Average PDoS, with respect to vacuum

For each snapshot PDoS, all eigenvalues were referenced to their vacuum level:

$$\epsilon_f = \epsilon_i - E_{vac} \tag{B.1}$$

Where ϵ_f is the final eigenvalue, ϵ_i is the original eigen value, and E_{vac} is the vacuum energy level. The vacuum energy level is set to 0 eV in Figure B.1. The snapshots were then averaged and a Gaussian smear of 0.1 was applied.

The hydrogen and oxygen contributions were separated on the basis of the material to which they belonged. H_w and O_w are hydrogen and oxygen from water, H_t and O_t are the hydrogen and oxygen from the top silanol groups that interface with water, H_b and O_b are from the bottom silanol groups that interface with vacuum, and finally, O is from SiO_2.

The band gap of WS_2 can be seen clearly in Figure B.1, with the top of the VBM at $\approx$ 6 eV in all water layers.

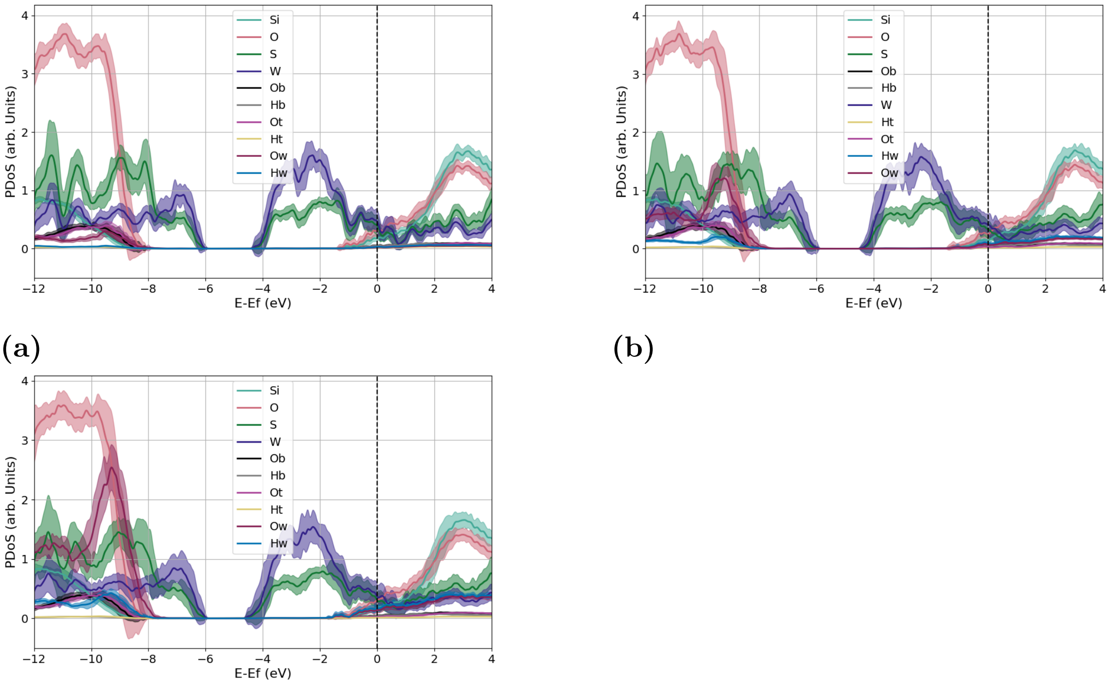

(a)

(b)

(c)

Figure B.1 The average PDoS of all snapshots from AIMD calculations. The 0 point marked with a dashed vertical line shows the vacuum energy level. From the systems: **a**) 1 layer, **b**) 2 layers **c**) 3 layers

B.2 LDoS: Relative atomic positions

The relative position of the interface $SiO_2/H_2O/WS_2$ atoms compared to the LDoS are shown in Figure B.2. The shared axis highlight the averaged interface position compared to the LDoS, with the 0.1 threshold highlighting the spatial dependence of CBM offset and VBM offset. The rest of the SiO_2 band alignment can be seen compared to the 20 $\mathring{A}$ cutoff as shown in the main text.

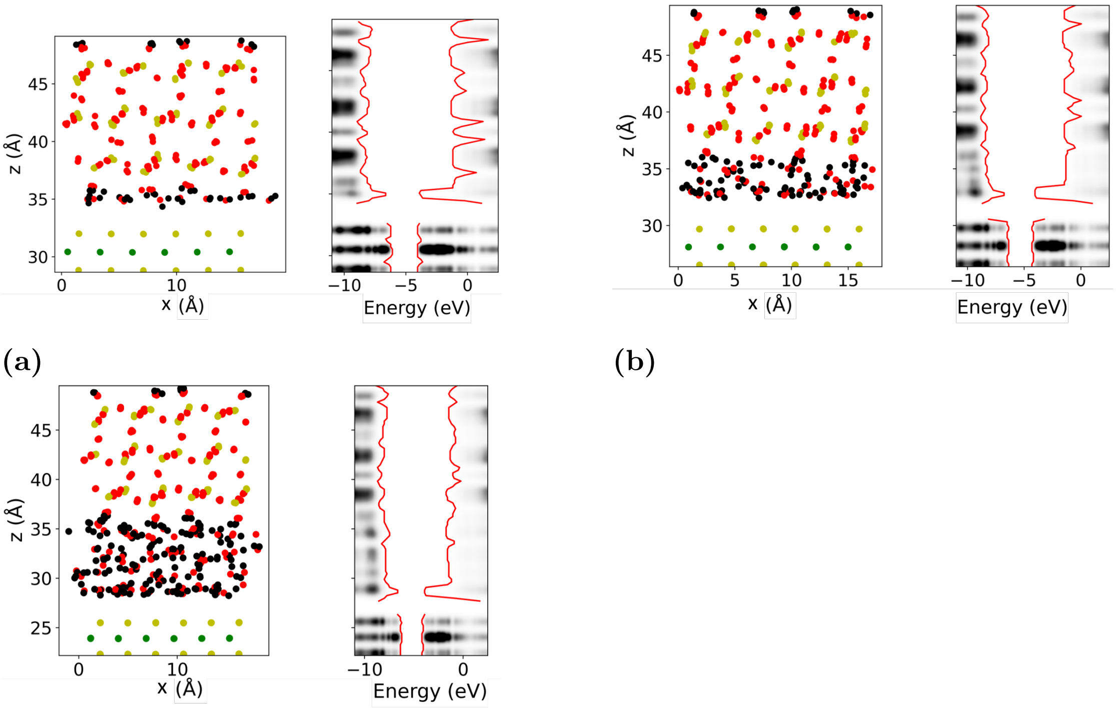

(a)

(b)

(c)

Figure B.2 Comparison of average position of the $SiO_2/H_2O/WS_2$ to the corresponding LDoS with a threshold value of 0.1. The systems shown are **a**) 1 water layer, **b**) 2 water layers, **c**) 3 water layers.

Appendix C

C.1 Impact of Water Energy Reference

The choice of energy reference for water significantly affects both adsorption and total energy change values. When only a single water molecule is present, these energy gains are higher due to the absence of hydrogen bonding. Conversely, in systems with extensive hydrogen bonding, the energy gains are lowered as the hydrogen bonds must be overcome to interact with WS_2, as shown in Figure C.1. Since neither extreme case—isolated water molecules nor bulk ice bonding—accurately represents the conditions studied, I selected a reference potential that accounts for the number of water molecules in each system. This approach, based on the geometry optimised energy of N water molecules (Equation 7.1), ensures that only the hydrogen bonding naturally present in a given system is considered. For example, in a system with two water molecules, the total energy gain reflects their interaction but excludes additional stabilisation from bulk water or ice structures. However, using different energy references means that adhesion and total energy change values across different N water systems are less directly comparable. Instead, they should be interpreted relative to the environmental conditions they represent, such as varying humidity levels. But as seen in Figure C.1, the same trends in adhesion energy and total energy change are seen with the same reference energy as well as with the energy reference accounting from the environmental conditions.

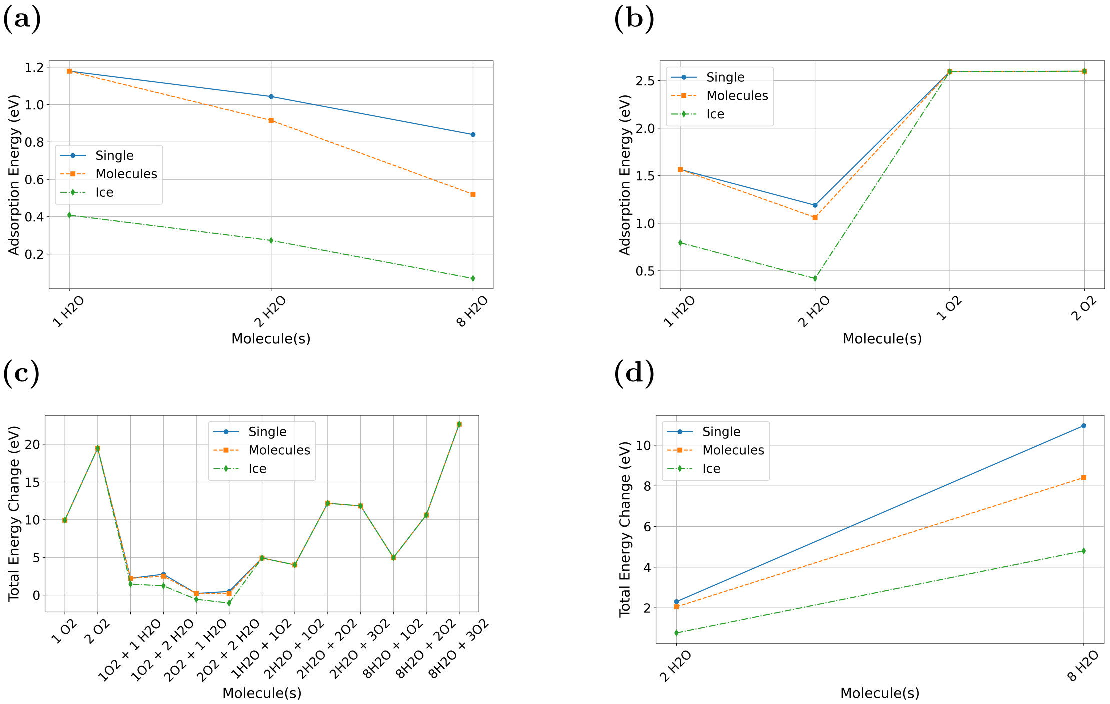

Figure C.1 Comparison of **a, b**) adsorption energies and **c, d**) total energy changes at the **a, c**) W-ZZ edge and **b, d**) armchair WS_2 edge, depending on the water reference energy (E_{Nmol}). The reference energies are given in the legend. "Single" refers to a single water molecule in vacuum, "Molecules" represents N water molecules optimised together, and "Ice" is the bulk ice Ih phase.

C.2 Projected Density of States

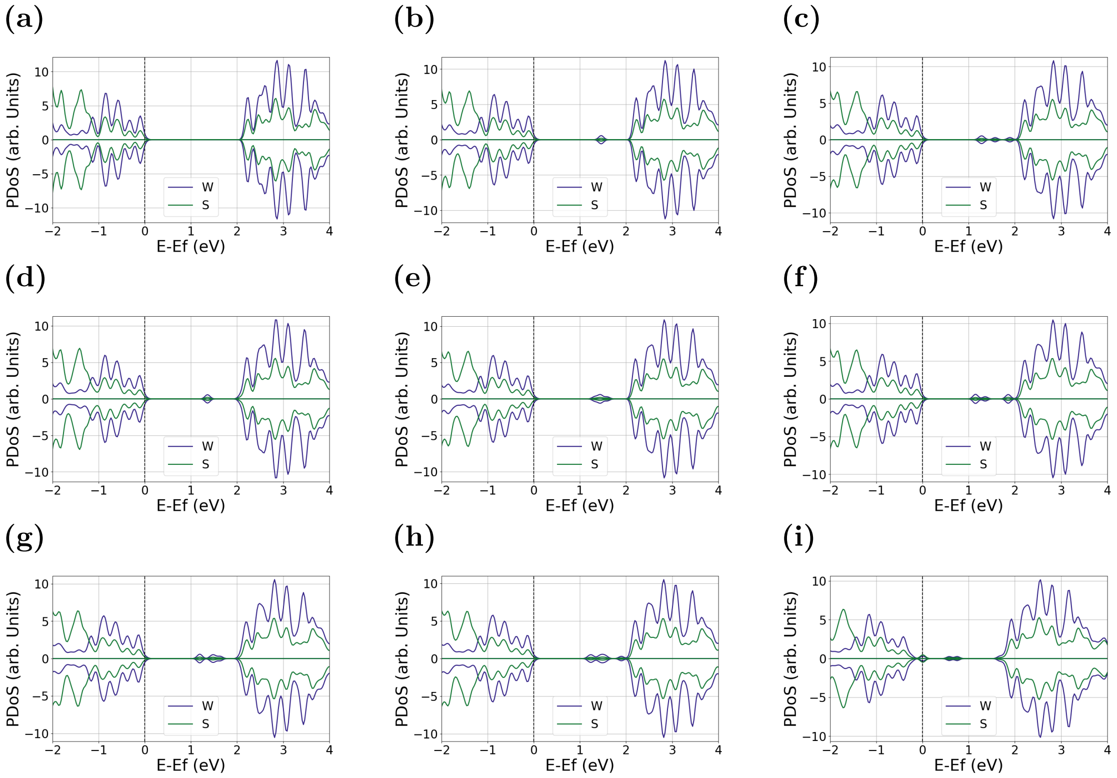

Figure C.2 All PDoS of sulphur vacancies used in this work. **a)** is a pristine WS$_2$ **b)** mono vacancy V$_S$ **c-e)** are di vacancies: **c)** sulphur vacancies are adjacent V_{2S}^{A}, **d)** vacancies are on opposite planes V_{2S}^{P}, and **f)** Sulphur vacancies are separated by a sulphur atom V_{2S}^{S}. **f-h)** are tri vacancies: **f)** is a hole V_{3S}, **g)** sulphur vacancies are in a line V_{3S}^{L}, **h)** Sulphur vacancies are separated by a sulphur atom V_{3S}^{LS}. **i)** the v_{WS_2} vacancy. Corresponding structures are found in Figure 7.4

C.3 Bader Charge Difference of Sulphur

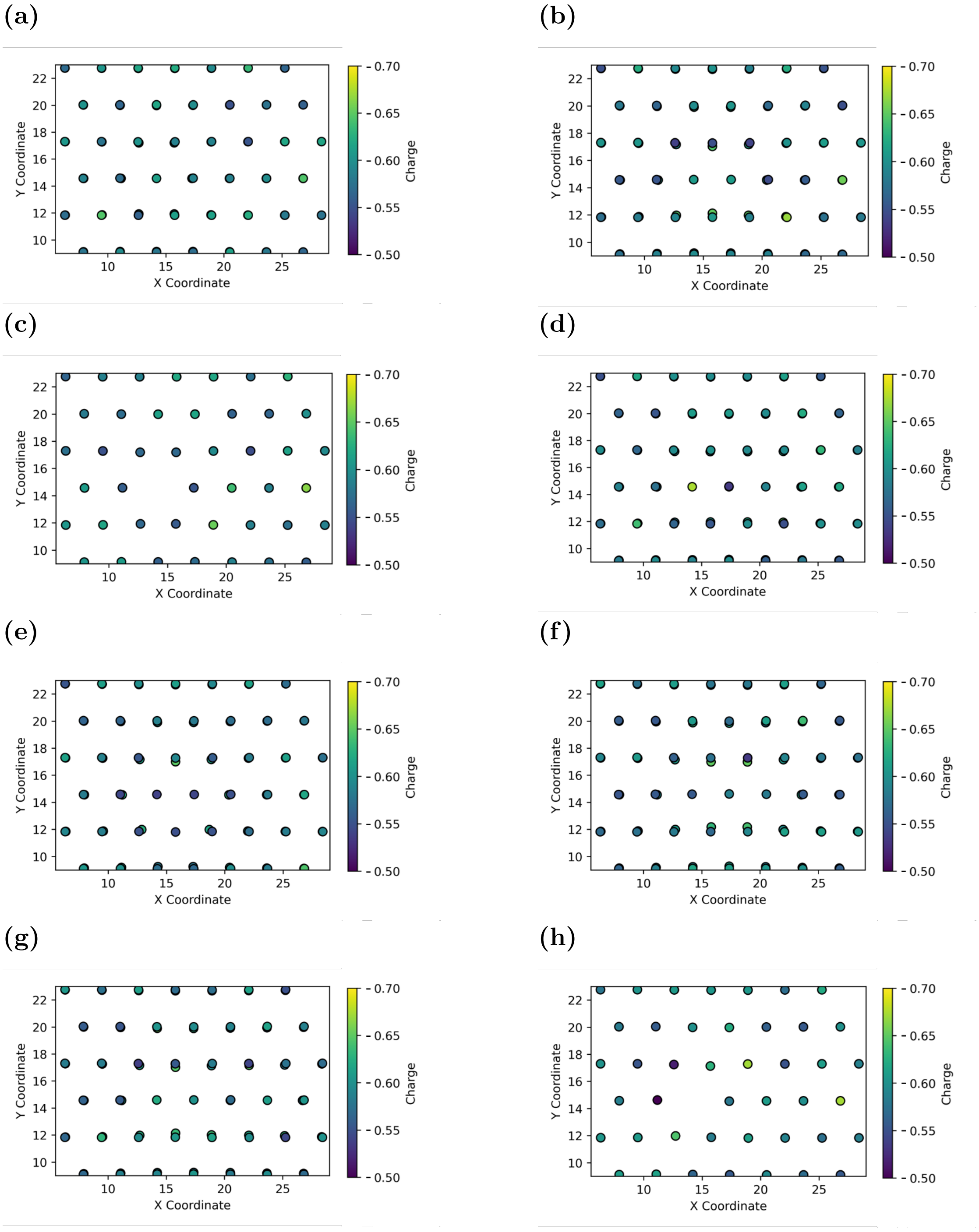

Figure C.3 Bader charges on sulphur surrounding the vacancies used in this work. **a)** V_S, **b)** V^A_{2S}, **c)** V^P_{2S}, **d)** V^S_{2S}, **f)** V^T_{3S}, **f)** V^L_{3S}, **g)** V^{LS}_{3S}, **h)** V_{WS_2}. Corresponding structures are found in Figure 7.4.

C.4 Bader Charge Difference of Tungsten, Larger Defects

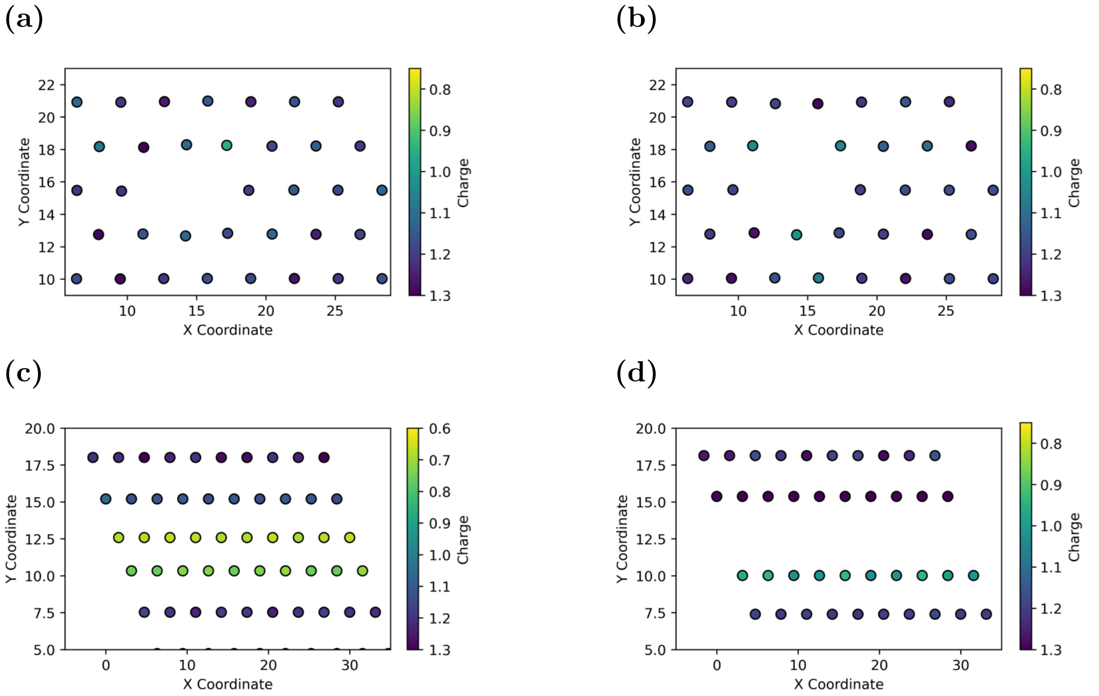

Figure C.4 Bader charges on tungsten for larger defects. **a)** $V_{2(WS_2)}$,**b)** $V_{3(WS_2)}$, **c)** $V_{10(S)}$, **d)** $V_{10(WS)}$. It is important to note the change in scale of the colour map in **c**); this is due to the large change in δe for this defect.

C.5 Snapshot from $8H_2O$ and $3O_2$ at the W-ZZ Edge

Two snapshots are chosen to illustrate the exact geometry and Bader charges during the dissociation of water molecules at the W-ZZ edge with $8H_2O$ and $3O_2$ molecules during geometry optimisation. In Figure C.5a, the chain of proton hopping can be seen in the top left corner, highlighted with an orange circle. This proton hopping can be seen in the corresponding Bader charges (Figure C.5b), with positively charged hydrogen in-between water molecules. Furthermore, the formation of O_2-H is indicated in the black circle, demonstrating the initiation of bonding between the oxygen molecule and a hydrogen from nearby water. This results in a more negatively charged oxygen atom and, consequently, a dipole is formed across the O-O bond.

Figure C.5c highlights the impact of W-O bond formation, marked by a black circle. Bader charge analysis in Figure C.5d shows that tungsten becomes more positively charged upon forming this bond. This supports the discussion in the main text, which suggests that less positively charged tungsten is more prone to oxidation. Here, oxygen increases tungsten's positive charge, effectively passivating the dangling bond.

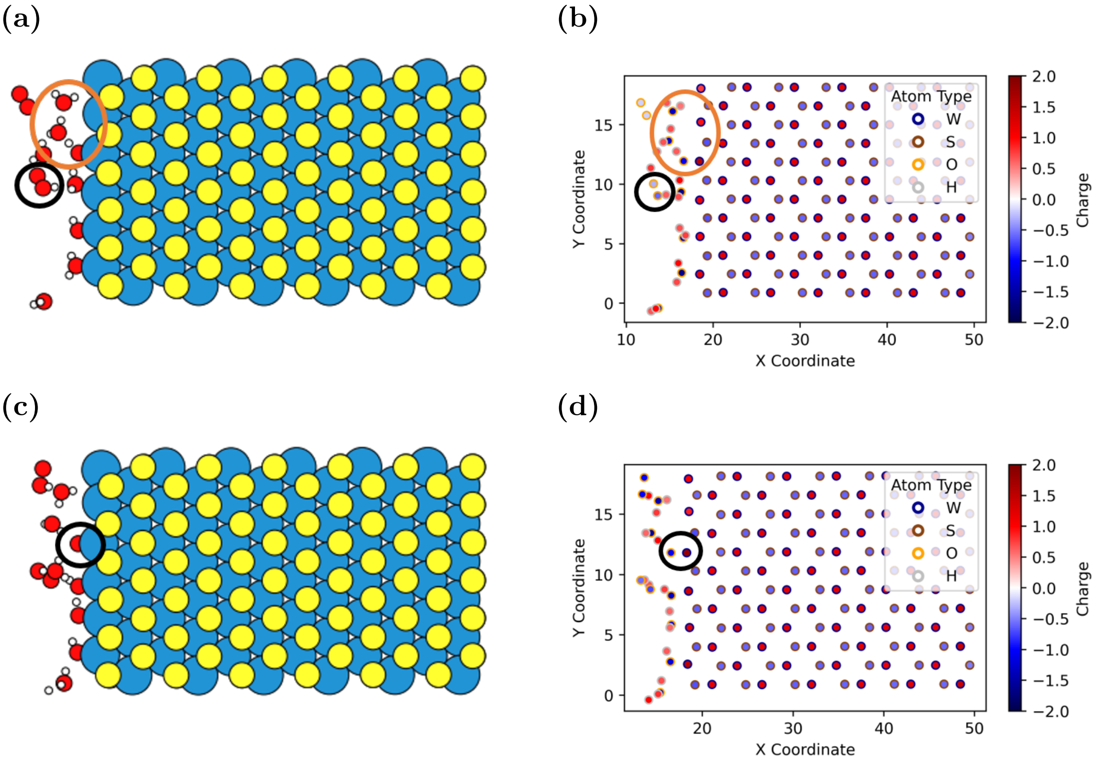

Figure C.5 Comparison of the geometry of water and oxygen at the W-ZZ edge with 8H_2O and 3O_2 molecules. **a-b**) are after 30 optimised steps, and **c-d**) are after 100 optimised steps. Black and Orange circles are provided to highlight areas discussed in the text.

C.6 Bader Charge Difference of Sulphur, Armchair Edge

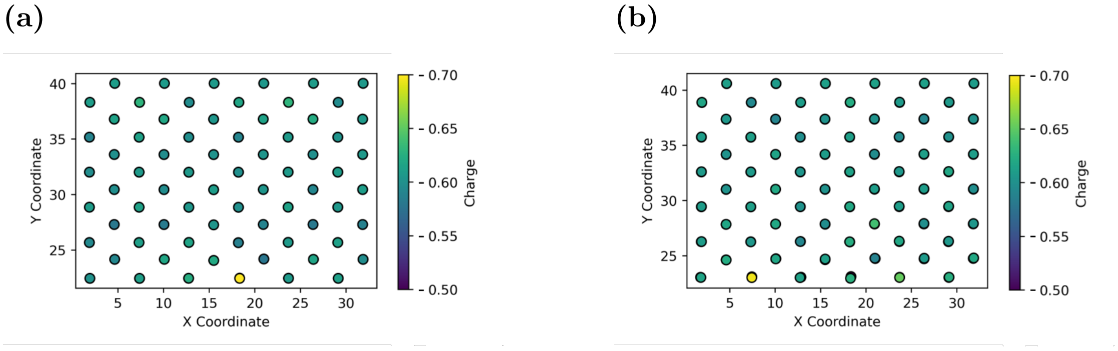

Figure C.6 Bader charges on sulphur at the WS_2 armchair edge where H_3O^+ is formed with **a**) two water molecules and **b**) eight water molecules. The stabilisation of H_3O^+ can be clearly seen by the increased e on the sulphur atoms (yellow atoms).

Appendix D

D.1 PSO Electronic Parameters

Table D.1: Optimised electronic parameters used in the skfs from PSO. Brackets for oxygen and hydrogen show the different training sets used.

Orbital	Param	W	S	H (WSOH)	H (SiOH)	O (WSOH)	O (SiOH)	Si
1s	r_0	-	-	2.79	2.69	-	-	-
	s	-	-	4.77	8.01	-	-	-
2s	r_0	-	-	-	-	4.74	6.06	-
	s	-	-	-	-	3.12	3.95	
2p	r_0	-	-	-	-	3.71	7.33	-
	s	-	-	-	-	6.18	4.31	
3s	r_0	-	6.95	-	-	-	-	4.11
	s	-	4.67	-	-	-	-	5.84
3p	r_0	-	3.07	-	-	-	-	3.21
	s	-	5.45	-	-	-	-	4.48
3d	r_0	-	4.61	-	-	1.41	1.85	6.28
	s	-	5.98	-	-	4.13	2.73	4.27
4f	r_0	2.84	-	-	-	-	-	-
	s	4.82	-	-	-	-	-	-
5d	r_0	4.63	-	-	-	-	-	-
	s	6.13	-	-	-	-	-	-
6s	r_0	2.54	-	-	-	-	-	-
	s	5.03	-	-	-	-	-	-
6p	r_0	3.37	-	-	-	-	-	-
	s	4.61	-	-	-	-	-	-

D.2 GPrep Training

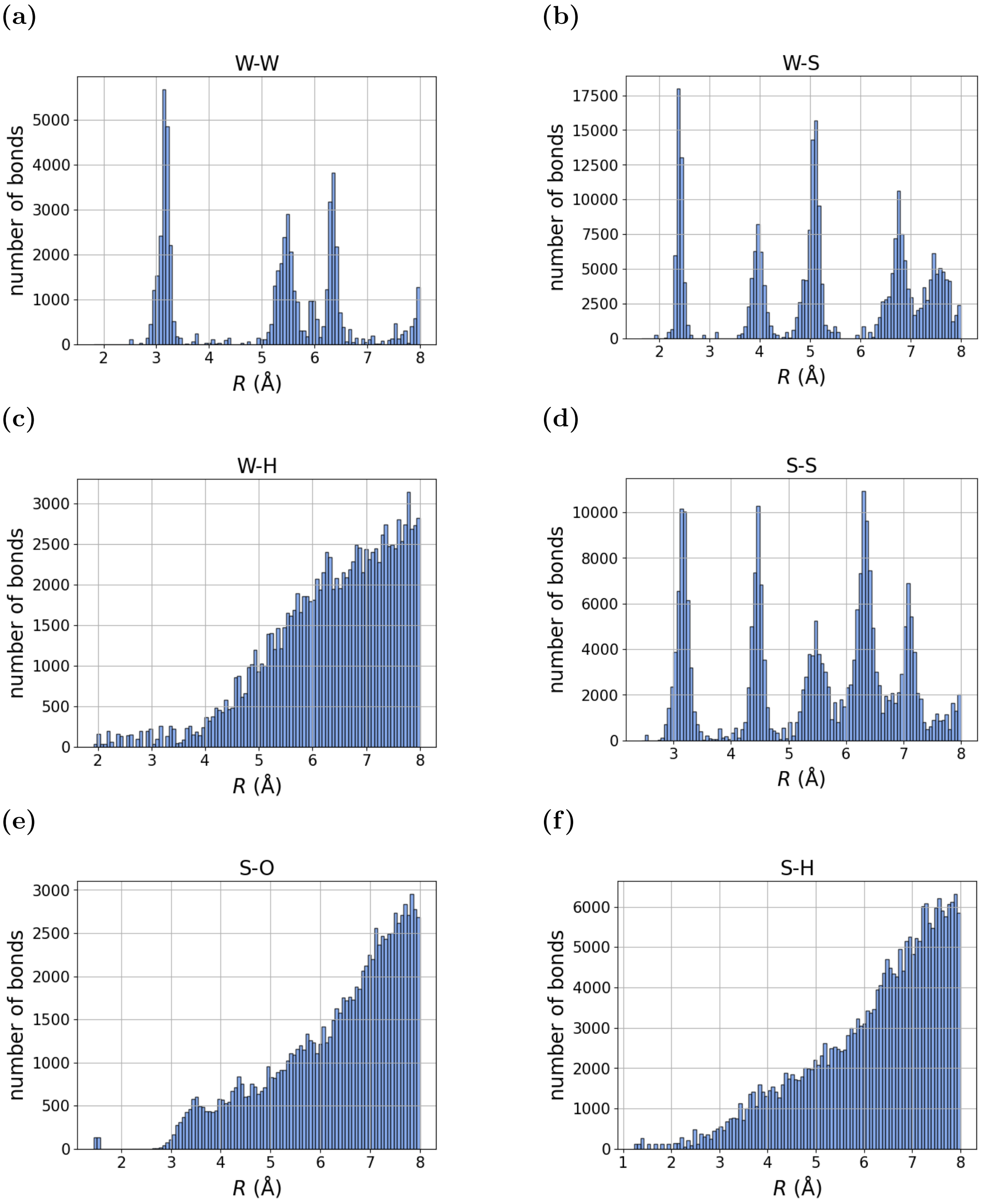

Figure D.1 The bond training data sets for the Gprep training data set. For ease of reading, the type of bond is given in the title i.e. **a**) are the W-W bond distances.

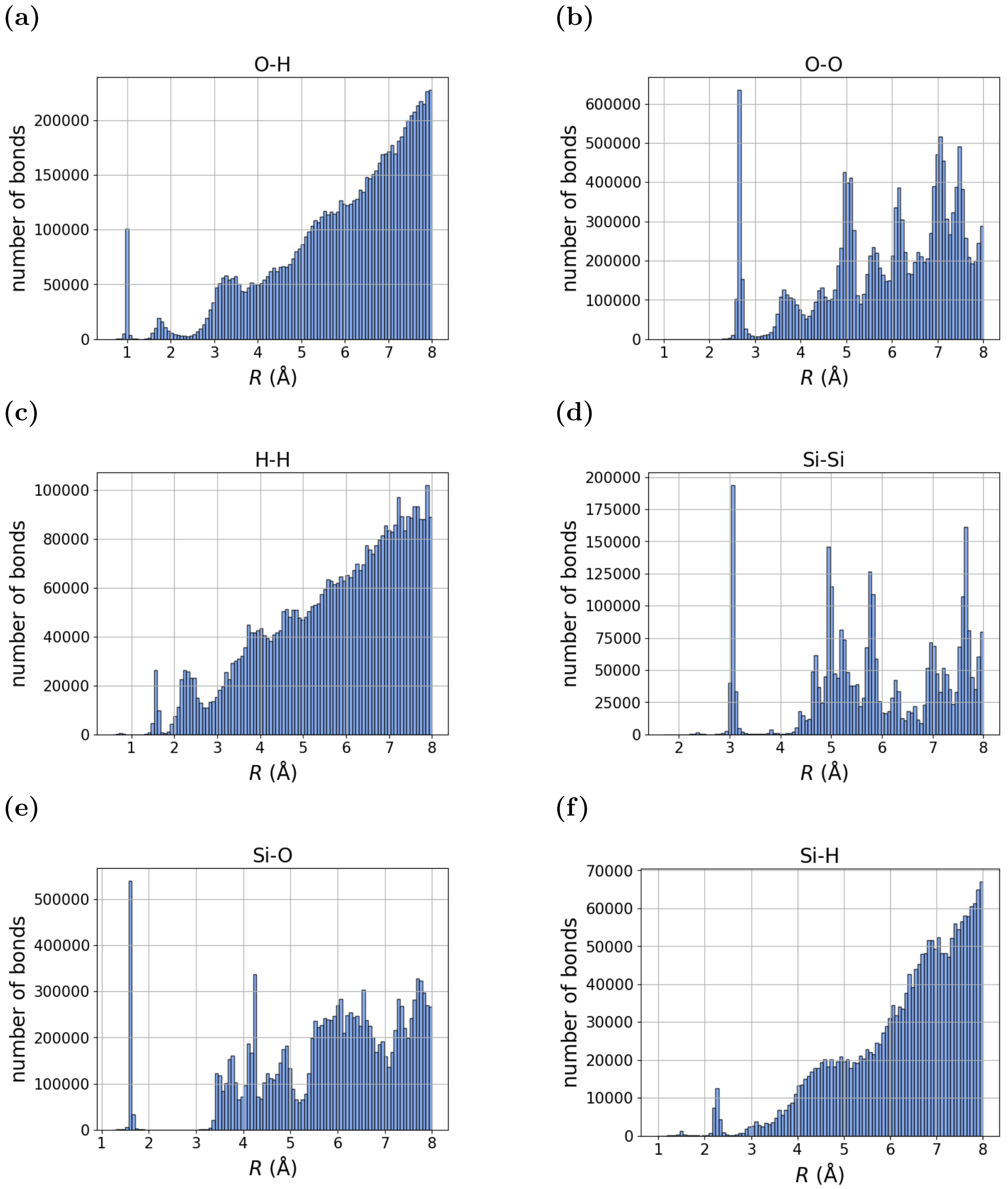

Figure D.2 Continuation of the bond training data sets for the Gprep training data set in Figure D.1.

Table D.2: Atom-atom parameters used to train GPrep potentials. N is the number of sparse points used in training the repulsive potential.

Param.	W-W	W-S	W-H	W-O	S-S	S-H	S-O	O-O	O-H	H-H	Si-Si	Si-H	Si-O
N	40	40	20	20	20	20	20	20	20	20	40	20	20
Start (Å)	2.0	1.9	1.3	1.0	1.2	1.5	1.5	1.5	0.5	0.5	1.5	1.0	1.0
Cutoff (Å)	5.5	4.5	4.4	4.5	4.6	3.7	4.5	3.1	2.0	1.75	5.5	2.55	3.5

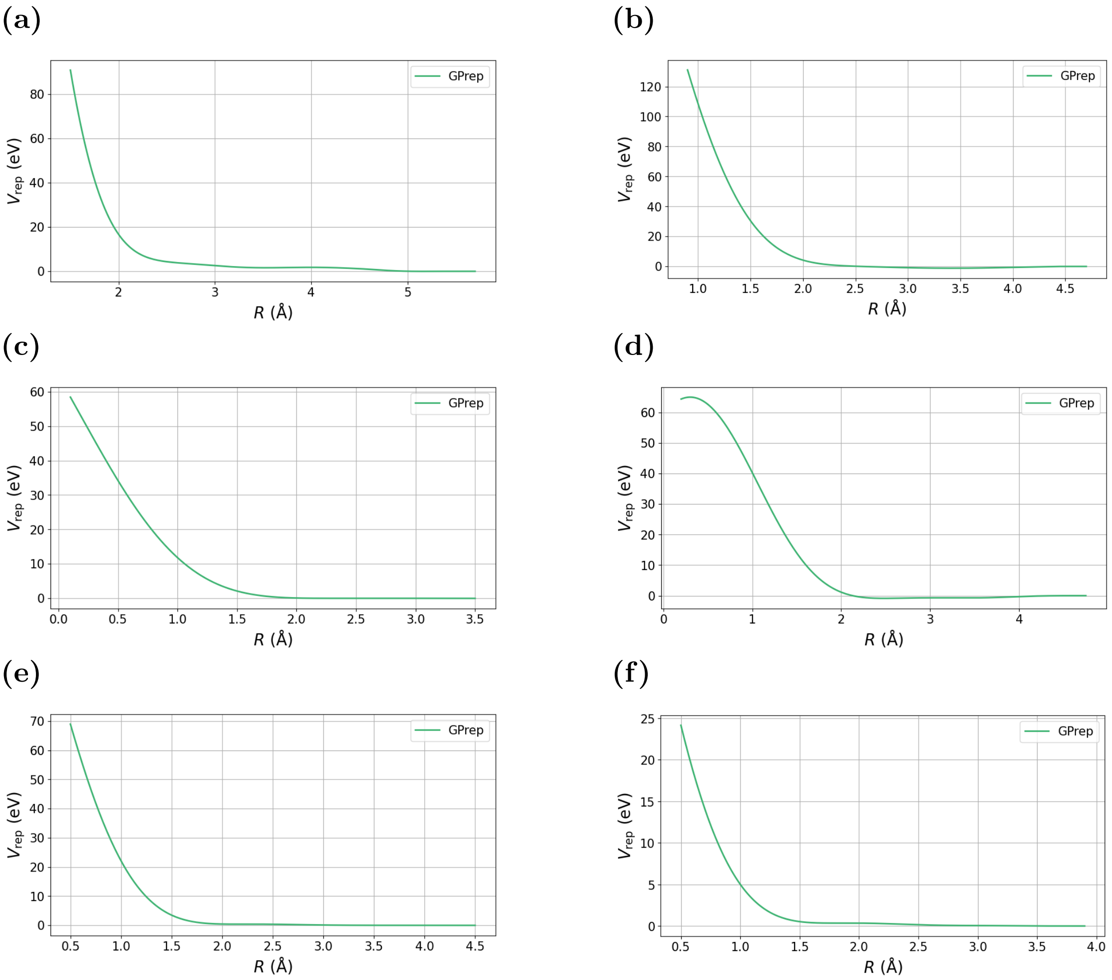

Figure D.3 The functional form of the repulsive potential for tungsten and sulphur: **a**) W-W, **b**) W-S, **c**) W-H, **d**) S-S, **e**) S-O, **f**) S-H.

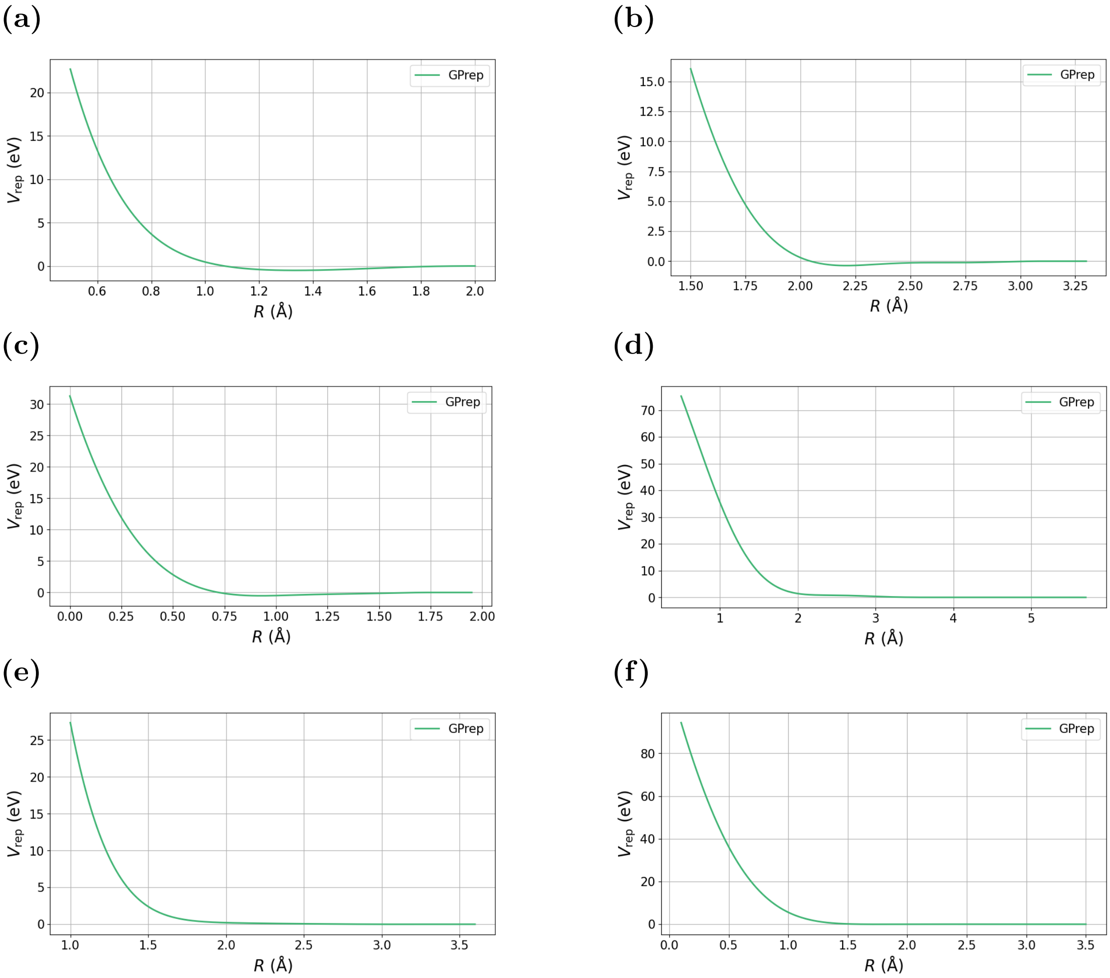

Figure D.4 A continuation of the functional form of the repulsive potential for silicon, oxygen and hydrogen: **a**) O-H, **b**) O-O, **c**) H-H, **d**) Si-Si, **e**) Si-O, **f**) Si-H.